REPORT DOCUMENTATION PAGE

Form Approved OMB NO. 0704-0188

The public reporting burden for this collection of information is estimated to average 1 hour per response, including the time for reviewing instructions, searching existing data sources, gathering and maintaining the data needed, and completing and reviewing the collection of information. Send comments regarding this burden estimate or any other aspect of this collection of information, including suggesstions for reducing this burden, to Washington Headquarters Services, Directorate for Information Operations and Reports, 1215 Jefferson Davis Highway, Suite 1204, Arlington VA, 22202-4302. Respondents should be aware that notwithstanding any other provision of law, no person shall be subject to any oenalty for failing to comply with a collection of information if it does not display a currently valid OMB control number.
PLEASE DO NOT RETURN YOUR FORM TO THE ABOVE ADDRESS.

1. REPORT DATE (DD-MM-YYYY)	2. REPORT TYPE	3. DATES COVERED (From - To)
28-02-2016	Final Report	20-Jun-2012 - 19-Jun-2015

4. TITLE AND SUBTITLE

Final Report: A Multiscale Atomistic Method for Long-Range Electrical Interactions with Application to Multiphysics Calculations in Functional Materials

5a. CONTRACT NUMBER
W911NF-12-1-0156

5b. GRANT NUMBER

5c. PROGRAM ELEMENT NUMBER
611102

6. AUTHORS

Kaushik Dayal

5d. PROJECT NUMBER

5e. TASK NUMBER

5f. WORK UNIT NUMBER

7. PERFORMING ORGANIZATION NAMES AND ADDRESSES

Carnegie Mellon University
5000 Forbes Avenue

Pittsburgh, PA 15213 -3815

8. PERFORMING ORGANIZATION REPORT NUMBER

9. SPONSORING/MONITORING AGENCY NAME(S) AND ADDRESS (ES)

U.S. Army Research Office
P.O. Box 12211
Research Triangle Park, NC 27709-2211

10. SPONSOR/MONITOR'S ACRONYM(S)
ARO

11. SPONSOR/MONITOR'S REPORT NUMBER(S)
61856-MA-YIP.4

12. DISTRIBUTION AVAILIBILITY STATEMENT

Approved for Public Release; Distribution Unlimited

13. SUPPLEMENTARY NOTES

The views, opinions and/or findings contained in this report are those of the author(s) and should not contrued as an official Department of the Army position, policy or decision, unless so designated by other documentation.

14. ABSTRACT

We aim to develop a robust and scalable strongly-coupled multiscale atomistic method with electric field-matter interactions that can scale to multimillions of atoms. Mathematically, we need to obtain efficient and accurate numerical methods to compute forces and energies in large discrete systems where the particle interaction is nonlinear and long-range. This is the mathematical idealization of a crystalline system that is close to periodic in much of the domain, but is defected in certain regions. The defects have an important role in functional materials, and we are trying to understand the structure and response of defects starting from physics-based models

15. SUBJECT TERMS

multiscale atomistics, electromagnetic interactions, functional materials

16. SECURITY CLASSIFICATION OF:			17. LIMITATION OF ABSTRACT	15. NUMBER OF PAGES	19a. NAME OF RESPONSIBLE PERSON
a. REPORT	b. ABSTRACT	c. THIS PAGE			KAUSHIK DAYAL
UU	UU	UU	UU		19b. TELEPHONE NUMBER 412-268-2949

Report Title

Final Report: A Multiscale Atomistic Method for Long-Range Electrical Interactions with Application to Multiphysics Calculations in Functional Materials

ABSTRACT

We aim to develop a robust and scalable strongly-coupled multiscale atomistic method with electric field-matter interactions that can scale to multimillions of atoms. Mathematically, we need to obtain efficient and accurate numerical methods to compute forces and energies in large discrete systems where the particle interaction is nonlinear and long-range. This is the mathematical idealization of a crystalline system that is close to periodic in much of the domain, but is defected in certain regions. The defects have an important role in functional materials, and we are trying to understand the structure and response of defects starting from physics-based models.

Enter List of papers submitted or published that acknowledge ARO support from the start of the project to the date of this printing. List the papers, including journal references, in the following categories:

(a) Papers published in peer-reviewed journals (N/A for none)

Received		Paper
02/28/2016	3.00	Lun Yang, Kaushik Dayal. Influence of strain on space-charge distribution at ferroelectric thin-film free surfaces, Acta Materialia, (11 2012): 0. doi: 10.1016/j.actamat.2012.07.050
TOTAL:	**1**	

Number of Papers published in peer-reviewed journals:

(b) Papers published in non-peer-reviewed journals (N/A for none)

Received		Paper
TOTAL:		

Number of Papers published in non peer-reviewed journals:

(c) Presentations

Number of Presentations: 0.00

Non Peer-Reviewed Conference Proceeding publications (other than abstracts):

Received Paper

TOTAL:

Number of Non Peer-Reviewed Conference Proceeding publications (other than abstracts):

Peer-Reviewed Conference Proceeding publications (other than abstracts):

Received Paper

TOTAL:

Number of Peer-Reviewed Conference Proceeding publications (other than abstracts):

(d) Manuscripts

Received	Paper	
02/28/2016	2.00	R. Mbarki, N. Baccam, Kaushik Dayal, P. Sharma. Piezoelectricity above the Curie temperature? Combining flexoelectricity and functional grading to enable high-temperature electromechanical coupling, Applied Physics Letters (03 2014)
08/30/2013	1.00	Jason Marshall, Kaushik Dayal. Atomistic-to-Continuum Multiscale Modeling with Long-Range Electrostatic Interactions in Ionic Solids, J Mech Phys Solids (04 2013)

TOTAL: **2**

Number of Manuscripts:

Books

Received Book

TOTAL:

Received Book Chapter

TOTAL:

Patents Submitted

Patents Awarded

Awards

Former PhD student, Jason Marshall, now a postdoc at Caltech, received the following awards:

Selected for an ORAU ARL Summer Internship for 2012 and 2013.
In 2013, he was Winner of Computational and Information Sciences Directorate, and ARL-wide Bronze Medalist at the ARL Summer Graduate Student Symposium.
Awarded two fellowships from Carnegie Mellon: Bertucci (2013), Northrop (2011)
Best Poster Award at US National Congress on Computational Mechanics

Current PhD student, Prashant Jha, received the following award:

Outstanding Teaching Assistant Award, 2013, at Carnegie Mellon

The PI (Dayal) received the following recognition:

Junior chair from Carnegie Mellon University, 2013-2016
ASCE Engineering Mechanics Da Vinci Early Career Award, 2013
Eshelby Award for Young Mechanics Faculty, 2013
Parkin Visiting Professorship, Department of Mathematics, University of Bath, 2016
NSF US Junior Oberwolfach Fellow, 2013
Invited Visitor to Hausdorff Mathematics Institute, University of Bonn (2012 and 2014; 2014 was not realized due to visa issues)
Invited speaker at the Max Planck Institute for Mathematics in the Sciences workshop on "Design of Materials"

Graduate Students

NAME	PERCENT_SUPPORTED	Discipline
Jason Marshall	0.50	
Prashant Jha	0.50	
Soumya Mukherjee	0.05	
Mahnoush Babaei	0.05	
FTE Equivalent:	**1.10**	
Total Number:	**4**	

Names of Post Doctorates

NAME	PERCENT_SUPPORTED
FTE Equivalent:	
Total Number:	

Names of Faculty Supported

NAME	PERCENT_SUPPORTED	National Academy Member
Kaushik Dayal	0.09	
FTE Equivalent:	**0.09**	
Total Number:	**1**	

Names of Under Graduate students supported

NAME	PERCENT_SUPPORTED
FTE Equivalent:	
Total Number:	

Student Metrics

This section only applies to graduating undergraduates supported by this agreement in this reporting period

The number of undergraduates funded by this agreement who graduated during this period: 0.00

The number of undergraduates funded by this agreement who graduated during this period with a degree in science, mathematics, engineering, or technology fields:..... 0.00

The number of undergraduates funded by your agreement who graduated during this period and will continue to pursue a graduate or Ph.D. degree in science, mathematics, engineering, or technology fields:..... 0.00

Number of graduating undergraduates who achieved a 3.5 GPA to 4.0 (4.0 max scale):..... 0.00

Number of graduating undergraduates funded by a DoD funded Center of Excellence grant for Education, Research and Engineering:..... 0.00

The number of undergraduates funded by your agreement who graduated during this period and intend to work for the Department of Defense 0.00

The number of undergraduates funded by your agreement who graduated during this period and will receive scholarships or fellowships for further studies in science, mathematics, engineering or technology fields: 0.00

Names of Personnel receiving masters degrees

NAME
Total Number:

Names of personnel receiving PHDs

NAME	
Jason Marshall	
Prashant Jha	
Total Number:	**2**

Names of other research staff

NAME	PERCENT_SUPPORTED
FTE Equivalent:	
Total Number:	

Sub Contractors (DD882)

Inventions (DD882)

Scientific Progress

See Attachment

Technology Transfer

Dr. Jarek Knap: We have had an extremely intensive collaboration. This has included a former PhD student – Jason Marshall – visiting ARL for 2 summers where he was selected for the ORAU internship program. While at ARL, Jason Marshall was Winner of Computational and Information Sciences Directorate, and ARL-wide Bronze Medalist at the ARL Summer Graduate Student Symposium. Dr. Knap also participated in Jason's PhD committee (through videoconference due to travel freezes). The method that was formulated at CMU was implemented in close collaboration with Dr. Knap, and is a part of the ARL code repository and available for use by ARL researchers. Dr. Knap continues to build up the capabilities of the code. Joint papers are in preparation.

Dr. Tim Breitzman: Dr. Breitzman is a mathematician in both the composites and the optics group at AFRL. He is strongly interested in a collaboration with us to exploit the capabilities of our method in applications of his group. He visited CMU for a day with a member of his group (Dr. Lauren Ferguson; AFRL researcher) and had extensive discussions with the PI. He and Dr. Ferguson also presented individual seminars. Dr. Breitzman invited the PI to spend the summer 2016 at AFRL.

Dr. Melanie Cole: Dr. Cole of SED/ARL organized a workshop on functional ceramics. She invited the PI to speak about the mathematical modeling which is supported by this grant. This led to a co-authored paper with her that includes many of the workshop speakers (10+ co-authors).

Final Report for Army Research Office (Numerical Analysis program) Young Investigator Grant (W911NF-12-1-0156)

A Multiscale Atomistic Method for Long-Range Electrical Interactions with Application to Multiphysics Calculations in Functional Materials

PI: Kaushik Dayal, Carnegie Mellon University (kaushik.dayal@cmu.edu)

Program manager: Joseph Myers, ARO

0. List of Appendixes, Illustrations and Tables

Preprints and PhD theses are attached as Appendixes to this document. Final versions of published / accepted papers are attached separately to the final report.

1. Statement of the problem studied

We develop a robust and scalable strongly-coupled multiscale atomistic method with electric field-matter interactions that can scale to multimillions of atoms. Mathematically, we need to obtain efficient and accurate numerical methods to compute forces and energies in large discrete systems where the particle interactions involve a combination of nonlinearity and long-range. This is the mathematical idealization of a crystalline system that is close to periodic in much of the domain, but is defected in certain regions. The defects have an important role in functional materials, and we are working to understand the structure and response of defects starting from physics-based models.

The key challenges are

- very large number of interactions – multi-million or much larger system size in terms of degrees of freedom,
- both short-range and long-range terms,
- short-range is very nonlinear and multi-body,
- long-range converges very slowly ("every charge interacts with every other charge"), but cannot be truncated (usual ideas of periodicity etc. can give qualitatively wrong results)
- the close-to-periodic regions are coarse-grained, but are strongly coupled to the defect region which are not coarse-grained

On the theoretical side, we have developed new continuum limits for systems with long-range interactions; this extends work by R. D. James (Univ. Minnesota) and co-workers. This enables the coarse-graining of these interactions away from defects. Future work will extend these to include positional disorder (due to thermal fluctuations).

Further, recent work by M. Luskin (Univ. Minnesota) and co-workers has provided careful mathematical analysis of coupling methods between coarse-grained and fine-grained. We have adapted these from short-range forces (by Luskin) to long-range forces.

Furthermore, while density functional theory (DFT) can't handle charges – rigorous results show that important aspects of charged behavior in crystals are unstable – the ready availability of "off-the-shelf" high-performance DFT codes enables calibration of short-range atomic interactions for quantitative predictions. This was not part of our focus, but is the focus of much research activity worldwide for a variety of materials. Our methods and code will benefit from these advances.

Finally, extremely large shared-memory systems (e.g. Blacklight and Greenfield at Pittsburgh Supercomputing Center, www.psc.edu) enabled our algorithms that exploit this hardware.

2. Summary of the most important results

One code that we have developed is a high-performance multiscale atomistics code for structural materials with multiple species. This builds on previous code developed by Dr. J. Knap (ARL) for single species systems. The capabilities of this code are unprecedented; it is now being applied by former PhD student Dr. Jason Marshall (now at Caltech) together with Dr. Knap to examine dislocation-void interaction in NiAl, a problem of interest to the Army. This is the largest, and only / first, calculation of this process that takes into account the full geometrical complexity and a sufficiently large domain that spurious boundary/image effects can be safely ruled out. It is providing important new physical insights that can impact materials-processing strategies. Two papers are in preparation on this work: one paper describing the methodological advances, and a second showing the application. Drs. Marshall and Knap are the authors of these papers.

Building further on this code, we have developed the first multiscale implementation of long-range electromagnetism and used this to study defect nucleation in ferroelectrics, of interest to ARL / SED [1]. This is the first calculation of defect structure in a realistic complex setting of a thin-film free surface with complex and spatially-heterogeneous electric fields. It has revealed unexpected new physics in the distortion around surface electrodes.

The method makes certain key assumptions, namely, that the lattice is crystalline far from the defect. It is distorted, but affinely so, thereby preserving crystalline order, with the distortion varying on a lengthscale much larger than the atomic spacing. This is the key fact that enables coarse-graining in our method and many others. In [4], we have examined initial approaches to relax this assumption and bring statistical mechanics into play.

In [5], we develop new non-reflecting boundary conditions based on perfectly-matched layers to examine electron structure and scattering at defects using the tight-binding approximation of quantum mechanics. While some prior works examined non-reflecting boundary conditions for the Schrodinger equation, these were all in the context of free-space scattering. Our approach is the first to look at scattering in a periodic medium with a defect.

[2] and [4] examine simplified model problems on field – matter interactions to provide physical insight. These are preliminary exploratory calculations for ongoing work to apply the multiscale atomistic method to understand respectively (1) the effect of strain gradients in inducing polarization in nominally non-polar solids, and (2) the transport of charges in complex heterogeneous fields. In (1), the strain gradients are extremely large in practical applications – close to the order of the atomic spacing – and hence are an example of a localized defect in the lattice (where a defect is defined as a breaking of crystalline order). In (2), while transport of charges requires molecular dynamics with its well-known time-scale issues, our multiscale method can be used to map out the free energy landscape as input to kinetic Monte Carlo methods.

Finally, [6] uses the notion of long-range nonlocal interactions at the molecular level to motivate (non-rigorously) a mesoscale model for topological defects in liquid crystal systems. Topological defects are difficult to regularize using standard approaches but is possible with this approach. We are working with mathematicians to develop a rigorous version of this model using the Boltzmann model as a starting point.

The thesis of Jason Marshall examines further examples and an extension of the method to full atomic accuracy at the defect core. The thesis is available at:

https://drive.google.com/file/d/0B5ExWrNV9OCgRVFKVFEwX2N6Qk0

3. Awards and Honors

Former PhD student, Jason Marshall, now a postdoc at Caltech, received the following awards:

- Selected for an ORAU ARL Summer Internship for 2012 and 2013.
- In 2013, he was Winner of Computational and Information Sciences Directorate, and ARL-wide Bronze Medalist at the ARL Summer Graduate Student Symposium.
- Awarded two fellowships from Carnegie Mellon: Bertucci (2013), Northrop (2011)
- Best Poster Award at US National Congress on Computational Mechanics

Current PhD student, Prashant Jha, received the following award:

- Outstanding Teaching Assistant Award, 2013, at Carnegie Mellon

The PI (Dayal) received the following recognition:

- Junior chair from Carnegie Mellon University, 2013-2016
- ASCE Engineering Mechanics Da Vinci Early Career Award, 2013
- Eshelby Award for Young Mechanics Faculty, 2013
- Parkin Visiting Professorship, Department of Mathematics, University of Bath, 2016
- NSF US Junior Oberwolfach Fellow, 2013

- Invited Visitor to Hausdorff Mathematics Institute, University of Bonn (2012 and 2014; 2014 was not realized due to visa issues)
- Invited speaker at the Max Planck Institute for Mathematics in the Sciences workshop on "Design of Materials"

4. Invited Presentations Related to the Research

1. Parkin Professorship Public Lecture at the University of Bath (scheduled for 2016)
2. Workshop on Design of Materials: From Grain Boundaries to Stochastic Homogenization at the Max Planck Institute for Mathematics in the Sciences
3. Mechanical Engineering Department Seminar, Pennsylvania State University
4. Civil and Environmental Engineering Seminar, University of Illinois (2015, 2014)
5. Applied Mathematics Seminar in the Department of Mathematics, Louisiana State University
6. Industrial Engineering Department Seminar, University of Pittsburgh.
7. Symposium on Multiferroic Materials and Multilayer Ferroic Heterostructures in the Electronic Materials and Applications Conference (canceled due to travel difficulty)
8. Symposium on Multiscale Modeling of Energy Conversion and Storage Materials at the Multiscale Materials Modeling Conference
9. Mechanical Engineering Department Seminar, University of Washington
10. Eshelby Award Seminar in the Mechanical Engineering Department, University of Houston
11. Workshop on Mathematics and Mechanics in the Search for New Materials at the Banff International Research Station
12. Summer School on Topics in Nonlinear PDEs and Calculus of Variations and Applications in Materials Science at the Center for Nonlinear Analysis
13. Fluids and Materials Seminar in the School of Mathematics, University of Bristol
14. Solid Mechanics Seminar, Brown University.
15. Center for Nonlinear Mechanics Seminar, University of Bath
16. Special Workshop on Mathematics and the Materials Genome Initiative at the Institute of Mathematics and its Applications
17. Mechanical Engineering Department Seminar, Florida State University
18. International Workshop on Mathematical and Mechanical Modeling for Materials at the City University of Hong Kong
19. NSF Workshop on Averaging Methods for Multiscale Phenomena in Engineering Materials

20. Center for Nonlinear Studies Seminar, Los Alamos National Laboratory
21. Army Research Laboratory Workshop on Complex Oxide and Multiferroic Thin Film Materials Science, Technologies, and Applications.

5. Papers Published / Submitted

[1] *Atomistic-to-Continuum Multiscale Modeling with Long-Range Electrostatic Interactions in Ionic Solids*. Jason Marshall and Kaushik Dayal. J. Mech. Phys. Solids, 62:137, 2014. Invited Article for the Rodney Hill Anniversary Issue.

[2] *Piezoelectricity above the Curie temperature? Combining flexoelectricity and functional grading to enable high-temperature electromechanical coupling*. Raouf Mbarki, Nadia Baccam, Kaushik Dayal, and Pradeep Sharma. Appl. Phys. Lett., 104:122904, 2014.

[3] *Influence of Strain on Space Charge Distribution at Ferroelectric Thin-Film Free Surfaces*. Lun Yang and Kaushik Dayal. Acta Mater., 60:6457, 2012.

[4] *Electroelasticity of polymer networks*. Noy Cohen, Kaushik Dayal, and Gal deBotton. Submitted.

[5] *Multiscale Real-Space Quantum-Mechanical Tight-Binding Calculations of Electronic Structure in Crystals with Defects using Perfectly Matched Layers*. Hossein Pourmatin and Kaushik Dayal. To appear in J. Comput. Phys.

[6] *Disclinations without Gradients: A Nonlocal Model for Topological Defects in Liquid Crystals*. Robert Macedo, Hossein Pourmatin, and Kaushik Dayal. Submitted.

Others are in preparation, based on thesis of Jason Marshall and Prashant Jha. 2 additional papers by Marshall and Knap, supported by this grant, are in preparation.

Atomistic Multiscale Modeling with Long-Range Electrostatic Interactions

Submitted in partial fulfillment of the requirements for

the degree of

Doctor of Philosophy

in

Civil and Environmental Engineering

Jason P. Marshall

B.S., Civil Engineering, California Polytechnic State University - San Luis Obispo
M.S., Civil and Environmental Engineering, Carnegie Mellon University

Carnegie Mellon University
Pittsburgh, PA

December, 2014

Acknowledgements

I would like to thank everyone that has helped me in the academic endeavor that I started years ago.

I want to start by thanking my advisor, Dr. Kaushik Dayal, for all of his support. I received an immense amount of advice, help, technical intuition, and support from Dr. Dayal. Without his guidance and mentoring none of this would have been close to being possible. He has faithfully navigated me through the academic world and this dissertation and I am greatly indebted to him.

I want to thank my advisor at ARL, Dr. Jaroslaw Knap. His help, advice, mentoring, and insight has been invaluable to both to my professional career and personally.

I also want to thank Dr. Jacobo Bielak, Dr. Shlomo Ta'asan, and Dr. Noel Walkington for their time and help as members of my committee. Additionally, the classes I have taken at CMU have all been outstanding and I want to thank the numerous instructors who have taught me over the years, especially Dr. Amit Acharya, Dr. Alan McGaughey, Dr. Jack Beuth, and Dr. John Kitchin. Dr. Garrett Hall, Dr. Eric Kasper, and Dr Gregg Fiegel will always have my thanks for supporting me in my academic endeavors at Cal Poly and motivating me to pursue an academic career. I will always be grateful to everyone I shared an office with at CMU, especially Amin Aghaei, Lun Yang, Abraham Chang-Tsan Lu, Hossein Pourmatin, Vaibhav Agrawal, Prashant Jha, Arnab Debnath, and Soumya Mukherjee and the interesting and unique discussion that we had. I want to thank all of my friends at CMU that spent time with me and helped me unwind outside of the confines of Porter Hall.

None of this would have been possible without the steadfast support of my family including my mom, Susan; dad, Kevin; brother, Kyle; and sister, Stacy. I would like to dedicate my Ph.D. to my mom for always putting everyone else ahead of herself and having to put up with 3 nerdy engineers and a doctor in the family.

I want to thank my fiance, Kristy, for always being there for me, putting up with my shenanigans and projects, and most of all for her constant support. We have experienced a lot of great joys together; in Pittsburgh; throughout the country; and I am excited for all of the future ones that occur in our journey together.

Last, but not least I would like to thank all of my financial sponsors: the CIT Dean's Fellowship, John and Claire Bertucci PhD Fellowship, US Junior Oberwolfach Fellows: NSF Workshop Travel Grant, Fenves Travel Grant, CMU-ICES Northrop Grumman Fellowship, NSF BEM Workshop Travel Fellowship, ICIAM Travel Grant, ORISE, ORAU, ARL, and the PSC.

Abstract

Modern technology is continually evolving and pushing the limits of our understanding of materials. This is especially true at the smallest length scales, where phenomenological and experimental data is challenging to acquire. Computational methodologies are becoming more important in understanding the physics of materials at these small length scales. Multiscale methods, in particular, are playing a prominent role in understanding the importance of defects and how they effect properties. We focus specifically on the Quasicontinuum Method (QC). We extend the local Cauchy-Born QC to long-range Coulombic interactions. We then use the method to simulate electrical and mechanical loading in an ionic solid. Next we extend an existing non-local QC force method that was initially intended for crystals with a single atomic species to a multi-lattice system. The problem is treated as the union of many simple lattice problems and implemented in an existing computational framework. The method is used to investigate void and vacancy defects in NiAl. Lastly, we develop a method for including electrostatic interactions in non-local QC based on the Fast Multipole Method (FMM). We use inspiration from the FMM to derive error bounds on our computed electrical quantities. The numerical error is investigated against a variety of simulation parameters and discussed. The final implementation is written for high performance computing applications and can be used to simulate a variety of materials. Overall, the newly developed methodology and code allows the simulation of defects at the atomistic length scale in ionic solids with real-space boundaries.

Keywords: multiscale modeling, electrostatics, Quasicontinuum (QC) Method, ionic solids, Fast Multipole Method (FMM)

Table of Contents

Acknowledgements ii

Abstract iv

List of Figures viii

1 Introduction 1

2 Local Atomistic-to-Continuum Multiscale Modeling with Long-Range Electrostatic Interactions in Ionic Solids 6

2.1 Abstract . . . 6
2.2 Introduction . . . 7
2.2.1 Notation . . . 12
2.3 Problem Formulation . . . 13
2.4 Electrostatic Interactions . . . 15
2.4.1 Why the Electrostatic Energy is Long-Range . . . 15
2.4.2 Existing Numerical Approaches to Compute Electrostatic Interactions . . . 19
2.4.3 Coarse-Graining the Electrostatic Field Energy . . . 20
2.4.4 Role of Boundaries in Compensating for the Non-uniqueness of Polarization . . . 29
2.5 Numerical Implementation . . . 36
2.5.1 Energy Minimization through Gradient Descent . . . 37
2.5.2 Local Quasicontinuum for Multi-lattices with Short-Range Interactions . . . 42
2.5.3 Coarse-graining of the Long-Range Electrostatic Interactions . 43

2.6 Crystal Free Surface Subject to Inhomogeneous Electric Fields 44
2.7 Discussion 48

3 Development of a Fully Non-Local Quasicontinuum Method for Simulating Atomistic Defects in Materials with Many Atomic Species 58

3.1 Abstract 58
3.2 Introduction 59
3.3 Methodology 61
3.3.1 Overview 61
3.3.2 Single Species: Problem statement 62
3.3.3 Single Species: Reduction of system degrees of freedom 63
3.3.4 Single Species: Reduced equilibrium equations 65
3.3.5 Single Species: Summation rules 67
3.3.6 Single Species: Adaptive meshing 69
3.3.7 Multiple species: Problem statement 69
3.3.8 Multiple Species: Reduction of system degrees of freedom . . . 71
3.3.9 Multiple Species: Summation rules 73
3.4 Computational implementation 75
3.4.1 Overview of single species NL-QC code 75
3.4.2 C++ class extension of Quasicontinuum to Quasicontinua . . 76
3.4.3 Verification of implementation 80
3.5 Numerical simulation of deformation around void defects in NiAl . . . 80
3.6 Discussion 87

4 Non-local quasicontinuum method with long-range, real-space electrostatics 88

4.1 Abstract 88
4.2 Introduction 89
4.3 Method 93
4.3.1 Preliminaries 93
4.3.2 Quasicontinuum Method 94

4.3.3 Electrostatic Summation Overview 96
4.3.4 Contribution from Single Unit Cell 97
4.3.5 Contribution from All Unit Cells in a Body 99
4.4 Numerical Implementation 104
4.5 Results 107
4.6 Discussion 110

5 Conclusions and Discussion **118**

Bibliography **120**

Appendix A Transformation of Unit Cell in a Crystal Lattice to Obtain a Unit Cell with One Face Parallel to a Given Plane **132**

Appendix B How To Run QC Code **135**

Appendix C QC Code Computational Scaling **146**

List of Figures

Figure 2.1 Domain Ω showing the separation of scales with sample charge distribution. 16

Figure 2.2 3 cases of charge arrangement: (i) net charge, (ii) net dipole but no net charge, and (iii) net quadrupole, but no net charge and no net dipole. 17

Figure 2.3 Charge distribution in the 1D illustrative example to show the effect of boundaries. 31

Figure 2.4 Decompose Ω into $\Omega_{\square}$ and $\Omega_{\#}$. 32

Figure 2.5 Change in charge and polarization due to a translation along $\boldsymbol{h}_1$ and $\boldsymbol{h}_2$ respectively in the special choice of unit cell. 33

Figure 2.6 Change in charge and polarization due a distortion of the unit cell in the special choice of unit cell. 34

Figure 2.7 Change in charge and polarization due a remapping of the unit cell from the special choice of unit cell. 35

Figure 2.8 The mesh of the entire specimen. The lengthscales are angstroms. 45

Figure 2.9 Close up view of the atomically-resolved portion of the sample. Without applied fields and loads, the surface of the specimen is flat. The surface feature is caused by an applied electric field. . . 46

Figure 2.10 Stress and polarization due to single point charge with an electrostatic scaling of 1. 52

Figure 2.11 Stress and polarization due to single point charge with an electrostatic scaling of 4. 52

Figure 2.12 Stress due to two point charges with an electrostatic scaling of 1. 53

Figure 2.13 Stress due to two closely-spaced point charges with an electrostatic scaling of 1. 53
Figure 2.14 Stress due to four point charges with an electrostatic scaling of 1. 54
Figure 2.15 Stress due to four closely-spaced point charges with an electrostatic scaling of 1. 54
Figure 2.16 Stress due to a dipole (two point charges of opposite sign) with an electrostatic scaling of 1. 55
Figure 2.17 Stress due to a point charge computed using a continuum phase-field model [82]. 55
Figure 2.18 Stress due to a point charge with electrostatic fields computed in the reference configuration. 56
Figure 2.19 Normalized Difference between Nonlinear and Linearized Strain Measure (ϵ_{22} component). 56
Figure 2.20 Fully atomic calculation for a sample with a point charge. The plot shows the energy difference from the state without any external charge with the electrostatic field energy subtracted. The entire computational domain is shown. 57
Figure 2.21 Stress and polarization due to mechanical indentation with no applied electric field. 57

Figure 3.1 Simple lattice in body Ω 63
Figure 3.2 Simple lattice with full atomistic and coarse-grained resolution 64
Figure 3.3 Simple lattice with multiple cluster scenarios. **Top Zoom**: Coarse-grained no cluster overlap. **Middle Zoom**: Coarse-grained with cluster overlap that must be resolved. **Bottom Zoom**: Fully resolved cluster is a single representative atom. 68
Figure 3.4 Multiple Species Lattice 71
Figure 3.5 Multiple Species Lattice with Multiple Triangulations 72

Figure 3.6 Multiple Species Lattice Clusters **Top Zoom**: Light blue and green atoms are in a cluster of dark blue and green representative atoms respectively. **Bottom Zoom**: The calculation of forces at dark blue and green atoms sums over interaction with all atoms within a cutoff radius regardless of species. . . 74
Figure 3.7 Typical mesh with coarse-graining far away from void with full atomistic resolution 81
Figure 3.8 Centrosymmetry parameter around vacancy after initial relaxation. 82
Figure 3.9 Centrosymmetry parameter around vacancy at volumetric expansion of 24 percent. 82
Figure 3.10 Centrosymmetry parameter around a void of 4 Ang. after initial relaxation. 83
Figure 3.11 Centrosymmetry parameter around a void of 4 Ang. after volumetric expansion of 16.5 percent. 83
Figure 3.12 Centrosymmetry parameter around a void of 6 Ang. after initial relaxation. 84
Figure 3.13 Centrosymmetry parameter around a void of 6 Ang. after volumetric expansion of 15 percent. 84
Figure 3.14 Centrosymmetry parameter around a void of 8 Ang. after initial relaxation. 85
Figure 3.15 Centrosymmetry parameter around a void of 8 Ang. after volumetric expansion of 13.5 percent. 85
Figure 3.16 Centrosymmetry parameter around a void of 10 Ang. after initial relaxation. 86
Figure 3.17 Centrosymmetry parameter around a void of 10 Ang. after volumetric expansion of 12 percent. 86

Figure 4.1 Body Ω with atomistic charges and charge neutral unit cells. 93
Figure 4.2 Schematic of unit cell geometry contributing to the electric field at a given point $\boldsymbol{x}^{\beta}$. 97

Figure 4.3 Full Ω domain broken down into fully resolved region $\Omega_{atomistic}$, a shell region Ω_{shell} centered at a point, $\boldsymbol{x}$, where the field is to be evaluated, and the far field region Ω_{far}. A single unit cell located at $\boldsymbol{x}'$ in the far field region is also shown. 103

Figure 4.4 Convergence of total possible error in electric field from error bound in Equation 4.26 for an infinite crystal. Each successive shell adds less total error as expected because of the increased distance from evaluation point. 108

Figure 4.5 Error bound for electric field with an exact atomistic summation performed with N unit cells. 109

Figure 4.6 Charge density on top 0001-plane of interior trapezoidal boundary between the exact atomistic region and the approximated region. The size of the exact atomistic region is 8 shells of trapezoidal unit cells. 112

Figure 4.7 Contribution to electric field in 0001-direction from top 0001-plane of interior trapezoidal boundary between the exact atomistic region and the approximated region. The size of the exact atomistic region is 8 shells of trapezoidal unit cells and the integration level is 1. 113

Figure 4.8 Contribution to electric field in 0001-direction from top 0001-plane of interior trapezoidal boundary between the exact atomistic region and the approximated region. The size of the exact atomistic region is 8 shells of trapezoidal unit cells and the integration level is 2. 114

Figure 4.9 Contribution to electric field in 0001-direction from top 0001-plane of interior trapezoidal boundary between the exact atomistic region and the approximated region. The size of the exact atomistic region is 8 shells of trapezoidal unit cells and the integration level is 3. 115

Figure 4.10 Numerical convergence of electric field contribution in 0001-direction from far field region using QC code with an infinite single crystal of wurtzite GaN. Integration notation denotes an increased used of numerical quadrature points used in solving the contribution from field terms. 116
Figure 4.11 Numerical convergence of electric field contribution in 0001-direction from exact shell region using QC code with an infinite single crystal of wurtzite GaN. 117

B.1 Main QC folder. 136
B.2 Source file folder. 137
B.3 Build script, part 1. 138
B.4 Build script, part 2. 139
B.5 Mesh generation input file. 140
B.6 Main driver input file, part 1. 142
B.7 Main driver input file, part 2. 143
B.8 Main driver input file, part 3. 144

C.1 Scaling results for exact cluster summation. 148
C.2 Scaling results for far field electric field contribution with a numerical integration level of 1. 149
C.3 Scaling results for far field electric field contribution with a numerical integration level of 2. 150
C.4 Scaling results for far field electric field contribution with a numerical integration level of 3. 151

1

Introduction

Smaller and faster are two important mantras in the design of cutting edge technologies. These mantras are especially true in regards to electronic devices. Designing next generation devices to meet these goals requires exploiting the inherent structure and properties of specific classes of materials. Electromechanical materials, which have a coupling between electrical and mechanical properties, are one such class. An important feature of these materials is near instantaneous electrical response (speed) at small length scales (size), in some cases even the atomistic length scale. Next generation devices currently being designed and developed with these materials include random access memories, actuators, and sensors, among many others [3, 64, 45]. Performing experiments on electromechanical materials, at the length scales sought for these devices, is both difficult and expensive, making design through experiments alone challenging. Computational methods are being actively sought by many researchers to augment experimental data and aid in the design of these devices. However, numerous challenges are inherent in any computational method that seeks to model materials at these length scales.

We highlight the importance of Gallium-Nitride (GaN) as an example of an impor-

tant electromechanical material and the challenges in simulating it. This is just one example, there are literally hundreds of materials equally as important. GaN is one of the most important and prevalently used materials in modern technologies. The widespread use of GaN can be attributed to its many useful properties. Applications that utilize GaN material properties include LED lighting[57], solar cells[70], High-electron-mobility transistors (HEMT)[53], and many other technologies[60, 32, 33]. In fact, the 2014 Nobel Prize in Physics was awarded to researchers for their work on creating blue LEDs with GaN[55, 26]. GaN's material properties and array of applications has led to a wide breadth of theoretical research at various length scales[11, 36, 81]. We only list a few sample publications at different length scales, there are hundreds of others that could be referenced as well. Even with this intense focus on GaN, additional research is needed, especially in regards to the role that electrostatic interactions play in GaN. We aim to to further investigate the role of electrostatics interactions, especially in systems with defects, non-periodic geometries, and non conducting boundary conditions.

One of the main challenges is that continuum theories break down, for all materials at small length scales, requiring the use of atomic theories, at a minimum, in areas of interest. However, modeling a complete system solely with atomic theories quickly becomes computationally intractable in size, because of the large number of degrees of freedom. The mechanics community has sought to overcome this challenge by developing multiscale methods that bridge the gap between continuum and atomistic length scales, some of these methods include [78, 68, 72]. The general goal is to provide atomistic resolution only in areas of interest and continuum resolution elsewhere. One of the methods that has experienced success in achieving this goal is the Quasicontinuum (QC) method. The QC method can be broken down into multiple sub-methods [68]. While there are many flavors of QC, a common feature is the use of interpolation functions for atomic positions to reduce the number of de-

grees of freedom in the system to more manageable levels. Energies or forces in the system are then evaluated through numerical quadrature rules and allow solutions to be found through minimization routines.

One important paradigm between these methods is local versus non local. Local methods, like [67], utilize the Cauchy Born rule with standard finite element quadrature rules to evaluate the energy. This method is considered local, because the quadrature rules depend only on variables at that individual quadrature point. An issue immediately arises, however, as the Cauchy Born rule assumes a periodic lattice inside each element. This assumption is valid only when the element size is large compared to the lattice length scale. Obviously in areas of interest, (for example, near defects, surfaces, domain walls, external loadings, etc.) the use of large elements does not provide adequate solution resolution. Researchers overcame this difficulty by introducing non local methods [40, 19] with different quadrature rules, typically based at nodes. These methods achieve full atomistic resolution, but are computationally and numerically more difficult to implement, because the quadrature rules are now non local. Essentially, the quadrature points are a function of variables at other quadrature points (non local) in addition to their own (local). This distinction between local and non local is important for later sections of this thesis.

While the QC method, along with other multiscale methods, is effective for the analysis of many types of materials, difficulties occur for electromechanical materials. Materials which current QC methods can model are characterized by interaction energies between atoms that are short ranged and can be approximated by a cutoff radius. Electromechanical materials, however, are long-ranged and therefore lack an effective cutoff radius. Because of the lack of cutoff radius, current multiscale methods are not valid for this important class of materials.

Even methods designed to specifically solve electromechanical systems have issues

that are difficult to overcome. The more commonly used methods include Ewald summations [21, 23, 74], Ewald-like summations[22, 23], and Fast Multipole Methods (FMM)[28]. The Ewald and Ewald-like summations assume some form of periodicity and do not allow easy implementation of far field boundary conditions. All of these methods, while computationally fast in comparison with the full summation, do not easily allow explicit handling of all electrostatic boundary conditions. The lack of explicit control of boundary conditions and assumption of periodicity inhibits the ability to model many geometries and defects important in materials like GaN. These boundary conditions are pivotal in ionic solids like GaN [23, 54, 2], especially in the simulation of defects. The FMM is a fantastic method, however, it is not as prevalently used in the atomistic and multiscale modeling field as other methods. Its algorithms are challenging and particularly difficult to implement in conjunction with other codes, especially in a high performance computing environment (HPC).

In Chapter 2, we formally extend the local QC method [67] to handle long range interactions present in electromechanical materials. A more complete introduction and background information for the specific problem is in Section 2.2. Our new method uses polarization as a multiscale mediator quantity to bridge the atomistic and continuum length scales. We use our method to analyze and gain insight into the fundamental physics of electromechanical materials. This work was done in collaboration with my advisor, Dr. Kaushik Dayal and is published in [49].

In Chapter 3, we extend the non-local cluster force QC method [40] to multiple lattices. This problem was first addressed in [42], though we develop our own computational implementation separate from that work. The complex QC method essentially treats the problem as the union of a number of simple lattice problems. The main difference between the complex lattice case and the simple lattice case is that in the complex lattice case each lattice interacts with the other. We address this issue by creating a new C++ class that computes the force interactions between any

two lattices in a domain. This work was done in collaboration with my mentor at the Army Research Laboratory, Dr. Jaroslaw Knap and is preparation to be submitted to IJNME [50].

In Chapter 4, we extend the work done in Chapter 3 to handle electrostatic interactions. We use a combination of the FMM [28] and Reaction Field (RF) method [73, 27, 6] to accomplish our goal. Essentially around a point of interest, we need to be able to calculate the electric field. All atoms that are near the evaluation point are handled explicitly. Contributions to the electric field from atoms farther away are approximated with the first term of the multipole expansion, the dipole term. We take all higher order moments as a bound on the error from the approximated field contributions. We derive both analytical error bounds and numerically simulate errors with the QC method. This work was in collaboration with both Dr. Dayal and Dr. Knap, and is in preparation to be submitted to SIAM MMS [48].

Additionally, in Appendices B and C we provide additional information on using the QC code and its computational scaling.

2

Local Atomistic-to-Continuum Multiscale Modeling with Long-Range Electrostatic Interactions in Ionic Solids

2.1 Abstract

We present a multiscale atomistic-to-continuum method for ionic crystals with defects. Defects often play a central role in ionic and electronic solids, not only to limit reliability, but more importantly to enable the functionalities that make these materials of critical importance. Examples include solid electrolytes that conduct current through the motion of charged point defects, and complex oxide ferroelectrics that display multifunctionality through the motion of domain wall defects. Therefore, it is important to understand the structure of defects and their response to electrical and mechanical fields. A central hurdle, however, is that interactions in ionic solids include both short-range atomic interactions as well as long-range electrostatic interactions. Existing atomistic-to-continuum multiscale methods, such as the Quasicontinuum method, are applicable only when the atomic interactions are short-range. In addition, quantum mechanics simulations via density functional models are unable

to capture key phenomena of interest in these materials.

To address this open problem, we develop a multiscale atomistic method to coarse-grain the long-range electrical interactions in ionic crystals with defects. In these settings, the charge density is rapidly varying, but in an almost-periodic manner. The key idea is to use the polarization density field as a multiscale mediator that enables efficient coarse-graining by exploiting the almost-periodic nature of the variation. In regions far from the defect, where the crystal is close-to-perfect, the polarization field serves as a proxy which enables us to avoid accounting for the details of the charge variation. We combine this approach for long-range electrostatics with the standard Quasicontinuum method for short-range interactions to achieve an efficient multiscale atomistic-to-continuum method. As a side note, we examine an important issue which is critical to our method: namely, the dependence of the computed polarization field on the choice of unit cell. Potentially, this is fatal to our coarse-graining scheme; however, we show that consistently accounting for boundary charges leaves the continuum electrostatic fields invariant to choice of unit cell.

Keywords: electromechanics, multiscale modeling, atomistics, long-range interactions, Quasicontinuum method

2.2 Introduction

Ionic crystals such as solid electrolytes and complex oxides are central to modern technologies for energy storage, sensing, actuation, and other functional applications. Atomic-scale defects often play a central role in these materials, not only to limit reliability, but more importantly to enable the functionalities that make these materials of critical importance. E.g., in solid electrolytes, conduction is mediated by charged point defects [37]; and in complex oxide ferroelectrics, functionality is mediated by planar domain wall defects, and loss of functionality often occurs when domain walls are "pinned" by charged oxygen vacancy point defects [64]. A fun-

damental understanding of these materials therefore requires an accounting of the atomic-level structure of the defects. This poses a multiscale problem: atomic-level resolution is required at the defect, while complex geometries and boundary conditions require the modeling of a large specimen.

While defects play a critical role in determining properties, they occupy a tiny volume of the lattice; an exceedingly large fraction of the crystal is close-to-perfect. This feature is exploited in most leading atomistic multiscale methods such as the Quasicontinuum (QC) method [68, 51]: typically, an adaptive coarse-graining is used with atomic resolution in the vicinity of the defect and a coarse-grained description further away as the crystal tends to a perfect lattice. Another important aspect of the coarse-graining is the use of sampling or quadrature to efficiently evaluate the energy in the coarse-grained region. It is essential that the atomic interactions are short-range to allow the evaluation of the energy at the quadrature points to be efficient. Therefore, existing multiscale methods cannot handle long-range electrostatic/ionic interactions which decay as $1/r$, where r is the separation between charges.

A symptom of this difficulty with electrostatic interactions can be observed in standard proofs of the Cauchy-Born (CB) theorem which require the interactions to decay faster than $1/r^3$ [24, 10]. Roughly, this implies that the standard CB theorem requires that the charge distribution in each unit cell of the lattice should not have net charge or net dipole character, but only higher-order multipoles. As shown in [35], it is not possible to define a meaningful energy density $W(\cdot)$ in such a setting, i.e., the standard decomposition of the energy used in elasticity

$$E = \int_{\Omega} W(\cdot)\, d\Omega - \int_{\partial\Omega} \text{boundary working}$$

is not valid. When long-range electrostatic forces are involved, $W(\cdot)$ does not depend solely on the local value of a field (the strain field in elasticity or the polarization field in electrostatics). Rather, it depends on the electrostatic fields in a nonlocal

manner as well as boundary conditions. While not always stated explicitly, some notion of the CB theorem is inherent in most atomistic multiscale formulations.

The restrictions described above on the nature of atomic-level interactions for conventional multiscale methods exclude an extremely large class of materials; essentially, all dielectrics, polarizable solids, and ionic solids. In dielectrics and polarizable solids, the non-vanishing dipole moment in the unit cell is central to the physics of dielectric response, spontaneous polarization. In ionic solids such as ionic conductors, the existence of charged defects is central to enabling conduction. Therefore, it is essential to develop methods that can handle long-range electrostatic interactions.

In this chapter, we present a multiscale method which is tailored to allow both short-range atomic interactions as well as long-range electrostatic interactions. Some key features of these interactions are as follows. The short-range atomic interactions can be highly nonlinear and involve complex multibody interactions; however, they are typically restricted to 2nd or 3rd nearest-neighbors in a lattice. The long-range electrostatic interactions have the opposite features: the interactions between charges are entirely pairwise, but the interactions between *every* pair of charges in the system can be non-negligible. A further important feature is that the short-range and electrostatic contributions to the total energy combine additively. These features enable us to leverage much of the existing work for short-range interactions. In particular, we can use a standard version of the Quasicontinuum method [67] for the short-range interactions in combination with a method that we develop for efficiently computing the electrostatic interactions.

While the presentation of our method in this chapter is largely formal, key aspects build on – and are supported by – rigorous results of James and Müller [35] and others following their work, e.g. [63]. We note that seminal formal results in this topic were earlier obtained by [75]. While these works deal with point dipoles arranged in a lattice, our focus is on charges; however, due to the fact that the net charge in each

unit cell of the lattice is 0, many of the key results carry over largely unchanged, as also noticed previously by [79, 59]. The central idea which we exploit is that a charged lattice can be coarse-grained by introducing a polarization density field. I.e., electrostatic quantities which in principle require the solution of a Poisson problem with a rapidly and almost-periodically oscillating forcing term due to charge density can instead be computed with a much smoother forcing which is related to the polarization density field.

Efficient and accurate methods for interactions in charged systems have a long history in numerical methods. The key challenge is the long-range nature of interactions: in principle, a system of N point charges requires $O(N^2)$ computations to determine quantities of interest namely the electric field or potential. For N of the order required for typical problems of interest today, this is completely infeasible. However, the seminal and beautiful Fast Multipole Method (FMM) of Greengard and Rokhlin [28] provided a breakthrough in enabling this in $O(N)$ calculations with a controlled error. A key strength of the FMM is that the charge distribution can be completely arbitrary and non-uniform; however, this generality also means that the method does not exploit the structure in a given problem. As noted above, in the problems of relevance here, the crystalline structure is lost in the vicinity of the defect, but large parts of the crystal are almost perfect. The FMM, however, is unable to exploit this structure, whereas our method is more tailored (and thereby also less general) and appears to scale almost independent of N asymptotically. Another leading method for atomic-level calculations with electrostatic interactions is the Ewald method (described in e.g. [76]). It is restricted to periodic settings and therefore inapplicable to multiscale calculations with defects and complex geometries and boundary conditions.

As mentioned above, our coarse-graining of electrostatic interactions is based on the notion of a polarization density field. However, it is well-known, e.g. [61], that

the polarization density of a periodic solid depends on the choice of unit cell. At first sight, this is a disturbing observation and much work has been done in the materials physics community on using quantum mechanical notions such as the Berry phase to obtain a unique choice of polarization for a given periodic charge distribution [61]. However, an important aspect of that approach is the insistence on starting from an infinite periodic solid. In both the formal calculations presented here, and the related rigorous calculations in the references above, the starting point is a finite periodic solid whose limit behavior is studied. From this "real-space" perspective, the boundaries of the crystal lattice enter naturally into the problem, in sharp contrast to starting from the infinite periodic solid where boundaries are ill-defined. The critical importance of the boundaries is that they, roughly speaking, compensate for the choice of unit cell. I.e., while different unit cell choices lead to different expressions for the polarization density, these also lead to different bound surface charges on the boundaries. When *both* the bulk bound charge and the surface bound charge are consistently accounted for in the calculations, the electric field and other quantities of relevance to the energy do not depend on the choice of unit cell up to an error that scales with size of the lattice and vanishes in the limit. Therefore, we take the view that a unique choice of unit cell to compute polarization density is unnecessary and any choice of unit cell is – in principle – equally valid. I.e., the polarization is an intermediate coarse-grained quantity, but there is no fundamental physical reason to have a specific choice. In practice, notions of crystal symmetry typically are most useful in selecting a unit cell. Heuristically, this perspective is comparable to the universally-accepted view in continuum mechanics that any reference configuration is – in principle – equally valid. While certain choices of reference configuration can lead to conceptual and algebraic simplifications, there is no fundamental physical preference for any specific choice. What is more relevant is that it is possible to go between different choices with appropriate transformations to the kinematic variables

and the energy densities.

The chapter is organized as follows.

- In Section 2.3, we formulate the problem at the atomic level and briefly describe the well-developed QC approach to handle short-range interactions.
- In Section 2.4, we describe our treatment of the long-range interactions. Formally, we show the appearance of the polarization as an intermediary multiscale quantity to link atomistic charge distributions with coarse-grained fields. We also examine the issue of the choice of unit cell for polarization; accounting consistently for the boundaries for a given unit cell does not affect the coarse-graining.
- In Section 2.5, we outline the kinematic coarse-graining which follows the complex local QC method [67] and other aspects of the numerical implementation.
- In Section 2.6, we outline the model material and its response to a variety of electrical and mechanical loadings.
- In Section 2.7, we discuss various aspects of the work including open problems for ongoing and future work.

2.2.1 Notation

Throughout the chapter, bold lowercase and uppercase letters denote vectors and tensors. The summation convention is *not* used in this chapter. Sums will be explicitly written out to avoid confusion except where stated.

We define L as a Bravais lattice with three independent lattice vectors that make up a unit cell.

$$L(\boldsymbol{e}_i, \boldsymbol{0}) = \left(\boldsymbol{x} \in \mathbb{R}^3,\, \boldsymbol{x} = \sum_i \nu^i \boldsymbol{e}_i \text{ where } \nu^i \in \mathbb{Z},\, i = 1, 2, 3 \right) \tag{2.1}$$

E_{total}	=	Total energy
E	=	Electrostatic energy
U	=	Interatomic potential energy (i.e. Lennard-Jones)
W	=	Short-range strain energy density (related to U)
Ω	=	Continuum body in the current configuration
Ω_0	=	Continuum body in the reference configuration
Q^s	=	Charge of the atomic species indexed by s
ρ	=	Charge density field in Ω
ϵ_0	=	dielectric constant for vacuum
$\mathbb{K}$	=	Dipole-dipole interaction electrostatic kernel
$\boldsymbol{u}$	=	Displacement field
$\boldsymbol{x}$	=	Slow variable representing position in current configuration
$\boldsymbol{y}$	=	Fast variable representing position in current configuration
$\boldsymbol{x}_0$	=	Position in reference configuration
$\boldsymbol{\zeta}^s$	=	Intra-unit cell position of species s, defined in the reference
$\boldsymbol{p}$	=	Polarization density field
ϕ	=	Electric potential
$\text{grad}_{\boldsymbol{x}}\,\phi$	=	Electric field
$\boldsymbol{F}$	=	Deformation gradient
J	=	$\det \boldsymbol{F}$
$\square_i$	=	ith unit cell
$\triangle_i$	=	ith partial unit cell
ϵ	=	Continuum material point lengthscale
l	=	Atomic lengthscale
L	=	Lengthscale over which continuum fields vary
$\mathcal{B}_\epsilon$	=	Ball of radius ϵ
$\mathcal{D}_\epsilon$	=	2D disk of radius ϵ
$\text{grad}_{\boldsymbol{x}_0}$	=	Gradient with respect to the reference configuration
$\text{grad}_{\boldsymbol{x}}$	=	Gradient with respect to the current configuration
σ	=	Surface charge due to non-neutral partial unit cells.

$\Omega_\#$ and $\Omega_\square$ represent the decomposition of Ω into the partial unit cells on the boundary ($\Omega_\#$), and the remainder $\Omega_\square := \Omega \backslash \Omega_\#$; see Figure 2.4.

2.3 Problem Formulation

We consider a crystal occupying a region Ω, composed of charged species indexed by s, each carrying a fixed charge Q^s. The notation of species is used broadly; it refers to ions and electrons, as well as electron "shells" as used in core-shell models [56]. We assume that the charges are all point charges, e.g. nuclei, or that they can be

represented through a center of charge as in electron shells. Therefore, the charge distribution $\rho(\boldsymbol{x})$ is a collection of Dirac charges.

The total energy in the body can be written in the form below:

$$E_{total} = \underbrace{\sum_{\substack{i \\ i \neq j}} U_i\left(\{\boldsymbol{r}_{ij}\}\right)}_{\text{short-range}} + \underbrace{\frac{1}{2}\sum_{\substack{i,j \\ i \neq j}} \frac{Q_i^s Q_j^s}{4\pi\epsilon_0 |\boldsymbol{r}_{ij}|}}_{\text{long-range}} \tag{2.2}$$

$\boldsymbol{r}_{ij}$ is the vector between charges i and j, and Q_i^s is the charge carried by ith atom of species s. The function U is the given short-range interatomic potential and can typically involve multibody interactions.

We restrict our attention to zero temperature. Our goal is to find local minimizers of E_{total} to obtain the equilibrium structure subject to applied mechanical and electrostatic loadings. Brute force minimization is infeasible even for the short-range contributions for realistically large systems. This motivated the QC method and related approaches [68, 51] for short-range interactions. We will use the so-called local QC multi-lattice method for the short-range energy largely following [67]. As noted above, there are two ingredients to this multiscale approach: first, a kinematic condensation of the degrees of freedom using interpolations, and second, efficient calculation of the energy sum by using sampling or quadrature in relatively uniform regions. The term *local* refers to the fact that we use a sampling approximation *everywhere* in the specimen including at the defect core where it is likely to be quite inaccurate.

We begin with the species in the reference configuration arranged in a periodic multi-lattice. The unit cell is denoted $\square$ and the atomic length scale l (Figure 2.1). In a perfect lattice with short-range interactions, the energy converges to $\int_\Omega W(\text{grad}_{\boldsymbol{x}_0}\, \boldsymbol{u}, \boldsymbol{\zeta}^s)\; dV_{\boldsymbol{x}_0}$. Here, W is the strain energy density, and $\text{grad}_{\boldsymbol{x}_0}\, \boldsymbol{u}$ and $\boldsymbol{\zeta}^s$ are the deformation gradient and the "shifts" or relative displacements between

lattices [10, 24]. While the expression for W is algebraically involved, it is conceptually simple and comes directly from U. In a perfect multi-lattice, there is a well-defined notion of energy per atom since every atom of a given species is in the same environment. Therefore, it is possible to define an energy density by finding the energy of the atoms in a unit cell and dividing the cell volume, which is precisely W. The energy naturally depends on the shape of the unit cell and the positions of the different species within it, and this information is contained in $\operatorname{grad}_{\boldsymbol{x}_0} \boldsymbol{u}$ and $\boldsymbol{\zeta}^s$ respectively. The QC method replaces the sum in (Equation 2.2) by sampling the energy density $W(\operatorname{grad}_{\boldsymbol{x}_0} \boldsymbol{u}, \boldsymbol{\zeta}^s)$ and using appropriate weights. In the more sophisticated formulations of QC, the energy is computed without this approximation in highly-distorted regions such as the vicinity of the defect [40]. In the local QC, the approximation is used throughout the specimen, including at the defect. For further details, we refer the reader to recent reviews of the extensive literature on applying QC to materials with short-range interactions [68, 51].

2.4 Electrostatic Interactions

In this section, we describe the formal calculations that enable us to efficiently account for the long-range electrostatic interactions. A key aspect is the appearance of the polarization density as a multiscale mediator. Because our treatment here is formal, we go between charge density fields and point charges as convenient by assuming that our calculations are valid even when the charge density field consists of Dirac masses. Rigorous treatments of many of the key aspects are available in the literature [35] and also are the focus of our ongoing work.

2.4.1 Why the Electrostatic Energy is Long-Range

We construct and examine some simple examples to understand why the electrostatics is denoted "long-range". E.g., the Lennard-Jones potential has interactions that

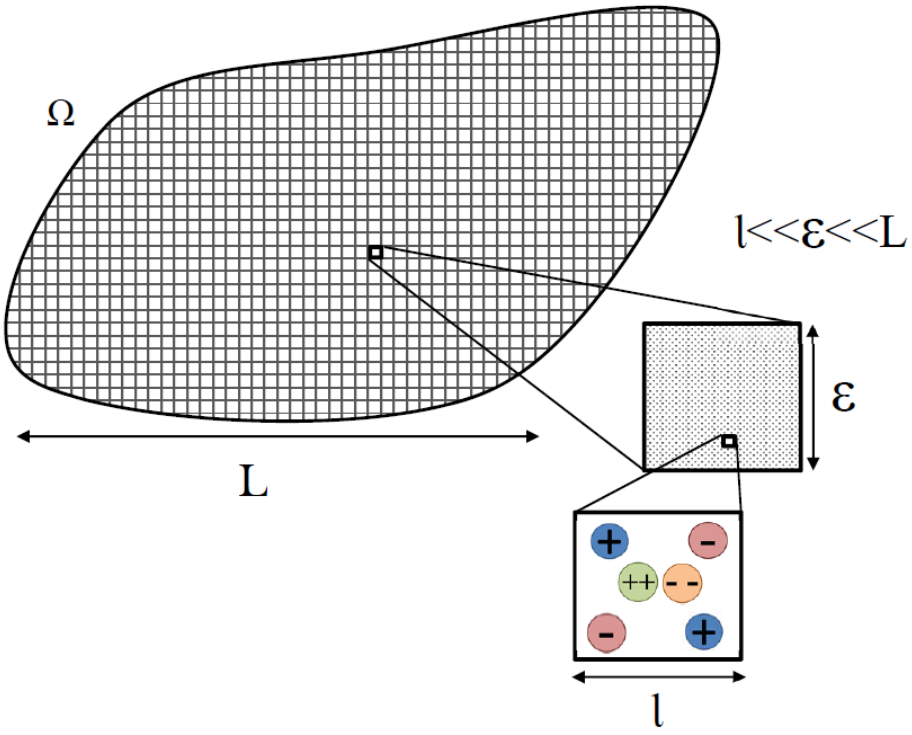


Figure 2.1: Domain Ω showing the separation of scales with sample charge distribution.

decay as r^{-6} and these interactions nominally extend to ∞. As we see, there are important differences when the interactions decay as r^{-1} in electrostatics.

Consider a uniform lattice and 3 cases of charge arrangement within in each unit cell: (i) a charge, (ii) a pair of equal and opposite charges forming a dipole, and (iii) two pairs of equal and opposite charges that form a quadrupole with zero dipole moment (Figure 2.2).

We first consider the lattice of charges. As a rough measure of energy density, we compute the energy of the charge in the chosen unit cell due to its interaction with all the other unit cells in the body. This is the product between the magnitude of the charge in the chosen unit cell with the electrostatic potential created by the rest of the body. The potential due to a charge at a distance r from the chosen unit cell scales as r^{-1}. Further, at a distance r from the chosen unit cell, we consider a spatial

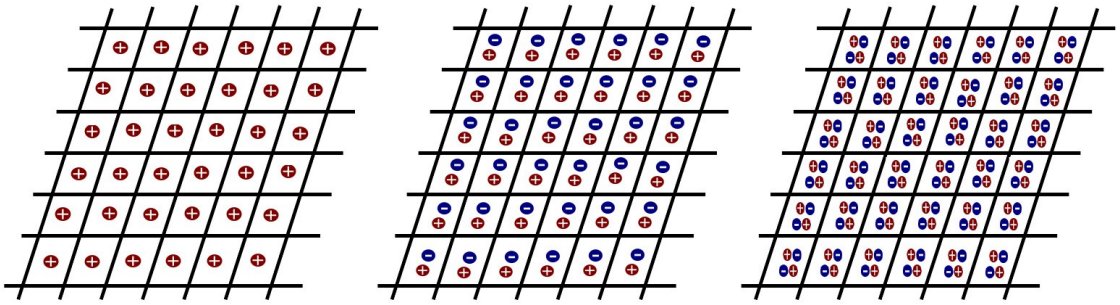


Figure 2.2: 3 cases of charge arrangement: (i) net charge, (ii) net dipole but no net charge, and (iii) net quadrupole, but no net charge and no net dipole.

region with the shape of a spherical shell with unit thickness. This shell has volume that scales as r^2 and therefore roughly contains r^2 charges. So the total potential at the chosen unit cell due to the rest of the system is $\sum_{r=1}^{\infty} \frac{1}{r} r^2 = \sum_{r=1}^{\infty} r \to \infty$. That is, the energy density of the body is unbounded in the large-body limit. The physical implication of this calculation is that large clusters of unbalanced charges have extremely high-energy and are thus unlikely to be observed in real materials.

Next consider the lattice of dipoles. As a rough measure of energy density, we compute the energy of the dipole in the chosen unit cell due to its interaction with all the other unit cells in the body. This is the product between the magnitude of the dipole in the chosen unit cell with the electrostatic field created by the rest of the body. The electric field due to a dipole at a distance r from the chosen unit cell scales as r^{-3}. Further, the shell at a distance r again contains roughly r^2 dipoles. So the total electric field at the chosen unit cell due to the rest of the body is $\sum_{r=1}^{\infty} \frac{1}{r^3} r^2 = \sum_{r=1}^{\infty} \frac{1}{r}$. This sum nominally also tends to infinity. However, the issue is more subtle. The full expression for the electric field due to a unit dipole oriented in the direction $\hat{\boldsymbol{n}}$ at a position $\boldsymbol{x}$ is $E_i = \sum_j \frac{\delta_{ij} - 3\hat{\boldsymbol{x}}_i \hat{\boldsymbol{x}}_j}{4\pi |\boldsymbol{x}|^3} \hat{n}_j$. Certain components of the summation have alternating sign, and this leads to conditionally convergent sums, and in general this sum is at the border of convergence / divergence. The physical implication of this

calculation is that the energy density of a large collection of dipoles is extremely sensitive to the precise boundary conditions that are imposed far away "at infinity". Alternatively, in a finite body, this says that the energy *density* at a given point is extremely sensitive to the distribution of dipoles throughout the entire body. This physical implication is the reason to denote electrostatic interactions as "long-range", namely, it is not possible to define a meaningful energy density that depends only on the local state of the crystal. The energy density at a given material point instead requires accounting for the state of the body at every other material point as well as boundary conditions. As we see below, this also poses practical difficulties for standard multiscale algorithms such as QC. This makes these methods inapplicable to an extremely broad class of solids: in all dielectrics, polarizable media, and ionic solids, the non-vanishing dipole moment in the unit cell is central to the physics of dielectric response, spontaneous polarization, and other key electrical properties.

Finally, consider the lattice of quadrupoles. As a rough measure of energy density, we compute the energy of the quadrupole in the chosen unit cell due to its interaction with all the other unit cells in the body. This is the product between the magnitude of the quadrupole in the chosen unit cell with the gradient of the electrostatic field created by the rest of the body. The electric field due to a quadrupole at a distance r from the chosen unit cell scales as r^{-5}. Further, the shell at a distance r contains again roughly contains r^2 quadrupoles. So the total electric field at the chosen unit cell due to the rest of the body is $\sum_{r=1}^{\infty} \frac{1}{r^5} r^2 = \sum_{r=1}^{\infty} \frac{1}{r^3}$. This sum converges rapidly. This setting corresponds to the case of metals and other systems with mobile electrons that allow the charge to redistribute itself to "shield" the dipole moment. This leads effectively to short-range interactions: though nominally the interactions are present at all values of r, the rapid convergence of the series allows truncation at finite cut-off without significant error. For this reason, among others, short-range potentials with interactions involving only nearest- and next-nearest-neighbors are

sufficiently accurate to model metallic and related systems.

2.4.2 Existing Numerical Approaches to Compute Electrostatic Interactions

The long-range nature of the electrical interactions described above leads to practical hurdles in atomic multiscale computations. Leading methods to handle these interactions are Ewald sums and the Fast Multipole Method (FMM). The Ewald method [29] assumes perfect periodicity. This is appropriate only for perfect crystals. Approximating defect calculations by periodic supercells has severe artifacts even with purely short-range interactions, a difficulty much more pronounced when interactions are long-range in nature. The fast multipole method (FMM) reduces the problem from $O(N^2)$ to $O(N)$, but is still extremely expensive with atomic multiscale calculations in crystals often as large as $N \sim 10^{21}$. In addition, the ability of FMM to deal with arbitrary charge distributions also implies that it does not exploit the close-to-uniform distortion away from the defect [7].

For short-range interactions, multiscale atomistic methods such as the QC method borrow ideas of quadrature rules from FEM [68, 51] to evaluate the energy at various sampling/quadrature atoms and then use quadrature weights. This idea depends critically on the energy evaluation at the quadrature point being a fast calculation. This is *not* a fast calculation if the quadrature charges interact directly with every other charge in the system. Therefore, these multiscale methods are applicable only to materials with short-range interactions. Multiscale QC-based methods for Orbital-Free Density Functional Theory – an empirical simplification of Density Functional Theory for metallic systems – use a continuous charge density rather than discrete point charges, but formally the issues are the same. Roughly, a *predictor solution* is patched together from the periodic solution in each "element", and then a *corrector solution* due to the defect is superposed. The efficiency and accuracy of this approach requires that the corrector solution can be coarsely resolved away from the defect

[25]. However, in general there is a spatially-varying dipole moment in the specimen and zero dipole in the free space; therefore, the periodic calculation in any element will have large errors because it replaces this complex environment by a charge distribution with uniform dipole density. Consequently, the corrector can require fine resolution over much of the domain, except in settings such as metallic systems with net zero local dipole where they are currently applied.

An alternate approach to accounting for the large number of charge-charge interactions is to rewrite the problem as the electrostatic Poisson equation. However, this will lead to a highly-oscillatory forcing term that fluctuates at the atomic lengthscale while the problem is posed over the entire specimen. Therefore, this does not solve the essential difficulty. While numerical homogenization approaches may be feasible because the forcing close-to-periodic in many regions of the sample, it is not clear how to obtain full resolution in the vicinity of the defect. Further, the Poisson equation can be thought of as a nonlocal constraint that must be appended to (Equation 2.2) in the minimization and therefore the essential non-local character remains.

2.4.3 Coarse-Graining the Electrostatic Field Energy

We now consider the coarse-graining of the electrostatic energy. As noted above, we will work with a charge density field ρ and assume that the coarse-graining is also valid for point charges by replacing ρ with appropriate Dirac masses. Our starting point is to write ρ following the ideas of 2-scale methods [4, 72]. I.e., we consider the setting where the charge density varies over 2 different lengthscales. There is a rapid almost-periodic variation of charge density at the lengthscale of the atomic unit cell (denoted l). In addition, there is a much slower variation over the characteristic continuum lengthscale denoted L. In the language of 2-scale methods, we can write the charge density field as $\rho(\boldsymbol{x}, \boldsymbol{y})$ with $\boldsymbol{y} := \boldsymbol{x}/l$ and ρ periodic (with period of order one) in the second argument. A heuristic picture is that $\boldsymbol{x}$ specifies the location of

the material point, and $\boldsymbol{y}$ specifies the location within the material point (Figure 2.1).

The electrostatic field energy can be written:

$$E = \int_{\boldsymbol{x},\boldsymbol{x}' \in \Omega} \frac{\rho(\boldsymbol{x})\rho(\boldsymbol{x}')}{|\boldsymbol{x} - \boldsymbol{x}'|} dV_{\boldsymbol{x}} dV_{\boldsymbol{x}'} \tag{2.3}$$

We wish to examine the limit of the energy in the following setting. We introduce a lengthscale ϵ that, roughly speaking, denotes the size of the continuum material point. The limit of interest is then $l/\epsilon \to 0$ and $\epsilon/L \to 0$, or $l \ll \epsilon \ll L$. Essentially, the physical interpretation of this limit is that the atomic unit cell is much smaller than a material point, and a material point is much smaller than the lengthscale over which continuum fields vary.

We can now rewrite E as

$$E = \sum_{\boldsymbol{x},\boldsymbol{x}' \in \Omega} \int_{(l\boldsymbol{y}) \in \mathcal{B}_\epsilon(\boldsymbol{x}), (l\boldsymbol{y}') \in \mathcal{B}_\epsilon(\boldsymbol{x}')} \frac{\rho(\boldsymbol{x},\boldsymbol{y})\rho(\boldsymbol{x}',\boldsymbol{y}')}{|\boldsymbol{x} + l\boldsymbol{y} - \boldsymbol{x}' - l\boldsymbol{y}'|} (l^3\, dV_{\boldsymbol{y}})(l^3\, dV_{\boldsymbol{y}'}) \tag{2.4}$$

The notation $\mathcal{B}_\epsilon(\boldsymbol{x})$ denotes a ball of radius ϵ centered at $\boldsymbol{x}$. We note that $(l\boldsymbol{y}) \in \mathcal{B}_\epsilon(\boldsymbol{x})$ implies $\boldsymbol{y} \in \mathcal{B}_{\epsilon/l}(\boldsymbol{x})$.

We break up E into 2 parts: a local term when $\boldsymbol{x} = \boldsymbol{x}'$, and a nonlocal term when $\boldsymbol{x} \neq \boldsymbol{x}'$:

$$\begin{aligned} E = & \underbrace{\sum_{\boldsymbol{x} \in \Omega} \int_{\boldsymbol{y},\boldsymbol{y}' \in \mathcal{B}_{\epsilon/l}(\boldsymbol{x})} \frac{\rho(\boldsymbol{x},\boldsymbol{y})\rho(\boldsymbol{x},\boldsymbol{y}')}{l\,|\boldsymbol{y} - \boldsymbol{y}'|} l^6\, dV_{\boldsymbol{y}} dV_{\boldsymbol{y}'}}_{\text{local term: } \boldsymbol{x}=\boldsymbol{x}'} \\ & + \underbrace{\sum_{\boldsymbol{x},\boldsymbol{x}' \in \Omega; \boldsymbol{x} \neq \boldsymbol{x}'} \int_{\boldsymbol{y} \in \mathcal{B}_{\epsilon/l}(\boldsymbol{x}), \boldsymbol{y}' \in \mathcal{B}_{\epsilon/l}(\boldsymbol{x}')} \frac{\rho(\boldsymbol{x},\boldsymbol{y})\rho(\boldsymbol{x}',\boldsymbol{y}')}{|\boldsymbol{x} + l\boldsymbol{y} - \boldsymbol{x}' - l\boldsymbol{y}'|} l^6\, dV_{\boldsymbol{y}} dV_{\boldsymbol{y}'}}_{\text{nonlocal term: } \boldsymbol{x}\neq\boldsymbol{x}'} \end{aligned} \tag{2.5}$$

In the limit that we will take, the nonlocal term represents the interactions between charges that are located at different material points $\boldsymbol{x}, \boldsymbol{x}'$, while the local term represents interactions between charges at the same material point.

We introduce some notation for what follows. We denote by $\square$ the rescaled atomic unit cell with characteristic dimension and volume of order 1. The atomic unit cell with characteristic dimensions l is denoted by $l\square$. We also use $\square_i$ and $l\square_i$ to denote the i-th atomic unit cell in a lattice.

The Local Contribution of the Electrostatic Energy

For a fixed $\boldsymbol{x}$, the charge $\rho(\boldsymbol{x}, \boldsymbol{y})$ is periodic in the second argument over $\square$. Therefore, we begin by rewriting the local term in (Equation 2.5) in terms of integrals over $\square_i$:

$$\sum_{\boldsymbol{x}\in\Omega} \sum_{\square_i,\square_{i'}\in\mathcal{B}_{\epsilon/l}(\boldsymbol{x})} \int_{\boldsymbol{y}\in\square_i,\boldsymbol{y}'\in\square_{i'}} l^5 \frac{\rho(\boldsymbol{x},\boldsymbol{y})\rho(\boldsymbol{x},\boldsymbol{y}')}{|\boldsymbol{y}-\boldsymbol{y}'|} dV_{\boldsymbol{y}} dV_{\boldsymbol{y}'} \tag{2.6}$$

The periodicity, and the fact that $\epsilon/l \to \infty$, together imply that every term in the sum relating the interaction between cells i and i' can be mapped to an interaction between cells 0 and some i''. Therefore, the local term can now be written

$$\sum_{\boldsymbol{x}\in\Omega} \left(\frac{\epsilon}{l}\right)^3 \int_{\boldsymbol{y}\in\square_0,\boldsymbol{y}'\in\mathcal{B}_{\epsilon/l}(\boldsymbol{x})} l^5 \frac{\rho(\boldsymbol{x},\boldsymbol{y})\rho(\boldsymbol{x},\boldsymbol{y}')}{|\boldsymbol{y}-\boldsymbol{y}'|} dV_{\boldsymbol{y}} dV_{\boldsymbol{y}'} \tag{2.7}$$

The factor $(\epsilon/l)^3$ is the number of terms in the sum that are replaced, obtained from dividing the volume of the ball of radius ϵ/l by the volume of $\square$.

This has the form of a Riemann sum: with $\epsilon \ll L$, the term ϵ^3 is the volume measure.

$$\sum_{\boldsymbol{x}\in\Omega} \epsilon^3 \left(\int_{\boldsymbol{y}\in\square_0,\boldsymbol{y}'\in\mathcal{B}_{\epsilon/l}(\boldsymbol{x})} l^2 \frac{\rho(\boldsymbol{x},\boldsymbol{y})\rho(\boldsymbol{x},\boldsymbol{y}')}{|\boldsymbol{y}-\boldsymbol{y}'|} dV_{\boldsymbol{y}} dV_{\boldsymbol{y}'} \right) \tag{2.8}$$

The term in the brackets is the integrand and must be well-behaved, i.e. neither blow up nor go to 0, in the limit $l \ll \epsilon$. The natural scaling is that the charge density must scale as $\rho(\boldsymbol{x}, \boldsymbol{y}) = \tilde{\rho}(\boldsymbol{X}, \boldsymbol{y})/l$ where $\tilde{\rho}$ is the charge density on the rescaled unit cell $\square$ with characteristic dimension 1, and $l\boldsymbol{X} = \boldsymbol{x}$. Note that $\tilde{\rho}$ has dimensions of charge per unit area. While this choice of scaling may appear arbitrary, we note that

it can be recognized as the classical dipole scaling from elementary electrostatics. That is, in constructing the notion of a point dipole, one starts with charges that are separated by a finite distance and then takes the limit of the charges approaching each other. However, this limit leads to a finite dipole moment only when the charge magnitude is assumed to scale inversely with separation, thereby leaving the product of charge and separation distance finite. It is precisely this scaling which is required here for a finite local electrostatic energy. In our setting, if, for example, we assumed a fixed charge density and allowed the lattice spacing to go to 0, charge neutrality would give us vanishing energy.

Using the charge scaling described above enables us to map the calculation of the integrand to a unit domain and gives the final form:

$$\int_{\boldsymbol{x}\in\Omega}\left(\int_{\boldsymbol{y}\in\square_0,\boldsymbol{y}'\in\mathcal{B}_{\epsilon/l}(\boldsymbol{x})}\frac{\tilde{\rho}(\boldsymbol{X},\boldsymbol{y})\tilde{\rho}(\boldsymbol{X},\boldsymbol{y}')}{|\boldsymbol{y}-\boldsymbol{y}'|}dV_{\boldsymbol{y}}dV_{\boldsymbol{y}'}\right)\,dV_{\boldsymbol{x}} \tag{2.9}$$

The energy in this form can be readily absorbed into standard energy densities that arise from applying the CB theorem to short-range interactions. This term has a number of different names: the Madelung energy in ionic solids [38], the Lorentz local field, the weak-short contribution [35].

As an example, we replace the charge density with a set of Dirac masses representing point charges. The charge density in the unit cell is $\tilde{\rho}(\boldsymbol{X},\boldsymbol{y})=\sum_{\boldsymbol{y}\in\square_0}Q^s\delta_{\boldsymbol{y}_s}(\boldsymbol{y})$ and extended periodically. The local energy has the form:

$$E_{local}=\int_{\Omega}\left(\sum_{i,j\in\square_0}Q^i\mathbb{S}^{ij}Q^j+\frac{1}{3}|\boldsymbol{p}(\boldsymbol{x})|^2+\boldsymbol{p}(\boldsymbol{x})\cdot\boldsymbol{S}\boldsymbol{p}(\boldsymbol{x})\right)\,dV_{\boldsymbol{x}} \tag{2.10}$$

where $\boldsymbol{p}(\boldsymbol{x}):=\sum_{\boldsymbol{y}\in\square_0}Q^s\boldsymbol{y}\delta_{\boldsymbol{y}_s}(\boldsymbol{y})$ is the polarization of the unit cell.

The quantities $\mathbb{S},\boldsymbol{S}$ are defined as:

$$\mathbb{S}^{ij}:=\lim_{\omega\to\infty}\sum_{\boldsymbol{y}^i\in\square}\sum_{\substack{\boldsymbol{z}\in L_1\setminus\boldsymbol{y}^i\\ \cap\mathcal{B}_\omega}}\frac{1}{4\pi\epsilon_0|\boldsymbol{y}^i-\boldsymbol{z}^j|},\quad \boldsymbol{S}:=\lim_{\omega\to\infty}\sum_{\substack{\boldsymbol{z}\in L_1\setminus\boldsymbol{0}\\ \cap\mathcal{B}_\omega}}\mathbb{K}(\boldsymbol{z}) \tag{2.11}$$

In the specific case that we have only 2 point charges in a unit cell, $\mathbb{S}$ vanishes and the local energy can be written in terms of $\boldsymbol{p}$ exclusively. The dipole kernel $\mathbb{K}$ is defined in (Equation 2.12).

An important point above is the presence of the limit in the definitions of $\mathbb{S}$ and $\boldsymbol{S}$. As noted previously, the full sums used above are conditionally convergent. The use of a limit is equivalent to enforcing a particular order of summation; in this case, it corresponds to using "neutral spheres" using the terminology of Ewald summation. Physically, it enforces that the far-field boundary conditions are set to 0. The local contribution then is simply the energy of a uniform lattice of charges with vanishing far-field electric field; the lattice is uniform because the entire lattice is located at a single material point. In general, there can be a non-vanishing far-field electric field due to the other material points and continuum-scale boundary conditions, and this is introduced through the non-local contribution in the next section.

Nonlocal Contribution of the Electrostatic Energy

We now focus on the nonlocal term in (Equation 2.5), i.e., the interactions between charges at different material points. This contribution provides an energy that is very different from the standard local continuum energies. In particular, those energies are developed from the CB theorem that in the limit does not have any direct atomic interactions between different material points. Here, we have a clear nonlocal character to the energy.

We first introduce some notation regarding the multipole expansion. Consider

the electrostatic interaction for charges located at $\boldsymbol{x}+l\boldsymbol{y}$ and $\boldsymbol{x}'+l\boldsymbol{y}'$:

$$\begin{aligned}\frac{1}{|\boldsymbol{x}+l\boldsymbol{y}-\boldsymbol{x}'-l\boldsymbol{y}'|} =& \frac{1}{|\boldsymbol{x}-\boldsymbol{x}'|}+\frac{\partial}{\partial(\boldsymbol{x}-\boldsymbol{x}')}\left(\frac{1}{|\boldsymbol{x}-\boldsymbol{x}'|}\right) l\cdot(\boldsymbol{y}-\boldsymbol{y}') \\ &+\frac{1}{2}\underbrace{\frac{\partial^2}{\partial(\boldsymbol{x}-\boldsymbol{x}')^2}\left(\frac{1}{|\boldsymbol{x}-\boldsymbol{x}'|}\right)}_{\mathbb{K}} l^2:(\boldsymbol{y}-\boldsymbol{y}')\otimes(\boldsymbol{y}-\boldsymbol{y}')+O(l^3)\end{aligned} \tag{2.12}$$

The operator $\mathbb{K}$ is the dipole kernel.

In the nonlocal term in (Equation 2.5), in anticipation of using the periodicity of $\rho(\boldsymbol{x},\boldsymbol{y})$ in $\boldsymbol{y}$ when $\boldsymbol{x}$ is held fixed, we reduce the integrations to unit cells $\square$:

$$\sum_{\boldsymbol{x},\boldsymbol{x}'\in\Omega;\boldsymbol{x}\neq\boldsymbol{x}'} \quad \sum_{\square_i\in\mathcal{B}_{\epsilon/l}(\boldsymbol{x});\square_{i'}\in\mathcal{B}_{\epsilon/l}(\boldsymbol{x}')} \quad \int_{\boldsymbol{y}\in\square_i,\boldsymbol{y}'\in\square_{i'}} \frac{\rho(\boldsymbol{x},\boldsymbol{y})\rho(\boldsymbol{x}',\boldsymbol{y}')}{|\boldsymbol{x}+l\boldsymbol{y}-\boldsymbol{x}'-l\boldsymbol{y}'|} l^6\, dV_{\boldsymbol{y}}dV_{\boldsymbol{y}'} \tag{2.13}$$

Assuming a separation of scales, i.e. $\epsilon \ll L$, the periodicity of ρ implies that the interaction between charges contained in $\mathcal{B}_{\epsilon/l}(\boldsymbol{x})$ and $\mathcal{B}_{\epsilon/l}(\boldsymbol{x}')$ can be replaced by interactions between charges in unit cells at $\boldsymbol{x}$ and $\boldsymbol{x}'$, and then multiplying by the number of unit cells in $\mathcal{B}_{\epsilon/l}(\boldsymbol{x})$ and $\mathcal{B}_{\epsilon/l}(\boldsymbol{x}')$.

$$\sum_{\boldsymbol{x},\boldsymbol{x}'\in\Omega;\boldsymbol{x}\neq\boldsymbol{x}'} \quad \left(\frac{\epsilon}{l}\right)^3\left(\frac{\epsilon}{l}\right)^3 \int_{\boldsymbol{y}\in\square,\boldsymbol{y}'\in\square} \frac{\rho(\boldsymbol{x},\boldsymbol{y})\rho(\boldsymbol{x}',\boldsymbol{y}')}{|\boldsymbol{x}+l\boldsymbol{y}-\boldsymbol{x}'-l\boldsymbol{y}'|} l^6\, dV_{\boldsymbol{y}}dV_{\boldsymbol{y}'} \tag{2.14}$$

Canceling the factors of l and using the notion of Riemann sums as above with ϵ^3 as the volume measure, we can write this as a double integral:

$$\int_{\boldsymbol{x},\boldsymbol{x}'\in\Omega;\boldsymbol{x}\neq\boldsymbol{x}'} \left(\int_{\boldsymbol{y}\in\square,\boldsymbol{y}'\in\square} \frac{\rho(\boldsymbol{x},\boldsymbol{y})\rho(\boldsymbol{x}',\boldsymbol{y}')}{|\boldsymbol{x}+l\boldsymbol{y}-\boldsymbol{x}'-l\boldsymbol{y}'|}\, dV_{\boldsymbol{y}}dV_{\boldsymbol{y}'}\right)\, dV_{\boldsymbol{x}}\, dV_{\boldsymbol{x}'} \tag{2.15}$$

As in the local contribution, we require the integrand in brackets above to be well-defined when $l\to 0$. Recall the dipole scaling $\rho=\tilde{\rho}/l$: the integrand is therefore well-behaved if $\frac{1}{|\boldsymbol{x}+l\boldsymbol{y}-\boldsymbol{x}'-l\boldsymbol{y}'|}$ scales as l^2.

We substitute the multipole expansion from (Equation 2.12) and notice immediately that the first term scales independently of l and the second term scales linearly in l. These would then potentially cause the integrand to diverge as $l \to 0$. However, we recall that each unit cell is charge-neutral, i.e. $\int_\square \tilde{\rho}(\boldsymbol{x}, \boldsymbol{y})\ dV_{\boldsymbol{y}} = 0$. This causes both the first and second terms in the multipole expansion to vanish. Physically, this means that the energy is unbounded if every unit cell is not charge-neutral, e.g. recalling the example in Section 2.4.1.

Next, we consider the term $\frac{1}{2}l^2\mathbb{K} : (\boldsymbol{y} - \boldsymbol{y}') \otimes (\boldsymbol{y} - \boldsymbol{y}')$. The terms containing $\boldsymbol{y} \otimes \boldsymbol{y}$ and $\boldsymbol{y}' \otimes \boldsymbol{y}'$ vanish from charge neutrality. The only remaining terms can be readily written as:

$$\int_{\boldsymbol{x},\boldsymbol{x}' \in \Omega; \boldsymbol{x} \neq \boldsymbol{x}'} \left(\mathbb{K}(\boldsymbol{x} - \boldsymbol{x}') : \underbrace{\int_{\boldsymbol{y} \in \square} \tilde{\rho}(\boldsymbol{X}, \boldsymbol{y}) \boldsymbol{y}\ dV_{\boldsymbol{y}}}_{\boldsymbol{p}(\boldsymbol{x})} \otimes \underbrace{\int_{\boldsymbol{y}' \in \square} \tilde{\rho}(\boldsymbol{X}', \boldsymbol{y}') \boldsymbol{y}'\ dV_{\boldsymbol{y}'}}_{\boldsymbol{p}(\boldsymbol{x}')} \right) dV_{\boldsymbol{x}}\ dV_{\boldsymbol{x}'}$$

$$= \int_{\boldsymbol{x},\boldsymbol{x}' \in \Omega; \boldsymbol{x} \neq \boldsymbol{x}'} \boldsymbol{p}(\boldsymbol{x}') \cdot \mathbb{K}(\boldsymbol{x} - \boldsymbol{x}') \boldsymbol{p}(\boldsymbol{x})\ dV_{\boldsymbol{x}}\ dV_{\boldsymbol{x}'} \tag{2.16}$$

where the terms containing $\boldsymbol{y} \otimes \boldsymbol{y}'$ and $\boldsymbol{y}' \otimes \boldsymbol{y}$ have been combined using symmetry.

Consider finally the terms denoted $O(l^3)$. These will all go to 0 as $l \to 0$. Physically, these terms represent the contributions from quadrupole and higher-order moments of the charge distribution, i.e. $\int_\square \tilde{\rho}(\boldsymbol{x}, \boldsymbol{y}) \boldsymbol{y} \otimes \boldsymbol{y}\ dV_{\boldsymbol{y}}$ and higher-order. We see that these terms vanish identically in the limit. Therefore, terms of higher-order than dipole do not appear in the nonlocal part of the continuum energy, recalling the example in Section 2.4.1. In general, all short-range forces – i.e. those that decay faster than dipolar interactions – do not contribute to the nonlocal term in the limit [24, 10].

Finally, a long but straightforward calculation using the divergence theorem and

integration-by-parts gives

$$\begin{aligned}
&\int_{\boldsymbol{x},\boldsymbol{x}'\in\Omega} \boldsymbol{p}(\boldsymbol{x}')\cdot\mathbb{K}(\boldsymbol{x}-\boldsymbol{x}')\boldsymbol{p}(\boldsymbol{x})\ dV_{\boldsymbol{x}}\ dV_{\boldsymbol{x}'} = \\
&\int_{\boldsymbol{x},\boldsymbol{x}'\in\Omega} \operatorname{div}\boldsymbol{p}(\boldsymbol{x}')G(\boldsymbol{x}-\boldsymbol{x}')\operatorname{div}\boldsymbol{p}(\boldsymbol{x})\ dV_{\boldsymbol{x}}\ dV_{\boldsymbol{x}'} \\
&+\int_{\boldsymbol{x},\boldsymbol{x}'\in\partial\Omega} \boldsymbol{n}\cdot\boldsymbol{p}(\boldsymbol{x}')G(\boldsymbol{x}-\boldsymbol{x}')\boldsymbol{n}\cdot\boldsymbol{p}(\boldsymbol{x})\ dS_{\boldsymbol{x}}\ dS_{\boldsymbol{x}'} \\
&-2\int_{\boldsymbol{x}\in\Omega,\boldsymbol{x}'\in\partial\Omega} \boldsymbol{n}\cdot\boldsymbol{p}(\boldsymbol{x}')G(\boldsymbol{x}-\boldsymbol{x}')\operatorname{div}\boldsymbol{p}(\boldsymbol{x})\ dV_{\boldsymbol{x}}\ dS_{\boldsymbol{x}'}
\end{aligned} \tag{2.17}$$

where G is the standard electrostatics Greens function and $\mathbb{K} := \nabla^2 G$ from (Equation 2.12). Note that the condition $\boldsymbol{x} \neq \boldsymbol{x}'$ has not been written for brevity. An important conclusion from the above formula is that $-\operatorname{div}\boldsymbol{p}$ is equivalent to a bulk charge density (the so-called "bound bulk charge density") and that $\boldsymbol{p}\cdot\boldsymbol{n}$ is equivalent to a surface charge density (the so-called "bound surface charge density"). In that perspective, the formula above simply gives the energy of this composite charge distribution using the usual Green's function relation between charge density and energy. When $\boldsymbol{p}$ is discontinuous along interior surfaces, this formula gives bound surface charges along these surfaces.

While we have derived the equivalent bound charges using standard integration formulas after taking the limit of the Riemann sum, it is straightforward to derive these directly. Essentially, we manipulate the Riemann sum using the standard approach in the Riemann sum proof of the divergence theorem (e.g., [71]). In the interior, we find $\operatorname{div}\boldsymbol{p}$ appearing and the boundaries of the infinitesimal element canceling with it's neighbors. On the boundary of $\partial\Omega$, there is no cancellation leading to the contribution $-\boldsymbol{p}\cdot\boldsymbol{n}$.

Boundary Contributions due to Partial Unit Cells

We consider now the role of boundaries. As we have mentioned above and will discuss below in detail, the value of the polarization depends on the chosen unit cell. Boundary contributions are essential to ensure that the coarse-grained electric fields and other quantities do not depend on the arbitrary choice of unit cell. There are two contributions: first, due to polarization terminations $-\boldsymbol{p}\cdot\boldsymbol{n}$, and second, surface charges due to partial unit cells on the surface that are not charge-neutral. The polarization terminations have already been accounted for as shown in (Equation 2.17). In this section, we consider the case of the surface charges due to partial non-charge-neutral unit cells.

For simplicity, we do not compute the total energy which will have straightforward but tedious cross-terms between interior bound charges (due to $\operatorname{div}\boldsymbol{p}$) and surface charges as can be seen (Equation 2.17). Instead, we compute the electric potential field due to the surface charges where the calculations are more transparent. In a formal setting, one can readily go between these calculations.

Consider a point $\boldsymbol{x}\in\partial\Omega$. At a point $\boldsymbol{x}'\neq\boldsymbol{x}$, the electric potential due to the charges at $\boldsymbol{x}$ is given by:

$$\phi(\boldsymbol{x}')=\sum_{\boldsymbol{x}\in\partial\Omega}\int_{l\boldsymbol{y}\in\mathcal{D}_\epsilon(\boldsymbol{x})\times Cl\boldsymbol{n}}\frac{\rho(\boldsymbol{x},\boldsymbol{y})}{|\boldsymbol{x}+l\boldsymbol{y}-\boldsymbol{x}'|}l^3\,dV_{\boldsymbol{y}} \tag{2.18}$$

Here $\mathcal{D}_\epsilon(\boldsymbol{x})$ is a 2D disk of radius ϵ located at $\boldsymbol{x}$. Therefore, $\mathcal{D}_\epsilon(\boldsymbol{x})\times l\boldsymbol{n}$ denotes a squat cylinder of height Cl oriented with axis $\boldsymbol{n}$ and cross section $\mathcal{D}_\epsilon(\boldsymbol{x})$. The vector $\boldsymbol{n}$ is the unit outward normal to Ω. It is implicit in the above formula that we are considering charges only in the partial unit cells.

We assume that the surface is a rational plane (see Appendix A for the definition). The integration above in the directions along the surface (i.e., normal to $\boldsymbol{n}$) can then be reduced to an integration over a single unit cell because of periodicity in those

directions[1]. The integration in the direction along $\boldsymbol{n}$ reduces simply to the partial unit cells on the boundary and is therefore independent of Cl. Following the ideas above for the volume contributions, we can then rewrite this as an integral over a unit cell by putting in the appropriate factor for the number of unit cells in the disk:

$$\phi(\boldsymbol{x}') = \sum_{\boldsymbol{x}\in\partial\Omega} \frac{\epsilon^2}{l^2} \int_{\boldsymbol{y}\in\triangle} \frac{\tilde{\rho}(\boldsymbol{X},\boldsymbol{y})/l}{|\boldsymbol{x}+l\boldsymbol{y}-\boldsymbol{x}'|} l^3 \, dV_{\boldsymbol{y}} \tag{2.19}$$

where we have used the notation $\triangle$ for partial non-neutral unit cells.

Therefore, we require that only the term independent of l from (Equation 2.12) appear above. Upon taking the Riemann sum and defining the surface charge density $\sigma(\boldsymbol{x})$, this gives the expected and simple result:

$$\phi(\boldsymbol{x}') = \int_{\boldsymbol{x}\in\partial\Omega} \frac{1}{|\boldsymbol{x}-\boldsymbol{x}'|} \underbrace{\left(\int_{\boldsymbol{y}\in\triangle} \tilde{\rho}(\boldsymbol{X},\boldsymbol{y}) \, dV_{\boldsymbol{y}} \right)}_{\sigma} \, dS_{\boldsymbol{x}} \tag{2.20}$$

While we have assumed for simplicity that $\boldsymbol{x} \neq \boldsymbol{x}'$, considering the case $\boldsymbol{x} = \boldsymbol{x}'$ and examining the energy would give us a local contribution analogous to that in the case of the bulk.

2.4.4 Role of Boundaries in Compensating for the Non-uniqueness of Polarization

It is well-known, e.g. [61], that the value of $\boldsymbol{p}$ in a periodic solid depends on the choice of unit cell. This would appear to be a fatal difficulty in using $\boldsymbol{p}$ as a multiscale mediator between the atomic-scale-variation of ρ and continuum-scale quantities. In the materials physics community, quantum mechanical notions are invoked to obtain a unique choice of polarization for a given periodic charge distribution [61]. However, from the perspective of the calculations above, we are simply coarse-graining classical

[1] It is not clear to us how to proceed without assuming that the surfaces are rational planes. Irrational surfaces cause severe difficulties in defining surface energies even in simpler models of solids [62].

electrostatic interactions and there is no reason for quantum mechanics to play any role. As we describe in this section, the difficulties noticed by [61] are entirely due to their starting-point of an infinite periodic solid. This makes the notion of boundaries ill-defined. If instead we begin from a finite solid and take the limit of lattice spacing being much smaller than the size of the body (the large-body limit), we see that the surface charges on the boundaries play a critical role. In short, while the polarization is itself not uniquely-defined, the electrostatic energy that comes from accounting for both the polarization and the surface charge is a unique quantity. While changing the unit cell changes the value of the polarization density, it also changes the boundary charge in the partial unit cells. These compensate to give the same value for the electrostatic energy.

One-Dimensional Illustrative Example

Consider a finite body $\Omega = (-L, L) \times (-1, 1) \times (-1, 1)$ with a one-dimensional charge distribution $\rho(\boldsymbol{x}) = \rho_0 \sin(2\pi \frac{x_1}{l})$ (Figure 2.3). We assume that L is an integer multiple of l, i.e. $nl = L$. Guided by the multipole expansion, we compute the dipole moment as the leading contributor to the behavior of the bar without using the fact that the charge distribution is in fact periodic in Ω. We then compare this to the result obtained by using polarization density field that is defined on the unit cell.

The total dipole moment of the bar $\boldsymbol{P} := \int_\Omega \rho(\boldsymbol{r}')\boldsymbol{r}' \, dV_{\boldsymbol{r}'}$ evaluates to $(1, 0, 0) \times \frac{-4\rho_0 Ll}{\pi}$.

The polarization density $\boldsymbol{p}$ in a single unit cell $l\square = (a, l + a) \times (-1, 1) \times (-1, 1)$ is defined as $\boldsymbol{p} := \frac{1}{\text{volume}(l\square)} \int_{\boldsymbol{r}' \in l\square} \rho(\boldsymbol{r}')\boldsymbol{r}' \, dV_{\boldsymbol{r}'}$. It evaluates to $(1, 0, 0) \times \frac{-\rho_0 l}{2\pi} \cos(2\pi \frac{a}{l})$. This is a classic example showing that $\boldsymbol{p}$ depends on the chosen unit cell, here parametrized by a [61]. From (Equation 2.17) and the associated discussion, we have no bulk charge because $\boldsymbol{p}$ is identical in each unit cell, but there is a surface charge density given by $-\boldsymbol{p} \cdot \boldsymbol{n}$. Therefore, there is a total charge of $\frac{2\rho_0 l}{\pi} \cos(2\pi \frac{a}{l})$

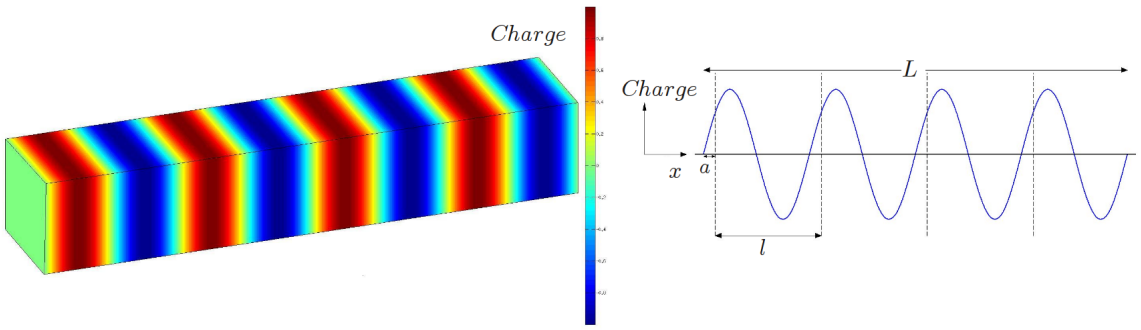


Figure 2.3: Charge distribution in the 1D illustrative example to show the effect of boundaries.

at $+L$, and $\frac{-2\rho_0 l}{\pi}\cos(2\pi\frac{a}{l})$ at $-L$. However, there are partial unit cells at each end: $(-L, -L+a)$ and $(L-l+a, L)$, and these are not charge neutral. The charge in these cells evaluates to $\frac{-2\rho_0 l}{\pi}\left(1-\cos(2\pi\frac{a}{l})\right)$ and $\frac{2\rho_0 l}{\pi}\left(1-\cos(2\pi\frac{a}{l})\right)$ respectively. Therefore the total charge at each end, both from the partial unit cells and from $-\boldsymbol{p}\cdot\boldsymbol{n}$, is $\pm\frac{2\rho_0 l}{\pi}$. These equal and opposite charges are separated by a distance $2L$. Therefore, this is a dipole of strength $\frac{-4\rho_0 lL}{\pi}$. Note that we have errors up to order l because the charges due to the polarization terminating on the surface are separated by $L-l$; however, the key point is that in the limit of $l \ll L$, we recover the dipole $\boldsymbol{P}$.

The General Case

The key lesson from the example above is that it is critical to account for the charge in the partial unit cells on the boundary. This ensures that the coarse-graining that exploits the polarization as a multiscale mediator does not depend on the choice of unit cell. We now examine this in the 3D setting.

First, we decompose Ω into $\Omega_\square$, with only complete unit cells, and $\Omega_\#$ with the surface layer of incomplete unit cells, Figure 2.4.

We now consider the unit cells adjacent to $\Omega_\#$. Our goal is to modify these

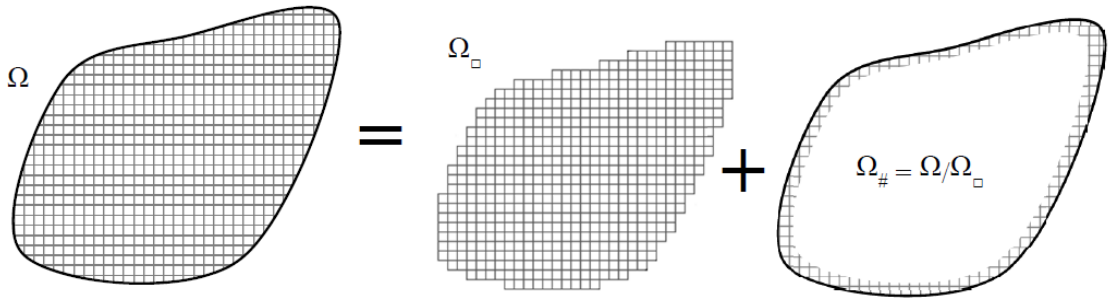


Figure 2.4: Decompose Ω into $\Omega_\square$ and $\Omega_\#$.

unit cells in various ways, and show that the resulting changes in surface charge and polarization density balance each other.

An important element of our strategy is to transform the given unit cell to a unit cell that has a face parallel to the surface under consideration. Appendix A shows that a unit cell with this property can always be found when the surface is rational. As in Section 2.4.3, we restrict attention to rational surfaces.

For this special choice of unit cell, we now consider the changes in surface charge and polarization density for various operations. We use the notation that the lattice vectors tangential to the surface are $\boldsymbol{h}_2$ and $\boldsymbol{h}_3$. We note that the volume of the unit cell can be written $\boldsymbol{h}_2 \times \boldsymbol{h}_3 \cdot \boldsymbol{h}_1 = |\boldsymbol{h}_2 \times \boldsymbol{h}_3| \boldsymbol{n} \cdot \boldsymbol{h}_1$.

First, consider translations of the unit cell as shown in Figure 2.5.

Consider Figure 2.5a. A translation along $\boldsymbol{h}_1$ causes an increase in the uncompensated surface charge area density $\Delta\sigma = \frac{1}{|\boldsymbol{h}_2 \times \boldsymbol{h}_3|} \int_{①} \rho$ in the partial unit cells. The increase in the polarization density in the translated unit cell is $\Delta\boldsymbol{p} = \frac{1}{|\boldsymbol{h}_2 \times \boldsymbol{h}_3| \boldsymbol{n} \cdot \boldsymbol{h}_1} \left(\int_{②} \rho \boldsymbol{y} - \int_{①} \rho \boldsymbol{y} \right)$. From the periodicity of the charge distribution $\rho(\boldsymbol{y} + \boldsymbol{h}_1) = \rho(\boldsymbol{y})$, we have $\Delta\boldsymbol{p} = \frac{1}{|\boldsymbol{h}_2 \times \boldsymbol{h}_3| \boldsymbol{n} \cdot \boldsymbol{h}_1} \boldsymbol{h}_1 \int_{②} \rho$. Therefore $\Delta\boldsymbol{p} \cdot \boldsymbol{n} = \Delta\sigma$.

Consider Figure 2.5b. A translation along either $\boldsymbol{h}_2$ or $\boldsymbol{h}_3$ causes no change in σ. The change in polarization is $\frac{1}{|\boldsymbol{h}_2 \times \boldsymbol{h}_3| \boldsymbol{n} \cdot \boldsymbol{h}_1} \boldsymbol{h}_2 \int_{②} \rho$. Therefore $\Delta\boldsymbol{p} \cdot \boldsymbol{n} = 0$.

In general, one can have a translation along any direction. Such a translation

can be decomposed into components along the lattice directions and the calculations above applied in succession to each direction.

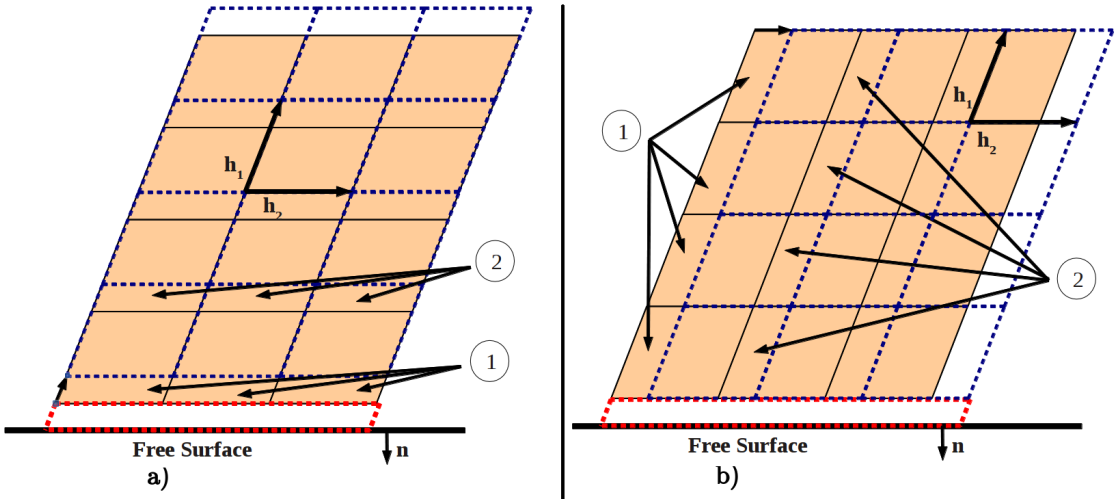


Figure 2.5: Change in charge and polarization due to a translation along $\boldsymbol{h}_1$ and $\boldsymbol{h}_2$ respectively in the special choice of unit cell.

Second, consider distortions of the unit cell as shown in Figure 2.6.

From reasoning following very closely the previous case of translations of the unit cell, we find that the relation $\Delta\boldsymbol{p} \cdot \boldsymbol{n} = \Delta\sigma$ holds here too.

Third, consider changes in the unit cell due to remapping of the lattice vectors as shown in Figure 2.7.

As noted in Appendix A, the relation between basis vectors $\{\boldsymbol{f}_1, \boldsymbol{f}_2, \boldsymbol{f}_3\}$ and $\{\boldsymbol{h}_1, \boldsymbol{h}_2, \boldsymbol{h}_3\}$ must be of the form: $\boldsymbol{f}_i = \sum_j \mu_i^j \boldsymbol{h}_j$ with μ_i^j a matrix of integers with determinant ± 1. An example of such a remapping is in Figure 2.7a.

As shown in the example in Figure 2.6bcde, regions of the original unit cell are mapped to the new unit cell. For instance, (1a) maps to (1b), (2a) maps to (2b), and (3a) maps to (3b). Each of these regions is translated by an integer linear combination of $\{\boldsymbol{h}_1, \boldsymbol{h}_2, \boldsymbol{h}_3\}$; however, each region may have a *different* integer combination translation. In addition, the uncompensated unit cell on the boundary also increases

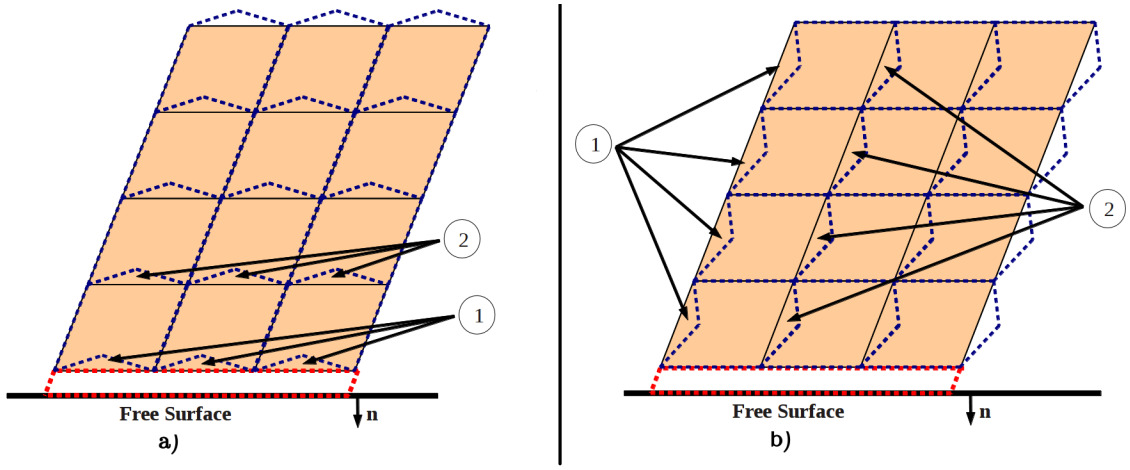


Figure 2.6: Change in charge and polarization due a distortion of the unit cell in the special choice of unit cell.

in extent (Figure 2.6f). As above, for a periodic charge distribution, when a charged region is translated by an integer multiple of a lattice vector, the consequent change in polarization is simply the total charge in the region times the translation distance. Therefore,

$$\Delta \boldsymbol{p} = \frac{1}{|\boldsymbol{h}_2 \times \boldsymbol{h}_3| \boldsymbol{n} \cdot \boldsymbol{h}_1} \left(\sum_i \nu_i^1 \boldsymbol{h}_1 \int_{A_i} \rho + \sum_i \nu_i^2 \boldsymbol{h}_2 \int_{A_i} \rho + \sum_i \nu_i^3 \boldsymbol{h}_3 \int_{A_i} \rho \right) \tag{2.21}$$

, where $\nu_i^1, \nu_i^2, \nu_i^3$ are integers.

The change in the uncompensated charge is simply $\Delta\sigma = \frac{1}{|\boldsymbol{h}_2 \times \boldsymbol{h}_3|} \sum_i \nu_i^1 \int_{A_i} \rho$ which is related to the extent of the translation along $\boldsymbol{h}_1$. This matches precisely with $\Delta \boldsymbol{p} \cdot \boldsymbol{n}$.

In the general case of modifying a given unit cell to another shape by any combination of the mechanisms studied above, we can conceptually consider mapping the given unit cell to the special unit cell with a surface-parallel face, conducting the modifications with the special unit cell, and then mapping to the desired final unit cell. Of course, in practice none of this need be done; as long as we are assured that changes in the unit cell are compensated by boundary charges appropriately, we can directly modify the unit cell as desired.

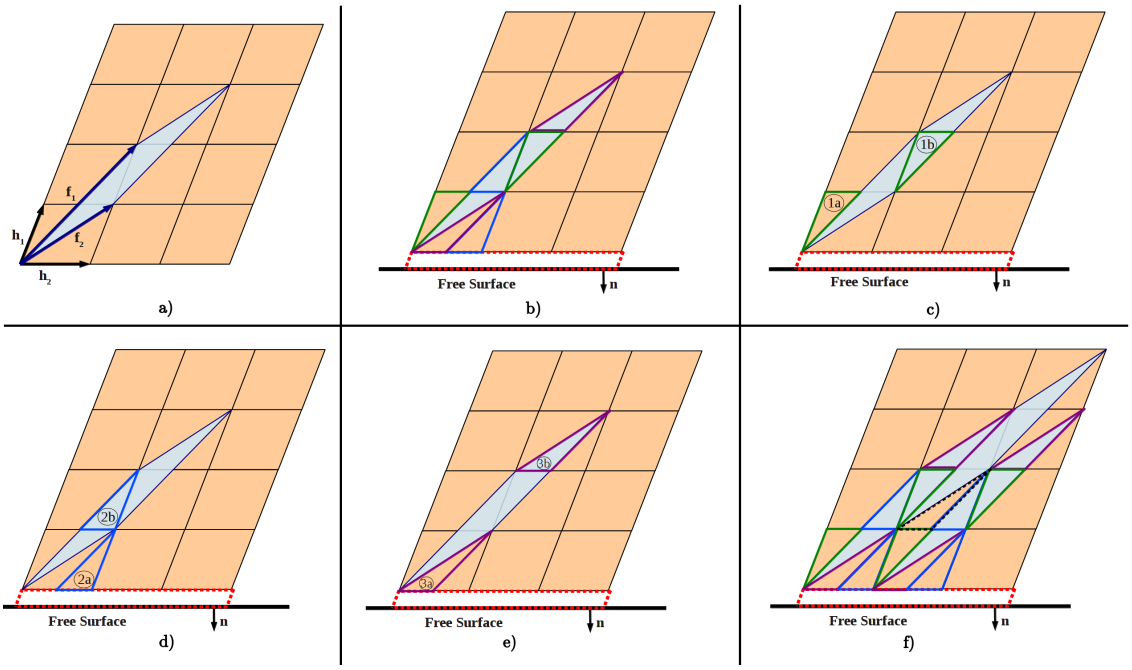


Figure 2.7: Change in charge and polarization due a remapping of the unit cell from the special choice of unit cell.

In the interior of the body, $\operatorname{div} \boldsymbol{p}$ changes by $O(l)$ when the unit cell is changed. This follows directly from the definition of $\boldsymbol{p}$ in (Equation 2.16) and the chain rule, using the fact that $\boldsymbol{X}/l = \boldsymbol{x}$. Therefore, the bound bulk charge density is the same in the limit of $l/L \ll 1$.

We note potential connections to ideas of Null-Lagrangians in the issue of a unique definition of the polarization [20]. Essentially, one can have different expressions for the free-energies, but these lead to the same Euler-Lagrange equation but with different boundary conditions. Similarly, different choices for the unit cell leave the bulk electrostatics unchanged, because the change in the bulk polarization is compensated by the boundary contributions.

2.5 Numerical Implementation

Our numerical implementation for the short-range interactions follows closely the standard QC, e.g. [67]. In standard QC, there are two essential steps: first, a reduction of degrees of freedom by interpolation, typically using linear shape functions inspired by finite elements, with atomic resolution in critical regions and coarse-grained elsewhere (Figure 2.8, Figure 2.9); and second, a fast estimation of the energy (or derivative of the energy with respect to the retained degrees of freedom) using Cauchy-Born sampling. Among the many variants of QC, we use the local QC for multi-lattices, following [67]. Local QC refers to the use of sampling *everywhere* in the specimen, not only in the coarse-grained region but also in regions with atomic resolution in the interpolation.

Dielectrics require a multi-lattice description because a dielectric response requires at least two charges in the unit cell that move independently to change the polarization in response to electromechanical fields. Essentially, the multi-lattice description uses $\boldsymbol{F}$ to track the deformation of the unit cell, and a set of vector-valued fields $\boldsymbol{\zeta}^s$ that track the position of individual species s within the unit cell. We use linear interpolation for the coarse-grained displacement field $\boldsymbol{u}$ implying that $\boldsymbol{F}$ is constant in a given element. To be consistent with this spatial variation of $\boldsymbol{F}$, we use the same "constant in each element" interpolation for $\boldsymbol{\zeta}^s$. If the element were of infinite extent, this choice of interpolation would ensure that the energy density converges to the standard Cauchy-Born theorem. In the local QC approximation, we estimate the energy of a given element by finding the energy density of atomic unit cells at the selected quadrature / sampling points and multiply by the appropriate weight.

This interpolation of the kinematic variables $\boldsymbol{F}, \boldsymbol{\zeta}^s$ implies that the polarization $\boldsymbol{p}$ is also constant in a given element. Therefore, in terms of effective bound charges,

we have no bound bulk charges ($\operatorname{div} \boldsymbol{p} = 0$), and we have surface charge density $(\boldsymbol{p}_1 - \boldsymbol{p}_2) \cdot \boldsymbol{n}$ at the element faces. In the coarse-grained local QC approximation, the evaluation of electrostatic fields consists simply of finding the fields set up by the charge distributions. One element of electrostatics is that the electric potential and field are naturally posed in the current configuration. Therefore, for numerical updates, we compute the electrostatic fields in the current and then pull back to the reference using standard electromechanical transformations [80]. We assume in the remainder of the chapter that we are dealing with point charges that can move around, but do not change their charge.

2.5.1 Energy Minimization through Gradient Descent

Our interest is in finding energy minimizers to the coarse-grained problem. Under the local QC approximation, the coarse-grained problem can be written as the standard continuum energy for electromechanical solids [65, 80]:

$$E = \underbrace{\int_{\Omega_0} W(\operatorname{grad}_{\boldsymbol{x}_0} \mathbf{u}, \boldsymbol{\zeta}^s)\, dV_{\boldsymbol{x}_0}}_{\text{short-range energy}} + \underbrace{\frac{\epsilon_0}{2} \int_{\mathbb{R}^3} |\operatorname{grad}_{\boldsymbol{x}} \phi|^2\, dV_{\boldsymbol{x}}}_{\text{long-range (non-local) energy}} \tag{2.22}$$

$$\operatorname{div}_{\boldsymbol{x}} \operatorname{grad}_{\boldsymbol{x}} \phi = \operatorname{div}_{\boldsymbol{x}} \boldsymbol{p} \tag{2.23}$$

The nonlocal expression in (Equation 2.17) can be transformed to the form above by first noting that the right side of (Equation 2.17) is entirely in terms of the electrostatic Greens function G. Therefore, the electrostatic field ϕ can be defined as the solution of the electrostatic equation with charges given by $-\operatorname{div} \boldsymbol{p}$ and $\boldsymbol{p} \cdot \boldsymbol{n}$. The energy density is then simply $|\operatorname{grad}_{\boldsymbol{x}} \phi|^2$. The surface charges due to $\boldsymbol{p} \cdot \boldsymbol{n}$ as well as due to incomplete unit cells appear in the boundary conditions for the electrostatic equation. The local contribution of the electrostatic energy has been absorbed into the short-range term. Note that the non-local energy integral is posed in the current configuration.

We use a gradient-flow evolution to find the (local) minimizers following [80, 84]. The independent variables that remain are $\boldsymbol{u}$ and $\boldsymbol{\zeta}^s$. The polarization is completely defined in terms of unit cell geometry $\boldsymbol{u}$ and intra-cell positions of the charges $\boldsymbol{\zeta}^s$, in turn defining the electrostatic potential ϕ through the electrostatic Poisson equation. Therefore, taking variations:

$$\operatorname{grad}_{\boldsymbol{x}_0} \boldsymbol{u} \to \operatorname{grad}_{\boldsymbol{x}_0} \boldsymbol{u} + \eta \operatorname{grad}_{\boldsymbol{x}_0} \boldsymbol{v} \quad , \quad \boldsymbol{\zeta}^s \to \boldsymbol{\zeta}^s + \eta \boldsymbol{\theta}^s \tag{2.24}$$

Additionally, the variation in the electric field is $\operatorname{grad}_{\boldsymbol{x}} \phi \to \operatorname{grad}_{\boldsymbol{x}} \phi + \eta \operatorname{grad}_{\boldsymbol{x}} \psi$ but this variation is constrained to variations in $\boldsymbol{p} \to \boldsymbol{p} + \eta \boldsymbol{q}$ by the Poisson equation, i.e. $\operatorname{div}_{\boldsymbol{x}} \operatorname{grad}_{\boldsymbol{x}} \psi = \operatorname{div}_{\boldsymbol{x}} \boldsymbol{q}$.

The definition of gradient flow results in the following statement:

$$\begin{aligned}\int_{\Omega_0} \left(\dot{\boldsymbol{u}} \cdot \boldsymbol{v} + \sum_s \dot{\boldsymbol{\zeta}}^s \cdot \boldsymbol{\theta}^s \right) \, dV_{\boldsymbol{x}_0} &= - \frac{\partial}{\partial \eta} E \left(\operatorname{grad}_{\boldsymbol{x}_0} \boldsymbol{u} + \eta \operatorname{grad}_{\boldsymbol{x}_0} \boldsymbol{v}, \boldsymbol{\zeta}^s + \eta \boldsymbol{\theta}^s \right) \Big|_{\eta=0} \\ &= \int_{\Omega} \left(\frac{\partial W}{\partial (\operatorname{grad}_{\boldsymbol{x}_0} \boldsymbol{u})} : \operatorname{grad}_{\boldsymbol{x}_0} \boldsymbol{v} + \sum_s \frac{\partial W}{\partial \boldsymbol{\zeta}^s} \cdot \boldsymbol{\theta}^s \right) \, dV_{\boldsymbol{x}_0} \\ &\quad + \epsilon_0 \int_{\mathbb{R}^3} \operatorname{grad}_{\boldsymbol{x}} \phi \cdot \operatorname{grad}_{\boldsymbol{x}} \psi \, dV_{\boldsymbol{x}}\end{aligned} \tag{2.25}$$

The nonlocal integral over $\mathbb{R}^3$ can be transformed by multiplying $\operatorname{div}_{\boldsymbol{x}} \operatorname{grad}_{\boldsymbol{x}} \psi = \operatorname{div}_{\boldsymbol{x}} \boldsymbol{q}$ by ϕ and integrating over $\mathbb{R}^3$. Using integration by parts on the left side and then pulling it back to the reference gives:

$$\int_{\Omega_0} \operatorname{grad}_{\boldsymbol{x}} \phi \cdot \boldsymbol{q} J \, dV_{\boldsymbol{x}_0} = \int_{\mathbb{R}^3} \operatorname{grad}_{\boldsymbol{x}} \phi \cdot \operatorname{grad}_{\boldsymbol{x}} \psi \, dV_{\boldsymbol{x}} \tag{2.26}$$

where J is the Jacobian of the deformation. This is substituted for the nonlocal

integral in (Equation 2.25) to get:

$$\int_{\Omega_0}\left(\dot{\boldsymbol{u}}\cdot\boldsymbol{v}+\sum_s\dot{\boldsymbol{\zeta}}^s\cdot\boldsymbol{\theta}^s\right)\,dV_{\boldsymbol{x}_0}=\int_{\partial\Omega_0}\frac{\partial W}{\partial(\mathrm{grad}_{\boldsymbol{x}_0}\,\boldsymbol{u})}:\boldsymbol{n}\boldsymbol{v}\;dS_{\boldsymbol{x}_0}$$
$$-\int_{\Omega_0}\left(\mathrm{div}_{\boldsymbol{x}_0}\frac{\partial W}{\partial(\mathrm{grad}_{\boldsymbol{x}_0}\,\boldsymbol{u})}\right)\cdot\boldsymbol{v}\;dV_{\boldsymbol{x}_0}$$
$$+\int_{\Omega_0}\sum_s\frac{\partial W}{\partial\boldsymbol{\zeta}^s}\cdot\boldsymbol{\theta}^s\;dV_{\boldsymbol{x}_0}+\epsilon_0\int_{\Omega_0}\mathrm{grad}_{\boldsymbol{x}}\,\phi\cdot\boldsymbol{q}J\;dV_{\boldsymbol{x}_0} \tag{2.27}$$

We now examine the relation between $\boldsymbol{q}$ and the variations $\boldsymbol{v}$ and $\boldsymbol{\theta}$. The polarization density $\boldsymbol{p}$ is defined by

$$\boldsymbol{p}=\frac{1}{\det(\boldsymbol{F})V_0}\sum_s Q^s\boldsymbol{F}\boldsymbol{\zeta}^s \tag{2.28}$$

Note that $\boldsymbol{\zeta}^s$ is the position of species s in the reference configuration, while $\boldsymbol{p}$ is the polarization density in the current configuration. Similarly, V_0 is the volume of the unit cell in reference configuration. Hence, both V_0 and $\boldsymbol{\zeta}^s$ are pushed forward to the current.

Taking the variation of $\boldsymbol{p}$

$$\boldsymbol{p}+\eta\boldsymbol{q}=\frac{1}{\det(\boldsymbol{F}+\eta\boldsymbol{G})V_0}\sum_s Q^s(\boldsymbol{F}+\eta\boldsymbol{G})(\boldsymbol{\zeta}^s+\eta\boldsymbol{\theta}^s) \tag{2.29}$$

where $\boldsymbol{G}:=\mathrm{grad}_{\boldsymbol{x}_0}\,\boldsymbol{v}$. Noting that $(\det(\boldsymbol{F}+\eta\boldsymbol{G}))^{-1}=\det(\boldsymbol{F})^{-1}\det(\boldsymbol{I}+\eta\boldsymbol{F}^{-1}\boldsymbol{G})^{-1}=\det(\boldsymbol{F})^{-1}\,(1-\eta\,\mathrm{tr}(\boldsymbol{F}^{-1}\boldsymbol{G})-O(\eta^2))$, we find:

$$\boldsymbol{q}=\frac{1}{\det(\boldsymbol{F})V_0}\sum_s Q^s\left(\boldsymbol{F}\boldsymbol{\theta}^s+\boldsymbol{\zeta}^s\cdot\mathrm{grad}_{\boldsymbol{x}_0}\,\boldsymbol{v}-\mathrm{tr}(\boldsymbol{F}^{-1}\,\mathrm{grad}_{\boldsymbol{x}_0}\,\boldsymbol{v})\boldsymbol{F}\boldsymbol{\zeta}^s\right) \tag{2.30}$$

after ignoring terms of order higher than linear in η. Using this expression for $\boldsymbol{q}$, we obtain the following expression for $\int_{\Omega_0}\mathrm{grad}_{\boldsymbol{x}}\,\phi\cdot\boldsymbol{q}J\;dV_{\boldsymbol{x}_0}$ after using integration-by-

parts and the divergence theorem:

$$\begin{aligned}\int_{\Omega_0} \operatorname{grad}_{\boldsymbol{x}} \phi \cdot \boldsymbol{q} J \; dV_{\boldsymbol{x}_0} &= \frac{1}{V_0} \sum_s Q^s \int_{\Omega} \operatorname{grad}_{\boldsymbol{x}} \phi \cdot (\boldsymbol{F}\boldsymbol{\theta}^s) \; dV_{\boldsymbol{x}_0} \\ + \frac{1}{V_0} \sum_s Q^s \left(\int_{\partial\Omega_0} \operatorname{grad}_{\boldsymbol{x}} \phi \boldsymbol{\zeta}^s : \boldsymbol{n}\boldsymbol{v} \; dS_{\boldsymbol{x}_0} - \int_{\Omega_0} \operatorname{div}_{\boldsymbol{x}_0} (\operatorname{grad}_{\boldsymbol{x}} \phi \boldsymbol{\zeta}^s) \cdot \boldsymbol{v} \; dV_{\boldsymbol{x}_0} \right) \\ - \frac{1}{V_0} \sum_s Q^s \Bigg(\int_{\partial\Omega_0} \operatorname{grad}_{\boldsymbol{x}} \phi \cdot (\boldsymbol{F}\boldsymbol{\zeta}^s) \, \boldsymbol{F}^{-T} : \boldsymbol{n}\boldsymbol{v} \; dS_{\boldsymbol{x}_0} \\ - \int_{\Omega_0} \operatorname{div}_{\boldsymbol{x}_0} \left(\operatorname{grad}_{\boldsymbol{x}} \phi \cdot (\boldsymbol{F}\boldsymbol{\zeta}^s) \, \boldsymbol{F}^{-T} \right) \cdot \boldsymbol{v} \; dV_{\boldsymbol{x}_0} \Bigg)\end{aligned} \tag{2.31}$$

Defining $\boldsymbol{A}^s := \operatorname{grad}_{\boldsymbol{x}} \phi \boldsymbol{\zeta}^s - \operatorname{grad}_{\boldsymbol{x}} \phi \cdot \boldsymbol{F}\boldsymbol{\zeta}^s \boldsymbol{F}^{-T}$, collecting terms in (Equation 2.31, Equation 2.27) and localizing using the arbitrariness of the variations gives us the compact form:

$$\dot{\boldsymbol{u}} = \operatorname{div}_{\boldsymbol{x}_0} \left(\frac{\partial W}{\partial \operatorname{grad}_{\boldsymbol{x}_0} \boldsymbol{u}} + \epsilon_0 \sum_s \frac{Q^s}{V_0} \boldsymbol{A}^s \right) \quad , \quad \dot{\boldsymbol{\zeta}}^s = -\frac{\partial W}{\partial \boldsymbol{\zeta}^s} - \epsilon_0 \frac{Q^s}{V_0} \operatorname{grad}_{\boldsymbol{x}} \phi \cdot \boldsymbol{F} \tag{2.32}$$

with the boundary term:

$$\left(\frac{\partial W}{\partial \operatorname{grad}_{\boldsymbol{x}_0} \boldsymbol{u}} + \epsilon_0 \sum_s \frac{Q^s}{V_0} \boldsymbol{A}^s \right) \cdot \boldsymbol{n} = 0 \tag{2.33}$$

These equations provide the gradient descent equations for the fields $\boldsymbol{u}$ and $\boldsymbol{\zeta}^s$. The equation for $\boldsymbol{u}$ involves a standard mechanical stress as well as a so-called Maxwell or electromechanical stress. The equation for $\boldsymbol{\zeta}^s$ is a local equation (i.e., not a PDE), but is coupled through W and the electric field to the nonlocal electrostatics and the PDE for momentum balance.

Electromechanical Transformations to the Reference Configuration

For simplicity, we solve the electrostatic Poisson equation in the current configuration for the electric potential $\phi(\boldsymbol{x})$ and compute the electric field $\operatorname{grad}_{\boldsymbol{x}} \phi(\boldsymbol{x})$ and rewrite

$\boldsymbol{x} = \boldsymbol{x}(\boldsymbol{x}_0)$ from the deformation map. In our setting, the energy (both short- and long-range) and electric fields are based entirely on the atomic position in the current configuration. Therefore, in common with much of continuum mechanics, the reference configuration can be considered simply a change of variables for bookkeeping convenience. It follows that the definition of electrical quantities in the reference configuration are not essential. This can also be readily observed from (Equation 2.31); the physical quantity of interest there is $\operatorname{grad}_{\boldsymbol{x}} \phi(\boldsymbol{x})$, and while it is certainly possible to define the electric field in the reference, it is not physically important.

This has led to a number of different proposals for referential electrical quantities in the literature. For instance, our (Equation 2.28) suggests that the reference polarization $\boldsymbol{p}_0(\boldsymbol{x}_0)$ is given by $\boldsymbol{p}(\boldsymbol{x}(\boldsymbol{x}_0)) = \det(\boldsymbol{F})^{-1}\boldsymbol{F}\boldsymbol{p}_0(\boldsymbol{x}_0)$, i.e. the polarization transforms as material line elements that carry charges but with an additional factor accounting for volume changes.

In [80], they assume instead $\boldsymbol{p}(\boldsymbol{x}(\boldsymbol{x}_0)) = \det(\boldsymbol{F})^{-1}\boldsymbol{p}_0(\boldsymbol{x}_0)$, and further assume that the reference electrostatic potential $\phi_0(\boldsymbol{x}_0) = \phi(\boldsymbol{x}(\boldsymbol{x}_0))$; this gives them that the electric field transforms as line elements using the identity $\operatorname{grad}_{\boldsymbol{x}} = \boldsymbol{F}^{-T} \operatorname{grad}_{\boldsymbol{x}_0}$. This is consistent with the differential geometric notion of the electric field as a 1-form, i.e. it is a quantity that is integrated along lines.

In [58], following [18], they use yet another transformation; they work with electric displacement $\boldsymbol{D}$ and electric field $\boldsymbol{E}$ as primary variables rather than polarization. These variables are motivated by the fact that the continuum problem posed in polarization and electric potential leads to a saddle-point variational problem, whereas the minimization structure is preserved in $\boldsymbol{D}$ and $\boldsymbol{E}$. The electrostatic equations in these variables are $\operatorname{div} \boldsymbol{D} = 0$ and $\operatorname{curl} \boldsymbol{E} = 0$. For $\boldsymbol{E}$, these imply it should transform as a material line element and matches with [80] as well as the differential geometric notion of the electric field as a 1-form. For $\boldsymbol{D}$ however, these imply a transformation $\boldsymbol{D} = \det(\boldsymbol{F})^{-1}\boldsymbol{F}^{-T}\boldsymbol{D}_0$ following the differential geometric notion of

the electric displacement as a 2-form, i.e. a quantity that is integrated over surfaces; this is obviously identical to the standard stress transformation. This differential geometric notion is also implicitly exploited in Section 4 of [41] in finding the appropriate averaging for the different field quantities. An essential practical advantage of this transformation that is exploited by [58] in their homogenization analysis is that the equations retain their structure in the reference configuration, i.e. $\mathrm{div}_{\boldsymbol{x}_0}\, \boldsymbol{D}_0 = 0$ and $\mathrm{curl}_{\boldsymbol{x}_0}\, \boldsymbol{E}_0 = 0$.

While the transformations proposed by these other workers are physically appealing for the reasons mentioned above, the transformation implied by the microscopic model of the polarization is also physically motivated. These different transformations are not consistent with preserving the relation $\boldsymbol{D} = \epsilon_0 \boldsymbol{E} + \boldsymbol{p}$ between corresponding quantities in the reference.

2.5.2 Local Quasicontinuum for Multi-lattices with Short-Range Interactions

We use standard finite element linear shape functions, N_a defined at the nodes a to approximate the displacements $\boldsymbol{u}$ of the lattice vectors:

$$\boldsymbol{u} \approx \sum_a \boldsymbol{u}_a N_a \Rightarrow \mathrm{grad}_{\boldsymbol{x}_0}\, \boldsymbol{u} \approx \sum_a \boldsymbol{u}_a \,\mathrm{grad}_{\boldsymbol{x}_0}\, N_a \tag{2.34}$$

where $\boldsymbol{u}_a$ are the nodal displacements. Defining $\boldsymbol{B}$ as the Piola-Maxwell stress tensor,

$$\mathrm{div}_{\boldsymbol{x}_0}\, \boldsymbol{B} = \mathrm{div}_{\boldsymbol{x}_0} \left(\frac{\partial W}{\partial \mathrm{grad}_{\boldsymbol{x}_0}\, \boldsymbol{u}} + \epsilon_0 \sum_s \frac{Q^s}{V_0} \boldsymbol{A}^s \right) \tag{2.35}$$

we can write (Equation 2.32) as $\boldsymbol{0} = \mathrm{div}_{\boldsymbol{x}_0}\, \boldsymbol{B}$. Standard nonlinear finite element methods can now be used; the key difference is that we need to compute the electromechanical contribution to the stress at every iteration. At the same time, we also iterate with respect to $\boldsymbol{\zeta}^s$ noting that our interpolation for these variables is piecewise constant, i.e. constant in a given element.

There are two short-range calculations: first, the Piola-Maxwell stress tensor, and second, the minimization over $\boldsymbol{\zeta}^s$. Following the complex local QC method [67], the deformation gradient and $\boldsymbol{\zeta}^s$ are related to the atomic displacements through the Cauchy-Born rule. We assume that the energy of each element can be approximated by assuming a homogeneous deformation of the crystal through the deformation gradient. Given an interatomic potential U, we use

$$\frac{\partial W}{\partial \text{grad}_{\boldsymbol{x}_0} \boldsymbol{u}} = \frac{1}{2V} \sum_{\text{atoms in cutoff}} \frac{\partial U}{\partial \boldsymbol{r}} \frac{\partial \boldsymbol{r}}{\partial \text{grad}_{\boldsymbol{x}_0} \boldsymbol{u}} \tag{2.36}$$

where $\boldsymbol{r}$ are the positions of the atoms and are obtained from $\boldsymbol{u}$ and $\boldsymbol{\zeta}^s$. Similarly, we can compute

$$\frac{\partial W}{\partial \boldsymbol{\zeta}^s} = \frac{1}{2V} \sum_{\text{atoms in cutoff}} \frac{\partial U}{\partial \boldsymbol{r}} \frac{\partial \boldsymbol{r}}{\partial \boldsymbol{\zeta}^s} \tag{2.37}$$

The minimization over the nodal values of $\boldsymbol{u}$ and the element values of $\boldsymbol{\zeta}^s$ are conducted in a coupled manner.

2.5.3 Coarse-graining of the Long-Range Electrostatic Interactions

The energy minimization calculation in (Equation 2.32) requires the electric field for a given distribution of charge, or equivalently for a given $\boldsymbol{p}$. As noted above, we have a constant $\boldsymbol{F}$ and $\boldsymbol{\zeta}^s$ field in each element, i.e. they are discontinuous only along element boundaries. Consequently, $\boldsymbol{p}$ as defined in (Equation 2.28) is also constant in each element and discontinuous along the element boundaries. These discontinuities in polarization result in surface charge densities $(\boldsymbol{p}_1 - \boldsymbol{p}_2) \cdot \boldsymbol{n}$. We compute the fields due to these relatively simple charge distributions using direct Greens function integrations.

2.6 Crystal Free Surface Subject to Inhomogeneous Electric Fields

We apply the methodology described above to a simple setting of a crystal with a free surface subject to an inhomogeneous external electric field due to a point charge above the surface. We use short-range potentials based on the bi-species Lennard-Jones model used for Ni-Mn by [31], giving a tetragonal neutral lattice with a body-centered ion and a charged shell. The polarization is oriented along the tetragonal direction when external fields are absent, thereby providing a spontaneous polarization. This provides a simple model of many widely-used perovskite ferroelectrics such as barium titanate and lead titanate.

Given that this is a model material rather than numerically accurate, we aim to elucidate the physics of electromechanics. There are two independent ratios of interest. One is the strength of the ionic charges v. the strength of the external charge. The other is the strength of ionic interactions v. the strength of the bonded interactions. We explore the effect of the former by increasing external charge while holding ionic charges fixed. We explore the effect of the latter by scaling the electrostatic interactions. This enables us to test a class of materials that range from non-ionic to ionic.

We consider a specimen with the spontaneous polarization oriented tangential to the surface. A single point charge is placed near the surface. In all of these examples, atomic resolution is used in regions of interest – particularly beneath the external charges – while coarser resolution is provided everywhere else. A fine mesh is introduced near the point charge with coarsening throughout the rest of the body. Figure 2.8 shows the full mesh, while Figure 2.9 shows the zoomed in atomistically resolved portion of the mesh with all atoms plotted in the current configuration. The black atoms are nodes while the green atoms are constrained by the interpolation.

We conduct three calculations with the electrostatic interactions scaled by factors

of $1, 2, 4$ respectively, while holding the charge location and strength fixed. For the given charge strength, a scaling by 1 produces a surface distortion near the point charge, while the scaling by 2 and 4 produce nucleation-like events[2]. Figure 2.10 shows the stress and polarization fields near the point charge for electrostatic scaling of 1. Similarly, Figure 2.11 shows the stress and polarization for the electrostatic scaling of 4.

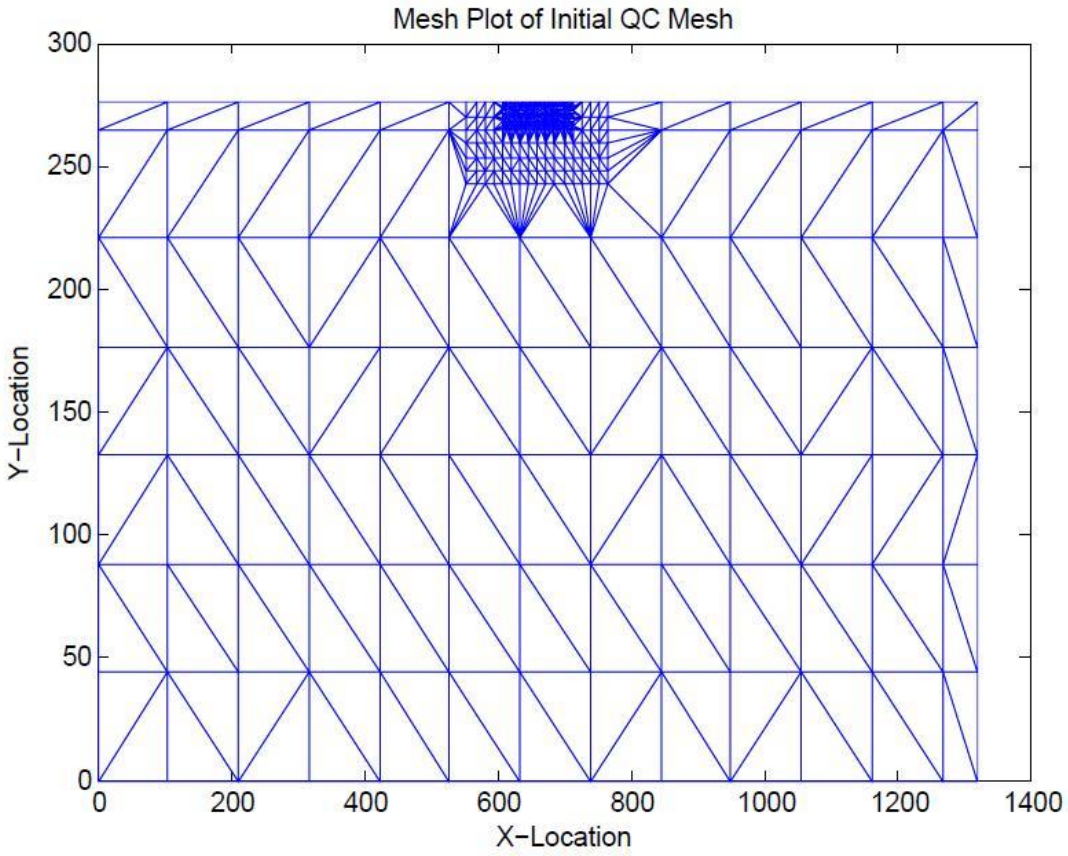


Figure 2.8: The mesh of the entire specimen. The lengthscales are angstroms.

The next set of calculations replaces the single point charge by multiple point charges (2 and 4 respectively), keeping the total charge the same as the case of the single point charge and with spacing between charges on the order of the height above

[2] A nucleation-like event refers to localized switching of polarization. We do not expect our method to be qualitatively accurate beyond this regime.

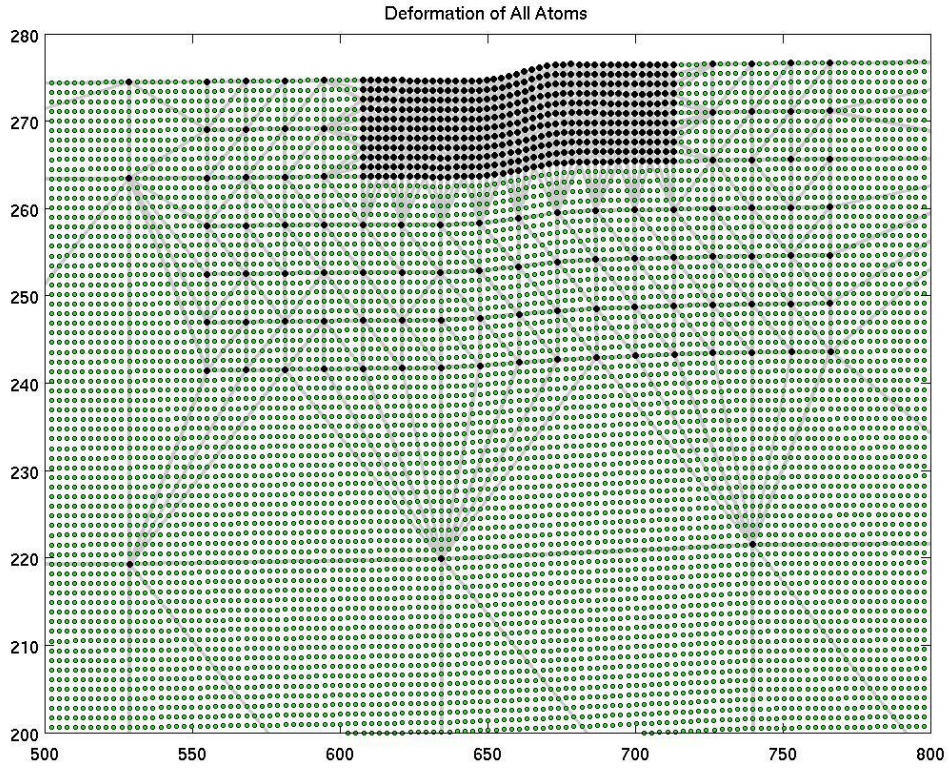


Figure 2.9: Close up view of the atomically-resolved portion of the sample. Without applied fields and loads, the surface of the specimen is flat. The surface feature is caused by an applied electric field.

the surface. In subsequent sets of simulations, these charges were moved closer to the surface until eventually a nucleation-like event occurred. Stress plots are provided for the 2 and 4 charges at various distances from the free surface in Figure 2.12-Figure 2.15.

An interesting feature is the presence of two stress lobes beneath the surface of the material. To further investigate this, we replace the point charge by a dipole (two charges with opposite signs). The resulting deformation as seen in Figure 2.16 is a depression instead of the up-down pattern seen in loadings with charges of the same sign. Additionally, the two stress lobes previously seen disappear and merge

into a single stress lobe beneath the surface.

The stress lobes in non-dipole loadings do not appear to match continuum phase-field calculations, Figure 2.17 following [82]. These continuum calculations are based on linearized electromechanics whereas the atomistic calculations in this chapter are inherently large-deformation. The small-deformation approximation implies that electric fields are computed in the reference as well as potential large rotations being ignored. Further, the material model is also linear elastic. To examine if these assumptions are responsible for the inability of continuum models to capture this feature, we perform the following tests. First, we use precisely our approach except that the electric fields are computed in the reference as in linearized electromechanics. The resulting stress field still shows the double-lobe structure, though with a slightly reduced magnitude (Figure 2.18). Second, we examine the geometric linearization of the strains; Figure 2.19 shows a plot of the normalized difference between the non-linear and linearized ϵ_{22} strain measures which are far too small to be the cause. Third, we test against a fully atomic level description without any coarse-graining. While the system size is small due to computational limitations of the electrostatics, we see a 2-lobe structure Figure 2.20. Algorithmic reasons prevent us from computing the stress and deformation gradient in the fully-atomic setting, so we instead examine the change in energy of each atom from the perfect crystal. While qualitative, this calculation supports the view that the double-lobe structure is an atomic effect that we are able to capture despite the local QC approximation.

Regarding the lack of agreement with continuum phase-field, we conjecture that this may simply be due to the gradient penalty preventing the development of fine-scale features such as the double-lobe. Our approach can be viewed as a phase-field method with no gradient penalty. In typical phase-field modeling, the gradient penalty is taken to significantly larger than justified by domain wall widths, because the goal there is to predict microstructure and not defect structure. This may cause

fine-scale features such as the double-lobe to be washed out. Of course, it is also debatable whether our fully local QC model is appropriate to model such fine-scale features.

Finally, we examine the effect of a mechanical indenter that is pressed into the surface. Plots of the stress and polarization are in Figure 2.21. These are largely as expected.

We note that in these calculations, the electrostatics appears to induce a length-scale. However, neither classical electrostatics not the local QC – which is essentially classical continuum mechanics with an atomically-informed constitutive model – has an intrinsic lengthscale. The induced lengthscale from the electrostatics is nonlocal though problem-dependent, i.e. it depends on sample size, boundary conditions, and so on.

2.7 Discussion

We have presented a multiscale atomistic method for ionic solids and other materials where electrostatic interactions are long-range. Our approach is based on using the polarization field as a multiscale mediator between atomic-level rapidly-varying charge distributions and the continuum scale electrical quantities. Our coarse-graining strategy relies on ideas developed by [35] and others that followed them [63, 80, 59]. The method that we have presented enables QC and other multiscale methods to go beyond purely short-range interactions, that are characteristic of many structural materials, to functional and electronic materials of interest today.

The method presented here is a first attempt towards the goal of understanding the multiscale electromechanics of defects in ionic solids. Consequently, there remain many important open questions.

1. The presentation here is based on energy minimization which implies zero tem-

perature; recent methods based on extending this to finite temperature in the setting of short-range interactions can perhaps be adapted to our setting [43]. An alternate approach is [69], where the powerful method of Effective Hamiltonians has been applied to study the finite temperature behavior of ferroelectrics in the local QC setting.

2. We have started from an atomic viewpoint in this chapter whereas QC methods have been demonstrated for the orbital-free density functional theory – a version of (ground state) density functional theory that is restricted to metals with mobile electrons. However, variants of density functional theory have difficulty with charged defects as rigorously demonstrated in [12]. In addition, density functional theory has important qualitative failings in computing bandgaps, van der Waals interactions, and so forth [39]. Therefore, it appears to be more useful to begin from the atomic level with well-calibrated and trustworthy potentials.

3. We have worked within the local QC setting which can alternately be considered a standard finite element approach with the constitutive relation being drawn from atomistics rather than a prescribed function. An important further step is to couple the coarse-grained model with a region with truly atomic resolution in the vicinity of the defect. In this regard, the key coarse-graining ideas presented here carry through to that setting. This open question is an area of our current research and we expect to report on this in the near future.

4. Our use of linear interpolation restricts us from capturing potentially important effects based on strain gradients, in particular the phenomenon of flexoelectricity that can be relevant at small scales [47]. However, this phenomenon is relevant at large strain gradients that typically can only occur in localized

regions of the sample. Therefore, a QC method that fully resolves the defect region can potentially capture this phenomenon even with linear interpolations.

5. Our coarse-graining of the electrostatics in this chapter assumed complete separation of scales. However, for a real calculation, this will naturally not be true. It is therefore important to study and quantify the errors when the separation of scales is large but not complete. This will enable the construction of an algorithm with controlled error tolerance. Directly related to this is the derivation of a rigorous limit as opposed to the formal presentation in this chapter. These related open questions are an area of our current research, following techniques in [63].

The example that we have studied of the double-lobe structure beneath a point charge provides an important motivation for the further development of our method. Atomic-scale features such as the double-lobe are of importance to phenomena such as domain nucleation and cannot be captured by continuum models. On the other hand, the limited size of our admittedly-unoptimized brute force atomic calculation shows the need for coarse-graining efforts.

Finally, we have examined the issue of whether polarization is unique. As noted above, evaluating the classical definition of polarization provides a unit cell-dependent quantity. This is obviously a potential disaster for a coarse-graining scheme based on the polarization field. The materials physics orthodoxy appeals to quantum mechanical concepts to fix a unique value of the polarization [61]. Continuum mechanicians have used variational notions to achieve similar ends [59]. The view that we have taken in this chapter is that there is simply no need to have a unique value for the polarization. When partial unit cells that provide boundary charges are accounted for consistently, the coarse-grained electric fields and other relevant quantities are independent of the choice of unit cell. The polarization is merely a multiscale in-

termediary. In continuum theories of electromechanical solids, e.g. [80, 65], the polarization appears in the standard local free energy density, not only in the electrostatics. In the local free energy density, the polarization can be considered as a quantity that tracks the atomic positions rather than relevant to electrostatics. In that perspective, the specific choice of unit cell is irrelevant. Broadly, the view advocated in this chapter is in the spirit of classical continuum mechanics: the polarization field simply provides some information about the atomic-level, and one can take any choice as long as consistent transformations between energy, kinematics, and boundaries are respected. The immediate analog in continuum mechanics is the freedom in the choice of reference configuration and the corresponding value of the deformation field and strain energy density response function as long as care is taken to define suitable transformations between different choices.

Acknowledgements

We thank ARO Numerical Analysis for financial support through a Young Investigator grant (W911NF-12-1-0156). Jason Marshall also acknowledges support from the Northrop Graduate Fellowship Award from Carnegie Mellon University. Kaushik Dayal also acknowledges support from AFOSR Computational Mathematics (FA9550-09-1-0393) and AFOSR Young Investigator Program (FA9550-12-1-0350). Kaushik Dayal thanks the Hausdorff Research Institute for Mathematics at the University of Bonn for hospitality. This research was also supported in part by the National Science Foundation through TeraGrid resources provided by Pittsburgh Supercomputing Center. We thank Richard D. James, Saurabh Puri, and Yu Xiao for useful discussions.

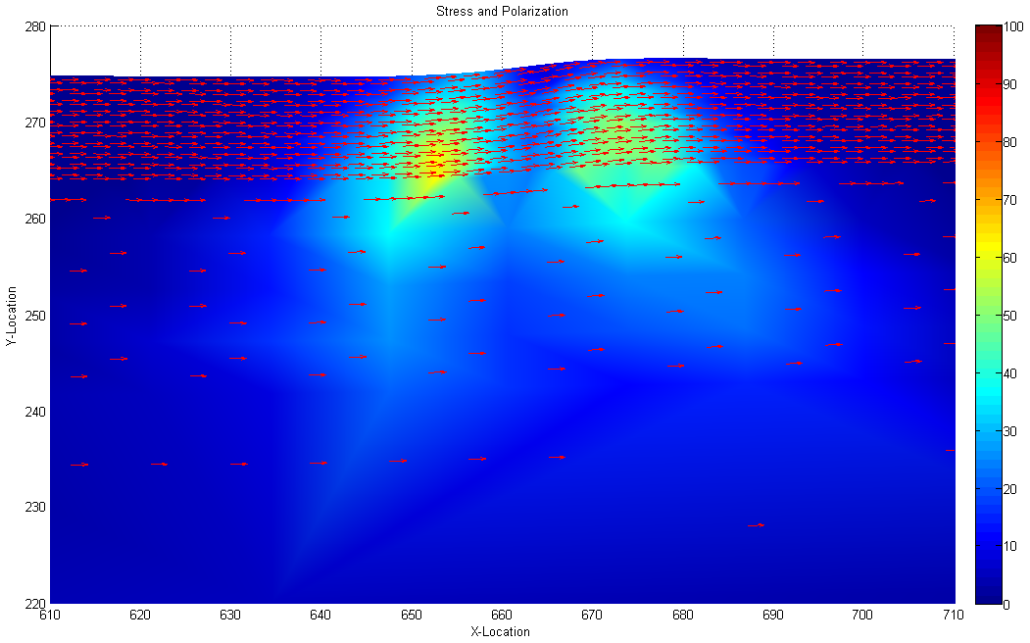


Figure 2.10: Stress and polarization due to single point charge with an electrostatic scaling of 1.

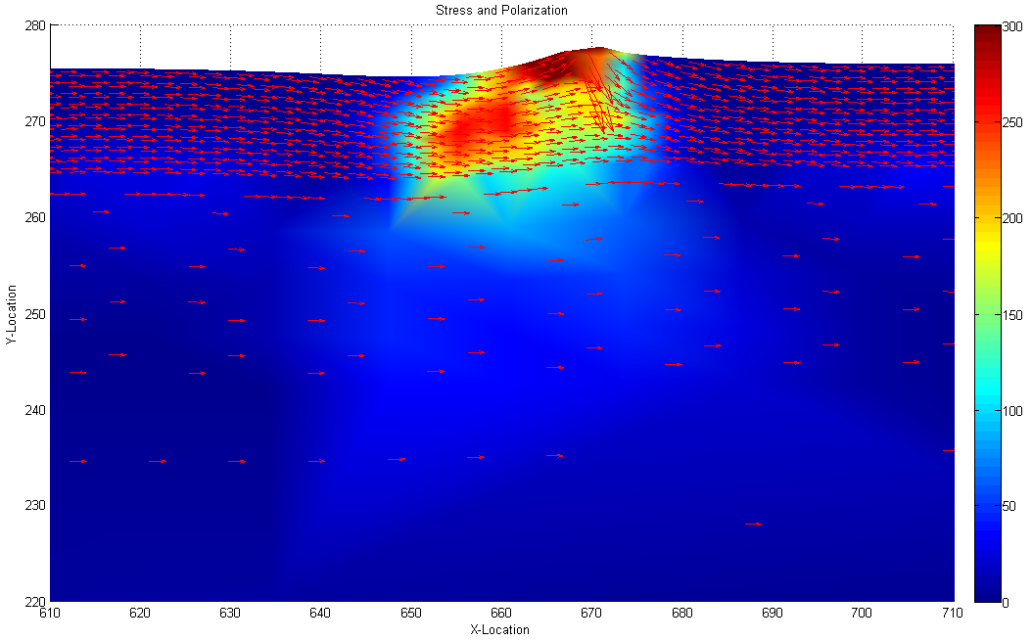


Figure 2.11: Stress and polarization due to single point charge with an electrostatic scaling of 4.

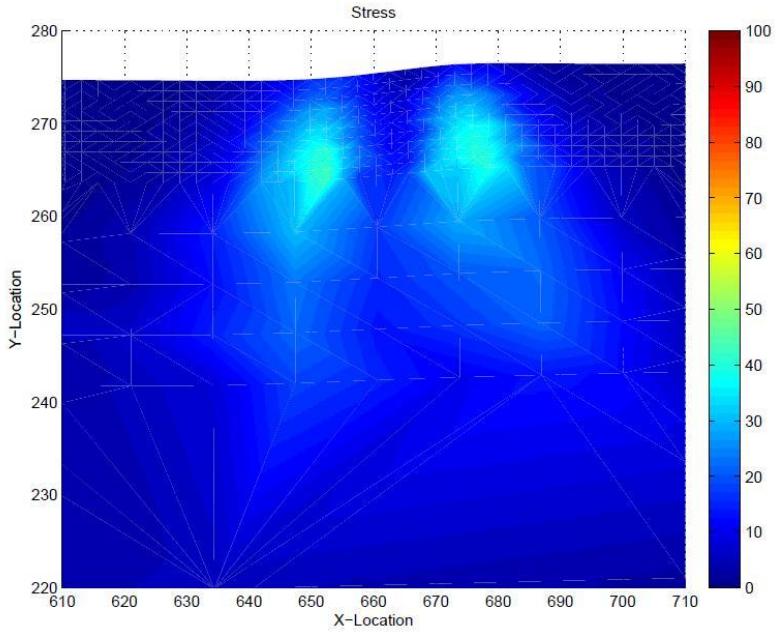


Figure 2.12: Stress due to two point charges with an electrostatic scaling of 1.

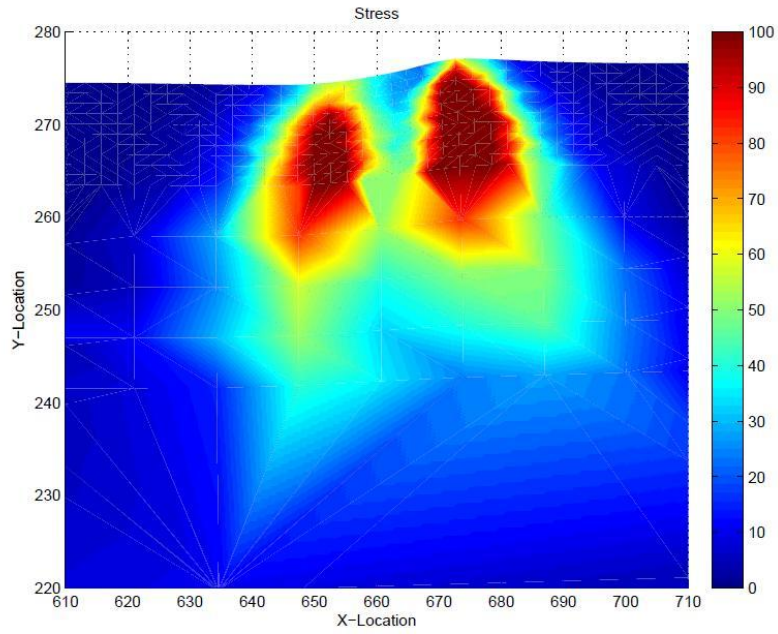


Figure 2.13: Stress due to two closely-spaced point charges with an electrostatic scaling of 1.

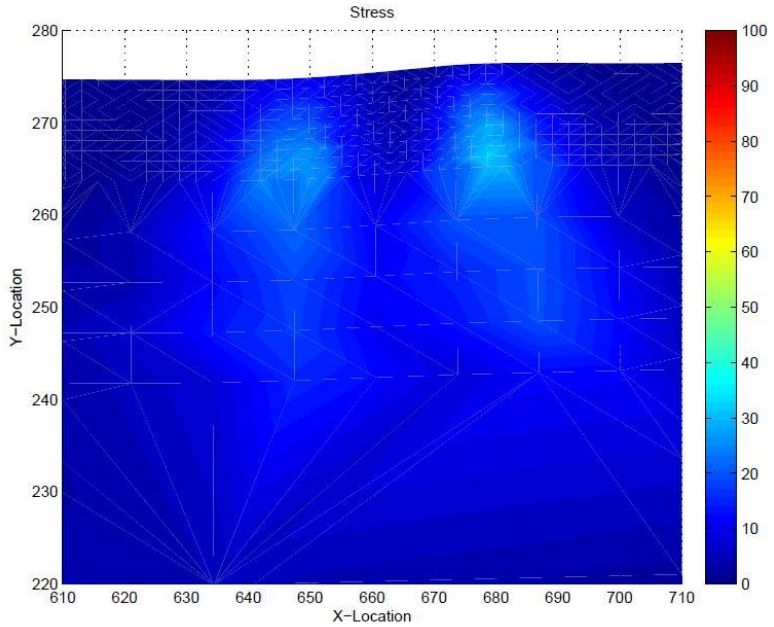


Figure 2.14: Stress due to four point charges with an electrostatic scaling of 1.

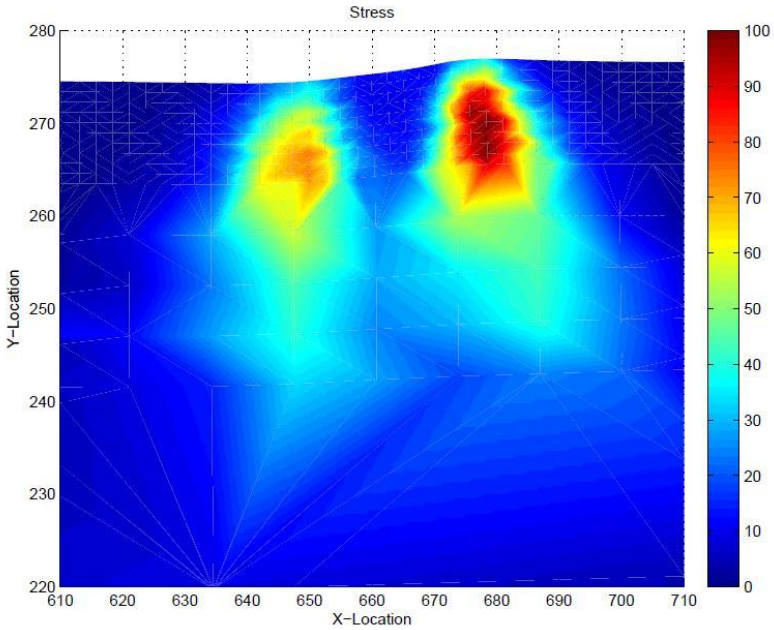


Figure 2.15: Stress due to four closely-spaced point charges with an electrostatic scaling of 1.

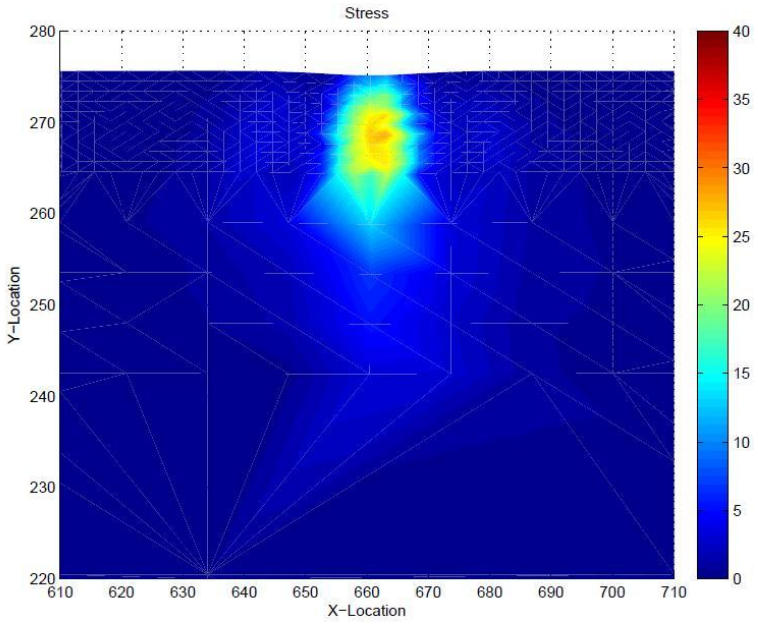


Figure 2.16: Stress due to a dipole (two point charges of opposite sign) with an electrostatic scaling of 1.

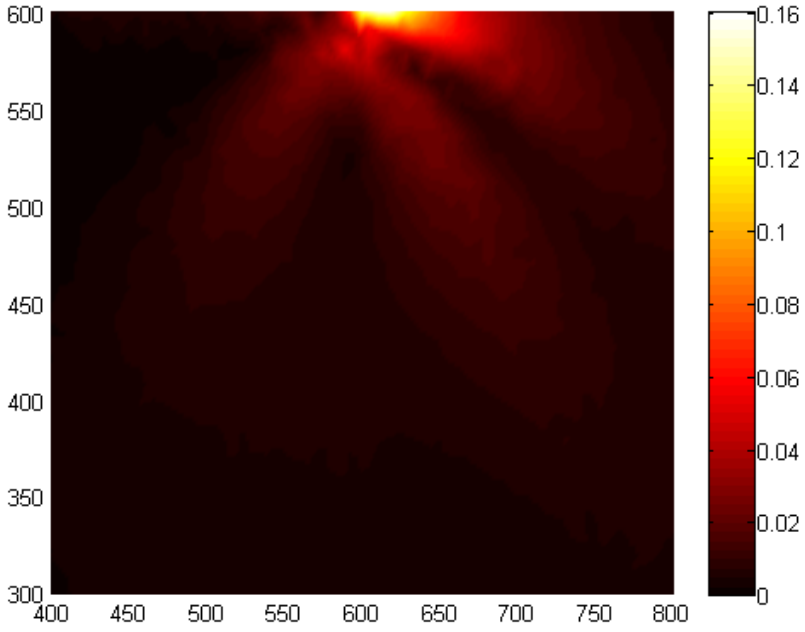


Figure 2.17: Stress due to a point charge computed using a continuum phase-field model [82].

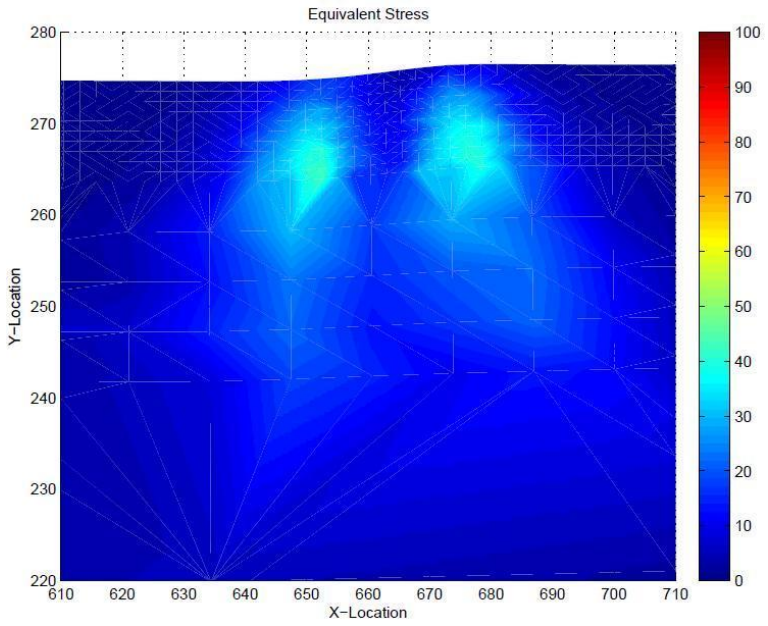


Figure 2.18: Stress due to a point charge with electrostatic fields computed in the reference configuration.

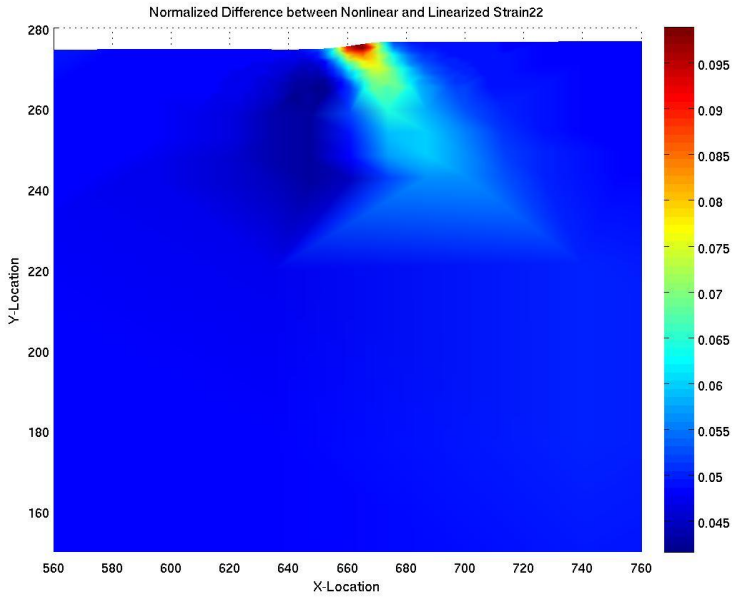


Figure 2.19: Normalized Difference between Nonlinear and Linearized Strain Measure (ϵ_{22} component).

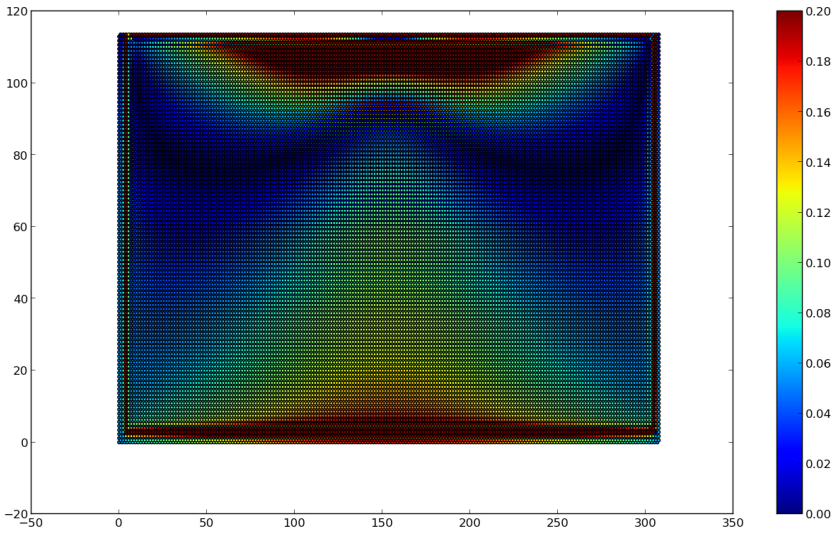


Figure 2.20: Fully atomic calculation for a sample with a point charge. The plot shows the energy difference from the state without any external charge with the electrostatic field energy subtracted. The entire computational domain is shown.

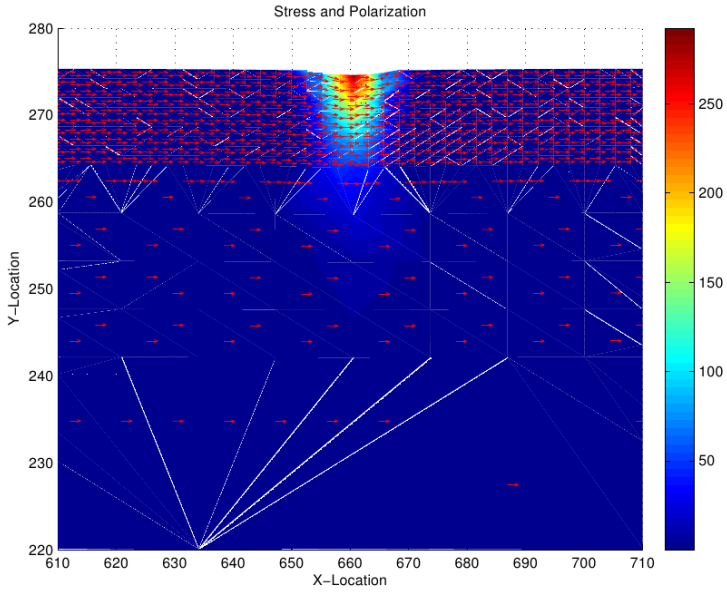


Figure 2.21: Stress and polarization due to mechanical indentation with no applied electric field.

3

Development of a Fully Non-Local Quasicontinuum Method for Simulating Atomistic Defects in Materials with Many Atomic Species

3.1 Abstract

Atomistic defects (e.g. voids, vacancies, domain walls, etc.) play a vital role in continuum level properties in materials ranging from high strength alloys like NiAl and TiAl to ionic solids like Ceria and Barium Titanate. Full atomistic resolution is required around these defects to fully understand the underlying physics, however, atomistic resolution cannot be obtained everywhere because of computational limits. Multiscale methods were developed to make problems tractable by providing atomistic resolution near defects and coarse-grained resolution elsewhere. A variety of methods have been proposed and developed, but relatively few have the ability to simulate materials with multiple species of atoms. In this work, we extend one of these multiscale methods, the non-local quasicontinuum method, to multiple species of atoms. We extend the method by treating the problem as the union of multiple single species (simple) lattice problems. Treating the problem in this manner allowed

the leveraging of existing simulation codes in the extension of the method. We use this newly developed method to simulate void relaxation in NiAl.

Keywords: non-local Quasicontinuum method; multi-lattice multiscale modeling; voids; NiAl

3.2 Introduction

Atomistic defects play a pivotal role in the structure and functional use of continuum level material properties. For example, the motion of charge defects enables the functionality in next generation solid oxide fuel cells and batteries; the motion of domain walls in ferroelectric materials enables the storage of state used in ferroelectric RAM; and void defects in high-temperature alloys play a role in ductility and plasticity important for lightweight turbine blades. Analyzing and understanding the underlying physics of these defects is critically important in device design, however, experiments are technically challenging, time consuming, and expensive to perform at the atomistic level. Numerical methods are being used to reduce the cost and decrease the time of material and device development. Properly resolving these material defects, however, requires full atomistic resolution at the core of the defect. Full atomistic resolution throughout a system quickly leads to computational intractability for length scales of interest. Multiscale methods like the Quasicontinuum (QC) Method [66, 67, 51, 40, 68], the Bridging Domain Method [78], and others were developed to provide atomistic resolution at defects, while coarse-graining farther away to reduce computational cost. These methods have been used to provide information about atomistic defects and structures for a variety of materials.

In this chapter, we focus on a specific version of the QC method developed in [40], which we call the non-local force QC method (NL-QC). This method formulates the atomistic problem at the force level and solves a system equations satisfying $\mathcal{F} = \mathbf{0}$, where $\mathcal{F}$ represents the forces on atoms in the system. The method has

currently been developed for simulating atomistic defects in materials with only a single species of atoms, for example, pure aluminum, nickel, copper, etc. Some work was previously done to extend the method to materials with multiple species of atoms (barium titanate and lead titanate) by Kowalewsky in her PhD thesis [42], but results were never published and access to the computational implementation is not available. Additionally, the work only allowed for simple pair potentials. While many body potentials like EAM [16] are conceptually similar to pair potentials, their computational implementation can be much more challenging in a multiscale framework. EAM potentials, however, provide some of the best models for a variety of materials and are essentially required to simulate certain alloys. The research presented in this chapter focuses on developing an extension to the NL-QC method for multiple species of atoms with no restrictions to interatomic pair potentials. We seek to achieve this goal through the following:

- Developing a mathematical framework for multiple lattices of atoms which results in the same formulation for the initial method developed in [40].
- Leveraging the existing computational implementation to speed development of the multi-lattice implementation.
- Testing the newly developed method with several patch tests to verify the correctness of the code.
- Analyzing void relaxation in nickel aluminide (B2-NiAl) subjected to volumetric expansion using EAM potentials [52, 8] to highlight an application of the new method.

3.3 Methodology

3.3.1 Overview

The NL-QC method, like most atomistic to continuum multiscale methods, addresses two main computational challenges. The first is the reduction of system degrees of freedom. Fully atomistic simulations at length scales of interest in device design can quickly approach 10^{23} degrees of freedom or higher. Performing these simulations is currently not computationally tractable. The number of degrees of freedom are reduced by keeping full atomistics at areas of interest and only tracking a subset of atoms elsewhere, called representative atoms in the case of NL-QC. The locations of all other atoms in the system are then approximated by shape functions attached to the rep atoms, the shape functions used in NL-QC are standard C^0 continuous functions from traditional finite element methods. This coarse-graining immediately reduces the number of degrees of freedom drastically and the system size is reduced to a computationally tractable level. The second main challenge is the rapid evaluation of the force or energy landscape throughout the system. Regardless of the number of atoms explicitly tracked with rep atoms, if the force or energy calculation needs to be performed at every atom in the system, the computational expense will quickly grow. This difficulty is overcome through the use of quadrature points. The use of numerical quadrature allows the forces to be evaluated at only a small subset of atoms. The NL-QC method uses cluster summation rules located at rep atoms for the rapid evaluation of forces. The combination of these two schemes in the NL-QC method allows single species systems to be analyzed that could not be handled with full atomistic simulations.

The initial implementation of the NL-QC method took a considerable amount of time and effort, especially in regards to the design of data structures and algorithms. The code was developed using a combination of fortran, C, and C++ and addi-

tionally takes advantage of PThreads for simulation in high performance computer environments. In light of the considerable development previously undertaken, we seek to utilize a significant portion of the initial single species NL-QC computational framework in the extension to multiple species of atoms. We achieve this by treating the problem as the union of many single species problems with additional functionality added at a few key locations. We start by reviewing the initial NL-QC method and then extending the method to many species of atoms within a properly defined mathematical framework. Approaching the problem in this manner allowed the maximum amount of code reuse and drastically reduced the mathematical complexity of the formulation.

3.3.2 Single Species: Problem statement

We start by considering a crystalline material within a d, dimensional reference domain, Ω, see Figure 3.1. The material initially consists of periodically repeating array of atomistic sites mapped one-to-one with a Bravais lattice, $\mathcal{L}$. We define a Bravais lattice, using basis vectors $a_i, i = 1, \ldots, d$, as the following:

$$\mathcal{L}(\boldsymbol{a}) = \left(\boldsymbol{X} \in \mathbb{R}^d,\ \boldsymbol{X} = l^i a_i \text{ where } l^i \in \mathbb{Z}^i,\ i = 1, \ldots, d\right). \tag{3.1}$$

Each coordinate, $\boldsymbol{X}$, in Ω identifies and locates an atom at a unique lattice site. We define $\boldsymbol{x}$ as the location of all atoms in the deformed (current) configuration. The same bookkeeping system as the reference configuration is used, but all atoms are allowed to deform. We initially assume that every atom in the system interacts with every other atom in the system through interatomic potentials ranging from simple pair potentials like Lennard-Jones to many body potentials like EAM [16]. The energy of an atom is now the sum of the interatomic potential with all other atoms. The potential energy, $E(\boldsymbol{x})$, in Ω is just the sum of all atomistic energies in the system. We write the total energy of the system, including external loading

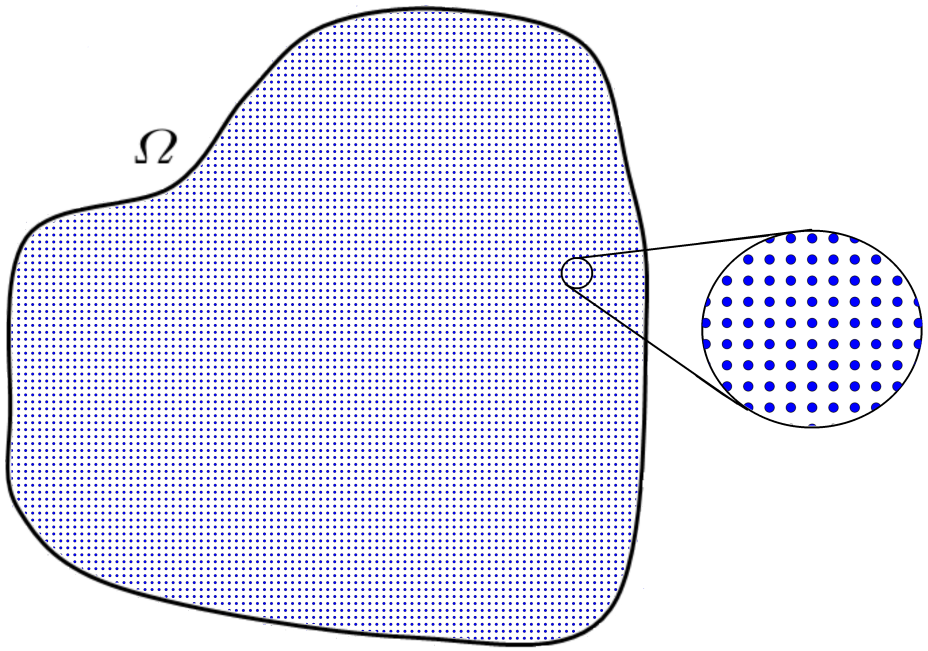


Figure 3.1: Simple lattice in body Ω

terms as:

$$\Phi(\boldsymbol{x}) = E(\boldsymbol{x}) + \Phi^{ext}(\boldsymbol{x}). \tag{3.2}$$

$\Phi^{ext}(\boldsymbol{x})$ includes all contributions from Neumann or Dirichlet boundary conditions, body loads, and/or any other external loading device. We seek to find local minimizers of $\Phi(\boldsymbol{x})$, which correspond to equilibrium configurations.

$$\min_{\boldsymbol{x}} \Phi(\boldsymbol{x}) \tag{3.3}$$

3.3.3 Single Species: Reduction of system degrees of freedom

In fully atomistic systems, the number of degrees of freedom quickly reaches computationally intractable levels for even modest sized domains. Modeling the complete atomistic system is not possible at this time. Thus, we reduce the number of degrees of freedom in the system by selecting a subset of atomistic sites $\boldsymbol{l}_h \subset \boldsymbol{l}$ with atomistic

locations $\boldsymbol{X}_h \subset \boldsymbol{X}$ and $\boldsymbol{x}_h \subset \boldsymbol{x}$ to explicitly model. We call this subset of atoms 'representative atoms'. We now seek a minimization over the representative atoms.

$$\min_{\boldsymbol{x}_h} \Phi(\boldsymbol{x}) \tag{3.4}$$

$\Phi(\boldsymbol{x})$ is still dependent on the position of all the atoms in Ω, but we are only explicitly tracking the representative atoms. We introduce a triangulation, it does not need to be structured, $\mathcal{T}_h$ over the representative atoms $\boldsymbol{X}_h$, see Figure 3.2, where the dark blue atoms are representative atoms. The top zoom out is a coarse-grained mesh, while the bottom zoom out is a fully resolved mesh. Shape (interpolation)

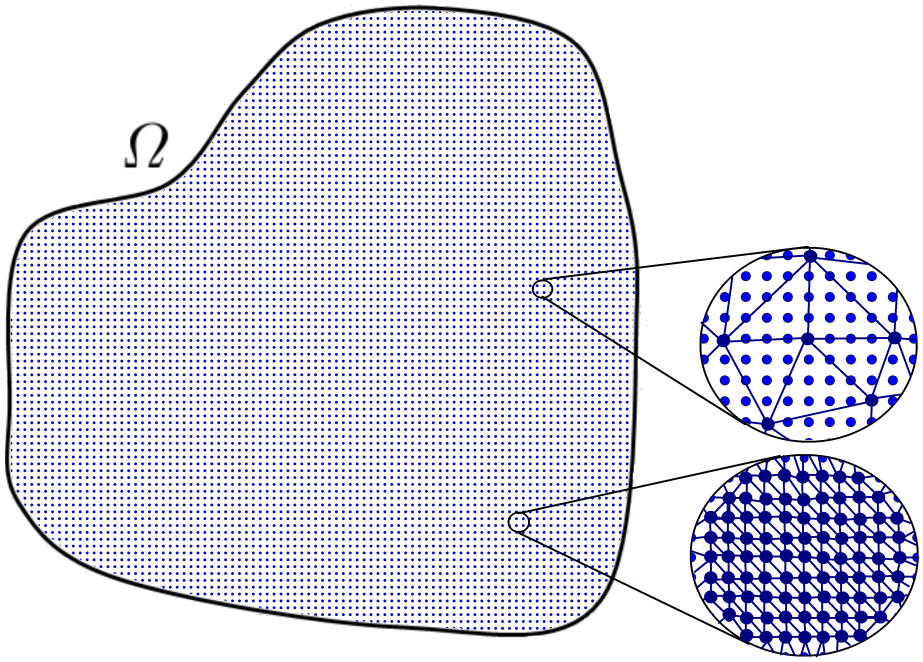


Figure 3.2: Simple lattice with full atomistic and coarse-grained resolution

functions defined on the simplices of the triangulation are then used to approximate the locations of all non representative atoms in the system.

$$\boldsymbol{x} = \mathcal{S}_h\left(\boldsymbol{X}(\boldsymbol{l}), \boldsymbol{x}_h\right) \tag{3.5}$$

The above equation maps atomistic sites to their location in the current configuration through the, $\mathcal{S}_h$, shape functions. In principle, any form or type of shape functions can be used, though throughout this chapter we define $\mathcal{S}_h$ to be standard piecewise linear shape functions. Given this definition of $\mathcal{S}_h$, the location of all atoms in Ω is only dependent on $\boldsymbol{x}_h$. $\Phi(\cdot)$ can now be written as a function of $\boldsymbol{x}_h$.

3.3.4 Single Species: Reduced equilibrium equations

The full energy minimization problem from Equation 3.3 can be rewritten in terms of the reduced energy:

$$\min_{\boldsymbol{x}_h} \Phi(\boldsymbol{x}_h). \tag{3.6}$$

The reduced equilibrium equations, which correspond to local energy minimizers are:

$$\mathcal{F}_h(\boldsymbol{x}_h) = \mathcal{S}_h(\mathcal{F}(\boldsymbol{x}), \boldsymbol{x}_h) = \boldsymbol{0}. \tag{3.7}$$

$\mathcal{F}_h(\boldsymbol{x}_h)$ is the total force at representative nodes $\boldsymbol{x}_h$. $\boldsymbol{x} = \mathcal{S}_h\left(\boldsymbol{X}(\boldsymbol{l}), \boldsymbol{x}_h\right)$ maps the atomistic locations in the reference to the current through the representative atom positions and triangulation shape functions. $\mathcal{S}_h(\mathcal{F}(\boldsymbol{x}), \boldsymbol{x}_h)$ maps the forces on $\boldsymbol{x}$ to forces on representative atoms $\boldsymbol{x}_h$ through the triangulation shape functions. The forces at a given atom $\boldsymbol{x}_i$ are:

$$\mathcal{F}(\boldsymbol{x}_i) = \Phi_{,\boldsymbol{x}_i}(\boldsymbol{x}_i) = \sum_{\boldsymbol{x}_p \in \mathcal{P}_r(\boldsymbol{x}_i)} \Psi_{,\boldsymbol{r}}(r)\boldsymbol{r}_{,\boldsymbol{x}_i}, \text{ where} \tag{3.8}$$

$\Psi(r)$ is the known interatomic potential for a given material and r is the distance between atoms i and j, $|\boldsymbol{x}_j - \boldsymbol{x}_i|$. Additionally, $\mathcal{P}_r$ is defined as follows:

$$\mathcal{P}_r(\boldsymbol{x}_i) = \{\boldsymbol{x}_p : |\boldsymbol{x}_j - \boldsymbol{x}_i| \leq R_p,\ i \neq j\}, \text{ where} \tag{3.9}$$

R_p is the potential cutoff radius.

Essentially, the forces are calculated at all atoms in Ω and distributed to representative atoms, $\boldsymbol{x}_h$, via the same linear shape functions used to determine the location of the non representative atoms in Ω. The reduced equilibrium equations currently still require calculating the force at every atom $\boldsymbol{x}$ in Ω, where the force is calculated by the full lattice sum of an atom interacting with every other atom within a cutoff radius. There are two difficulties that need to be overcome:

1. Evaluating the forces at every atom is prohibitively expensive. Quadrature rules need to be introduced to evaluate the forces at selected quadrature points to approximate the full system. We use the same cluster summation rules centered at representative atoms from the initial NL-QC development [40]. The specific form of the cluster summation rule will be explained below.

2. In the full atomistic calculation every atom interacts with every other atom in the system. We decrease the number of calculations by assuming that all interatomic potentials are short-ranged and can be approximated with an effective cutoff radius, R_p. Any atoms outside the cutoff radius will not effect the evaluation of the forces. When we say short-range, we mean that the interatomic potential has to decay at least as fast as r^{-4}, where r is the distance between two atoms. This assumption eliminates the modeling of Coulombic and Coulombic-like interactions and restricts the class of materials that can be simulated. Previous work has extended some QC methods to handle Coulombic interactions [49], while work is ongoing to extend the NL-QC to Coulombic interactions, thereby relaxing the short-ranged interatomic potential assumption.

3.3.5 Single Species: Summation rules

As stated above the full force calculation, essentially $\sum_{\boldsymbol{x}\in\Omega}\mathcal{F}(\boldsymbol{x})$, is very computationally expensive and needs to be reduced for realistic length scales of Ω. This reduction is achieved through the use of quadrature. Forces are calculated at a subset of atoms, $\boldsymbol{x}_q \subset \{\boldsymbol{x}\}$ and may or may not have any relation to the representative atoms $\boldsymbol{x}_h$. These forces at quadrature points are then multiplied by a weight that is essentially the number of atoms that the quadrature point approximates and is analagous to volume in a classical continuum mechanics setting. The reduced equilibrium equation can now be written as:

$$\mathcal{F}_h(\boldsymbol{x}_h) \approx \sum_{\boldsymbol{x}_q\subset\boldsymbol{x}\in\Omega} Q(\boldsymbol{x}_q)\mathcal{S}_h(\mathcal{F}(\boldsymbol{x}_q),\boldsymbol{x}_h) = \boldsymbol{0}, \text{ where} \tag{3.10}$$

$Q(\boldsymbol{x}_q)$ is the quadrature weight at $\boldsymbol{x}_q$. The above equation is the general form of quadrature, but many different types of quadrature rules can be selected. For example, the natural first choice for quadrature points would be $\boldsymbol{x}_q = \boldsymbol{x}_h$, where the quadrature points are the exact same as the representative atoms. Knap and Ortiz [40] showed that this choice of summation rule suffered from rank-deficiency. They overcame this difficulty by using a cluster summation rule centered at representative atoms. The cluster summation rule evaluates forces at atoms within a given cluster radius of a representative atom and uses those forces to approximate the total force at a representative atom. The reduced equilibrium equation for this specific rule looks like:

$$\mathcal{F}_h(\boldsymbol{x}_h) \approx \sum_{\boldsymbol{x}_h\subset\boldsymbol{x}\in\Omega} Q(\boldsymbol{x}_h)\left[\sum_{\boldsymbol{x}_c\in\mathcal{C}(\boldsymbol{x}_h)} \mathcal{S}_h(\mathcal{F}(\boldsymbol{x}_c),\boldsymbol{x}_h)\right] = \boldsymbol{0}. \tag{3.11}$$

$\mathcal{C}(\boldsymbol{x}_h)$ is a cluster of atoms defined by $\mathcal{C}(\boldsymbol{x}_h) = \{\boldsymbol{x} : |\boldsymbol{x}-\boldsymbol{x}_h| \leq R_c\}$, where R_c is the cluster radius centered at $\boldsymbol{x}_h$. $\mathcal{F}(\boldsymbol{x}_c)$ is calculated by summing the force over all of the atoms that a given cluster atom $\boldsymbol{x}_c$ interacts with. In a triangulation for a real

problem, there will be areas of high and low representative atom density. In areas of low density, which correspond to a coarse-grained approximation of the atomistics, clusters will not overlap and Equation 3.11 is used as expected with no issues. Conversely, in areas of high density, specifically where triangulation is reduced to every atom being a representative atom, the cluster summation rule evolves directly to a full force calculation. This situation corresponds to a fully resolved, completely atomistic area. The intermediate area between a coarse-grained and a fully resolved triangulation can have overlaps between clusters. The question in this case is which cluster should an atom $\boldsymbol{x}$ belong to? This question is resolved by choosing the nearest representative atom, in the case that two or more representative atoms are the same distance, the conflict is resolved randomly. Figure 3.3 highlights the three different scenarios.

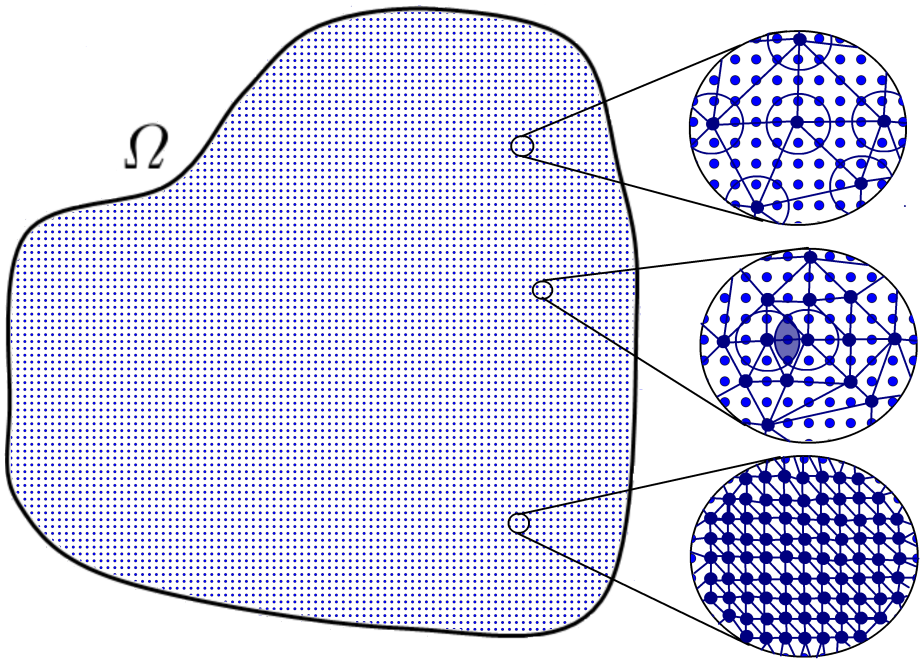


Figure 3.3: Simple lattice with multiple cluster scenarios. **Top Zoom**: Coarse-grained no cluster overlap. **Middle Zoom**: Coarse-grained with cluster overlap that must be resolved. **Bottom Zoom**: Fully resolved cluster is a single representative atom.

3.3.6 Single Species: Adaptive meshing

In the previous section, we discussed various mesh refinement levels, but never discussed how those were obtained. At the beginning of a simulation, a generic mesh is known a priori, tailored to the specifics of the problem. A fully resolved mesh is specified around atomistic defects and is slowly coarse-grained with increasing distance from the atomistic defect or defects. It is unknown if an initial mesh has enough atomistic resolution for a given applied loading, so an adaptive meshing algorithm is used. This algorithm refines the mesh if the strain is above a given tolerance level. In practice, the tolerance level is set so that crystallographic slips of a full Burgers vector are resolved with full atomistic resolution. Specific details of the adaptive meshing algorithm and tolerance parameter can be found in [40].

3.3.7 Multiple species: Problem statement

In the previous sections, we outlined the single species NL-QC method. We now seek to extend this method to multiple species of atoms by treating the problem as the union of multiple single species problems. We again start by considering a crystalline material within Ω, except now there are multiple species of atoms, N^s, denoted by Greek letters (α, β, etc.). The same definition of a simple Bravais lattice is used, except a few modifications are made.

$$\mathcal{L}^\alpha(\boldsymbol{a}^\alpha) = \left(\boldsymbol{X}^\alpha \in \mathbb{R}^d,\ \boldsymbol{X}^\alpha = l^{\alpha,i}a_i^\alpha + \boldsymbol{b}^\alpha \text{ where } l^{\alpha,i} \in \mathbb{Z}^i,\ i = 1,\ldots,d\right). \tag{3.12}$$

1. We introduce a shift vector, $\boldsymbol{b}^\alpha$, that denotes the relative displacement between lattices. This shift vector establishes a global coordinate system. Essentially, each lattice has its own local coordinate system determined by $l^{\alpha,i}a_i^\alpha$, that is transformed to the global coordinate system through the shift vector. Typically, we take the 0^{th} lattice to have the same local coordinate system as the global coordinate system by setting $\boldsymbol{b}^0 = \boldsymbol{0}$, though this choice does not have

to be made.

2. We allow each simple lattice to have different lattice vectors $\boldsymbol{l}$ and lattice constants $\boldsymbol{a}$. These different vectors and constants are very important for modeling different material phases. A good example of this occurs in NiAl, which can form in many different phases including B2-NiAl and $L1_2$-Ni_3Al.

B2-NiAl is perhaps the simplest case of a multi-lattice and can be thought of as a cubic lattice of Ni and a cubic lattice of Al offset by half of the lattice constant a in a d dimensional space. In this case, the lattice vectors and constants are the same, $\boldsymbol{l}^0 = \boldsymbol{l}^1$ and $\boldsymbol{a}^0 = \boldsymbol{a}^1$, where 0 and 1 denote Ni and Al. The shift between the two lattices can then be set by defining $b_i^0 = 0$ and $b_i^1 = l^{1,i}a_i^1/2$.

The $L1_2$-Ni_3Al phase is slightly more complicated. This phase can be thought of as a cubic lattice of Al intersected with an fcc lattice of Ni. In this case the shift vectors $\boldsymbol{b}^\alpha$ are important, but additionally, the lattice vectors $\boldsymbol{l}^\alpha$ and lattice constants $\boldsymbol{a}_i^\alpha$ are different and describe a cubic and fcc lattice respectively. The different lattice vectors and constants allow much more complicated phases to be easily modeled and are pivotal for being able to simulate many different phases.

We now define a complex Bravais lattice as $\mathbb{L}$, where all of the atomistic locations in the reference coordinate system are denoted by $\mathbb{X}$.

$$\mathbb{L} = \mathcal{L}^0 \cup \mathcal{L}^1 \cup \cdots \cup \mathcal{L}^{N^s}, \quad \mathbb{X} = \boldsymbol{X}^0 \cup \boldsymbol{X}^1 \cup \cdots \cup \boldsymbol{X}^{N^s} \tag{3.13}$$

For illustration purposes only, $N^s = 2$ is chosen and shown in Figure 3.4. The location of all atoms in the current configuration, energy in Ω, and energy minimization equations proceed as expected:

$$\mathcal{X} = \boldsymbol{x}^0 \cup \boldsymbol{x}^1 \cup \cdots \cup \boldsymbol{x}^{N^s}. \tag{3.14}$$

$$\Phi(\mathcal{X}) = E(\mathcal{X}) + \Phi^{ext}(\mathcal{X}). \tag{3.15}$$

$$\min_{\mathcal{X}} \Phi(\mathcal{X}) \tag{3.16}$$

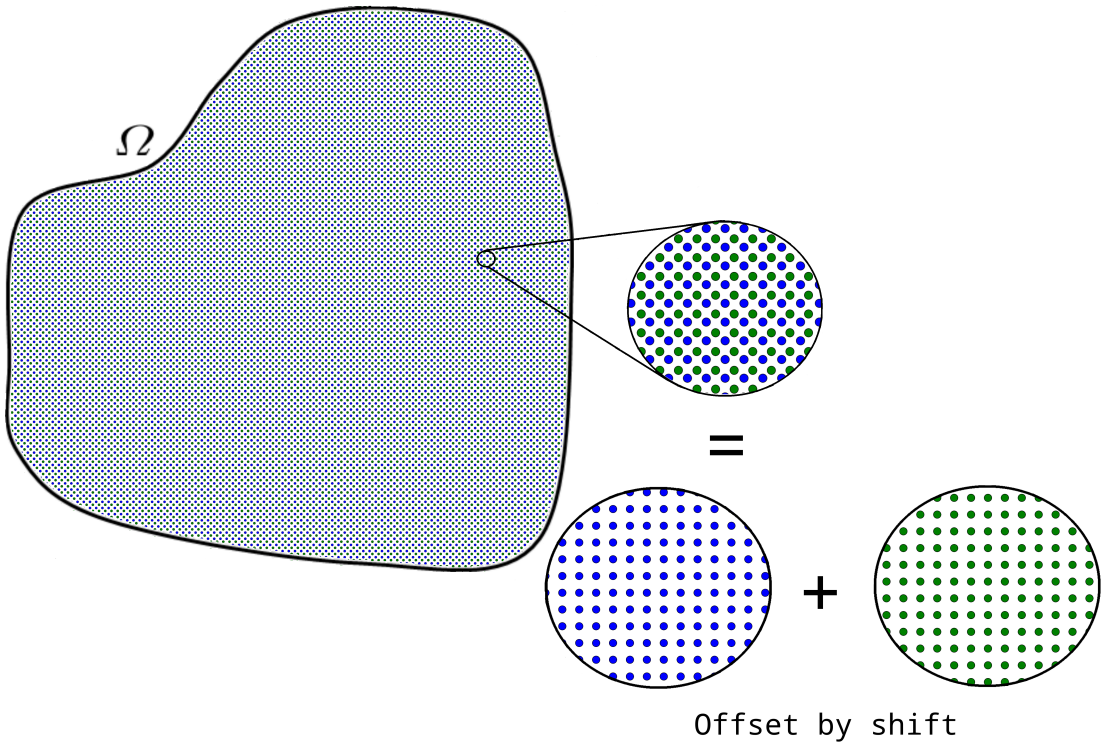


Figure 3.4: Multiple Species Lattice

3.3.8 Multiple Species: Reduction of system degrees of freedom

We now seek to reduce the number of degrees of freedom in Ω by selecting a subset of each α lattice to be representative atoms. These representative atoms will only be used to interpolate and simulate atoms within the same lattice, i.e. Ni representative atoms would not be used to interpolate Al atoms in NiAl. Thus, we select a subset of atomistic sites $\boldsymbol{l}_h^\alpha \subset \boldsymbol{l}^\alpha$ with atomistic locations $\boldsymbol{X}_h^\alpha \subset \boldsymbol{X}^\alpha$ and $\boldsymbol{x}_h^\alpha \subset \boldsymbol{x}^\alpha$ to explicitly model. The full set of representative atoms is now $\mathcal{X}_h = \boldsymbol{x}_h^0 \cup \boldsymbol{x}_h^1 \cup \cdots \cup \boldsymbol{x}_h^{N^s}$. Triangulations, $\mathcal{T}_h^\alpha$, are introduced for *each* lattice $\mathcal{L}^\alpha$ using representative atoms $\boldsymbol{X}_h^\alpha$, see Figure 3.5. A set of piecewise linear shape functions are defined over each triangulation to interpolate positions of non representative atoms of the same species.

$$\boldsymbol{x}^\alpha = \mathcal{S}_h^\alpha \left(\boldsymbol{X}^\alpha(\boldsymbol{l}^\alpha), \boldsymbol{x}_h^\alpha \right) \tag{3.17}$$

There are several important points to note:

- Triangulations *need* not be structured.
- Triangulations for different species of atoms do *not* need to have the same structure.
- There is no limit on the number of species in a material, and thus no limit on the number of triangulations.
- Because of the separate triangulations, adaptive meshing stays the exact same as in the single species case for each lattice.

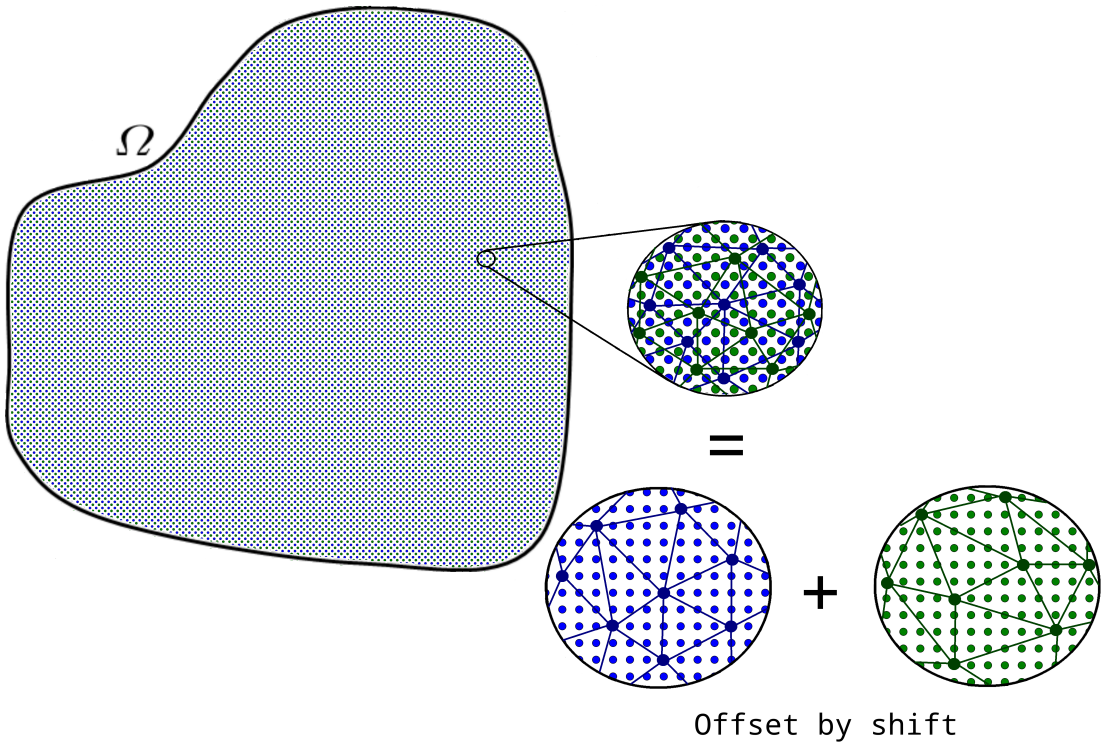


Figure 3.5: Multiple Species Lattice with Multiple Triangulations

With the equations to locate every atomic location in Ω now defined, the minimization of the energy occurs over all of the representative atoms.

$$\min_{\mathcal{X}_h} \Phi(\mathcal{X}_h) \tag{3.18}$$

3.3.9 Multiple Species: Summation rules

We now seek to solve the reduced equilibrium equations for Ω, this amounts to simultaneously solving the equilibrium equations for all N^s species of atoms.

$$\mathcal{F}_h^0(\boldsymbol{x}_h^0) = \mathbf{0}, \quad \mathcal{F}_h^1(\boldsymbol{x}_h^1) = \mathbf{0}, \quad \ldots, \quad \mathcal{F}_h^{N^s}(\boldsymbol{x}_h^{N^s}) = \mathbf{0} \tag{3.19}$$

We use the same cluster summation rules for a single species of atom for each α^{th} species of atom to reduce the force calculation.

$$\mathcal{F}_h^\alpha(\boldsymbol{x}_h^\alpha) \approx \sum_{\boldsymbol{x}_h^\alpha \subset \boldsymbol{x}^\alpha \in \Omega} Q(\boldsymbol{x}_h^\alpha) \left[\sum_{\boldsymbol{x}_c^\alpha \in \mathcal{C}(\boldsymbol{x}_h^\alpha)} \mathcal{S}_h^\alpha(\mathcal{F}^\alpha(\boldsymbol{x}_c^\alpha), \boldsymbol{x}_h^\alpha) \right] = \mathbf{0}. \tag{3.20}$$

Until this point, all calculations for the α^{th} species have been treated completely separately. That distinction changes with the calculation of the forces on an atom. An individual atom 'sees' other atoms through interatomic potentials, while the potentials may change depending on which species are interacting, fundamentally there is no unique distinction between atoms of different species. This is the main difference between multi-lattice NL-QC and simple lattice NL-QC, during the calculation of forces, atom $\boldsymbol{x}$ sees all other atoms within a cutoff radius, regardless of species. Thus, the force calculation is now:

$$\mathcal{F}^\alpha(\boldsymbol{x}_i^\alpha) = \Phi_{,\boldsymbol{x}_i^\alpha}(\boldsymbol{x}_i^\alpha) = \sum_{\beta=0}^{N^s} \left[\sum_{\boldsymbol{x}_p^\beta \in \mathcal{P}_r^{\alpha\beta}} \Psi_{,\boldsymbol{r}}^{\alpha\beta}(r) \boldsymbol{r}_{,\boldsymbol{x}_i^\alpha} \right], \text{ where} \tag{3.21}$$

$\Psi^{\alpha\beta}(r)$ is the interatomic potential between α and β species of atoms and r is the distance between atoms i and j, $|\boldsymbol{x}_j^\beta - \boldsymbol{x}_i^\alpha|$. Additionally, $\mathcal{P}_r^\alpha$ is defined as follows:

$$\mathcal{P}_r^{\alpha\beta} = \{\boldsymbol{x}_p^\beta : |\boldsymbol{x}_j^\beta - \boldsymbol{x}_i^\alpha| \leq R_p,\ i \neq j \text{ if } \alpha = \beta\}, \text{ where} \tag{3.22}$$

R_p is the potential cutoff radius centered at $\boldsymbol{x}_i^\alpha$. Figure 3.6 highlights the formation of clusters and how atoms interact in the force calculation.

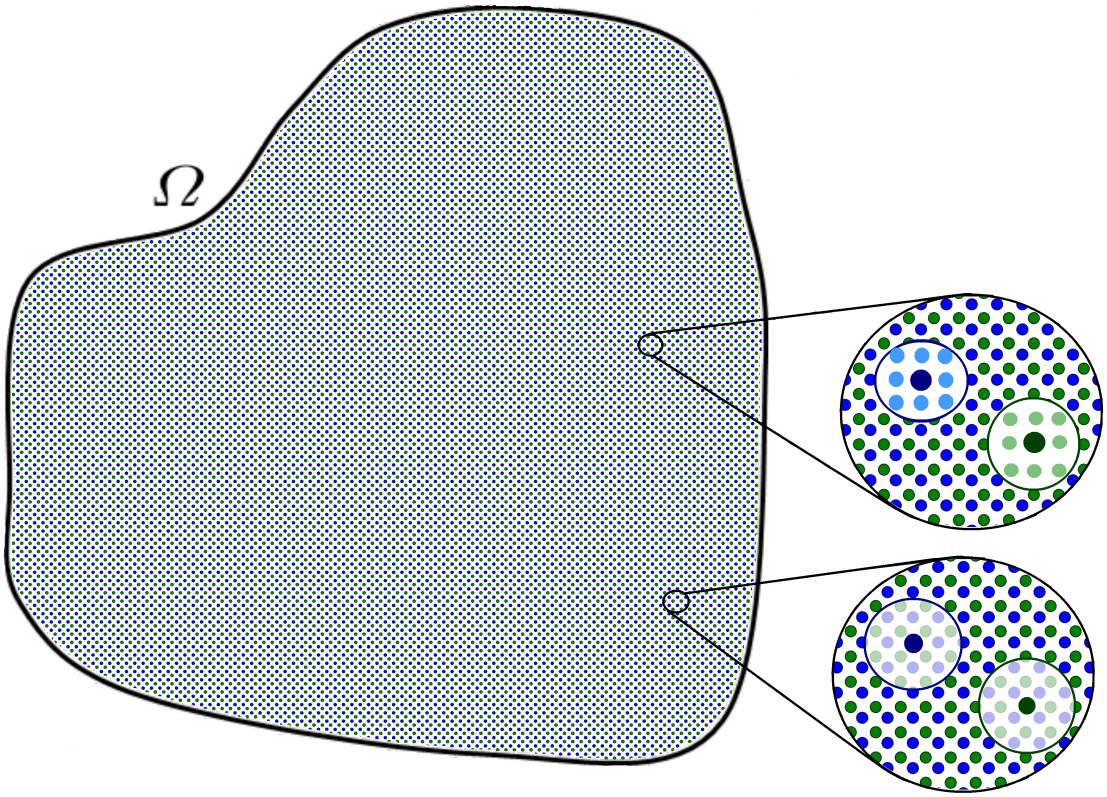


Figure 3.6: Multiple Species Lattice Clusters **Top Zoom**: Light blue and green atoms are in a cluster of dark blue and green representative atoms respectively. **Bottom Zoom**: The calculation of forces at dark blue and green atoms sums over interaction with all atoms within a cutoff radius regardless of species.

Notes

- The notation for multiple species of atoms evolves exactly to the existing formulation for the single species NL-QC, if the number of species is taken as 1.

This evolution further ensures the consistency of the multiple species method with the initial formulation

- An initial error estimate of the single species cluster summation rule was conducted in [40] based on different sizes of cluster radii, calculation of cluster weights, and other factors. A subsequent analysis conducted in [46] showed that the cluster summation rule introduced error into the model. Additional quadrature rules were proposed for the NL-QC method to reduce this error [30, 34], however, these rules have their own issues. At this time, it is our opinion that there is no clear 'best' quadrature rule currently available in literature. Research is ongoing in the QC field to develop better quadrature rules. For these reasons, we chose to extend NL-QC to multiple species using the same cluster summation rule developed in [40]. If a 'best' quadrature rule becomes available, conversion of the code and details of multiple species NL-QC to this quadrature rule can be undertaken following the same procedure illustrated above.

3.4 Computational implementation

3.4.1 Overview of single species NL-QC code

The single species NL-QC code was initially developed using a combination of Fortran, C, and C++. Additionally, extensive work was done on implementing advanced data structures, enhancing calculation speeds using local processor caches, and parallelizing algorithms using PThreads. The code starts by initializing data structures, building neighbor lists, computing forces on nodes, and then minimizing the forces using a nonlinear conjugate gradient algorithm. The general flow of the code is

below:

```
InitializeDataStructures(...);
BuildNeighborList(...);
ComputeForces(...);
while(not converged){
    RebuildNeighborListIfNecessary(...);
    ComputeForces(...);
    UpdateRepAtomLocationsWithCG(...);
}
OutputResults(...);
```

3.4.2 C++ class extension of Quasicontinuum to Quasicontinua

In developing the extension of NL-QC to multiple species, our goals was to reuse as much of the existing code as possible. We achieved this by creating a C++ class for a single Quasicontinuum, which holds all of the data structures for a single species or lattice of atoms. Essentially all of the data structures for the original code are replicated and initialized each time we instantiate a new Quasicontinuum lattice. For example, if we wanted to simulate NiAl, we would instantiate a Ni Quasicontinuum lattice and an Al Quasicontinuum lattice, where each Quasicontinuum lattice keeps track of its own data. A Quasicontinua class was then created to hold all N^s Quasicontinuum instances and enable easy access to each Quasicontinuum. Additional C++ classes were implemented for communicating necessary data between different lattices.

One of these additional C++ classes is the BuildCrossNeighborList class, which calculates and stores all atomistic neighbors of a site, regardless of which atomic species or lattice the neighbor belongs to. The BuildCrossNeighborList class stores

the neighbor sites and locations in separate hash tables for quick searches and minimal duplication of data. A second class was created to allow implementation of EAM potentials. EAM potentials are different from traditional pair potentials, like Lennard-Jones, in that they are a many body potential. Equations 3.23 and 3.24 show the form of the energy in a system of atoms.

$$E_{tot} = \frac{1}{2} \sum_{i,j(j \neq i)} \Psi_{\alpha_i \alpha_j}(r_{ij}) + \sum_i F_{\alpha_i}(\bar{\rho}_i), \text{ where} \tag{3.23}$$

i and j are individual atoms, α_i is the species of the i^{th} atom, α_j is the species of the j^{th} atom, F_{α_i} is the embedding energy, and $\bar{\rho}$ is the total charge density of an atom.

$$\bar{\rho}_i = \sum_{i \neq j} \rho_{\alpha_j}(r_{ij}), \text{ where} \tag{3.24}$$

ρ_{α_j} is a known function of charge density. The many body nature of the potential comes from the fact that to calculate the embedding energy, the charge density at an atom must be known. However, the charge density of an atom is dependent on all other atoms within a given cutoff radius all of which must be known before the calculation of forces. We created the EAM class to precompute the charge density, based on CrossNeighborList data, at all necessary atoms before the density is needed to compute forces and energies. Finally, a ComputeCrossForces class was created, which takes neighbor list and EAM data as an input, and calculates all forces on atoms in clusters and subsequently forces on representative atoms. All of these classes were developed using PThreads for seamless integration into the existing code for high performance computing environments. The computational flow of the extension

of NL-QC to multiple species of atoms is below.

```
for(i=0;i< N^s;++i){
    iQuasicontinuum = Quasicontinuum::InitializeDataStructures(...);
    Quasicontinua::insert(iQuasicontinuum);
}
for(i=0;i< N^s;++i){
    iQuasicontinuum = Quasicontinua::getQuasicontinuum(i);
    iQuasicontinuum.BuildNeighborList(...);
    iQuasicontinuum.BuildCrossNeighborList(...);
    iQuasicontinuum.EAM(...);
}
for(i=0;i< N^s;++i){
    iQuasicontinuum = Quasicontinua::getQuasicontinuum(i);
    iQuasicontinuum.ComputeForces(...);
    iQuasicontinuum.ComputeCrossForces(...);
}
```

```
while(not converged){
    for(i=0;i< N^s;++i){
        iQuasicontinuum = Quasicontinua::getQuasicontinuum(i);
        iQuasicontinuum.RebuildNeighborListIfNecessary(...);
        iQuasicontinuum.RebuildCrossNeighborListIfNecessary(...);
        iQuasicontinuum.EAM(...);
    }
    for(i=0;i< N^s;++i){
        iQuasicontinuum = Quasicontinua::getQuasicontinuum(i);
        iQuasicontinuum.ComputeForces(...);
        iQuasicontinuum.ComputeCrossForces(...);
    }
    for(i=0;i< N^s;++i){
        iQuasicontinuum = Quasicontinua::getQuasicontinuum(i);
        iQuasicontinuum.UpdateRepAtomLocationsWithCG(...);
    }
}
for(i=0;i< N^s;++i){
    iQuasicontinuum = Quasicontinua::getQuasicontinuum(i);
    iQuasicontinuum.OutputResults(...);
}
```

3.4.3 Verification of implementation

We verified the new code with several simple patch tests. The first test, verified the correct calculation of **0** forces and charge densities in undeformed B2-NiAl using the potential developed in [52]. In the next test we applied a simple affine shear deformation to the system. The results again produced **0** forces in the system, as required. Finally, we applied the same affine shear deformation, but this time only to the boundary nodes. The system was then allowed to minimize using the implemented nonlinear conjugate gradient algorithm. The final equilibrium atomistic positions corresponded exactly to the expected affine deformation, to within numerical tolerance. The passing of these simple tests gives us a confidence that the implementation is correct.

3.5 Numerical simulation of deformation around void defects in NiAl

We use the method to simulate the deformation around various sized voids in NiAl subject to volumetric expansion. NiAl is modeled in its B2 phase with an EAM potential [52, 8]. We show a typical mesh used in Figure 3.7. Near the void, full atomistic resolution is used with coarse-graining occurring farther away from the defect. Void sizes from 2-10 Angstroms are simulated subject to load increments of volumetric expansion. We apply the deformation to the system, let the atoms relax and then apply the next loading. Figure 3.8 and Figure 3.9 show the centrosymmetry parameter around a 2 Angstrom void (in this case only a vacancy) after initial relaxation and at a volumetric expansion of 24 percent. Figure 3.10 and Figure 3.11 show the centrosymmetry parameter around a 4 Angstrom void after initial relaxation and at a volumetric expansion of 16.5 percent. Figure 3.12 and Figure 3.13 show the centrosymmetry parameter around a 6 Angstrom void after initial relaxation and at a volumetric expansion of 15 percent. Figure 3.14 and Figure 3.15 show

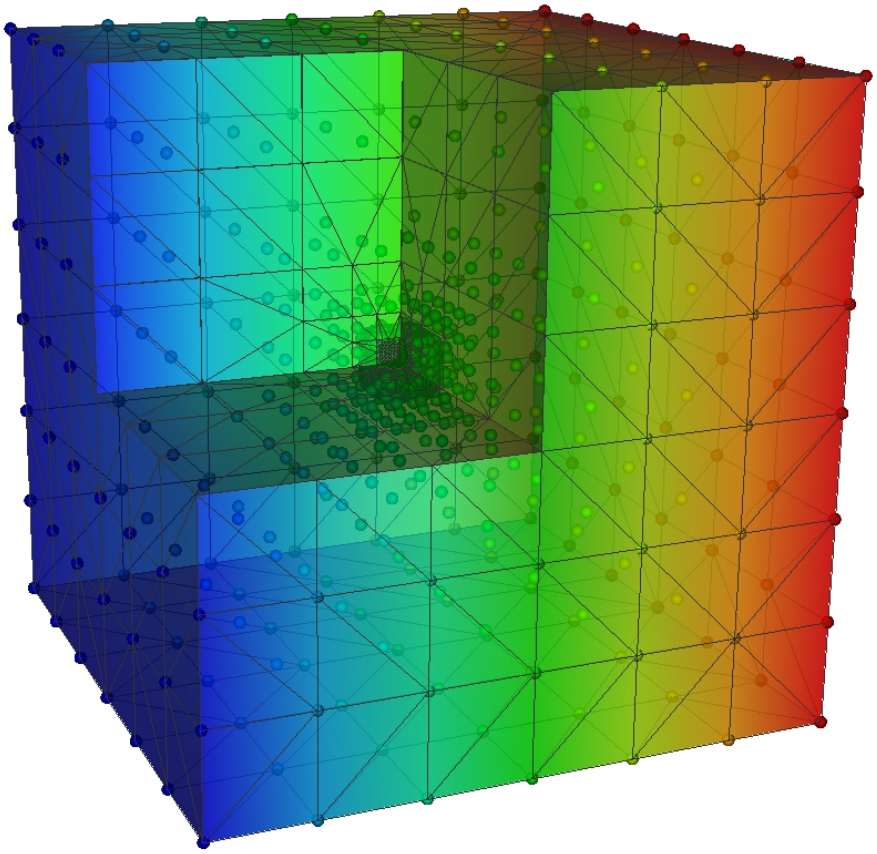


Figure 3.7: Typical mesh with coarse-graining far away from void with full atomistic resolution

the centrosymmetry parameter around a 8 Angstrom void after initial relaxation and at a volumetric expansion of 13.5 percent. Figure 3.16 and Figure 3.17 show the centrosymmetry parameter around a 10 Angstrom void at after initial relaxation and at a volumetric expansion of 12 percent.

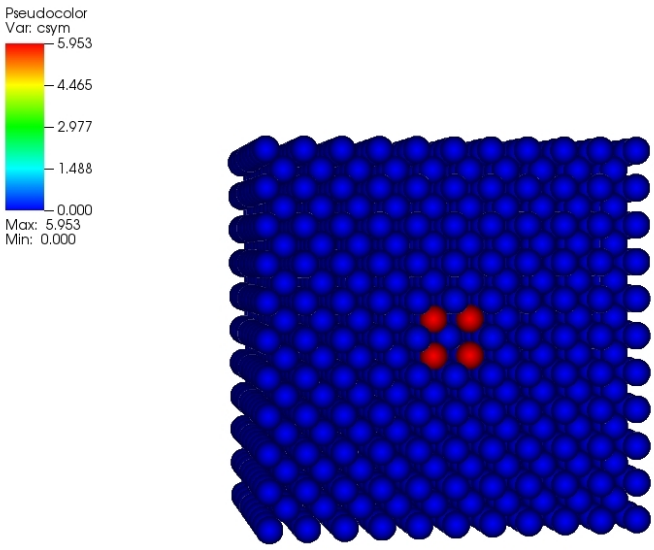


Figure 3.8: Centrosymmetry parameter around vacancy after initial relaxation.

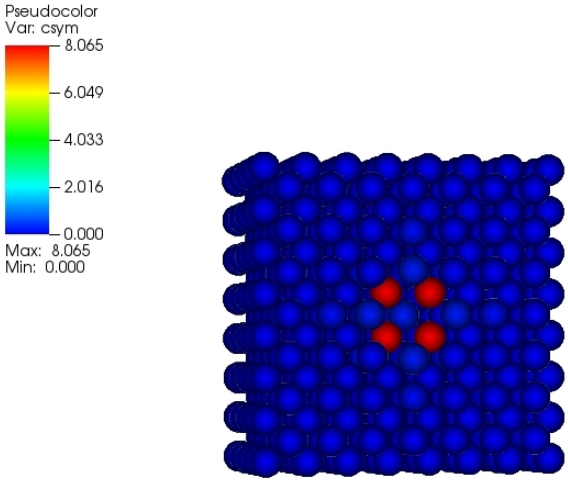


Figure 3.9: Centrosymmetry parameter around vacancy at volumetric expansion of 24 percent.

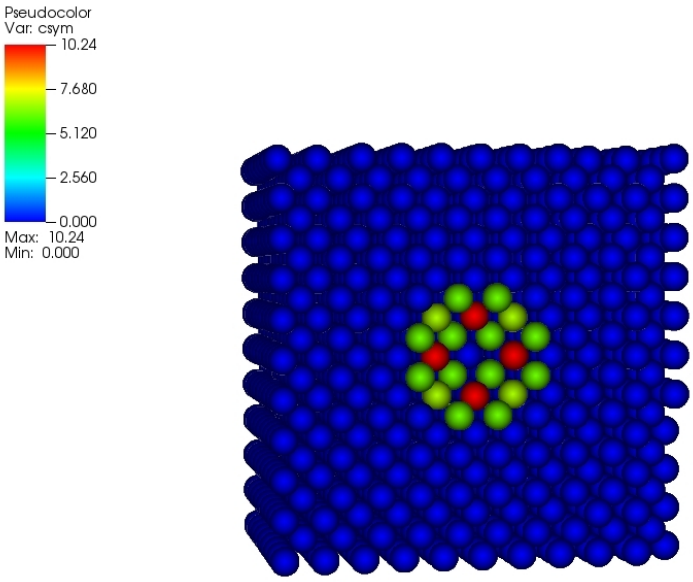


Figure 3.10: Centrosymmetry parameter around a void of 4 Ang. after initial relaxation.

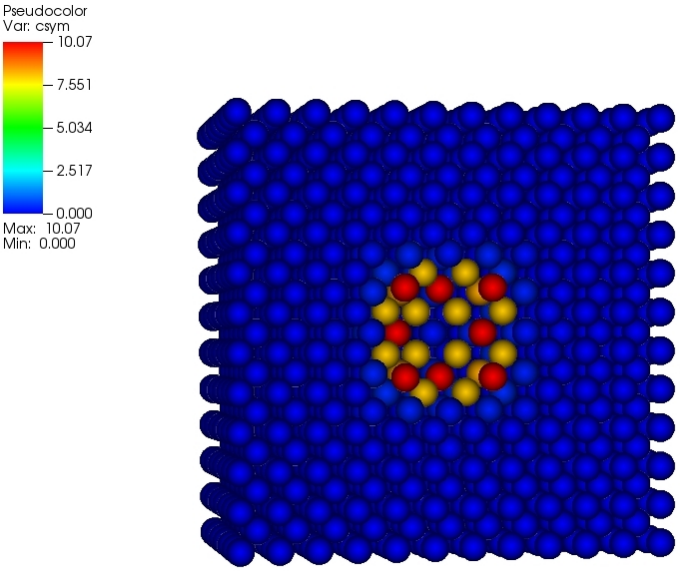


Figure 3.11: Centrosymmetry parameter around a void of 4 Ang. after volumetric expansion of 16.5 percent.

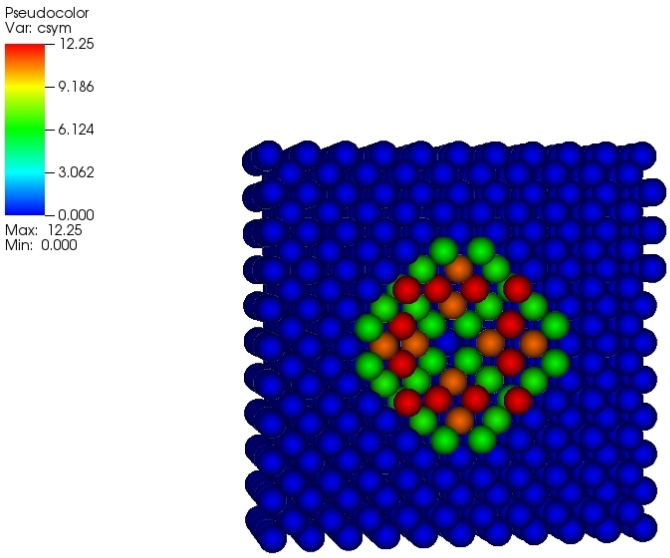


Figure 3.12: Centrosymmetry parameter around a void of 6 Ang. after initial relaxation.

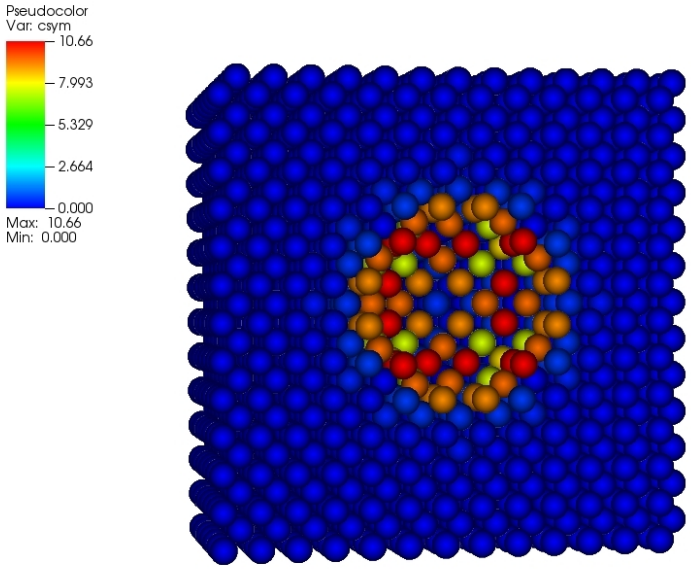


Figure 3.13: Centrosymmetry parameter around a void of 6 Ang. after volumetric expansion of 15 percent.

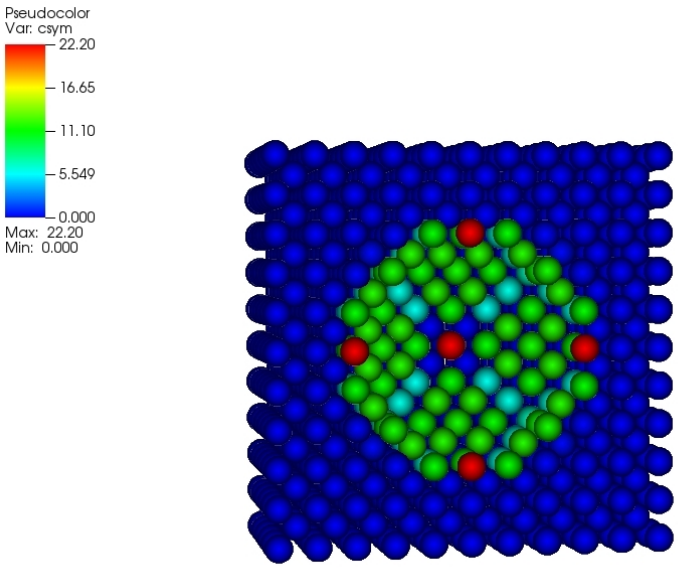


Figure 3.14: Centrosymmetry parameter around a void of 8 Ang. after initial relaxation.

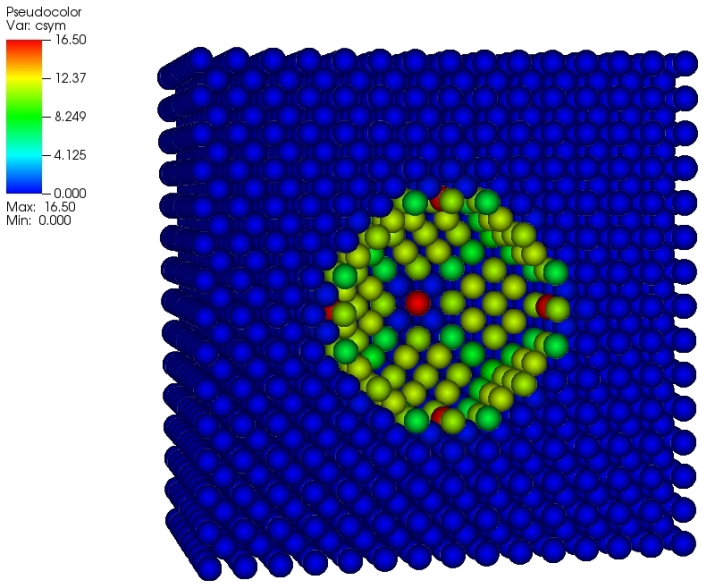


Figure 3.15: Centrosymmetry parameter around a void of 8 Ang. after volumetric expansion of 13.5 percent.

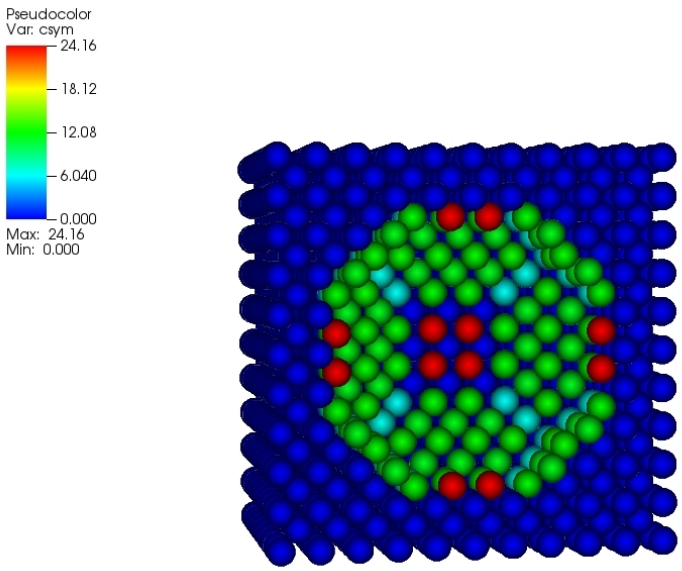


Figure 3.16: Centrosymmetry parameter around a void of 10 Ang. after initial relaxation.

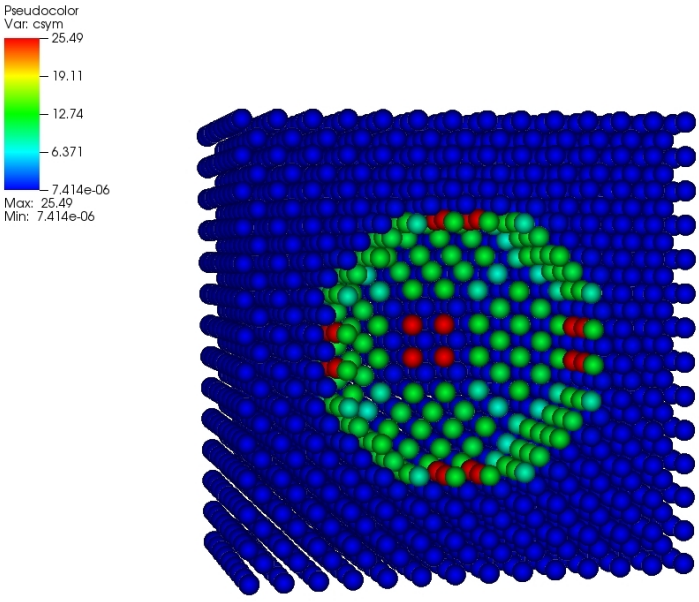


Figure 3.17: Centrosymmetry parameter around a void of 10 Ang. after volumetric expansion of 12 percent.

3.6 Discussion

In this chapter, we extended the non-local force QC method to multiple lattices. We treated the problem as the union of many simple lattice problems and then allowed the force calculation to communicate relevant information between the lattices. The method was verified with a variety of simple tests after implementation in a high performance computing framework. We used the method to simulate void relaxation in B2 NiAl for multiple void sizes from a vacancy to 1nm. We intend to continue loading these voids until dislocation nucleation occurs from the void to understand how void size effects plasticity.

Acknowledgements

Jason Marshall would like to thank ORAU, ORISE, and ARL for financial support, hospitality, and computational resources during his summer research internships at the lab.

4

Non-local quasicontinuum method with long-range, real-space electrostatics

4.1 Abstract

We develop a method for simulating ionic solids with long-range electrostatic interactions, without assuming periodicity. The new methodology can be described as a combination of the Reaction Field and Fast Multipole methods. The methodology we use allows for the evolution of a body potentially with defects (domain walls, vacancies, etc.) subject to electrostatic and mechanical loadings. Additionally we allow explicit handling of multiple types of electrical boundary conditions. The problem we are interested in is essentially calculating the electric field at a given location from a multi-lattice of charges. Generally speaking, we want to break up the electric field calculation into two components. The first component is an exact summation region near the location of interest. The second component includes all parts of a body outside of this region that are away from defects. The problem is too computationally expensive to perform exact summations everywhere, so we calculate an approximated electric field from the far field region using ideas from the

Fast Multipole Method.

In this chapter, we derive the method by performing a Taylor series expansion of the standard Coulombic kernel for charges. We start by considering a single unit cell of charges, where the net charge of the unit cell is zero. We work only with the dipole expansion term and consider all higher order moments as bounds on the error of the expansion. A summation over a large number of unit cells in a body is performed. The dipole term is transformed into a standard divergence term, while the error term is integrated over shells of expanding unit cells centered at the point of interest. An error bound for the calculation of the electric field at a point of interest is analytically derived and numerically modeled for GaN, though the analysis can be extended to any ionic solid material. We then use the error bound as a criterion to determine the size of the exact summation region around an evaluation point for the electric field. Our work has been implemented within an existing Quasicontinuum Method code for multiscale modeling and high performance computing.

Keywords: Quasicontinuum (QC) method; electrostatics; Fast Multipole Method(FMM); Reaction Field(RF) method; ionic solids

4.2 Introduction

Electrostatic (Coulombic) interactions play a prominent role in the structure of all materials. These interactions fundamentally take place at the quantum length scale and occur between electrons and protons. Modeling materials at this fundamental length scale is quite challenging, even with sophisticated methods like density-functional theory (DFT). DFT simulations are typically comprised of hundreds of atoms, but occasionally are used to model systems with thousands or even tens of thousands of atoms, though these simulations are rare. These simulations struggle to provide detail at the larger length scales important in engineering, where the number of atoms in a system can be orders of magnitude higher than DFT can handle.

Conversely, classical continuum methods provide coarse-grained information at the engineering design length scale, but cannot fully resolve the underlying structure of materials. Atomistic methods like molecular dynamics [23] and multiscale methods like QC [68, 51] are in between the two in terms of both the largest accessible length scale and highest resolution of the underlying material structure. The material input parameters in atomistic methods can be thought of as the interatomic potentials. Interatomic potentials essentially approximate the underlying energy and force interactions between atoms ranging from bonds between pairs of atoms (Lennard-Jones, Buckingham, etc. [23]) to many body interactions (EAM[16, 17], MEAM[5], etc.). Many interatomic potentials do not explicitly include Coulombic terms, but instead include them in an approximate way. The underlying structure of the material is essential to this choice.

The Coulombic interaction kernel is shown in Equation 4.1, where q_i and q_j are the effective charge of two different atoms and r_{ij} is the separation between the two charges.

$$W = \frac{q_i q_j}{4\pi\varepsilon_0 r_{ij}} \tag{4.1}$$

This interaction energy is long-ranged, because of its slow $1/r$ decay and can be a divergent series when summed over many interacting atoms depending on the underlying structure. In ionic solids like (GaN, Ceria, $BaTiO_3$), the situation is better and the Coulombic energy effectively decays as $1/r^3$, because of the orientation of atomic charges in the crystal structure. Interatomic potentials for ionic solids explicitly include these Coulombic interactions. Calculating the energy in a system then requires adding the interactions between all atoms in the system, resulting in a conditionally convergent sum due to the effective $1/r^3$ decay. Metallic solids, however, are different because the Coulombic energy decays as $1/r^5$ due to the different orientation of atomic charges in the crystal structure. In this case, most interatomic potentials do

not explicitly include Coulombic interactions. Instead the Coulombic energy is included with the other short-range interactions. This is valid because the Coulombic sum is absolutely convergent in metals and a cutoff radius typical for short-range potentials can be applied. A more detailed description of why electrostatic interactions are long-ranged can be found in [49].

In this chapter, we focus specifically on ionic solids, where the electrostatic interaction is explicitly included in an interatomic potential. While the problem starting from the quantum length scale has already been simplified with an effective charge on atoms instead of handling individual protons and electrons, performing the full summation is still quite challenging. The full atom-atom interaction summation is not feasible due to its large computational cost. In its place, many methods have been developed to approximate the summation. One class of methods are the Ewald [21, 23] and Ewald-like summations [22, 23]. These methods break up the full summation into a real-space component and an imaginary space component, both of which are fast to calculate. The real space component adds the Coulombic interactions from atoms within a small cutoff radius r, while the imaginary space component adds the interactions from all atoms outside the cutoff radius. These methods are quick and effective, but they suffer from a few drawbacks.

- Boundary conditions beyond simple (cube, sphere) geometries are difficult to handle.

- The imaginary space component assumes some form of periodicity to perform the summation. If the far field atoms are varying in position from the assumed periodicity, then this assumption does not capture that variation.

Another prominent method for electrostatics is the fast multipole method (FMM) [28, 7, 14]. This method performs a Taylor series expansion of the Coulombic kernel about a cluster of charges. The method then calculates the higher order moments

from the cluster and approximates the net interaction with the resulting moments. The error in the method can be controlled based on the distance of a cluster from the point of interest and the number of moments included in the approximation. FMM, however, is not as widely used in the atomistic modeling world as other fields. Some of the challenges are its complex algorithms and subsequent high degree of computational implementation difficulty, especially in a high performance computing environment.

The last prominent method that we want to highlight is the Reaction Field (RF) method [73, 27, 6]. This method is prominently used in computational chemistry for molecules surrounded by a homogeneous liquid or solid. The Coulombic interactions in this method are included exactly within a cutoff radius around a molecule or molecules. Outside of this cutoff radius, a far field term arises by assuming an electrically active homogeneous medium typically a liquid or a solid. This medium then acts on the molecules within the cutoff radius via a constant electric field arising from continuum level calculations. The exact values of the field are calculated by solving Maxwell's electrostatic equation in the body containing the homogeneous medium. The far field domain has two important boundaries, one on the exterior and one on the interior around the exact summation region that result in the applied field. The interior boundary is typically taken as a sphere, though it does not need to be.

In the atomistic mechanics field, the Ewald and Ewald-like methods are most prevalently used, but introduce the serious limitations stated above. We seek to develop a method that does not have these limitations, which we achieve in a new method that can be described as a combination of FMM and the RF method. Our work in this chapter extends our initial research ([49], Chapter 2) on modeling materials with Coulombic interactions. The enhanced method developed in this chapter can simulate 3-D problems, is fully non-local, unlike our previous work, and is im-

plemented in a high performance computing framework.

4.3 Method

4.3.1 Preliminaries

We start by assuming an atomistic body, Ω, see Figure 4.1. Ω is a perfect single crystal with multiple species of atoms per unit cell. The location of unit cells are denoted by $\boldsymbol{X}$ in the reference configuration and $\boldsymbol{x}$ in the current configuration, while the locations of specific atoms within a unit cell are denoted by $\boldsymbol{y}^\alpha$. Each unit cell is referenced by a unique triple integer $\mathcal{I} \in \mathbb{Z}^3$ that locates the specific unit cell within a lattice. We assume an effective charge on each atom that is denoted by q^α, where α is the species of atom in the unit cell. The charge on an atom does not need to be discrete, but we assume that it is and extend to a continuum charge density later on with a Dirac delta function centered at all $\boldsymbol{y}^\alpha$ atomic locations. Additionally, all unit cells of atoms must be charge neutral and have a length scale of l.

$$\sum_\alpha q^\alpha = 0 \tag{4.2}$$

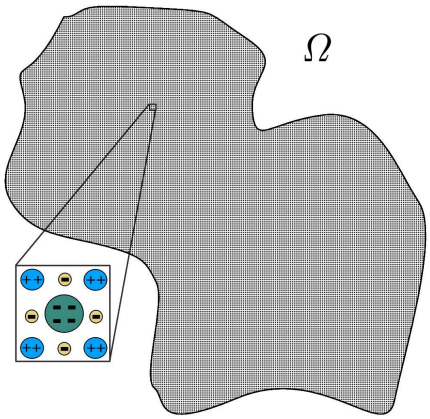


Figure 4.1: Body Ω with atomistic charges and charge neutral unit cells.

4.3.2 Quasicontinuum Method

The QC method is a powerful tool for solving large atomistic systems. The method was originally developed by Tadmor, et. al. in 1996 [66]. Since then multiple versions of the method have been developed, more information on the specific methods can be found in these review articles [68, 51]. In our previous work with electrostatic interactions, we used a purely Cauchy-Born variant of QC [49]. This version of QC is valid in large elements, where the deformation gradient is slowly varying. The version is not valid near defects or areas of high deformation, which we are mainly interested in due to the interesting physics occurring in these regions. For this work we use the non-local cluster force QC [40], specifically a variant for multi-lattices [42, 50] that is valid near areas of high deformation.

We will now give a brief overview of the QC method, for more in depth details, see [40, 42, 50]. In this version of QC, we are interested in finding local minimizers of the energy, $\Phi(\boldsymbol{x}+\boldsymbol{y}^{\beta})$, in a body Ω, see Equation 4.3. These minimizers correspond to equilibrium configurations of Ω subject to any defects or external loadings in the system. In the remainder of this section, we will use the notation $\boldsymbol{x}^{\beta}=\boldsymbol{x}+\boldsymbol{y}^{\beta}$.

$$\min_{\boldsymbol{x}^{\beta}} \Phi(\boldsymbol{x}^{\beta}) \tag{4.3}$$

As an atomistic system becomes large, explicitly tracking all atoms in Ω is not computationally possible, so we introduce a coarse-graining approximation in slowly deforming regions. The coarse-graining is achieved by only tracking a subset of atoms, which we call representative atoms, $\boldsymbol{x}_h^{\beta}$. In areas with defects or external loadings, every atom $\boldsymbol{x}^{\beta}$ is a representative atom $\boldsymbol{x}_h^{\beta}$ to achieve full atomistic resolution. The regions of high deformation are initially chosen at the beginning of a calculation, but adaptive meshing has been implemented and can be used to adjust the fully resolved regions, where necessary. In regions far away from the high deformation areas, we only select a small subset of atoms to be representative atoms. The locations of all

other atoms are then interpolated using standard shape functions, $\mathcal{S}_h^\beta$, based on the representative atoms.

$$\boldsymbol{x}^\beta = \mathcal{S}_h^\beta \left(\boldsymbol{X}^\beta(\mathcal{I}), \boldsymbol{x}_h^\beta \right) \tag{4.4}$$

In our multi-lattice case, each atom within a unit cell will be interpolated from a set of shape functions, $\mathcal{S}_h^\beta$, and representative atoms $\boldsymbol{x}_h^\beta$ of the same β species. Hence, there are $max(\beta)$ sets of representative atoms and triangulated meshes that shape functions, $\mathcal{S}_h^\beta$, are built from.

We can now write the equilibrium configurations of Ω in terms of the representative atoms.

$$\min_{\boldsymbol{x}_h^\beta} \Phi(\boldsymbol{x}_h^\beta) \tag{4.5}$$

Local minimizing states of these equilibrium configurations correspond to the forces, $\mathcal{F}^\beta(\boldsymbol{x}^\beta)$, equaling zero in Ω. However, the computational expense is again too high to solve for the forces for all atoms in a system. Thus, the forces are only explicitly calculated on representative atoms, where an approximated force is calculated from a cluster summation rule [40].

$$\mathcal{F}_h^\beta(\boldsymbol{x}_h^\beta) \approx \sum_{\boldsymbol{x}^\beta \in \mathcal{C}(\boldsymbol{x}_h^\beta)} \mathcal{Q}(\boldsymbol{x}^\beta) \mathcal{S}_h^\beta(\mathcal{F}^\beta(\boldsymbol{x}^\beta), \boldsymbol{x}_h^\beta) \tag{4.6}$$

$\mathcal{C}(\boldsymbol{x}_h^\beta)$ denotes a cluster of $\boldsymbol{x}^\beta$ atoms centered around a representative atom, $\boldsymbol{x}_h^\beta$. $\mathcal{Q}(\boldsymbol{x}^\beta)$ is the summation weight on the cluster atom. Equation 4.6 essentially calculates a weighted force on a representative atom from a cluster of atoms, this effective force can then be used to find equilibrium configurations in Ω. Each atom can only belong to a single cluster to meet the summation rule requirements in [40] and only atoms of the same β species are used in a cluster around $\boldsymbol{x}_h^\beta$. Thus, in areas of high deformation, where every atom is a representative atom, the force calculation is exact and essentially devolves into molecular statics. Away from these regions, the

force is only approximated. We now use a conjugate gradient algorithm to solve for zero forces at all representative atoms.

$$\mathcal{F}_h^\beta(\boldsymbol{x}_h^\beta) = \mathbf{0} \tag{4.7}$$

The only thing still needed to perform the minimization is a way to calculate forces on a given atom, $\mathcal{F}^\beta(\boldsymbol{x}^\beta)$. We start by breaking up the $\mathcal{F}^\beta(\boldsymbol{x}^\beta)$ calculation into two components, the typical short-range interactions and the long-range interactions.

$$\mathcal{F}^\beta(\boldsymbol{x}^\beta) = \mathcal{F}^\beta_{short}(\boldsymbol{x}^\beta) + \mathcal{F}^\beta_{electrostatic}(\boldsymbol{x}^\beta) \tag{4.8}$$

QC methods typically calculate $\mathcal{F}^\beta(\boldsymbol{x}^\beta)$ using interatomic potentials that are only short-ranged with a cutoff radius. Long-range interactions have been included in non-local QC methods, but to the best of the authors' knowledge only with Ewald sums [42]. We will not provide any more explanation for calculating short-range forces from interatomic potentials, because they have been extensively covered in the mechanics literature. Instead we focus specifically on including the long-range electrostatic interactions, which we develop in the following section.

4.3.3 Electrostatic Summation Overview

Calculating the electrostatic force on an atom requires knowing the electric field E and multiplying it by the charge on the atom q^β. In this section of the chapter, we occasionally use indicial notation where a_i denotes a vector and i runs over 1 to the number of spatial dimensions of Ω.

$$\mathcal{F}^\beta_{electrostatic}(\boldsymbol{x}^\beta) = q^\beta E_i(\boldsymbol{x}^\beta) \tag{4.9}$$

We use a standard definition of the electric field, which is related to the electric potential by $E = -\nabla\phi$. The force on a β atom can now be written as the explicit sum over all α atoms $\in \Omega$ interacting through the standard kernel.

$$\mathcal{F}^\beta_{electrostatic}(\boldsymbol{x}^\beta) = q^\beta \sum_{\boldsymbol{x}' \in \Omega} \sum_{\alpha} \frac{q^\alpha (x_i^\beta - x_i' - y_i^\alpha)}{4\pi\varepsilon_0 |\boldsymbol{x}^\beta - \boldsymbol{x}' - \boldsymbol{y}^\alpha|^3} \tag{4.10}$$

From here, we will focus on calculating the electric field at any given point, $\boldsymbol{x}^\beta$.

4.3.4 Contribution from Single Unit Cell

We start with the contributions from a single unit cell as seen in Figure 4.2. The field

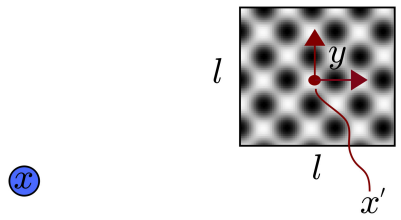


Figure 4.2: Schematic of unit cell geometry contributing to the electric field at a given point $\boldsymbol{x}^\beta$.

can be written in terms of an integral instead of a sum, assuming that each discrete charge is approximated by a dirac delta function. The resulting charge distribution is $\rho(\boldsymbol{y})$.

$$\begin{aligned} 4\pi\epsilon_0 E_i^{cell}(\boldsymbol{x}) &= \sum_\alpha \frac{q^\alpha (x_i^\beta - x_i' - y_i^\alpha)}{|\boldsymbol{x}^\beta - \boldsymbol{x}' - \boldsymbol{y}^\alpha|^3} \\ &= \int_{\boldsymbol{y}} \frac{\rho(\boldsymbol{y}^\alpha)(x_i^\beta - x_i' - y_i^\alpha)}{|\boldsymbol{x}^\beta - \boldsymbol{x}' - \boldsymbol{y}^\alpha|^3}\, d^3\boldsymbol{y} \end{aligned} \tag{4.11}$$

We are interested in the contribution to the electric field with respect to two competing length scales $|\boldsymbol{x}^\beta - \boldsymbol{x}'|$, the distance between the evaluation point and the unit cell, and l the characteristic length of a unit cell. We choose the following scalings to evaluate these competing length scales, with $\square$ representing a cell as a unit cube.

$$y_i = l\tilde{y}_i, \text{ hence } \; d^3\boldsymbol{y} = l^3\, d\square \tag{4.12}$$

$$\rho(\boldsymbol{y}) = \tilde{\rho}(\tilde{\boldsymbol{y}})/l \tag{4.13}$$

The electric field can now be written in terms of the scaling parameter l.

$$4\pi\epsilon_0 E_i^{cell}(\boldsymbol{x}) = \int_{\square} \frac{l^2\rho(\tilde{\boldsymbol{y}})(x_i^\beta - x_i' - l\tilde{y}_i^\alpha)}{|\boldsymbol{x}^\beta - \boldsymbol{x}' - l\tilde{\boldsymbol{y}}^\alpha|^3}\, d\square \tag{4.14}$$

We now perform a Taylor series expansion of the kernel function about $\tilde{\boldsymbol{y}} = \boldsymbol{0}$, essentially the multipole expansion commonly used in FMM. We only show the first 3 terms, but each higher order term adds an additional scaling of l and an additional derivative on the kernel.

$$\begin{aligned} 4\pi\epsilon_0 E_i^{cell}(\boldsymbol{x}) \approx \int_{\square} l^2\tilde{\rho}(\tilde{\boldsymbol{y}}) \Bigg(& \frac{x_i^\beta - x_i'}{|\boldsymbol{x}^\beta - \boldsymbol{x}'|^3} + \tilde{y}_j l \frac{3\left(x_j^\beta - x_j'\right)\left(x_i^\beta - x_i'\right) - r^2\delta_{ij}}{|\boldsymbol{x}^\beta - \boldsymbol{x}'|^5} \\ & + \frac{1}{2}\tilde{y}_j\tilde{y}_k l^2 \nabla_i\nabla_j\nabla_k \left(\frac{1}{|\boldsymbol{x}^\beta - \boldsymbol{x}'|}\right) + \dots \Bigg)\, d\square \end{aligned} \tag{4.15}$$

Note that each of the 3 terms are simply the n^{th} derivatives, $\nabla^n(1/r)$, of the kernel function, where $r = |\boldsymbol{x}^\beta - \boldsymbol{x}'|$. The first term immediately goes away because we assume that the unit cell is charge neutral.

$$\int_{\square} \tilde{\rho}(\tilde{\boldsymbol{y}})\, d\square = 0 \tag{4.16}$$

We now use the polarization density in its customary form to modify the first term.

$$p_i(\boldsymbol{x}') = \tilde{p}_i(\boldsymbol{x}') = \frac{\int \tilde{\rho}(\tilde{\boldsymbol{y}})\tilde{y}_i\, d\square}{\int d\square} \tag{4.17}$$

All factors of l cancel in the scaled version of the polarization density. Thus, the unscaled and scaled polarization are identical. This is the reason why the scaling for the charge density was initially chosen as $\rho(\boldsymbol{y}) = \tilde{\rho}(\tilde{\boldsymbol{y}})/l$. The electric field now can

be written in terms of the polarization density.

$$4\pi\epsilon_0 E_i^{cell}(\boldsymbol{x}^\beta) \approx p_j(\boldsymbol{x}')l^3 \frac{3\left(x_j^\beta - x_j'\right)\left(x_i^\beta - x_i'\right) - r^2\delta_{ij}}{|\boldsymbol{x}^\beta - \boldsymbol{x}'|^5} + \int_\square \frac{1}{2}\tilde{y}_j\tilde{y}_k l^4 \nabla_i\nabla_j\nabla_k \left(\frac{1}{|\boldsymbol{x}^\beta - \boldsymbol{x}'|}\right) d\square + \dots \tag{4.18}$$

All terms beyond the dipole correspond to higher order multipoles that could be explicitly included in the calculation. The FMM does exactly that and controls the error in the electric field calculation by including higher order multipole terms as necessary. The number of terms to be included depends on the distance between the source cluster and the evaluation point namely $|\boldsymbol{x}^\beta - \boldsymbol{x}'|$. We choose to only include the dipole term in the calculation of the electric field and consider all higher order terms as a bound on the error in the electric field calculation. As the distance $|\boldsymbol{x}^\beta - \boldsymbol{x}'|$ decreases, the error in the electric field has the potential to grow and make this approximated calculation perform poorly. Thus, we only use this approximation at distances where the error bound is small. All unit cells that are close to the point of evaluation will be calculated following the exact explicit sum. In the following sections we will calculate the electric field from all unit cells in Ω. Additionally, we will derive a bound on the error in the electric field from all unit cells. We will use that error bound to determine where our approximated method can be used in Ω for a specific evaluation point $\boldsymbol{x}^\beta$.

4.3.5 Contribution from All Unit Cells in a Body

Working only with the dipole term to start, we want to calculate the total electric field from all unit cells located at $\boldsymbol{x}' \in \Omega$. Due to the fact that the governing electrostatic equations are linear, we can simply add the contribution from each individual unit

cell to get the total electric field.

$$\begin{aligned} 4\pi\epsilon_0 E_i^{approx}(\boldsymbol{x}^\beta) &\approx \sum_{\boldsymbol{x}'\in\Omega} 4\pi\epsilon_0 E_i^{cell}(\boldsymbol{x}^\beta) \\ &\approx \sum_{\boldsymbol{x}'\in\Omega} p_j(\boldsymbol{x}') l^3 \frac{3\left(x_j^\beta - x_j'\right)\left(x_i^\beta - x_i'\right) - r^2\delta_{ij}}{|\boldsymbol{x}^\beta - \boldsymbol{x}'|^5} \end{aligned} \tag{4.19}$$

We pass from the sum to an integral over Ω by assuming that $|\Omega| > l^3$. Additionally, we convert the integral to its div $\boldsymbol{p}$ form using integration by parts.

$$\begin{aligned} 4\pi\epsilon_0 E_i^{approx}(\boldsymbol{x}^\beta) &\approx \int_\Omega p_j(\boldsymbol{x}')\nabla_i\nabla_j\left(\frac{1}{|\boldsymbol{x}^\beta - \boldsymbol{x}'|}\right) d^3\boldsymbol{x}' \\ &\approx \int_\Omega -\nabla_j p_j(\boldsymbol{x}')\left(\frac{x_i^\beta - x_i'}{|\boldsymbol{x}^\beta - \boldsymbol{x}'|^3}\right) d^3\boldsymbol{x}' + \int_{d\Omega} p_j(\boldsymbol{x}') n_j \left(\frac{x_i^\beta - x_i'}{|\boldsymbol{x}^\beta - \boldsymbol{x}'|^3}\right) dS \end{aligned} \tag{4.20}$$

We now work with the higher order terms, which we call the error, $\Psi(\boldsymbol{x}^\beta)$, and can write as a series of terms.

$$\begin{aligned} \Psi(\boldsymbol{x}^\beta) &= \int_\square \tilde{\rho}(\tilde{\boldsymbol{y}})\frac{1}{2}\tilde{y}_j\tilde{y}_k l^4 \nabla_i\nabla_j\nabla_k\left(\frac{1}{|\boldsymbol{x}^\beta - \boldsymbol{x}'|}\right) + \dots \\ &\leq \frac{Q}{2} l^4 \nabla_i\nabla_j\nabla_k\left(\frac{1}{|\boldsymbol{x}^\beta - \boldsymbol{x}'|}\right) + \dots \\ &\leq \frac{Q}{2}\sum_{p=4}^{\infty}\frac{l^p}{|\boldsymbol{x}^\beta - \boldsymbol{x}'|^p} \end{aligned} \tag{4.21}$$

$$Q = \int_\square |\tilde{\rho}(\tilde{\boldsymbol{y}})|\, d\square \tag{4.22}$$

By summing over the error from all unit cells in Ω and again passing from the summation to an integral by assuming $|\Omega| > l^3$, we arrive at the following.

$$\Psi(\boldsymbol{x}^\beta) \leq \frac{Q}{2}\int_\Omega \sum_{p=4}^{\infty}\frac{l^{p-3}}{|\boldsymbol{x}^\beta - \boldsymbol{x}'|^p}\, d^3\boldsymbol{x}' \tag{4.23}$$

We note that in the limit of $l \to 0$ all error terms go exactly to zero. The approximation becomes exact in the limit as expected and shown previously in [35, 49]. As $|\boldsymbol{x} - \boldsymbol{x}'|^p$ gets larger, the relative error decreases. We capture this relationship by breaking up the integral over Ω into n shells of unit cells. In each integral, we will assume a fixed value of n for the shell and the maximum error as a function of nl. nl in this case, is the smallest scaled value of $|\boldsymbol{x}^\beta - \boldsymbol{x}'|^p$ in a given shell, which leads to the largest possible error. We will also assume for the time being that Ω is in the entire space of $\mathbb{R}^3$, thus we will sum over n shells from a minimum n_{min} to ∞. In the case of a real system, the summation can simply be cutoff when the n^{th} shell is outside of the actual domain Ω.

$$
\begin{aligned}
\Psi(\boldsymbol{x}^\beta) &\leq \frac{Q}{2} \sum_{n=n_{min}}^{\infty} \int_{S\Omega(n)} \sum_{p=4}^{\infty} \frac{l^{p-3}}{|\boldsymbol{x}^\beta - \boldsymbol{x}'|^p} \, d^3\boldsymbol{x}' \\
&\leq \frac{Q}{2} \sum_{n_{min}}^{\infty} \sum_{p=4}^{\infty} \frac{l^{p-3}}{(nl)^p} \int_{S\Omega(n)} d^3\boldsymbol{x}' \\
&\leq \frac{Q}{2} \sum_{n_{min}}^{\infty} \sum_{p=4}^{\infty} \frac{l^{p-3}}{(nl)^p} \frac{4\pi}{3} \left(((n+1)l)^3 - (nl)^3\right) \\
&\leq \frac{4\pi Q}{6} \sum_{n_{min}}^{\infty} \sum_{p=4}^{\infty} \frac{l^{p-3}}{(nl)^p} \left(((n+1)l)^3 - (nl)^3\right) \\
&\leq \frac{4\pi Q}{6} \sum_{n_{min}}^{\infty} \sum_{p=4}^{\infty} \frac{l^{p-3}}{(nl)^p} \left(3n^2 + 3n + 1)l^3\right) \\
&\leq C_1 \sum_{n_{min}}^{\infty} \sum_{p=4}^{\infty} \frac{3n^2 + 3n + 1}{n^p}
\end{aligned}
\tag{4.24}
$$

Now if we take the limit of $n \to \infty$, we obtain the same result of the error being identically zero as when the limit of $l \to 0$. We have just slightly tweaked our perspective. Now instead of shrinking the unit cell size, we are increasing the distance $|\boldsymbol{x}^\beta - \boldsymbol{x}'|$ between the unit cell location and the evaluation point. The electric field

can now be written in terms of the div $\boldsymbol{p}$ term along with an associated error.

$$E_i^{approx}(\boldsymbol{x}^\beta) \approx \int_\Omega -\nabla_j p_j(\boldsymbol{x}') \left(\frac{x_i^\beta - x_i'}{4\pi\varepsilon_0 |\boldsymbol{x}^\beta - \boldsymbol{x}'|^3} \right) d^3\boldsymbol{x}' + \int_{d\Omega} p_j(\boldsymbol{x}') n_j \left(\frac{x_i^\beta - x_i'}{4\pi\varepsilon_0 |\boldsymbol{x}^\beta - \boldsymbol{x}'|^3} \right) dS \tag{4.25}$$

$$\Psi(\boldsymbol{x}^\beta) \leq C_2 \sum_{n_{min}}^{\infty} \sum_{p=4}^{\infty} \frac{3n^2 + 3n + 1}{n^p} \tag{4.26}$$

This approximation will only be used in regions far enough away from the evaluation point to maintain the total error in the electric field below an acceptable tolerance level.

We break up Ω into 3 distinct domains for each evaluation point, $\boldsymbol{x}$, see Figure 4.3. $\Omega_{atomistic}$ is the region where the QC meshes are fully resolved and defects or external loadings exist. For example, if a charge vacancy is modeled, the surrounding region would be fully resolved. We note that in the fully resolved region, we relax the assumption of charge neutrality because the full summation is used and the polarization does not need to be defined or calculated. The electric field from this portion of Ω will be included using the exact summation. Ω_{shell} is a set of shells of unit cells that are centered at $\boldsymbol{x}^\beta$. The size of this region is determined by the input acceptable error tolerance. All unit cells within this domain will be included exactly as well.

$$E_i^{exact}(\boldsymbol{x}^\beta) = \int_{\Omega_{atomistic} \cup \Omega_{shell}} \int_\square \frac{\rho(\boldsymbol{x}', \boldsymbol{y})(x_i^\beta - x_i' - y_i)}{4\pi\varepsilon_0 |\boldsymbol{x}^\beta - \boldsymbol{x}' - \boldsymbol{y}|^3} \, d^3\boldsymbol{y} \, d^3\boldsymbol{x}' \tag{4.27}$$

The contribution to the electric field from all other unit cells in Ω_{far} will be approx-

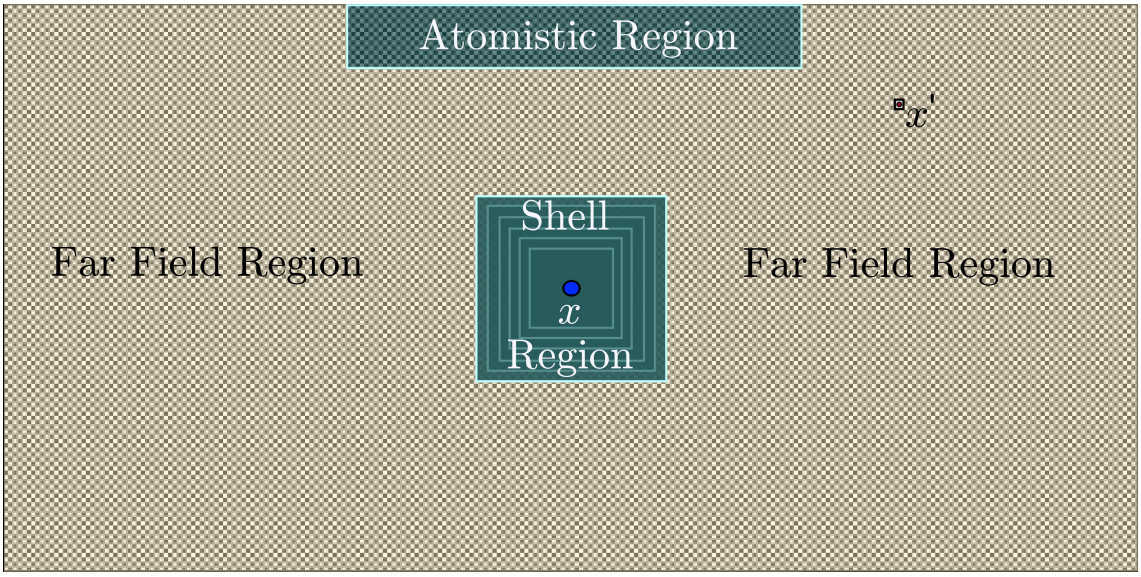


Figure 4.3: Full Ω domain broken down into fully resolved region $\Omega_{atomistic}$, a shell region Ω_{shell} centered at a point, $\boldsymbol{x}$, where the field is to be evaluated, and the far field region Ω_{far}. A single unit cell located at $\boldsymbol{x}'$ in the far field region is also shown.

imated using Equation 4.25.

$$\Omega_{far} = \Omega \setminus \Omega_{atomistic} \cup \Omega_{shell} \tag{4.28}$$

The full electric field can now be written as the combination of the contributions from the approximated far field domain and the exact atomistic domains with the associated error in Equation 4.26.

$$\begin{aligned} E_i(\boldsymbol{x}^\beta) &\approx E_i^{exact}(\boldsymbol{x}^\beta) + E_i^{approx}(\boldsymbol{x}^\beta) \\ &\approx \int_{\Omega_{far}} -\nabla_j p_j(\boldsymbol{x}') \left(\frac{x_i^\beta - x_i'}{4\pi\varepsilon_0 |\boldsymbol{x}^\beta - \boldsymbol{x}'|^3} \right) d^3\boldsymbol{x}' \\ &\quad + \int_{d\Omega_{far}} p_j(\boldsymbol{x}') n_j \left(\frac{x_i^\beta - x_i'}{4\pi\varepsilon_0 |\boldsymbol{x}^\beta - \boldsymbol{x}'|^3} \right) dS \\ &\quad + \int_{\Omega_{atomistic} \cup \Omega_{shell}} \int_{\square} \frac{\rho(\boldsymbol{x}', \boldsymbol{y})(x_i^\beta - x_i' - y_i)}{4\pi\varepsilon_0 |\boldsymbol{x}^\beta - \boldsymbol{x}' - \boldsymbol{y}|^3} \, d^3\boldsymbol{y} \, d^3\boldsymbol{x}' \end{aligned} \tag{4.29}$$

We note that the only source of error is from the approximated region, which is controlled by the size of the shell region. The full atomistic regions contribute zero error to the electric field, because they are exactly summed. In section 4.5, we will evaluate the error both analytically and numerically in the electric field using material properties for GaN at a variety of different n shell region sizes.

4.4 Numerical Implementation

A detailed description of the QC code can be found in [40, 50], we will just highlight the basics of the code and the additions necessary to calculate the electrostatic forces. The non electrostatic portion of the QC code is a mix of C, C++, and Fortran, with a majority of the code written in C. The code takes lattices as an input and meshes each lattice separately. Data structures including hash tables and neighbor lists are used to store the required information for calculating forces on atoms. A variety of mechanical loads can be applied and the code solves the forces equal to 0 in the body subject to these external loads.

We implemented our electrostatics method in the code by creating a C++ singleton class that handles all electrostatic calculations. The base QC code then calls methods that update the electrostatic data whenever the electric field is required. The electric field is calculated in three steps upon request from the base QC code. The first step is to account for the contribution from all exact summations, see Equation 4.27. This region includes shells of unit cells around an atom of interest and all atomistically resolved domains in the triangulated meshes. We use hash tables keyed by the triple integer of lattice coordinates unique to each atom to store lists of atoms in these region for quicker evaluation. The size of the shell region is controlled via an input integer that denotes the number of shells of unit cells to include. The contribution to the electric field from this exact region is then summed using the

standard kernel.

The second step is to include all contributions to the electric field from the approximated far field interactions. Polarization density is calculated using Equation 4.17 throughout Ω. We assume constant polarization in each element of a triangulated mesh. We then use the polarization density field to calculate the electric field with the first part of Equation 4.25. The far field contribution thus evolves into calculating the jump in polarization, $[\![\boldsymbol{p}_2 - \boldsymbol{p}_1]\!] = \sigma$, between elements and the divergence on all boundary terms, $\boldsymbol{p} \cdot \boldsymbol{n}$. The exterior boundaries are simply controlled with input options of a free surface boundary, a charge-neutralized (infinite domain) boundary, or a specified charge density on the boundary. The contribution to the electric field from the jump in polarization terms and the exterior boundaries are solved using Equation 4.25 with a basic adaptive numerical integration scheme. The interior boundary between the approximated and the exact region, however, requires additional work.

In Section 4.3.5, we took the full summation of shells of unit cells around the atom of interest, essentially in a spherical manner. However, implementation of this spherical summation of atoms is not truly spherical when interfacing with Cartesian based unit cells. The boundary of the full atomistic region approximates a sphere, but is not exact. As the number of shells included in the full atomistic region is increased, the boundary approximation becomes better. For the range of shells that we are interested in, however, this approximation is still not good enough and the additional numerical error is large. In principle, this issue shouldn't exist, because the far field terms would approximate the correct boundary in conjunction with the exact region. Implementation proved too challenging to eliminate the excess numerical error, though. Instead we use trapezoidal shells of unit cells, which are much simpler to implement and do not have the additional numerical error. The

additional numerical error does not exist, because we precisely match the shape of the interior boundary in the far field region with the exact shell region.

The far field approximation for the interior boundary amounts to finding the intersection of a trapezoidal box with a triangulated mesh of potentially rapidly changing element size. A $\boldsymbol{p}\cdot\boldsymbol{n}$ contribution to the electric field then occurs on this intersection, where the polarization comes from the intersected element. We solve this intersection for all required field calculations with the use of CGAL[1], a computational geometry library. The contribution to the electric field is then computed using the integral in Equation 4.25 with a basic adaptive numerical integration scheme. The CGAL library unfortunately introduces several additional library dependencies into the code, but gives the advantage of greatly speeding up the calculation of the trapezoidal box versus triangulated mesh intersections. The full exact region geometry, does not match our original derivation, but we are including more unit cells in this region and less in the approximated region. Thus, the only consequence is that our error bound is higher than necessary.

The final step is to calculate the contribution to the electric field from external loadings. These loading can come in the form of an applied field on the body, a set of point charges near a surface, or a vacancy/void in the body. In the case of an applied field the proper terms are directly added, while the standard kernel is used to add point charge interactions to atoms in Ω. The void/vacancy case is not really an external loading, but is a defect which is natively simulated in the fully resolved portion of the mesh. Because this defect is in the exact summation region, no changes are required, the atom or atoms in question are simply not included in the summation.

We note that the above steps are done for every representative atom in Ω. If the electric field is needed at an atom, $\boldsymbol{x}^{\beta}$, that it is not a representative atom,

the electric field is interpolated at that location using shape functions. We assume that the interpolation of the electric field is valid and expect this assumption to be acceptable. We note that at any locations where the electric field is needed, the deformation field and hence the electric field will be slowly varying. With the electric field calculated , the base QC code requests the electric field at all required atoms and calculates the force by multiplying by the charge on the atom. This force is then added in the relevant places of the base QC code to the short-range forces from the other portion of a given interatomic potential, see Equation 4.8. The total resulting forces are then minimized to less than a given tolerance level with a conjugate-gradient algorithm.

All electrostatic calculation in the code are implemented with threading for high performance computing. We use a queue structure for each thread to grab additional chunks of work. There are multiple potential optimizations in terms of work chunk size, the number of threads, and the underlying data structures sizes. The optimal parameterization will depend on material properties, system geometry, and computational hardware, among other factors.

4.5 Results

We now present convergence results for our electrostatic summation method. All results are for a single crystal of wurtzite GaN. The wurtzite crystal structure has 4 atoms per unit cell, 2 Ga and 2 N atoms. We assume a crystal structure parameterization from a GaN core-shell potential [83]. GaN is a III-IV type semiconductor with polarization in the 0001 direction [77]. The effective charges are +2 for Ga, -2.5 for the N (electron) shell, and 0.5 for the N core. All of the following results assume charge neutralized boundary conditions, thus the size of the simulation does not matter, only the size of the exact summation region.

We start by computing the formal error bound from Equation 4.26. The C_2 constant is calculated from the GaN wurtzite structure. We calculate the total error in the electric field at a single evaluation point assuming an infinite surrounding crystal. The total error converges in Figure 4.4 to a singular value as expected from the convergence properties of Equation 4.26. We also calculate the error bound if

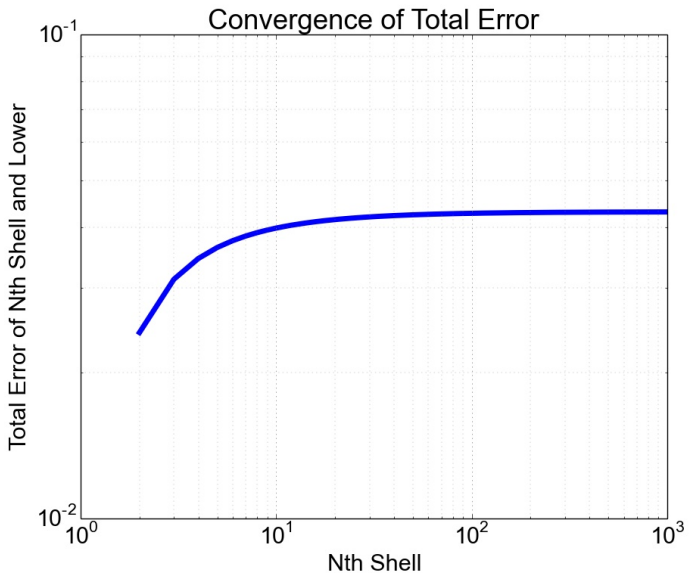


Figure 4.4: Convergence of total possible error in electric field from error bound in Equation 4.26 for an infinite crystal. Each successive shell adds less total error as expected because of the increased distance from evaluation point.

a calculation is performed with the exact atomistic region the size of N shells of unit cells in Figure 4.5. Hence, if $1e^{-3}$ is an acceptable error bound on the electric field, around 13 shells of unit cells surrounding the evaluation point need to be exactly summed. The contribution to the electric field from the rest of Ω can use the approximated method.

We now calculate the error in the electric field from the actual implementation in the QC code. GaN in the wurtzite configuration only has polarization in the 0001-direction, so the interior boundary with the exact atomistic region will only have

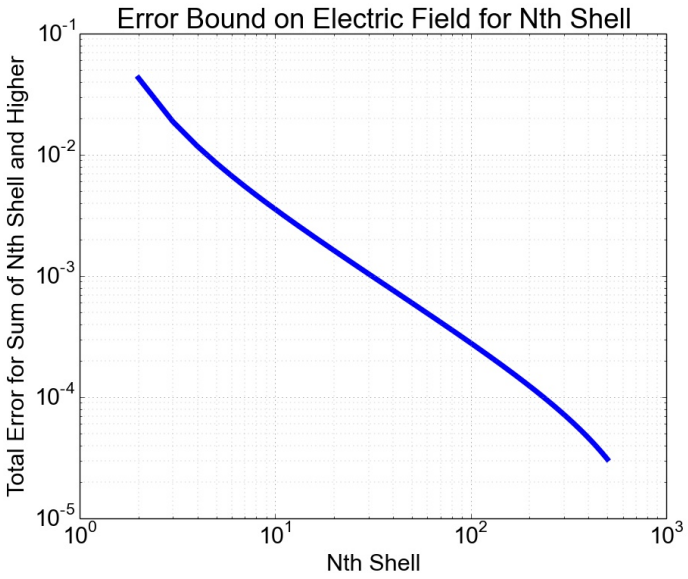


Figure 4.5: Error bound for electric field with an exact atomistic summation performed with N unit cells.

a charge distribution on the 0001 faces of the trapezoidal shell. Figure 4.6 shows the charge density from the interior boundary of the exact atomistic region and the approximated region centered about an evaluation point $\boldsymbol{x}$. Figure 4.7 shows the contribution to the electric field in the 0001-direction from the same interior boundary. Figure 4.8 and Figure 4.9 are also provided to spatially show the contribution to the electric field from the far field region with different levels of integration. Figure 4.10 shows the convergence of the electric field calculations for a single evaluation point. The three line plots show the different levels of adaptive quadrature used to solve Equation 4.25. The resulting convergence is well below the error bound from Figure 4.5 and decreases as expected. We also show the convergence of the exact shell region. It stands to reason that if the far field contributions converge to a value that the exact shell region must as well. This convergence is shown in Figure 4.11 and is very similar as expected to the far field region convergence.

4.6 Discussion

We have developed a method for calculating electrostatic interactions without assuming periodic boundary conditions. Our method is a combination of FMM and the RF method. The RF method assumes a homogeneous domain outside of an exactly computed region. We do essentially the same thing, except we do not assume a homogeneous domain and instead allow the body to vary accordingly with the external loadings. The far field terms are calculated using only the dipole moment, which is essentially a simple form of FMM. The method has been implemented in a high performance computing framework and coupled with an existing QC implementation. Currently, our electrostatic method has only been implemented with the one QC code. However, our electrostatic method is compatible with all QC methods and can be implemented in other methods outside of the QC specific field. A variety of electrostatic and mechanical boundary conditions can be applied to a system. Additionally, the error in the electrostatic method can be controlled by the size of the exact atomistic region surrounding a point of evaluation. We showed the resulting error both analytically and numerically. The numerical error is below the analytical error bound as required.

This method for performing electrostatic calculations provides a high degree of control to a user. Users need to weigh the computational cost, numerical error, method error, problem size, error tolerance, and computational hardware when running simulations. A number of scenarios that a user might encounter are highlighted below.

- $\uparrow$ exact atomistic region, $\downarrow$ method error, $\uparrow$ computational expense
- $\uparrow$ numerical quadrature, $\downarrow$ the numerical error, $\uparrow$ computational expense
- $\uparrow$ defect size/effective range, $\uparrow$ problem size, small $\uparrow$ method error, $\uparrow$ computa-

tional expense

A number of other scenarios exist, but the end result is that a user has to make the decision for a variety of input parameters depending on the specific problem of interest. We are currently using the method to apply various types of loadings on an ionic solid and are investigating the computational scaling of the method.

Acknowledgements

This work used the Extreme Science and Engineering Discovery Environment (XSEDE), which is supported by National Science Foundation grant number TG-DMR120046. Specifically, it used the Blacklight system at the Pittsburgh Supercomputing Center (PSC). Jason Marshall would like to thank the John and Claire Bertucci PhD Fellowship for support in conducting this work. Jason Marshall would also like to thank ORAU, ORISE, and ARL for financial support, hospitality, and computational resources during his summer research internships at the lab.

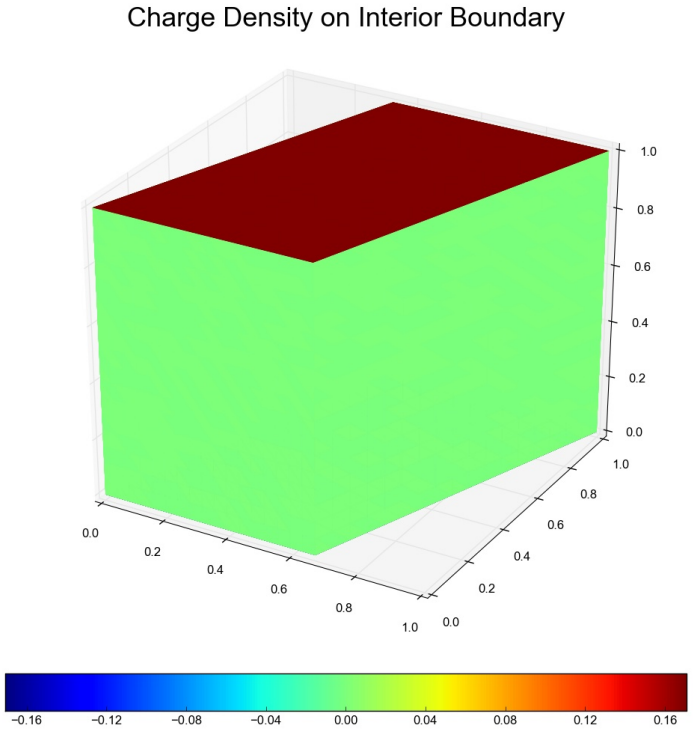


Figure 4.6: Charge density on top 0001-plane of interior trapezoidal boundary between the exact atomistic region and the approximated region. The size of the exact atomistic region is 8 shells of trapezoidal unit cells.

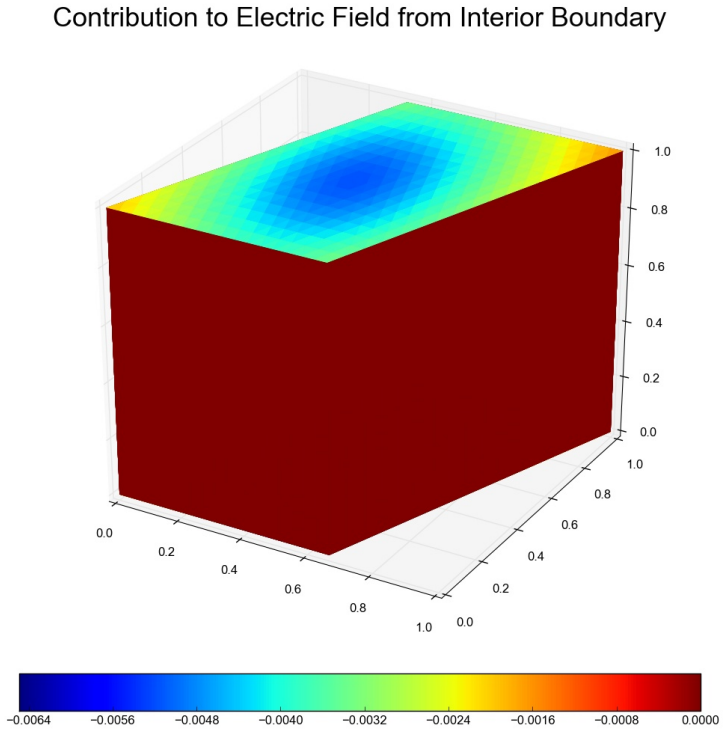


Figure 4.7: Contribution to electric field in 0001-direction from top 0001-plane of interior trapezoidal boundary between the exact atomistic region and the approximated region. The size of the exact atomistic region is 8 shells of trapezoidal unit cells and the integration level is 1.

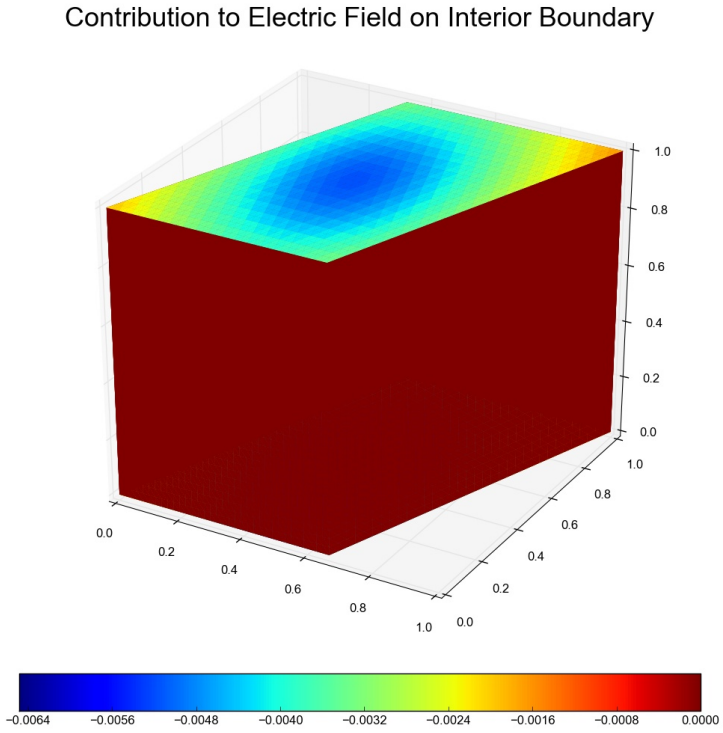


Figure 4.8: Contribution to electric field in 0001-direction from top 0001-plane of interior trapezoidal boundary between the exact atomistic region and the approximated region. The size of the exact atomistic region is 8 shells of trapezoidal unit cells and the integration level is 2.

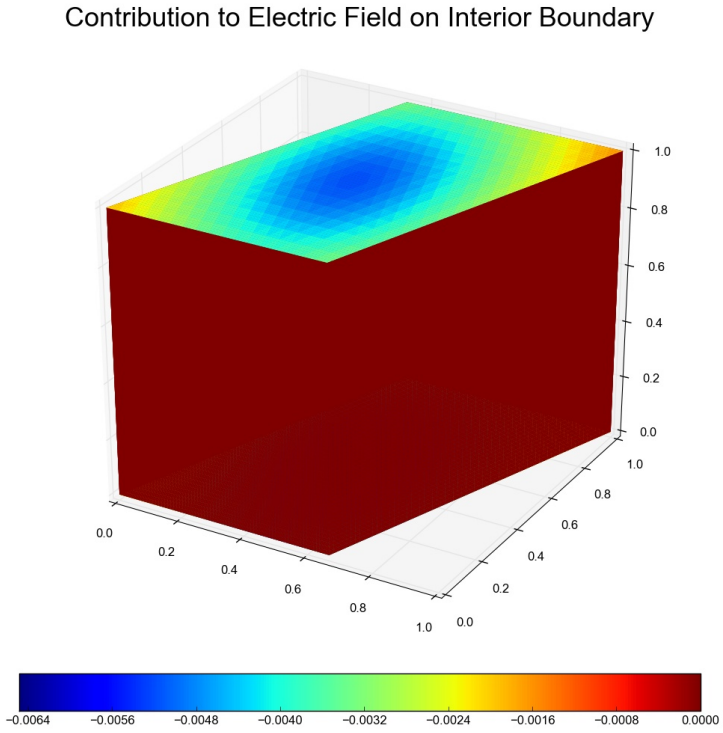


Figure 4.9: Contribution to electric field in 0001-direction from top 0001-plane of interior trapezoidal boundary between the exact atomistic region and the approximated region. The size of the exact atomistic region is 8 shells of trapezoidal unit cells and the integration level is 3.

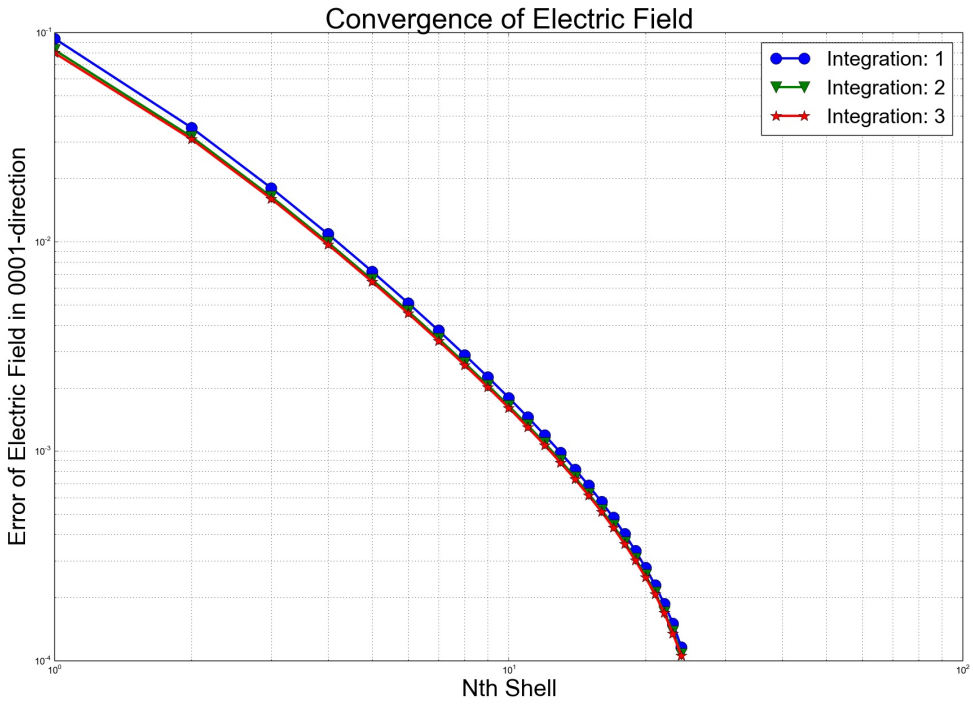


Figure 4.10: Numerical convergence of electric field contribution in 0001-direction from far field region using QC code with an infinite single crystal of wurtzite GaN. Integration notation denotes an increased used of numerical quadrature points used in solving the contribution from field terms.

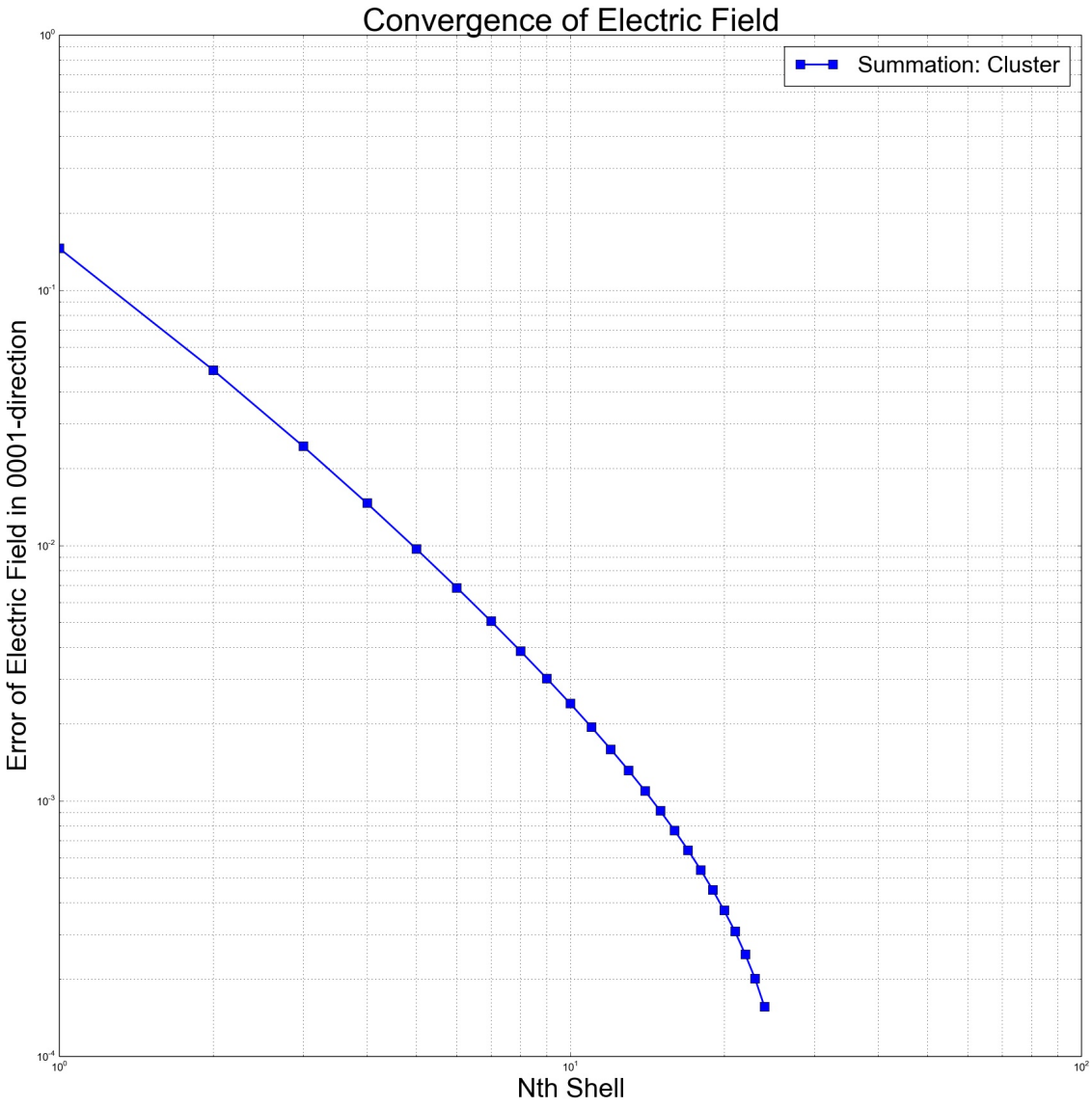


Figure 4.11: Numerical convergence of electric field contribution in 0001-direction from exact shell region using QC code with an infinite single crystal of wurtzite GaN.

5

Conclusions and Discussion

Our focus in this thesis was to extend multiscale methods, specifically the QC method to long-range electrostatic interactions without assuming periodicity in ionic solids. We achieved this in Chapter 2 by using polarization as a multiscale linking quantity between atomistic and continuum scale electrical quantities. Our coarse-graining strategy relies on ideas developed by [35] and others that followed them [63, 80, 59]. The method that we have presented enables QC and other multiscale methods to go beyond purely short-range interactions, that are characteristic of many structural materials, to functional and electronic materials of interest today. We used the method to investigate some electromechanical properties of an ionic solid. Additionally, we discuss the importance of boundary conditions and the details of calculating the polarization.

In Chapter 3 we extend a non-local cluster force QC method originally developed by [40] to multiple lattices. We did this by treating the problem as the union of many simple lattice problems, some of the work follows unpublished results from [42]. We test and verify the implementation in a high performance computing code. Results

from the relaxation of nanovoids from a vacancy to 1nm are presented. These voids are also relaxed subject to various increments of volumetric expansion. We show the centrosymmetry parameter changing between the relaxed initial configuration and the relaxed configuration subjected to volumetrically expanded boundary conditions.

In Chapter 4 we extend the results from Chapter 3 to ionic solids. We add electrostatic interactions by calculating the full charge-charge interaction summation for atoms that are close to the evaluation point. Farther away, we develop and use a method following ideas from the FMM [28, 7, 14]. Essentially, we include interactions from the approximated region with just the first term (dipole) from the multipole expansion. All higher order moments are treated as a bound on the maximum error in the approximated region. We then calculate the error bound both analytically and numerically for GaN and compare the results.

In the Appendices, we write a manual for using the simulation code from Chapters 3 and 4. We are continuing to use the code to investigate interesting physical phenomenon in a variety of materials and hope that future users of the code find it useful. This thesis also motivates future work including, tighter error bound derivations, computational scaling tests, and inclusion of higher order moments in the approximated region to reduce the size of the exact region.

Bibliography

[1] "CGAL, Computational Geometry Algorithms Library," http://www.cgal.org.

[2] *Appendix F: Mathematical Aspects of Ewald Summation.* John Wiley & Sons, Inc., 2008. [Online]. Available: http://dx.doi.org/10.1002/9780470164112.app6.

[3] C. H. Ahn, K. M. Rabe, and J.-M. Triscone, "Ferroelectricity at the nanoscale: Local polarization in oxide thin films and heterostructures," *Science*, vol. 303, no. 5657, pp. 488–491, 2004. [Online]. Available: http://www.sciencemag.org/content/303/5657/488.abstract.

[4] G. Allaire, "Homogenization and two-scale convergence," *SIAM Journal on Mathematical Analysis*, vol. 23, no. 6, pp. 1482–1518, 1992.

[5] M. I. Baskes, "Modified embedded-atom potentials for cubic materials and impurities," *Phys. Rev. B*, vol. 46, pp. 2727–2742, Aug 1992. [Online]. Available: http://link.aps.org/doi/10.1103/PhysRevB.46.2727.

[6] S. Bauer, G. Mathias, and P. Tavan, "Electrostatics of proteins in dielectric solvent continua. i. an accurate and efficient reaction field description," *The Journal of Chemical Physics*, vol. 140, no. 10, pp. –, 2014. [Online]. Available: http://scitation.aip.org/content/aip/journal/jcp/140/10/10.1063/1.4867280.

[7] R. Beatson and L. Greengard, "A short course on fast multipole methods," *Wavelets, multilevel methods and elliptic PDEs*, pp. 1–37, 1997.

[8] C. A. Becker, "Atomistic simulations for engineering: Potentials and challenges," in *Tools, Models, Databases and Simulation Tools Developed and Needed to Realize the Vision of ICME*, ser. ASM, 2011.

[9] K. Bhattacharya, *Microstructure and Martensite: Why it Forms and how it Gives Rise to the Shape-memory Effect*. Oxford University Press, 2003, vol. 2.

[10] X. Blanc, C. Le Bris, and P.-L. Lions, "From Molecular Models to Continuum Mechanics," *Archive for Rational Mechanics and Analysis*, vol. 164, no. 4, pp. 341–381, 2002.

[11] P. Bogusl/awski, E. L. Briggs, and J. Bernholc, "Native defects in gallium nitride," *Phys. Rev. B*, vol. 51, pp. 17 255–17 258, Jun 1995. [Online]. Available: http://link.aps.org/doi/10.1103/PhysRevB.51.17255.

[12] E. Cancès and V. Ehrlacher, "Local defects are always neutral in the Thomas–Fermi–von Weiszäcker theory of crystals," *Archive for rational mechanics and analysis*, vol. 202, no. 3, pp. 933–973, 2011.

[13] P. S. Center. (2014, Nov.) Computing resources - blacklight. [Online]. Available: http://www.psc.edu/index.php/computing-resources/blacklight#hardware.

[14] H. Cheng, L. Greengard, and V. Rokhlin, "A fast adaptive multipole algorithm in three dimensions," *Journal of Computational Physics*, vol. 155, no. 2, pp. 468 – 498, 1999. [Online]. Available: http://www.sciencedirect.com/science/article/pii/S0021999199963556.

[15] H. Childs, E. Brugger, B. Whitlock, J. Meredith, S. Ahern, D. Pugmire, K. Biagas, M. Miller, C. Harrison, G. H. Weber, H. Krishnan, T. Fogal, A. Sanderson, C. Garth, E. W. Bethel, D. Camp, O. Rübel, M. Durant, J. M. Favre, and P. Navrátil, "VisIt: An End-User Tool For Visualizing and Analyzing Very Large Data," in *High Performance Visualization–Enabling Extreme-Scale Scientific Insight*, Oct 2012, pp. 357–372.

[16] M. S. Daw and M. I. Baskes, "Embedded-atom method: derivation and application to impurities, surfaces, and other defects in metals," *Phys. Rev. B*, vol. 29, no. 17, pp. 6443–6453, 1984.

[17] M. S. Daw, S. M. Foiles, and M. I. Baskes, "The embedded-atom method: a review of theory and applications," *Materials Science Reports*, vol. 9, no. 78, pp. 251 – 310, 1993. [Online]. Available: http://www.sciencedirect.com/science/article/pii/092023079390001U.

[18] A. Dorfmann and R. Ogden, "Nonlinear electroelasticity," *Acta Mechanica*, vol. 174, no. 3-4, pp. 167–183, 2005.

[19] B. Eidel and A. Stukowski, "A variational formulation of the quasicontinuum method based on energy sampling in clusters," *Journal of the Mechanics and Physics of Solids*, vol. 57, no. 1, pp. 87–108, 2009. [Online]. Available: http://www.sciencedirect.com/science/article/pii/S0022509608001683.

[20] J. Ericksen, "Nilpotent energies in liquid crystal theory," *Archive for Rational Mechanics and Analysis*, vol. 10, no. 1, pp. 189–196, 1962.

[21] P. P. Ewald, "Die berechnung optischer und elektrostatischer gitterpotentiale," *Annalen der Physik*, vol. 369, no. 3, pp. 253–287, 1921.

[22] C. J. Fennell and J. D. Gezelter, "Is the ewald summation still necessary? pairwise alternatives to the accepted standard for long-range electrostatics," *The Journal of Chemical Physics*, vol. 124, no. 23, pp. –, 2006. [Online]. Available: http://scitation.aip.org/content/aip/journal/jcp/124/23/10.1063/1.2206581.

[23] D. Frenkel and B. Smit, *Understanding molecular simulation: from algorithms to applications*. Academic press, 2001, vol. 1.

[24] G. Friesecke and R. D. James, "A scheme for the passage from atomic to continuum theory for thin films, nanotubes and nanorods," *Journal of the Mechanics and Physics of Solids*, vol. 48, no. 6, pp. 1519–1540, 2000.

[25] V. Gavini, K. Bhattacharya, and M. Ortiz, "Quasi-continuum orbital-free density-functional theory: A route to multi-million atom non-periodic DFT calculation," *Journal of the Mechanics and Physics of Solids*, vol. 55, no. 4, pp. 697–718, 2007.

[26] E. Gibney, "Nobel for blue led that revolutionized lighting," *Nature*, vol. 514, pp. 152–153, 2014.

[27] M. K. Gilson, M. E. Davis, B. A. Luty, and J. A. McCammon, "Computation of electrostatic forces on solvated molecules using the poisson-boltzmann equation," *The Journal of Physical Chemistry*, vol. 97, no. 14, pp. 3591–3600, 1993.

[28] L. Greengard and V. Rokhlin, "A fast algorithm for particle simulations," *Journal of computational physics*, vol. 73, no. 2, pp. 325–348, 1987.

[29] M. Griebel, S. Knapek, and G. Zumbusch, *Numerical simulation in molecular dynamics*. Springer Berlin, 2007.

[30] M. Gunzburger and Y. Zhang, "A quadrature-rule type approximation to the quasi-continuum method," *Multiscale Model. Simul.*, vol. 8, no. 2, pp. 571–590, 2010.

[31] F. E. Hildebrand and R. Abeyaratne, "An atomistic investigation of the kinetics of detwinning," *Journal of the Mechanics and Physics of Solids*, vol. 56, no. 4, pp. 1296–1319, 2008. [Online]. Available: http://www.sciencedirect.com/science/article/B6TXB-4PR3GKV-1/2/d22748f49a45ca8ac53106c132a5ac58.

[32] D. Hofstetter, S.-S. Schad, H. Wu, W. J. Schaff, and L. F. Eastman, "Gan/aln-based quantum-well infrared photodetector for 1.55 μm," *Applied Physics Letters*, vol. 83, no. 3, pp. 572–574, 2003. [Online]. Available: http://scitation.aip.org/content/aip/journal/apl/83/3/10.1063/1.1594265.

[33] Y. Huang, X. Duan, Y. Cui, and C. M. Lieber, "Gallium nitride nanowire nanodevices," *Nano Letters*, vol. 2, no. 2, pp. 101–104, 2002. [Online]. Available: http://dx.doi.org/10.1021/nl015667d.

[34] M. Iyer and V. Gavini, "A field theoretical approach to the quasi-continuum method," *J. Mech. Phys. Solids*, vol. 59, no. 8, pp. 1506–1535, 2011.

[35] R. D. James and S. Müller, "Internal variables and fine-scale oscillations in micromagnetics," *Continuum Mechanics and Thermodynamics*, vol. 6, pp. 291–336, 1994, 10.1007/BF01140633. [Online]. Available: http://dx.doi.org/10.1007/BF01140633.

[36] Y.-R. Jeng, P.-C. Tsai, and T.-H. Fang, "Molecular dynamics investigation of the mechanical properties of gallium nitride nanotubes under tension and fatigue," *Nanotechnology*, vol. 15, no. 12, p. 1737, 2004. [Online]. Available: http://stacks.iop.org/0957-4484/15/i=12/a=006.

[37] V. Kharton, F. Marques, and A. Atkinson, "Transport properties of solid oxide electrolyte ceramics: a brief review," *Solid State Ionics*, vol. 174, no. 1, pp. 135–149, 2004.

[38] C. Kittel and P. McEuen, *Introduction to solid state physics*. Wiley New York, 1996, vol. 7.

[39] J. Klimeš and A. Michaelides, "Perspective: Advances and challenges in treating van der Waals dispersion forces in density functional theory," *The Journal of Chemical Physics*, vol. 137, p. 120901, 2012.

[40] J. Knap and M. Ortiz, "An analysis of the quasicontinuum method," *Journal of the Mechanics and Physics of Solids*, vol. 49, no. 9, pp. 1899–1923, 2001.

[41] R. V. Kohn and S. P. Shipman, "Magnetism and homogenization of microresonators," *Multiscale Modeling & Simulation*, vol. 7, no. 1, pp. 62–92, 2008.

[42] O. Kowalewski, "Theory of complex lattice quasicontinuum and its application to ferroelectrics," Ph.D. dissertation, California Institute of Technology, 2005.

[43] Y. Kulkarni, J. Knap, and M. Ortiz, "A variational approach to coarse graining of equilibrium and non-equilibrium atomistic description at finite temperature," *Journal of the Mechanics and Physics of Solids*, vol. 56, no. 4, pp. 1417–1449, 2008.

[44] C. E. Leiserson, R. L. Rivest, C. Stein, and T. H. Cormen, *Introduction to algorithms*. The MIT press, 2001.

[45] M. E. Lines and A. M. Glass, *Principles and Applications of Ferroelectrics and Related Materials*. Oxford University Press, 1977.

[46] M. Luskin and C. Ortner, "An analysis of node-based cluster summation rules in the quasicontinuum method," *SIAM J. Numer. Anal.*, vol. 47, pp. 3070–3086, 2009.

[47] M. Majdoub, P. Sharma, and T. Cagin, "Enhanced size-dependent piezoelectricity and elasticity in nanostructures due to the flexoelectric effect," *Physical Review B*, vol. 77, no. 12, p. 125424, 2008.

[48] J. Marshall and K. Dayal, "Non local multiscale modeling of electrostatic interactions in ionic solids," *In preparation*.

[49] ——, "Atomistic-to-continuum multiscale modeling with long-range electrostatic interactions in ionic solids," *Journal of the Mechanics and Physics of Solids*, vol. 62, no. 0, pp. 137 – 162, 2014, sixtieth anniversary issue in honor of Professor Rodney Hill. [Online]. Available: http://www.sciencedirect.com/science/article/pii/S0022509613002093.

[50] J. Marshall and J. Knap, "Development of a fully non-local quasicontinuum method for simulating atomistic defects in materials with many atomic species," *In preparation*.

[51] R. E. Miller and E. Tadmor, "A unified framework and performance benchmark of fourteen multiscale atomistic/continuum coupling methods," *Modelling and Simulation in Materials Science and Engineering*, vol. 17, no. 5, p. 053001, 2009.

[52] Y. Mishin, M. J. Mehl, and D. A. Papaconstantopoulos, "Embedded-atom potential for b2-nial," *Phys. Rev. B*, vol. 65, 2002.

[53] U. K. Mishra, P. Parikh, Y.-F. Wu *et al.*, "Algan/gan hemts-an overview of device operation and applications," *PROCEEDINGS-IEEE*, vol. 90, no. 6, pp. 1022–1031, 2002.

[54] M. Neumann, "Dipole moment fluctuation formulas in computer simulations of polar systems," *Molecular Physics*, vol. 50, no. 4, pp. 841–858, 1983.

[55] D. Normile, "Physicists change the light bulb," *Science*, vol. 346, no. 6206, pp. 149–150, 2014. [Online]. Available: http://www.sciencemag.org/content/346/6206/149.2.short.

[56] S. R. Phillpot, S. B. Sinnott, and A. Asthagiri, "Atomic-level simulation of ferroelectricity in oxides: Current status and opportunities," *Annu. Rev. Mater. Res.*, vol. 37, pp. 239–270, 2007.

[57] F. A. Ponce and D. P. Bour, "Nitride-based semiconductors for blue and green light-emitting devices," *Nature*, vol. 386, pp. 351 – 359, 1997.

[58] P. Ponte Castañeda and M. Siboni, "A finite-strain constitutive theory for electro-active polymer composites via homogenization," *International Journal of Non-Linear Mechanics*, vol. 47, no. 2, pp. 293–306, 2012.

[59] S. Puri and K. Bhattacharya, "Definition of the Atomic-level Polarization," unpublished.

[60] F. Qian, Y. Li, S. Gradečak, H.-G. Park, Y. Dong, Y. Ding, Z. L. Wang, and C. M. Lieber, "Multi-quantum-well nanowire heterostructures for wavelength-controlled lasers," *Nature materials*, vol. 7, no. 9, pp. 701–706, 2008.

[61] R. Resta and D. Vanderbilt, "Theory of Polarization: A Modern Approach," in *Physics of Ferroelectrics*, ser. Topics in Applied Physics. Springer Berlin / Heidelberg, 2007, vol. 105, pp. 31–68. [Online]. Available: http://dx.doi.org/10.1007/978-3-540-34591-6_2.

[62] P. Rosakis, "Continuum surface energy from a lattice model," *arXiv preprint arXiv:1201.0712*, 2012.

[63] A. Schlömerkemper and B. Schmidt, "Discrete-to-Continuum Limit of Magnetic Forces: Dependence on the Distance Between Bodies," *Archive for rational mechanics and analysis*, vol. 192, no. 3, pp. 589–611, 2009.

[64] J. F. Scott, *Ferroelectric memories*. Springer, 2000, vol. 3.

[65] Y. Shu and K. Bhattacharya, "Domain patterns and macroscopic behaviour of ferroelectric materials," *Philosophical magazine b*, vol. 81, no. 12, pp. 2021–2054, 2001.

[66] E. B. Tadmor, M. Ortiz, and R. Phillips, "Quasicontinuum analysis of defects in solids," *Philosophical Magazine A*, vol. 73, no. 6, pp. 1529–1563, 1996.

[67] E. B. Tadmor, G. S. Smith, N. Bernstein, and E. Kaxiras, "Mixed finite element and atomistic formulation for complex crystals," *Phys. Rev. B*, vol. 59, no. 1, pp. 235–245, Jan 1999.

[68] E. Tadmor and R. Miller, "The theory and implementation of the quasicontinuum method," in *Handbook of Materials Modeling*. Springer, 2005, pp. 663–682.

[69] E. Tadmor, U. Waghmare, G. Smith, and E. Kaxiras, "Polarization switching in PbTiO3: an ab initio finite element simulation," *Acta Materialia*, vol. 50, no. 11, pp. 2989–3002, 2002.

[70] K. Tanabe, "A review of ultrahigh efficiency iii-v semiconductor compound solar cells: Multijunction tandem, lower dimensional, photonic up/down conversion and plasmonic nanometallic structures," *Energies*, vol. 2, no. 3, pp. 504–530, 2009. [Online]. Available: http://www.mdpi.com/1996-1073/2/3/504.

[71] K.-T. Tang, *Mathematical Methods for Engineers and Scientists 2: Vector Analysis, Ordinary Differential Equations and Laplace Transforms*. Springer, 2007, vol. 3.

[72] L. Tian, L. Tevet-Deree, G. DeBotton, and K. Bhattacharya, "Dielectric elastomer composites," *Journal of the Mechanics and Physics of Solids*, vol. 60, no. 1, pp. 181–198, 2012.

[73] I. G. Tironi, R. Sperb, P. E. Smith, and W. F. van Gunsteren, "A generalized reaction field method for molecular dynamics simulations," *The Journal of Chemical Physics*, vol. 102, no. 13, pp. 5451–5459, 1995. [Online]. Available: http://scitation.aip.org/content/aip/journal/jcp/102/13/10.1063/1.469273.

[74] A. Y. Toukmaji and J. A. Board, "Ewald summation techniques in perspective: a survey," *Computer Physics Communications*, vol. 95, no. 2-3, pp. 73–92, 1996. [Online]. Available: http://www.sciencedirect.com/science/article/pii/0010465596000161.

[75] R. A. Toupin, "The elastic dielectric," *J. Rational Mech. Anal*, vol. 5, no. 6, pp. 849–915, 1956.

[76] M. Tuckerman, *Statistical Mechanics: Theory and Molecular Simulations*. Oxford University Press, UK, 2008.

[77] A. F. Wright, "Elastic properties of zinc-blende and wurtzite aln, gan, and inn," *Journal of Applied Physics*, vol. 82, no. 6, pp. 2833–2839, 1997.

[78] S. Xiao and T. Belytschko, "A bridging domain method for coupling continua with molecular dynamics," *Computer Methods in Applied Mechanics and Engineering*, vol. 193, no. 1720, pp. 1645 – 1669, 2004, ¡ce:title¿Multiple Scale Methods for Nanoscale Mechanics and Materials¡/ce:title¿. [Online]. Available: http://www.sciencedirect.com/science/article/pii/S004578250400026X.

[79] Y. Xiao, "The influence of oxygen vacancies on domain patterns in ferroelectric perovskites," Ph.D. dissertation, California Institute of Technology, 2004.

[80] Y. Xiao and K. Bhattacharya, "A continuum theory of deformable, semiconducting ferroelectrics," *Archive for Rational Mechanics and Analysis*, vol. 189, no. 1, pp. 59–95, 2008.

[81] J. Xu, W.-Y. Yin, and J. Mao, "Transient thermal analysis of gan heterojunction transistors (hfets) for high-power applications," *Microwave and Wireless Components Letters, IEEE*, vol. 17, no. 1, pp. 55–57, Jan 2007.

[82] L. Yang and K. Dayal, "Free surface domain nucleation in a ferroelectric under an electrically charged tip," *Journal of Applied Physics*, vol. 111, no. 1, pp. 014 106–014 106, 2012.

[83] P. Zapol, R. Pandey, and J. D. Gale, "An interatomic potential study of the properties of gallium nitride," *Journal of Physics: Condensed Matter*, vol. 9, no. 44, p. 9517, 1997. [Online]. Available: http://stacks.iop.org/0953-8984/9/i=44/a=008.

[84] W. Zhang and K. Bhattacharya, "A computational model of ferroelectric domains. Part I: model formulation and domain switching," *Acta materialia*, vol. 53, no. 1, pp. 185–198, 2005.

Appendix A

Transformation of Unit Cell in a Crystal Lattice to Obtain a Unit Cell with One Face Parallel to a Given Plane

We show in this section that any crystal lattice can be described by a unit cell with one face parallel to a given plane. This is an essential ingredient of our proof that the change in polarization due a change in the lattice unit cell is balanced by a corresponding change in surface charge density.

We first show the following proposition.

Proposition A.0.1. *Consider a crystal described by lattice vectors* $\{\boldsymbol{f}_1, \boldsymbol{f}_2, \boldsymbol{f}_3\}$ *and reciprocal lattice vectors* $\{\boldsymbol{f}^1, \boldsymbol{f}^2, \boldsymbol{f}^3\}$. *Consider a rational plane*[1] *with normal* $\boldsymbol{n}$.

This lattice can also be described by lattice vectors $\{\boldsymbol{g}_1, \boldsymbol{g}_2, \boldsymbol{g}_3\}$, *where* $\boldsymbol{g}_2 \perp \boldsymbol{n}$,

[1] A rational plane has a normal $\boldsymbol{n}$ that can be represented $\boldsymbol{n} = \sum_i n_i \boldsymbol{f}^i$ with n_i integers.

$\boldsymbol{g}_3 = \boldsymbol{f}_3$, *and* $\boldsymbol{g}_1$ *will be shown below to exist.*

Proof. Result 3.1 of [9] states that a crystal described by lattice vectors $\{\boldsymbol{f}_1, \boldsymbol{f}_2, \boldsymbol{f}_3\}$ can equivalently be described by lattice vectors $\boldsymbol{g}_1, \boldsymbol{g}_2, \boldsymbol{g}_3$ if and only if these satisfy $\boldsymbol{g}_i = \sum_j \mu_i^j \boldsymbol{f}_j$ with μ_i^j being a 3×3 matrix of integers with determinant ± 1.

We have $\boldsymbol{g}_3 = \boldsymbol{f}_3$, therefore $\mu_3^1 = \mu_3^2 = 0$ and $\mu_3^3 = 1$. Set $\boldsymbol{g}_2 = M_1 \boldsymbol{f}_1 + M_2 \boldsymbol{f}_2$ with $M_1 = -\frac{n_2}{\gcd(n_2, n_1)}$ and $M_2 = \frac{n1}{\gcd(n_2, n_1)}$. This choice ensures the following: $\boldsymbol{g}_2 \perp \boldsymbol{n}$, M_1 and M_2 are integers, and $\gcd(M_1, M_2) = 1$. It implies that $\mu_2^1 = M_1, \mu_2^2 = M_2, \mu_2^3 = 0$.

The remaining step to complete the proof is to show that we can find $\boldsymbol{g}_1$ which satisfies $\boldsymbol{g}_i = \sum_j \mu_i^j \boldsymbol{f}_j$ where μ_i^j has the restrictions mentioned above. Write $\boldsymbol{g}_1 = N_1 \boldsymbol{f}_1 + N_2 \boldsymbol{f}_2 + N_3 \boldsymbol{f}_3$. Then $\det \mu = 1$ gives us the condition $N_1 M_2 - M_1 N_2 = 1$. The extended Euclidean algorithm provides the existence of integer solutions N_1 and N_2 to this equation [44]. In general, this algorithm provides integer solutions m, n to the equation $am + bn = \gcd(a, b)$ where a, b are given integers. While the algorithm is constructive and ensures existence of solutions, it does not provide explicit forms for the solutions.

Therefore, there exists $\boldsymbol{g}_1 = N_1 \boldsymbol{f}_1 + N_2 \boldsymbol{f}_2 + N_3 \boldsymbol{f}_3$ where N_1, N_2 are obtained from the algorithm above and N_3 can be arbitrary. □

We wish to show that given a crystal described by lattice vectors $\{\boldsymbol{f}_1, \boldsymbol{f}_2, \boldsymbol{f}_3\}$, we can equivalently describe the crystal by lattice vectors $\{\boldsymbol{h}_1, \boldsymbol{h}_2, \boldsymbol{h}_3\}$ with $\boldsymbol{h}_2 \perp \boldsymbol{n}$ and

$\boldsymbol{h}_3 \perp \boldsymbol{n}$. The vector $\boldsymbol{n}$ is the unit normal to a rational plane.

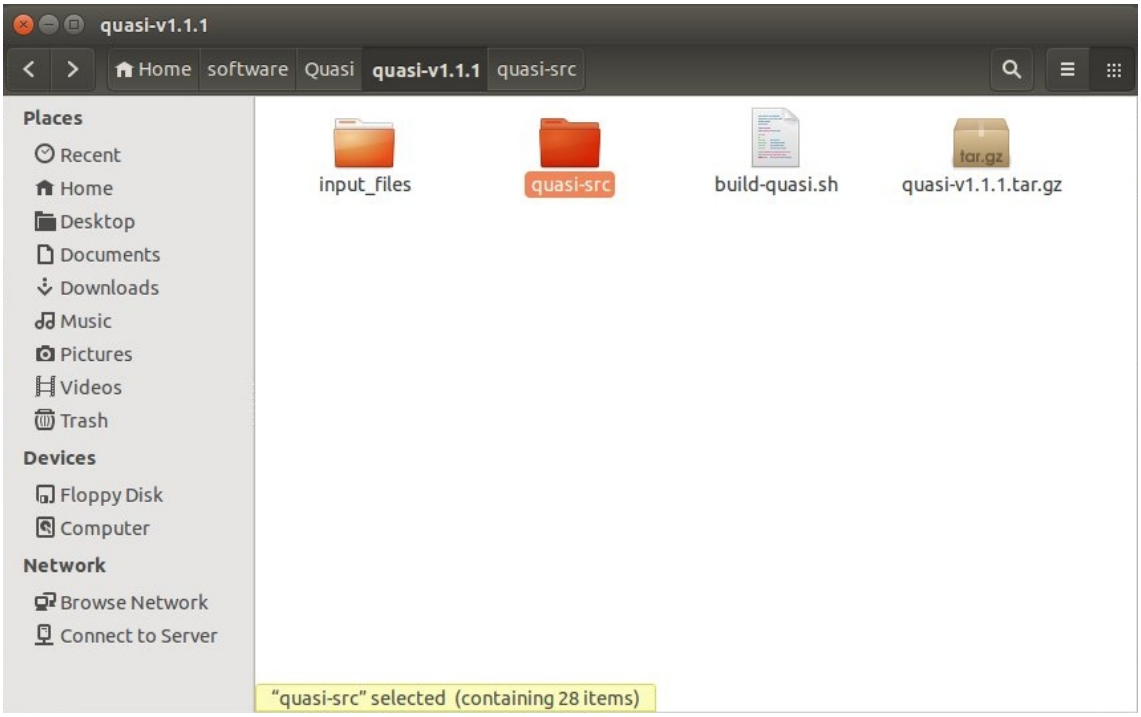
We simply apply the proposition above twice in succession. First, we use the proposition to transform from $\{\boldsymbol{f}_1, \boldsymbol{f}_2, \boldsymbol{f}_3\}$ to $\{\boldsymbol{g}_1, \boldsymbol{g}_2 \perp \boldsymbol{n}, \boldsymbol{g}_3 = \boldsymbol{f}_3\}$. We then use the proposition again to transform from $\{\boldsymbol{g}_1, \boldsymbol{g}_2, \boldsymbol{g}_3\}$ to $\{\boldsymbol{h}_1, \boldsymbol{h}_2 = \boldsymbol{g}_2, \boldsymbol{h}_3 \perp \boldsymbol{n}\}$. Therefore, the final description has $\{\boldsymbol{h}_1, \boldsymbol{h}_2 \perp \boldsymbol{n}, \boldsymbol{h}_3 \perp \boldsymbol{n}\}$. The condition $\det \mu = \pm 1$ ensures linear independence; in fact, it preserves the volume of the unit cell.

Appendix B

How To Run QC Code

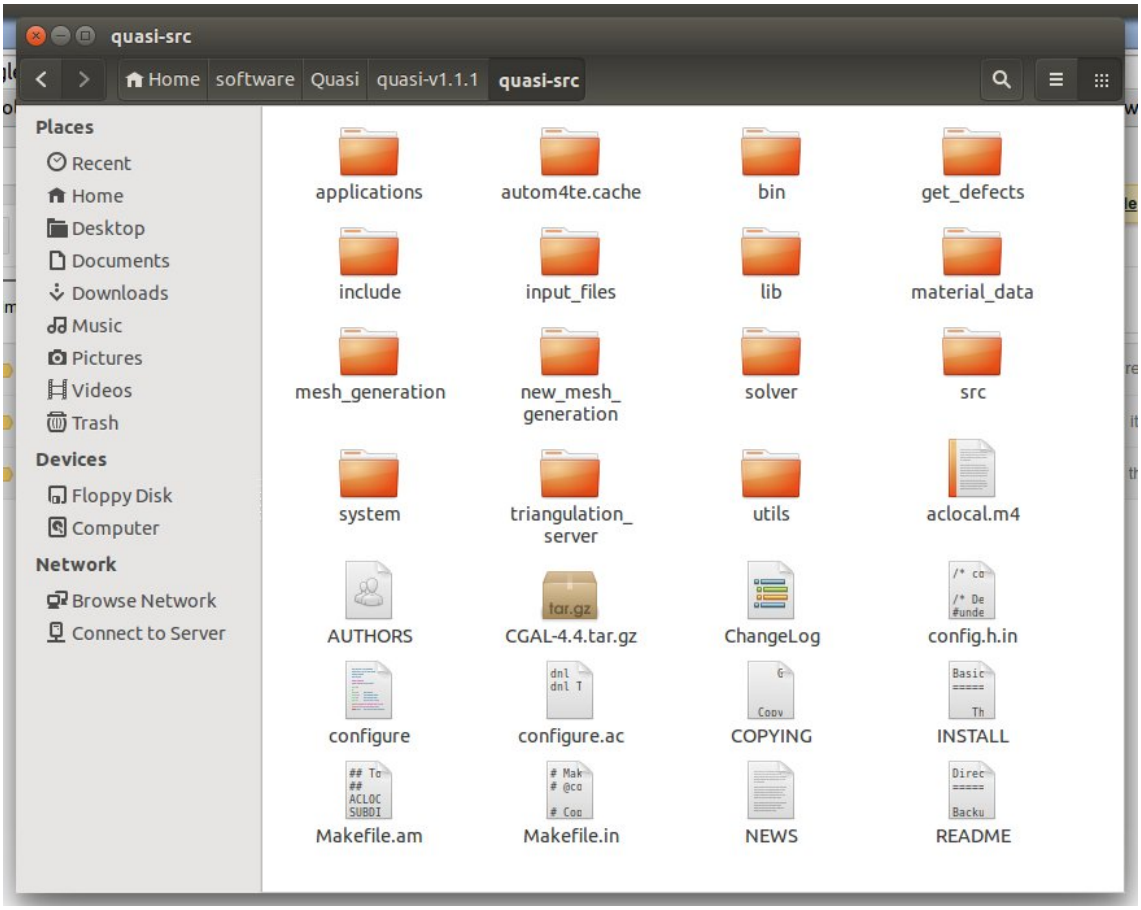
In this appendix, we will provide documentation for running the QC code. We start with the contents of the main folder, B.1. Inside this folder are the main QC source files, a directory of input files with inputs for NiAl and GaN, a build script for the source files, and a .tar.gz of everything for easy movement. All of the files for compilation are in the quasi-src folder, B.2. The src sub folder is a static library of QC functions with all header files in the include folder. The mesh generation folder does exactly as it says and has a variety of mesh generation files. The triangulation_server folder serves as a server for building meshes in the main code. The applications folder contains the main driver folders and files for the QC program. The file CGAL-4.4.tar.gz is the repository for CGAL, directly downloaded from the CGAL website [1]. All other folders contain information and files, but are not needed by a typical user.

The first step of using the QC code is to build it. We have made a script for automatically taking care of the build process for several architectures, B.3 and B.4. In the first part of the script, the user needs to specify the absolute path of the



B.1: Main QC folder.

main quasi folder with quasi_loc. The build directory also needs to be specified with an absolute or a relative path by defining build_directory. Additionally paths for dependencies and libraries need to be included with -I or -L options, if they are not available system wide. This is shown for several architectures including a standard desktop with Ubuntu and Blacklight, an XSEDE resource. If the code is being run on a machine with modules then the modules just need to be added. The code has the following dependencies mpfr, qt (>4.0), gmp, boost(>1.50), cmake (>3.0), and gcc (>4.8) Lastly, the Fortran, C, and C++ compilers that are to be used need to be specified. The second part of the script takes care of the build process for CGAL, the static quasi library, and the main driver code under applications/nano-indentation in the build directoy. Various levels of output can be shown in the terminal or output to files in the relevant build director. The goal of this script file is to ease the build difficulty, though it is not a black box. Users need to be somewhat fluent in linux



B.2: Source file folder.

commands to build the program.

With the code built, several input files need to be generated before simulations can occur. The first step is to generate the mesh files. We have solely been using the indent_fcc file in the main input file folders, B.5, and subsequent code in quasi-src/mesh-generation, though others could be used. This input and code needs to be run once for ever lattice in a given system. We show a typical one for GaN.

- **material:** specifies the lattice type, in the GaN case it would be Ga, N core, or N shell (actual name does not matter, but helps for clarity).
- **atomistic:** denotes a region that is fully resolved a number of shells away. In

```
#!/bin/bash

# set options
quasi_loc="insert src location"
#quasi_loc="/usr/users/8/jmarsha2/quasiSRC-5-28-14"
numThreads="1"
runCommand="./quasi"
build_directory="./quasi-v1.1-build"
# dependencies boost, mpfr, qt4, gmp, cmake
#directory_for_dependencies="-I/usr/local/lib/"
directory_for_dependencies="-I/usr/local/packages/Boost/boost_1_50_0/include"
directory_for_libraries="-L/usr/local/packages/Boost/boost_1_50_0/lib"
#PATH=/data/myscripts:$PATH
#export PATH=$PATH:/usr/local/packages/Boost/boost_1_50_0/lib
#
# gcc compilers defined in shell
#
#Fortran_Compiler="gfortran"
#C_Compiler="gcc"
#CXX_Compiler="g++"

#
# gcc compilers built locally (Desktop)
#
# dependencies boost, mpfr, qt4, gmp, cmake
#Fortran_Compiler="gfortran"
#C_Compiler="gcc"
#CXX_Compiler="g++"
#Fortran_Compiler="/home/jason/software/gcc4.9.0BUILD/bin/x86_64-unknown-linux-gnu-gfortran"
#C_Compiler="/home/jason/software/gcc4.9.0BUILD/bin/x86_64-unknown-linux-gnu-gcc"
#CXX_Compiler="/home/jason/software/gcc4.9.0BUILD/bin/x86_64-unknown-linux-gnu-g++"

#
# gcc compilers built locally (Blacklight)
#
#Fortran_Compiler="/usr/users/8/jmarsha2/gcc4.9.0/bin/x86_64-unknown-linux-gnu-gfortran"
#C_Compiler="/usr/users/8/jmarsha2/gcc4.9.0/bin/x86_64-unknown-linux-gnu-gcc"
#CXX_Compiler="/usr/users/8/jmarsha2/gcc4.9.0/bin/x86_64-unknown-linux-gnu-g++"
#export LD_LIBRARY_PATH=/usr/users/8/jmarsha2/gcc4.9.0/lib64

#
# gcc compilers in module (Blacklight)
#
source /usr/share/modules/init/bash
module load mpfr/3.1.2
module load qt/4.6.3
module load gmp/6.0.0
module load boost/boost_1.50.0
module load cmake/3.0.1
module load gcc/4.8.2
Fortran_Compiler="gfortran"
C_Compiler="gcc"
CXX_Compiler="g++"
```

B.3: Build script, part 1.

our example, we specify a 2x2x2 unit cell radius, so the total atomistic region would be 5x5x5, one unit cell as the base, and two in the plus and minus directions.

```
################################################################################
# SHOULD NOT NEED TO MODIFY BELOW HERE
################################################################################

# get pwd and date
MY_PWD=$(pwd)
dateDay=`date +%Y-%m-%d`

# build CGAL
echo '************************************************'
echo '               Building CGAL 4.4 ...            '
echo '************************************************'
cd $quasi_loc
rm -rf CGAL-4.4
tar -zxf "CGAL-4.4.tar.gz"
cd CGAL-4.4
cgalconfigOUT="cgal-configure-results-$dateDay.txt"
cgalmakeOUT="cgal-make-results-$dateDay.txt"
cmake -DBUILD_SHARED_LIBS=FALSE . #> $cgalconfigOUT 2>&1
make #> $cgalmakeOUT 2>&1
echo '************************************************'
echo '               Building CGAL 4.4 ... Done       '
echo '************************************************'

# build directory
cd $MY_PWD
mkdir $build_directory
cd $build_directory

quasi_configure=$quasi_loc"/configure"
C_FLAGS=""
CXX_FLAGS=""
CPP_FLAGS="-std=c++11 -O2 -frounding-math "$directory_for_dependencies
LD_FLAGS=$directory_for_libraries
configOUT="quasi-configure-results-$dateDay.txt"
makeOUT="quasi-lib-make-results-$dateDay.txt"
makeOUT2="quasi-main-make-results-$dateDay.txt"
outputOUT="results-$dateDay.txt"

# build quasi
echo '************************************************'
echo '               Building Quasi 1.0 ...           '
echo '************************************************'
F77=$Fortran_Compiler CC=$C_Compiler CXX=$CXX_Compiler CFLAGS=$C_FLAGS CXXFLAGS=$CXX_FLAGS CPPFLAGS=
$CPP_FLAGS LDFLAGS=$LD_FLAGS $quasi_configure #> $configOUT 2>&1
make -j $numThreads #> $makeOUT 2>&1
cd applications/nano-indentation
make -j $numThreads #> $makeOUT2 2>&1
echo '************************************************'
echo '               Building Quasi 1.0 ... Done      '
echo '************************************************'
```

B.4: Build script, part 2.

- **full:** specifies the full system size and will be calculated below.
- **indentor:** specifies the location, if the indentor is to be used, if not any values are acceptable.
- **lattice_type:** exactly what you would expect. 0=fcc, 1=bcc, 2=wurtzite, others can be added in the code.

```
# GaN
material          Nc
atomistic         2 2 2
# z is half, if problem_size == 1
full              24 24 12
indentor          0 0
output            GaN_6.inp.gz
lattice_type      2
lattice_constant 3.229234 3.229234 5.162889

#sum of n_levels and atomistic * 2 must equal full atomistic
#and must be divisible by last level size
mesh_levels       2
n_level           0 4
n_level           1 6
#n_level           2 4
#n_level           3 16
#n_level           4 48
#n_level           5 48
#n_level           6 48
#n_level           7 48
#n_level           8 48
# problem size 0 = non-mirrored z plane, 1 = mirrored z plane
problem_size      1
# zplane 0 = normal creation, 1 = only add nodes in z plane
zplane            0
```

B.5: Mesh generation input file.

- **lattice_constant:** relevant lattice parameters.
- **mesh_levels:** is the number of coarse graining that are to occur.
- **n_level:** two parameters must be specified, the level number and the jump in unit cells. The full size must be calculated from these levels and is twice the atomistic plus the sum of the level jumps. Hence $2 \times (2 + 4 + 6) = 24$, so the full size would be 24x24x24.
- **problem_size:** specifies if the full mesh is to be used or only a half mesh. Hence, if only a half size is used (0), the full problem size is now 24x24x12.

Note that the full domain size must be divisible by the last coarse-grain jump size.

- **zplane:** is used to build pillars. The domain is essentially the size of the x and y atomistic region z tall. The full parameter would thus be the atomistic size in the x and y direction and the z direction comes from the number of specified coarse-grain levels.

Additionally, the output parameter can be anything, but must end in .inp.gz. There needs to be one mesh file per lattice with the naming convention of "name".inp.gz for the base lattice and "name"_n.inp.gz, where n starts at 2. These mesh files need to be moved to the main driver folder in the build directory, in this case applications/nano-indentation.

We also need to make the input for the main driver code, B.6, B.7, and B.8.

- **number_threads:** number of pthreads to solve the problem with.
- **periodic:** not used.
- **data_file:** mesh input file, only list the base lattice input file, code will automatically read in all others assuming proper naming.
- **materials_file:** not used.
- **indentor parameters:** self explanatory. Specifics can be found in the indent.c source file.
- **void parameters:** self explanatory. Specific void types can be found in internal_void.c.
- **numLoads:** number of load increments to apply to system.
- **boundaryFlag:** switches between applying the load on all atoms, just the boundaries, or the incremental deformation is turned off.

```
#
# setup input
#
number_threads  1
periodic
data_file       GaN.inp.gz
materials_file  materials.dat

#
# indenter info (0=off,1=on)
#
radius           700
constant         100
displacement     0.0    0.0   -0.1
position         1000000.0 1000000.0 1000000.0
indentEnable     0
#position         s/2    s/2    s/1

#
# void info (0=false,1=true)
#
voidEnable       0
#voidCenter       77.54 44.64 87.2
#voidCenter       697.536 401.76 747.97
voidCenter       348.5 200.9 372.24
#voidCenter       34.3044 34.3044 34.3044
voidNumParams    2
voidParams       8.53 16.0
voidType         V
#voidNumParams    1
#voidParams       2.0
#voidType         C

#
# loading info (flags: -1=off, 0=all atoms, 1=boundaries)
#
numLoads         0
boundaryFlag     -1
F1               0.0000 0.0000 0.0000
F2               0.0000 0.0000 0.0000
F3               0.0000 0.0000 0.0000
# charge number, charge increment, charge location
#charge           0 -1.0 52.8 38.64 430.0
# relax atomistic electro, used for surfaces (0 do not relax, 1 do relax)
relax_electro_atomistic 0
```

B.6: Main driver input file, part 1.

- **F1-F3:** incremental deformation matrix to be applied to the system.
- **charge:** incremental charge to be applied to the system. (charge num, strength,

```
numLattice       6
shift            0 0.0 0.0 0.0 -1
shift            1 1.614617 0.9321995596 2.5814445 -1
shift            2 0.0 0.0 1.990655112 -1
shift            3 1.614617 0.9321995596 4.572099612 -1
shift            4 0.0 0.0 1.987572867 -1
shift            5 1.614617 0.9321995596 4.569017367 -1
potential        GaNCoreShellCorrect 10.0 0
max_num_shells   32

# electrostaticBCS
# 0 - charge neutralized, 1 - free surface, 2 - specify charge density
# value only used for case 2
xBeginElectroBCS 0 0.0
xEndElectroBCS   0 0.0
yBeginElectroBCS 0 0.0
yEndElectroBCS   0 0.0
zBeginElectroBCS 0 0.0
zEndElectroBCS   0 0.0

# remove residual forces
# 0 - do not remove, 1 - remove
# all non atomic atoms
allResidual    1
xBeginResidual 1
xEndResidual   1
yBeginResidual 1
yEndResidual   1
zBeginResidual 1
zEndResidual   1

#
# CG info
#
tolerance        1.0e-2
maxIterations    0
debugLevel       2
lineTolerance    1.0e-6
lineIterations   0
remeshTolerance  10.0
#remeshTolerance  0.002

#
# neighbor list flag if 0 do not save locations, if 1 do save
#
crossNeighListFlag 1

# set eam method (0 = from neighbor lists, 1 = from cluster calculation)
eam_method        0

#
# process restart file for defects (0 off, 1 on)
#
getDefectsFlag   0
defectCenter     45.7392 45.7392 45.7392
defectBox        5.0 5.0 5.0
defectLat        2.8587
```

B.7: Main driver input file, part 2.

```
#
# add node options (flag 0 = use cutoff number, flag = 1 use remesh number)
#
addNodeFlag      1
addNodeRestartNum 0
addNodeCutoff    50
```

B.8: Main driver input file, part 3.

x, y, z).

- **relax_electro_atomistic:** 0 do not relax surface and apply negative dead loads to correct for boundary interactions, 1 do relax surface forces.
- **numLattice:** number of lattices in the unit cell or system.
- **shift:** shift for each lattice in unit cell, last parameter determines is used for core-shell models.
- **potential:** specifies the potential to use and cutoff radius. See ComplexInput.cc, input.c, and PairPotentials.cc for more details and for implementation of new potentials.
- **max_num_shells:** used to index shells of atoms, the larger the number the more required memory. Program will exit if not enough shells allocated.
- **electrostatic bcs:** self explanatory
- **residual forces:** used to remove forces, if the input structure is not at equilibrium.
- **conjugate gradient:** see CGNonLinearSolver.cc.
- **crossNeighListFlag:** switches between different methods for computing neighbor lists. Suggest only using 1 at this time.
- **eam_metho:** switches between different methods for calculating eam densities, suggest only using 0 at this time.

- **get defect parameters:** used for post-processing only, outputs .3D, and .pdb full atomistic files from specified region with centrosymmetry parameter. Used to see dislocation nucleation and surfaces.
- **remesh parameters:** used to specify the largest number of nodes added before moving on to next step or number of times remeshing can occur.

This file must be named quasi.ini. The code can be run in a standard way "./quasi" from the build directory (application/nano-indentation). The results of the code are output into a numbered folder with 2 main file types: the first is a node*.plt.gz file that has deformations and other variable information on the mesh. This file is easily viewed in Visit [15]. The second file type is a restart*.inp.gz, which outputs a configuration that can be restarted from. Additionally, a couple of run time options are available for the code, the most used are -n number_threads and -r restart_file_name.

Lastly, support for this code can be found from Jason Marshall at his email address: jason.p.marshall at gmail.com.

Appendix C

QC Code Computational Scaling

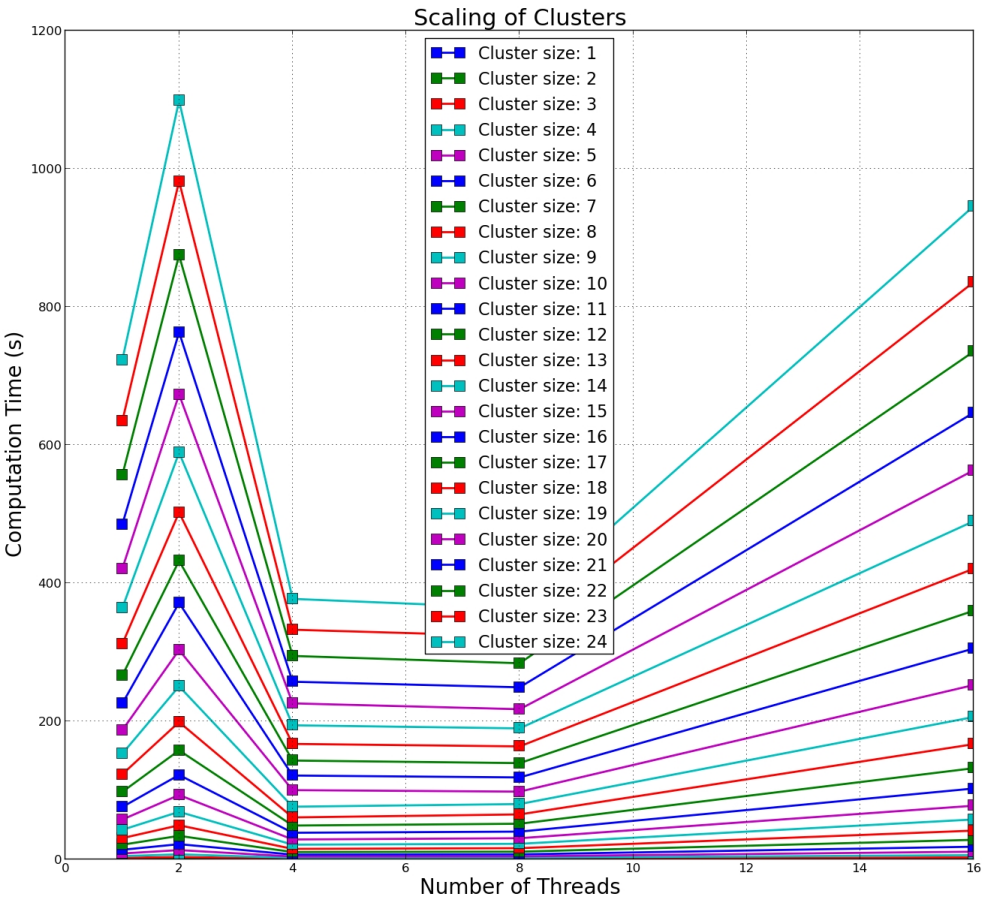
Scaling results for the QC code are presented in this Appendix. All tests were performed on Blacklight a high performance computing resource at the Pittsburgh Supercomputing Center under XSEDE. The specs for Blacklight are quoted directly from the website. "Blacklight is an SGI UV 1000cc-NUMA shared-memory system comprising 256 blades. Each blade holds 2 Intel Xeon X7560 (Nehalem) eight-core processors, for a total of 4096 cores across the whole machine. Each core has a clock rate of 2.27 GHz, supports two hardware threads and can perform 9 Gflops. The sixteen cores on each blade share 128 Gbytes of local memory. Users can run shared memory jobs of up to 16 Tbytes." [13]

We test the scaling results only for the electrostatic algorithms in the code. The first result is for just the exact calculations. These calculations include the time spent to calculate all atoms within a shell region and any atoms in the fully resolved atomistic region, see Figure C.1. The next set of results are just for the far field contributions to the electric field. Each of the three figures show results for different levels of numerical integration. As expected, more integration points increase the

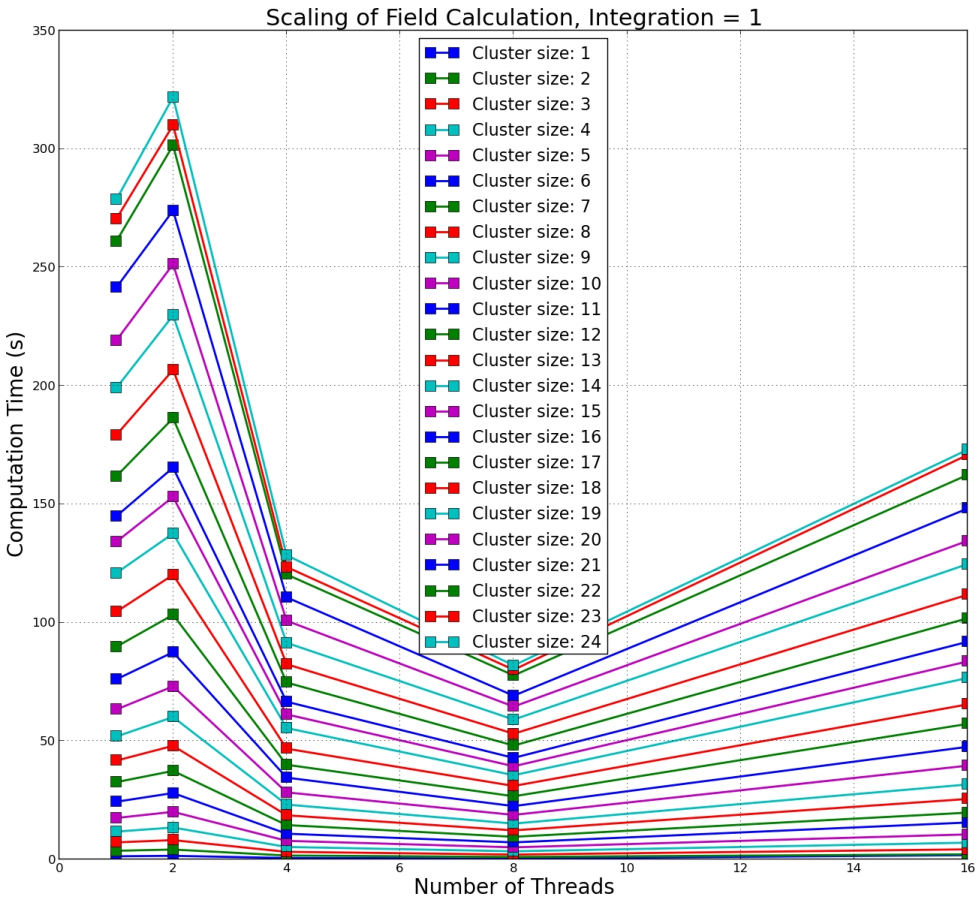
computational time, see Figures C.2, C.3, and C.4.

The results upon initial inspection are not promising. Upon closer inspection, however, there is reason to be optimistic. For small clusters, there is essentially no speed up with any number of threads. This is expected because of the minimal amount of work. As the number of clusters and amount of work is increased, some speedup is noticed with more threads. The uneven speedup can be most likely be attributed to the lack of optimization undertaken in the testing. Thread affinity was not set and is probably playing a large role in the poor scaling results. While Blacklight can be viewed essentially as a single computer, where all memory can be accessed from all processing units, the time taken to reach a memory location is not equal. Even on a single blade, the communication cost between a core on one Nehalem processor pays a time penalty of 1.3 to reach memory on the other processor as compared to no penalty to reach memory on its own processor. Thus, a time penalty is paid if the memory is not localized. The test for scaling did not take advantage of memory locality. Additionally, without setting the thread affinity, the first 2 threads were most likely placed on separate Nehalem cores, which could explain the increase in time when going from 1 thread to 2. Not setting thread affinity also allows threads to move around between different processing units, this migration thrashes the cache and also contributes to the memory access issues.

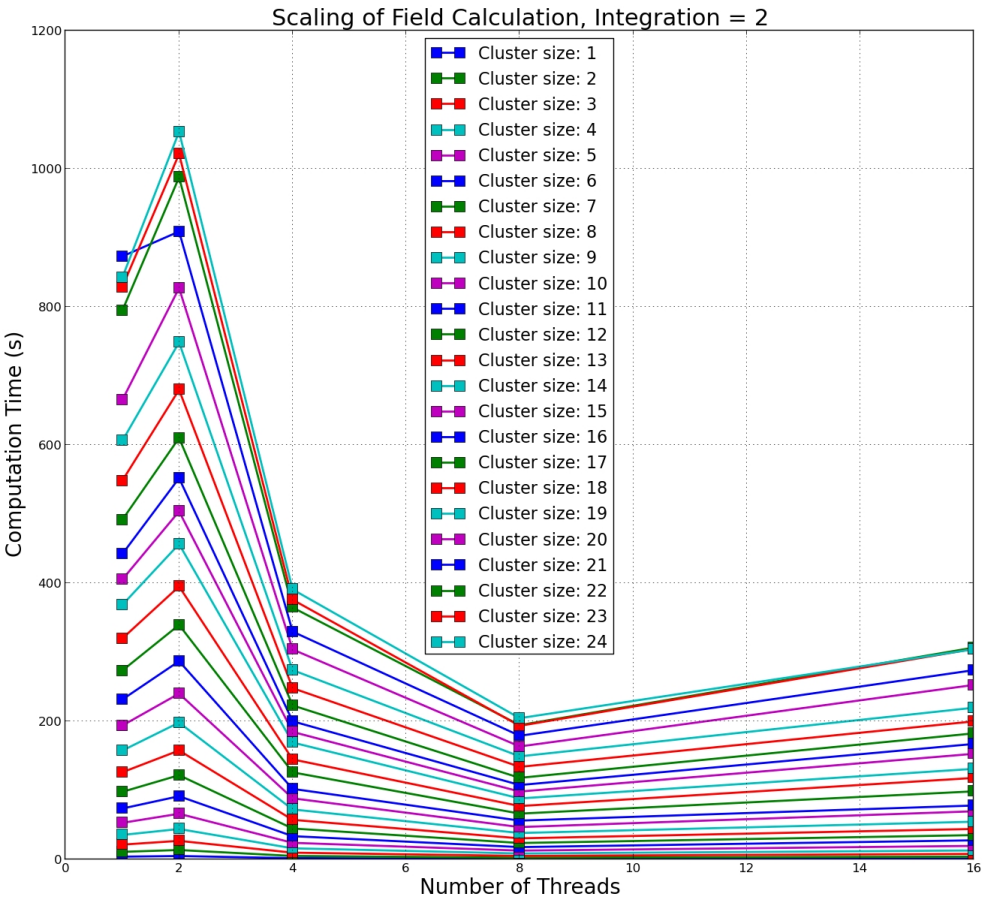
The code implemented has the capability to set thread affinity already built in. Additionally, data locality in the code can be implemented to minimize the memory access times. The ideal optimization of the above factors will be both problem and hardware dependent. Testing is ongoing to determine the optimal configuration for Blacklight and in the future other computational resources.



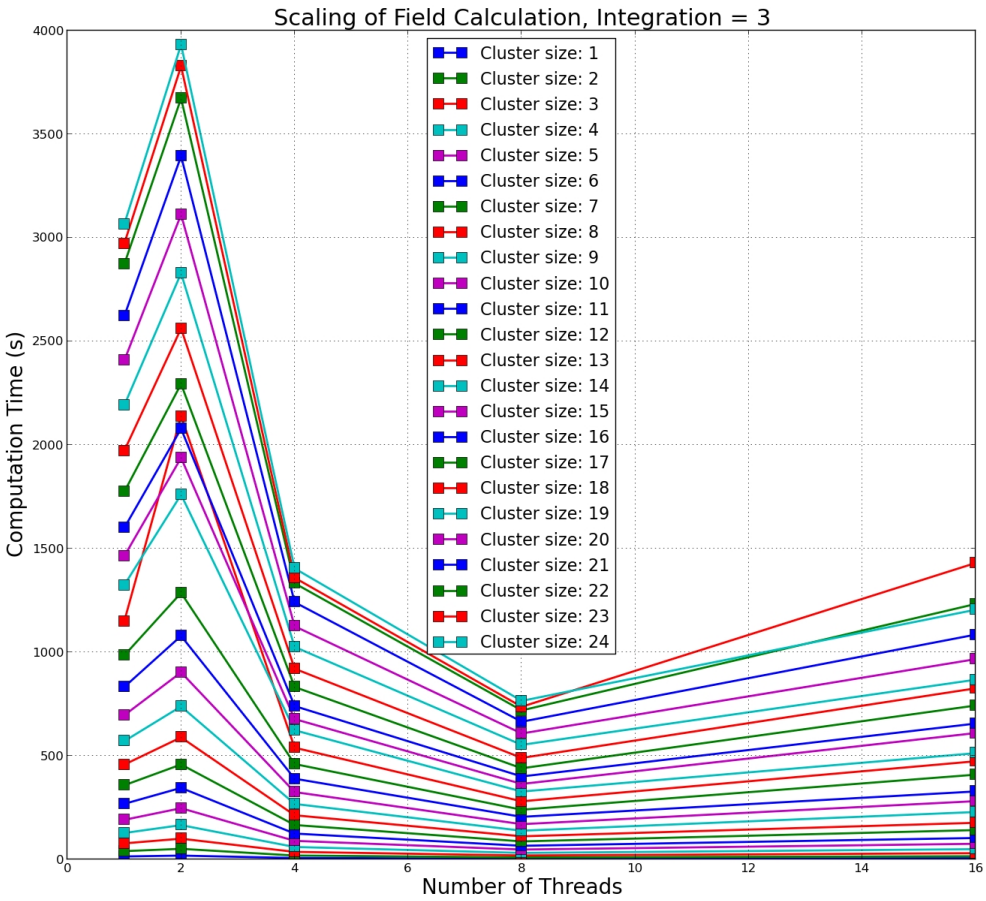
C.1: Scaling results for exact cluster summation.



C.2: Scaling results for far field electric field contribution with a numerical integration level of 1.



C.3: Scaling results for far field electric field contribution with a numerical integration level of 2.



C.4: Scaling results for far field electric field contribution with a numerical integration level of 3.

ELECTROELASTICITY OF POLYMER NETWORKS

NOY COHEN[1], KAUSHIK DAYAL[2], AND GAL DEBOTTON[1,3]

[1]DEPT. OF MECHANICAL ENGINEERING, BEN-GURION UNIVERSITY, BEER-SHEVA 84105, ISRAEL;

[2]CARNEGIE MELLON UNIVERSITY, PITTSBURGH, PENNSYLVANIA 15213, USA;

[3]DEPT. OF BIOMEDICAL ENGINEERING, BEN-GURION UNIVERSITY, BEER-SHEVA 84105, ISRAEL;

ABSTRACT. A multiscale analysis of the electromechanical coupling in elastic dielectric is conducted, starting from the discrete monomer level through the polymer chain and up to the macroscopic level. Three models for the local relations between the molecular dipoles and the electric field that can fit a variety of dipolar monomers are considered. The entropy of the network is accounted for within the framework of statistical mechanics with appropriate kinematic and energetic constraints. At the macroscopic level closed form explicit expressions for the behaviors of amorphous dielectrics and isotropic polymer networks are determined. None of which admits the commonly assumed linear relation between the polarization and the electric field. The analysis reveals the dependence of the macroscopic coupled behavior on three primary microscopic parameters: the model assumed for the local behavior, the intensity of the local dipole, and the length of the chain. We show how these parameters influence the directional distributions of the monomers and the hence the resulting overall response of the network. In particular, the dependences of the polarization and the polarization induced stress on the deformation of the dielectric are illustrated. More surprisingly, we also reveal a dependence of the stress on the electric field which stems from the kinematic constraint imposed on the chains.

1. INTRODUCTION

Electro-active polymers (EAPs) are materials that deform in response to electrostatic excitation. Due to their light weight, flexibility and availability these materials can be used in a wide variety of applications such as artificial muscles (Bar-Cohen, 2001), energy-harvesting devices (McKay et al., 2010), micropumps (Rudykh et al., 2012), and tunable wave guides (Shmuel et al., 2012), among others. The principle of the actuation is based on the attraction between two oppositely charged electrodes attached to the faces of a thin soft elastomer sheet. Due to Poisson's effect, the sheet expands in the transverse direction. Toupin (1956), in his pioneering analysis, found that this electromechanical coupling is characterized by a quadratic dependence on the applied electric field, and this was later verified experimentally (Pelrine et al., 2000b;

Kofod et al., 2003; Wissler and Mazza, 2007). However, EAPs have a low energy-density in comparison with other actuators such as piezoelectrics and shape memory alloys (Bar-Cohen, 2001) and their feasibility is limited due to the high electric fields ($\sim 100\,\mathrm{MV/m}$) required for a meaningful actuation. The latter is a result of the relatively low ratio between the dielectric and the elastic moduli (Pelrine et al., 2000a). Specifically, common flexible polymers have low dielectric moduli while polymers with high dielectric moduli are usually stiff. Nevertheless, a few recent works suggest that this ratio may be improved. Huang et al. (2004) demonstrated experimentally that organic composite EAPs experience more than 8% actuation strain in response to an activation field of $20\,\mathrm{MV/m}$. The experimental work of Stoyanov et al. (2010) showed that the actuation can be dramatically improved by embedding conducting particles in a soft polymer. In parallel, theoretical works dealing with the enhancement of coupling in composites also hint at the possibility of improved actuation with an appropriate adjustment of their microstructure (e.g., deBotton et al., 2007; Xie et al., 2008; Rudykh et al., 2013; Tian et al., 2012; Galipeau and Ponte Castaneda, 2012; Lopez-Pamies, 2014; Spinelli et al., 2015, among others). These findings motivate an in-depth multiscale analysis of the electromechanical coupling in EAPs which is inherent from their microstructure.

We note that the response of polymers to purely mechanical loadings was extensively investigated at all length scales. A *macroscopic level* analysis and models describing the behavior of soft materials undergoing large deformation, such as polymers, were developed by Ogden (1997). The *microscopic level* analysis of Kuhn and Grün (1942) yielded a Langevin based constitutive relation and paved the way to various multiscale models such as the 3-chain model (Wang and Guth, 1952), the tetrahedral model (Flory and Rehner, 1943; Treloar, 1946) and the 8-chain model (Arruda and Boyce, 1993). The use of statistical mechanics in the analysis of mechanical systems was discussed by Su and Purohit (2012), and by Warner and Terentjev (2003) for polymer-based liquid crystal elastomer active materials.

The electric response of dielectrics to electrostatic excitation was examined by Tiersten (1990) and Hutter et al. (2006), among others, macroscopically as well as through their microstructure. Starting with the examination of a single charge under an electric field, the relations between the different macroscopic electric quantities, such as the electric displacement, the electric field and the polarization, and the microscopic quantities, such as the free and bound charge densities and the dipoles were defined and analyzed.

A *macroscopic level* analysis of the coupled electromechanical response of dielectrics began with the work of Toupin (1956). Later on, an invariant-based representation of the constitutive behavior of EAPs was introduced by Dorfmann and Ogden (2005) and extended to anisotropic materials by Bustamante (2009). The possible influence of the deformation and its rate on the electromechanical coupling was investigated by Zhao and Suo (2008); Ask et al. (2012b,a); Jiménez and McMeeking (2013); Gei et al. (2013) and Deng et al. (2014). Initial multiscale *physically motivated* analyses of the electromechanical response were performed by Cohen and deBotton (2014), Cohen and deBotton (2015) and Cohen et al. (2015).

In this work, a multiscale entropy-based analysis of the response of a dielectric to an electromechanical loading is introduced. Employing the dipole models proposed by Stockmayer (1967) and Cohen and deBotton (2015), we start by analyzing both the mechanical and the electrical behavior of the dipolar monomers. Next, in order to determine the configuration of a polymer chain, we maximize its entropy and find the most probable distribution of the dipolar monomers composing it under given chain constraints. An integration over all dipolar monomers distributed according to the obtained conformation yields the entropy of the polymer chain. Lastly, assuming that the response of the polymer and its chains is strictly elastic, we employ the first and the second laws of thermodynamics and integrate over all chains to determine the macroscopic response.

We begin this work with a short theoretical background, followed by a thermodynamical analysis of the response of polymers in accordance with McMeeking et al. (2007); Tian et al. (2012); Cohen and deBotton (2014) and Cohen and deBotton (2015). In section 3 we analyze the microstructure of a polymer chain using statistical considerations through the entropy. Section 4 deals with the behavior of amorphous dielectrics subjected to a purely electrical loading and a comparison with a well-known macroscopic model is made. Next, we consider polymer networks under electro-mechanical loadings, and determine the evolution of the microstructure and the macroscopic response. A few conclusions are gathered in section 6.

2. Theoretical background

Consider the deformation of a dielectric body from a referential configuration to a current one due to an electro-mechanical loading. The body occupies a region $V_0 \subset \mathbb{R}^3$ with a boundary ∂V_0 before the deformation and a region $V \subset \mathbb{R}^3$ with a boundary ∂V at the current configuration. $\mathbf{x_0}$ and $\mathbf{x}$ denote the locations of the material points before and after the deformation, respectively.

The mapping of the material points from the reference to the current configuration is $\mathbf{x} = \boldsymbol{\varphi}(\mathbf{x_0})$ and the corresponding deformation gradient is

$$\mathbf{F} = \nabla_{\mathbf{x_0}} \boldsymbol{\varphi}(\mathbf{x_0}), \tag{1}$$

where $\nabla_{\mathbf{x_0}}$ is the gradient operation with respect to the referential coordinate system. The ratio between the volumes of an infinitesimal element in the current and the reference configurations, $J = \det(\mathbf{F})$, is strictly positive. The velocity of the material points is $\mathbf{v}(\mathbf{x})$ and the spatial velocity gradient is

$$\mathbf{L} = \nabla_{\mathbf{x}} \mathbf{v} = \dot{\mathbf{F}} \mathbf{F}^{-1}, \tag{2}$$

where the gradient $\nabla_{\mathbf{x}}$ is carried out with respect to the current coordinate system.

The body is subjected to an electric field $\mathbf{E}(\mathbf{x})$, satisfying Faraday's law $\nabla_{\mathbf{x}} \times \mathbf{E} = \mathbf{0}$ throughout the entire space. Consequently, a scalar electric potential ϕ can be defined such that $\mathbf{E} = -\nabla_{\mathbf{x}} \phi$. The electric displacement field is

$$\mathbf{D}(\mathbf{x}) = \varepsilon_0 \mathbf{E}(\mathbf{x}) + \mathbf{P}(\mathbf{x}), \tag{3}$$

where ε_0 is the permittivity of vacuum and $\mathbf{P}(\mathbf{x})$ is the polarization, or the electric dipole-density. If a linear relation is assumed between the polarization and the electric field, then $\mathbf{P} = \chi \varepsilon_0 \mathbf{E}$ where χ is the susceptibility. In this case $\mathbf{D} = \varepsilon_0 \varepsilon_r \mathbf{E}$ where $\varepsilon_r = \chi + 1$ is the relative permittivity. We recall that in vacuum $\mathbf{P} = \mathbf{0}$. In ideal dielectrics or in a continuum with no free charges the electric displacement field is governed by the equation

$$\nabla_{\mathbf{x}} \cdot \mathbf{D} = 0. \tag{4}$$

The electrical boundary conditions are given in terms of either the electric potential or the charge per unit area ρ_a, such that $\mathbf{D} \cdot \hat{\mathbf{n}} = -\rho_a$, where $\hat{\mathbf{n}}$ is the outward pointing unit normal to the boundary in the current configuration. Practically, in common EAPs settings, ρ_a is the charge on the electrodes (Carpi et al., 2010). The mechanical boundary conditions are given in terms of the displacement or the mechanical traction $\mathbf{t}$. Due to the presence of the electric field in the surrounding space, on the boundary the *true* or the *current* stress in the body $\boldsymbol{\sigma}$ satisfies the condition $[\boldsymbol{\sigma} - \boldsymbol{\sigma}^v]\,\hat{\mathbf{n}} = \mathbf{t}$, where

$$\boldsymbol{\sigma}^v = \varepsilon_0 \left(\mathbf{E} \otimes \mathbf{E} - \frac{1}{2} (\mathbf{E} \cdot \mathbf{E}) \mathbf{I} \right), \tag{5}$$

is the Maxwell stress in vacuum and $\mathbf{t}$ is the mechanical traction. In the body the stress satisfies the equilibrium equation

$$\nabla_{\mathbf{x}} \cdot \boldsymbol{\sigma} = \mathbf{0}. \tag{6}$$

Following McMeeking et al. (2007), the first law of thermodynamics states that

$$\frac{\mathrm{d}}{\mathrm{d}t}\int_{V_0} H\left(\mathbf{F},\mathbf{E}\right)\mathrm{d}V_0 - \frac{\mathrm{d}}{\mathrm{d}t}\int_{\mathbb{R}^3}\frac{\varepsilon_0}{2}\mathbf{E}\cdot\mathbf{E}\,\mathrm{d}V = \frac{\mathrm{d}W}{\mathrm{d}t} + T\frac{\mathrm{d}}{\mathrm{d}t}\int_{V_0} S\left(\mathbf{F},\mathbf{E}\right)\mathrm{d}V_0, \tag{7}$$

where H and S are the electrical enthalpy-density and the entropy-density functions per unit referential volume, respectively, W is the work of the external electrical and mechanical sources and T is the absolute temperature. We point out that the rate of the electrical enthalpy-density function is proportional to the rate of the internal energy-density function (McMeeking et al., 2007; Cohen and deBotton, 2014) and stems from the application of the electric field, hence it is assumed that the variations of the total electrical enthalpy are negligible, i.e. $\frac{\mathrm{d}}{\mathrm{d}t}\int_{V_0} H\left(\mathbf{F},\mathbf{E}=\mathbf{0}\right)\mathrm{d}V_0 = 0$ (Treloar, 1975). The entropy-density function depends on the internal structure of the dielectric and evolves with the external loading.

The rate of work of the external sources is

$$\frac{\mathrm{d}W}{\mathrm{d}t} = \int_{\partial V}\mathbf{t}\cdot\mathbf{v}\,\mathrm{d}A - \int_{\partial V}\rho_a\frac{\mathrm{d}\phi}{\mathrm{d}t}\,\mathrm{d}A, \tag{8}$$

where we neglect body forces and assume no free charges in the material (Dorfmann and Ogden, 2014). Eq. (8) can be written as (Tian et al., 2012)

$$\frac{\mathrm{d}W}{\mathrm{d}t} = \int_{V}\left(\boldsymbol{\sigma}-\boldsymbol{\sigma}^{v}-\mathbf{E}\otimes\mathbf{P}\right):\mathbf{L}\,\mathrm{d}V + \int_{\mathbb{R}^3\setminus V}\left(\boldsymbol{\sigma}-\boldsymbol{\sigma}^{v}\right):\mathbf{L}\,\mathrm{d}V - \int_{V}\mathbf{P}\cdot\dot{\mathbf{E}}\,\mathrm{d}V - \frac{\mathrm{d}}{\mathrm{d}t}\int_{\mathbb{R}^3}\frac{\varepsilon_0}{2}\mathbf{E}\cdot\mathbf{E}\,\mathrm{d}V. \tag{9}$$

The rate of the electrical enthalpy is given via (Cohen and deBotton, 2014)

$$\frac{\mathrm{d}}{\mathrm{d}t}\int_{V_0} H\left(\mathbf{F},\mathbf{E}\right)\mathrm{d}V_0 = \int_{V}\frac{1}{J}\left(\frac{\partial H\left(\mathbf{F},\mathbf{E}\right)}{\partial\mathbf{F}}\mathbf{F}^{T}:\mathbf{L} + \frac{\partial H\left(\mathbf{F},\mathbf{E}\right)}{\partial\mathbf{E}}\cdot\dot{\mathbf{E}}\right)\mathrm{d}V, \tag{10}$$

and the rate of the entropy is

$$\frac{\mathrm{d}}{\mathrm{d}t}\int_{V_0} S\left(\mathbf{F},\mathbf{E}\right)\mathrm{d}V_0 = \int_{V}\frac{1}{J}\left(\frac{\partial S\left(\mathbf{F},\mathbf{E}\right)}{\partial\mathbf{F}}\mathbf{F}^{T}:\mathbf{L} + \frac{\partial S\left(\mathbf{F},\mathbf{E}\right)}{\partial\mathbf{E}}\cdot\dot{\mathbf{E}}\right)\mathrm{d}V, \tag{11}$$

Substituting Eqs. (9), (10) and (11) into Eq. (7) and collecting the coefficients of $\mathbf{L}$ and $\dot{\mathbf{E}}$ yields

$$0 = \int_V \left(\boldsymbol{\sigma} - \boldsymbol{\sigma}^v - \mathbf{E} \otimes \mathbf{P} - \frac{1}{J} \left(\frac{\partial H(\mathbf{F},\mathbf{E})}{\partial \mathbf{F}} - T \frac{\partial S(\mathbf{F},\mathbf{E})}{\partial \mathbf{F}} \right) \mathbf{F}^T \right) : \mathbf{L} \, \mathrm{d}V + \int_{\mathbb{R}^3/V} (\boldsymbol{\sigma} - \boldsymbol{\sigma}^v) : \mathbf{L} \, \mathrm{d}V$$
$$+ \int_V \left(\frac{1}{J} \left(T \frac{\partial S(\mathbf{F},\mathbf{E})}{\partial \mathbf{E}} - \frac{\partial H(\mathbf{F},\mathbf{E})}{\partial \mathbf{E}} \right) - \mathbf{P} \right) \cdot \dot{\mathbf{E}} \, \mathrm{d}V. \tag{12}$$

We follow Coleman and Noll (1963), and postulate that the latter holds for every admissible process. Therefore,

$$\boldsymbol{\sigma} = \boldsymbol{\sigma}^m + \mathbf{E} \otimes \mathbf{P} + \boldsymbol{\sigma}^v, \tag{13}$$

where

$$\boldsymbol{\sigma}^m = \frac{1}{J} \left(\frac{\partial H(\mathbf{F},\mathbf{E})}{\partial \mathbf{F}} - T \frac{\partial S(\mathbf{F},\mathbf{E})}{\partial \mathbf{F}} \right) \mathbf{F}^T, \tag{14}$$

and

$$\mathbf{P} = \frac{1}{J} \left(T \frac{\partial S(\mathbf{F},\mathbf{E})}{\partial \mathbf{E}} - \frac{\partial H(\mathbf{F},\mathbf{E})}{\partial \mathbf{E}} \right). \tag{15}$$

In the surrounding space $\boldsymbol{\sigma} = \boldsymbol{\sigma}^v$.

The stress in Eq. (13) can be viewed as the sum of three contributions. For conciseness we will refer to the stress component $\boldsymbol{\sigma}^m$ as the *mechanical* stress and to the component $\mathbf{E} \otimes \mathbf{P}$ as the polarization stress. The first term accounts for the evolution of the internal structure of the dielectric following the electro-mechanical loading. The second term, the polarization stress, stems from the application of an electric field over a polarizable medium. A similar decomposition was encountered in the phenomenological invariant-based framework of Dorfmann and Ogden (2005) and in the multi-scale analysis of dielectrics of Cohen and deBotton (2014), among others. The decomposition of the stress in these works was to a sum of (1) a mechanical stress attributed to purely mechanical sources, (2) a polarization stress resulting from the applied electric field, and (3) the Maxwell stress in vacuum, where the latter two are similar to the second and the third terms in Eq. (13). However, it is important to note that any decomposition is essentially artificial, since from a practical point of view only the total stress can be measured in experiments. Eq. (15) reveals that the polarization depends on the variations of the microstructure caused by the external loadings.

3. Entropy-driven electroelasticity of a polymer network

Polymers are commonly used dielectric materials with a multiscale hierarchical structure of a large number of polymer chains, where each chain is a long string of repeating dipolar

monomers. The monomers can move or rotate relative to their neighbors thus providing the chains a freedom to deform (Flory, 1953). In this work the basic building block is the dipolar monomer which is treated as a small rigid rod and as a single dipole from a mechanical and an electrostatic viewpoint, respectively.

3.1. **A chain of monomers.** We begin our analysis with a single chain with n dipolar monomers. The length of the line segment between the contact points of a monomer with its neighbors is l. The chain is subjected to an electric field $\mathbf{E} = E\hat{\mathbf{E}}$ and a mechanical deformation such that at the current configuration the vector connecting its two ends is $\mathbf{r}$. We prescribe a coordinate system $\left\{\hat{\mathbf{E}}, \hat{\mathbf{Y}}, \hat{\mathbf{Z}}\right\}$, where $\hat{\mathbf{Y}}$ and $\hat{\mathbf{Z}}$ span the plane perpendicular to $\hat{\mathbf{E}}$. In this system a unit vector is

$$\hat{\boldsymbol{\xi}} = \cos\theta\hat{\mathbf{E}} + \sin\theta\left(\cos\phi\hat{\mathbf{Y}} + \sin\phi\hat{\mathbf{Z}}\right), \tag{16}$$

where $0 \leq \theta < \pi$ is the angle between $\hat{\boldsymbol{\xi}}$ and the electric field and $0 \leq \phi < 2\pi$ is the angle of the projection on the plane perpendicular to $\hat{\mathbf{E}}$ with $\hat{\mathbf{Y}}$. We also define the differential solid angle $\mathrm{d}\Gamma = \sin\theta\,\mathrm{d}\theta\,\mathrm{d}\phi$.

The number of possible configurations of the chain is

$$\Omega = \frac{n!}{\Pi_i\left(n^{(i)}!\right)}, \tag{17}$$

where $n^{(i)}$ is the number of dipolar monomers aligned along $\hat{\boldsymbol{\xi}}$ in the range $\theta^{(i)} \leq \theta < \theta^{(i)} + \mathrm{d}\theta$ and $\phi^{(i)} \leq \phi < \phi^{(i)} + \mathrm{d}\phi$. For convenience we define $\hat{\boldsymbol{\xi}}^{(i)}$ as the unit vector corresponding to $\theta^{(i)}$ and $\phi^{(i)}$. Consequently, the entropy of the chain is

$$S_C = k\,\ln\left(\Omega\right) = k\left(n\,\ln\left(n\right) - n - \sum_i n^{(i)}\,\ln\left(n^{(i)}\right) + \sum_i n^{(i)}\right), \tag{18}$$

where Stirling's approximation is employed and k is the Boltzmann constant. The chain is subjected to three constraints:

$$\sum_i n^{(i)} = n, \tag{19}$$

$$\sum_i l\,n^{(i)}\hat{\boldsymbol{\xi}}^{(i)} = \mathbf{r}, \tag{20}$$

and

$$\sum_i n^{(i)} h^{(i)} = H_C, \tag{21}$$

where $h^{(i)}$ is the electrical enthalpy of a monomer directed along $\hat{\boldsymbol{\xi}}^{(i)}$ and H_C is the enthalpy of the chain.

We assume that the polymer chain occupies the most probable configuration $\left\{n^{(1)}, n^{(2)}, \ldots\right\}$ under the given constraints, and therefore we are interested in maximizing the entropy,

$$S_C = k\left(\ln(\Omega) + \alpha\left(\sum_i n^{(i)} - n\right) + \boldsymbol{\tau}\cdot\left(\sum_i n^{(i)}\hat{\boldsymbol{\xi}}^{(i)} - \frac{\mathbf{r}}{l}\right) + \gamma\left(\sum_i n^{(i)} h^{(i)} - H_C\right)\right), \tag{22}$$

where α, $\boldsymbol{\tau}$ and γ are Lagrange multipliers (e.g., Davidson, 1962). The derivative of S_C with respect to $n^{(i)}$ is

$$\frac{\partial S_C}{\partial n^{(i)}} = k\left(-\ln\left(n^{(i)}\right) + \alpha + \boldsymbol{\tau}\cdot\hat{\boldsymbol{\xi}}^{(i)} + \gamma h^{(i)}\right) = 0, \tag{23}$$

from which we determine

$$n^{(i)} = \exp\left(\alpha + \boldsymbol{\tau}\cdot\hat{\boldsymbol{\xi}}^{(i)} + \gamma h^{(i)}\right). \tag{24}$$

Upon substitution of the latter into Eq. (22), the maximum entropy that can be achieved by the system is

$$S_C = k\left(n\,\ln(n) - \alpha\, n - \boldsymbol{\tau}\cdot\frac{\mathbf{r}}{l} - \gamma\, H_C\right). \tag{25}$$

We follow the works of Kuhn and Grün (1942) and Treloar (1975), among others, and assume that the polymer chains do not interact with one another. Consequently, in a volume element $\mathrm{d}V_0$, the total entropy-density and the total electrical enthalpy-density functions are obtained via $S = \frac{1}{\mathrm{d}V_0}\sum_k S_C^{(k)}$ and $H = \frac{1}{\mathrm{d}V_0}\sum_k H_C^{(k)}$, respectively. Differentiating Eq. (7) for the first law of thermodynamics with respect to the enthalpy of the k-th chain we obtain

$$\frac{\partial H}{\partial H_C^{(k)}} = T\,\frac{\partial S}{\partial H_C^{(k)}}, \tag{26}$$

from which we derive the relation

$$\gamma = -\frac{1}{k\,T}, \tag{27}$$

where Eq. (25) is used.

From the constraint Eq. (19), (23) and (27)

$$\sum_i n^{(i)} = \exp(\alpha)\int \exp\left(\boldsymbol{\tau}\cdot\hat{\boldsymbol{\xi}} - \frac{h}{k\,T}\right)\mathrm{d}\Gamma = n, \tag{28}$$

where Eq. (27) is used and the summation is replaced by an integral over the orientations of the monomers. Therefore,

$$\exp(\alpha) = \frac{n}{Z}, \tag{29}$$

where

$$Z = \int \exp\left(\boldsymbol{\tau}\cdot\hat{\boldsymbol{\xi}} - \frac{h}{kT}\right) \mathrm{d}\Gamma, \tag{30}$$

is the partition function. Subsequently, we define the probability density function (PDF) that a monomer is in the direction $\hat{\boldsymbol{\xi}}$ and has an electrical-enthalpy h as

$$p\left(\hat{\boldsymbol{\xi}}, h\right) = \frac{1}{Z}\exp\left(\boldsymbol{\tau}\cdot\hat{\boldsymbol{\xi}} - \frac{h}{kT}\right), \tag{31}$$

and we note that $\int p\,\mathrm{d}\Gamma = 1$, and Eq. (24) can be rewritten as $n^{(i)} = n\,p$. An implicit equation from which the Lagrange multiplier $\boldsymbol{\tau}$ is computed follows from constraint Eq. (20),

$$\int \hat{\boldsymbol{\xi}}\,p\,\mathrm{d}\Gamma = \frac{\mathbf{r}}{n\,l}, \tag{32}$$

where again the summation is replaced by an integration over all possible orientations of the monomers. We note that $n\,l$ is the contour length of the chain.

In order to compute the polarization and the total stress acting on a polymer according to Eqs. (15) and (13), respectively, we first formally differentiate the entropy of the chain Eq. (25) with respect to a given quantity $\bullet$,

$$\frac{\partial S_C}{\partial \bullet} = k\left(-\left(\frac{\partial \alpha}{\partial \bullet}n + \frac{\partial \boldsymbol{\tau}}{\partial \bullet}\cdot\frac{\mathbf{r}}{l}\right) - \frac{\boldsymbol{\tau}}{l}\cdot\frac{\partial \mathbf{r}}{\partial \bullet} + \frac{1}{kT}\frac{\partial H_C}{\partial \bullet}\right). \tag{33}$$

By differentiating Eq. (28) with respect to $\bullet$, it follows that

$$\begin{aligned} n\frac{\partial}{\partial \bullet}\left(\int p\,\mathrm{d}\Gamma\right) &= n\left(\frac{\partial \alpha}{\partial \bullet}\int p\,\mathrm{d}\Gamma + \frac{\partial \boldsymbol{\tau}}{\partial \bullet}\cdot\int \hat{\boldsymbol{\xi}}\,p\,\mathrm{d}\Gamma - \frac{1}{kT}\int \frac{\partial h}{\partial \bullet}p\,\mathrm{d}\Gamma\right) \\ &= n\frac{\partial \alpha}{\partial \bullet} + \frac{\partial \boldsymbol{\tau}}{\partial \bullet}\cdot\frac{\mathbf{r}}{l} - \frac{n}{kT}\int \frac{\partial h}{\partial \bullet}p\,\mathrm{d}\Gamma = 0, \end{aligned} \tag{34}$$

where Eq. (32) is used, and consequently

$$\frac{n}{kT}\int \frac{\partial h}{\partial \bullet}p\,\mathrm{d}\Gamma = \frac{\partial \alpha}{\partial \bullet}n + \frac{\partial \boldsymbol{\tau}}{\partial \bullet}\cdot\frac{\mathbf{r}}{l}. \tag{35}$$

Substituting Eq. (35) into Eq. (33) yields

$$\frac{\partial S_C}{\partial \bullet} = \frac{1}{T}\left(\frac{\partial H_C}{\partial \bullet} - n\int \frac{\partial h}{\partial \bullet}p\,\mathrm{d}\Gamma - \frac{kT\boldsymbol{\tau}}{l}\cdot\frac{\partial \mathbf{r}}{\partial \bullet}\right). \tag{36}$$

3.2. **The polymer network.** Following the premise that the chains do not interact with one another we have that

$$\frac{\partial S}{\partial \bullet} = \frac{1}{\mathrm{d}V_0} \sum_k \frac{\partial S_C^{(k)}}{\partial \bullet}, \tag{37}$$

where the summation is carried over all the chains.

Making use of Eqs. (36) and (37), Eq. (14) can be written as

$$\boldsymbol{\sigma}^m = \frac{1}{J\,\mathrm{d}V_0} \sum_k \left(n \left(\int \frac{\partial h}{\partial \mathbf{F}}\, p\, \mathrm{d}\Gamma \right)^{(k)} + \frac{k\,T\,\boldsymbol{\tau}^{(k)}}{l} \cdot \frac{\partial\, \mathbf{r}^{(k)}}{\partial \mathbf{F}} \right) \mathbf{F}^T. \tag{38}$$

The mechanical stress is composed of two parts: the first is related to the change in the electrical energy of the single monomer with respect to the mechanical deformation, and the second accounts for the mechanical forces deforming the end-to-end vector. Note that in many materials and regimes of practical importance, it is reasonable to assume that the monomer is rigid compared to the polymer chain. In that case, the enthalpy of the monomer does not depend on the deformation gradient, and the variation with respect to it vanishes. We also recall that previous works by Dorfmann and Ogden (2005); Thylander et al. (2012) and Cohen and deBotton (2014) among others suggested a decomposition of the stress reminiscent of the one obtained in Eq. (13). In some of these works it was assumed that $\boldsymbol{\sigma}^m$ depends on $\mathbf{F}$ only. In this work, since $\boldsymbol{\tau} = \boldsymbol{\tau}(\mathbf{F}, \mathbf{E})$, we find that this mechanical stress component is influenced by the applied electric field too. We finally note that for $\mathbf{E} = \mathbf{0}$ the well-known result of Kuhn and Grün (1942) is recovered.

By substituting Eqs. (36) and (37) into Eq. (15), the polarization is

$$\mathbf{P} = -\frac{1}{J\,\mathrm{d}V_0} \sum_k \left(n \left(\int \frac{\partial h}{\partial \mathbf{E}}\, p\, \mathrm{d}\Gamma \right)^{(k)} + \frac{k\,T\,\boldsymbol{\tau}^{(k)}}{l} \cdot \frac{\partial\, \mathbf{r}^{(k)}}{\partial \mathbf{E}} \right), \tag{39}$$

where once again the summations are carried over all of the chains. The polarization Eq. (39) can also be viewed as the sum of two contribution. The first term is associated with the variation of the electrical enthalpies of the monomers as a result of the applied external electric field, and the second attributes to the reorientation of the chains in response to the electric field.

4. Analyses of isotropic networks with different monomers

In order to demonstrate the merit of the results developed so far, we examine a few specific cases, starting with the purely electrical behavior of amorphous dielectrics and tackle the electro-mechanical response of polymers next. To this end, we assume that the interaction between the

external electric field and the dielectric is solely through the dipolar molecules, and that the external electric field is larger than the electric fields induced on a dipole by its neighbors, thus deeming the internal interactions negligible.

4.1. **The local behavior of the monomer.** Following Cohen and deBotton (2015), we assume that the dependence of the dipole vector $\mathbf{m}$ on the electric field can be approximated by the first order Taylor expansion series about $\mathbf{E} = \mathbf{0}$. Specifically, in the monomer local coordinate system we assume that

$$\mathbf{m}(\mathbf{E}) = \mathbf{m}_0 + \mathbf{M}\,\mathbf{E}. \tag{40}$$

The first and second terms in Eq. (40) represent a spontaneous polarization and a linear dependence on the electric field, respectively.

While this relation superficially appears linear, it is important to notice that it is in fact nonlinear. To see this, consider a single monomer, and assume a linear response $\mathbf{m} = \mathbf{M}\mathbf{E}$, with $\mathbf{M}$ a constant tensor. This response must be invariant under any orthogonal transformation $\mathbf{R}$, i.e. $\mathbf{m} \to \mathbf{R}\mathbf{m}$ and $\mathbf{E} \to \mathbf{R}\mathbf{E}$. This implies the trivial response $\chi = \chi\mathbf{I}$. However, Eq. (40) is written in the monomer local coordinate system. Therefore, both $\mathbf{m}_0$ and $\mathbf{M}$ are functions of $\hat{\boldsymbol{\xi}}$ and transform accordingly. This enables nontrivial response and conforms to invariance under orthogonal transformations, at the cost of being nonlinear. This nonlinearity is conceptually analogous to the nonlinear strain measures that are required in elasticity for rotational invariance. It can be contrasted with crystalline materials in which the crystal lattice provides a "background"; there, one does not require invariance under any orthogonal transformation $\mathbf{R}$, but only those that are in the symmetry point group of the crystal (e.g., James and Müller, 1994; Marshall and Dayal, 2014). In the crystal setting, a linear response is an adequate first-order approximation. In the current setting of monomers, the nonlinearity of the response is essential and is the first-order model. This precludes us from directly using many developed tools in statistical mechanics that can allow closed-form solutions for harmonic energies (e.g., Su and Purohit, 2012).

The corresponding electrical enthalpy of a dipole oriented along $\hat{\boldsymbol{\xi}}$ is (Blythe and Bloor, 2008; Cohen and deBotton, 2014)

$$h = -\mathbf{m}\cdot\mathbf{E}. \tag{41}$$

For later reference we note that $h \neq h(\mathbf{F})$. Next, we list the three specific models for the local relation (40) that will be utilized in the forthcoming analyses.

The first corresponds to a spontaneous dipole, or a rigid dipole with a constant magnitude $\mathfrak{K}$ (Davidson 1962; Blythe and Bloor 2008),

$$\mathbf{m}_S = \mathfrak{K}\,\hat{\boldsymbol{\xi}}. \tag{42}$$

Following a concept proposed by Stockmayer (1967), Cohen and deBotton (2015) introduced the second model of a uniaxial dipole whose magnitude depends on the electric field. Specifically,

$$\mathbf{m}_U = \frac{\mathfrak{K}_U^2}{k\,T}\hat{\boldsymbol{\xi}}\otimes\hat{\boldsymbol{\xi}}\,\mathbf{E}, \tag{43}$$

where we formally normalize by $k\,T$ so that $\mathfrak{K}_U$ has the units of a dipole.

Another type of dipole discussed by Stockmayer (1967) was represented by Cohen and deBotton (2015) as the transversely isotropic (TI) model. In this case the dipole

$$\mathbf{m}_{TI} = \frac{1}{2}\frac{\mathfrak{K}_{TI}^2}{k\,T}\left(\mathbf{I}-\hat{\boldsymbol{\xi}}\otimes\hat{\boldsymbol{\xi}}\right)\mathbf{E}, \tag{44}$$

is perpendicular to $\hat{\boldsymbol{\xi}}$ and $\mathfrak{K}_{TI}$ has the units of a dipole.

For convenience, throughout this work we set $\mathfrak{K}_U = \mathfrak{K}_{TI} = \mathfrak{K}$. This will ensure that three dielectrics composed of a random and uniform distribution of spontaneous, uniaxial and TI dipoles admit the same behavior in the limit of infinitesimal deformations and small electric fields.

4.2. **The purely electrical response of amorphous dielectrics.** Consider an amorphous dielectric with $n_0 = \frac{n}{\mathrm{d}V_0}$ dipoles per unit referential volume subjected to an electric field $\mathbf{E}$. We are concerned with the purely electrical response, and to eliminate the mechanical constraint (20) we set $\boldsymbol{\tau} = 0$ in Eq. (39). The resulting polarization of the dielectric is

$$\mathbf{P} = n_0 \int \mathbf{m}\,p\,\mathrm{d}\Gamma, \tag{45}$$

where Eqs. (30) and (31) result in the Boltzmann distribution $p = \frac{1}{Z}\exp\left(\frac{\mathbf{m}\cdot\mathbf{E}}{k\,T}\right)$ with $Z = \int \exp\left(\frac{\mathbf{m}\cdot\mathbf{E}}{k\,T}\right)\mathrm{d}\Gamma$ and $J = 1$. Next, we consider the three local behaviors of the dipoles.

With Eq. (45), the polarization of the dielectric is

$$\mathbf{P}_S = n_0\,\mathfrak{K}\,\mathfrak{L}\,(\omega)\;\hat{\mathbf{E}}, \tag{46}$$

where $\omega \equiv \frac{\mathfrak{K}\,E}{k\,T}$ and $\mathfrak{L}\,(\omega) = \coth\omega - \frac{1}{\omega}$ is the Langevin function. Note that as $E\to\infty$ (or $\omega\to\infty$) all dipoles tend to align with the electric field and therefore $\mathbf{P}_S \to n_0\,\mathfrak{K}\,\hat{\mathbf{E}}$. At small

electric fields the Taylor expansion series up to first order in ω is

$$\mathbf{P}_S \approx \frac{n_0 \, \aleph}{3} \, \omega \, \hat{\mathbf{E}}, \tag{47}$$

where at $E = 0$ (or $\omega = 0$) we find that $\mathbf{P}_S = \mathbf{0}$ due to the initial random distribution of the dipoles. The corresponding expression for the initial susceptibility

$$\chi_0 \approx \frac{n_0 \aleph^2}{3 \, k \, T \, \varepsilon_0}, \tag{48}$$

is in agreement with the results of Debye (1929), Fröhlich (1949), Davidson (1962) and Blythe and Bloor (2008).

We consider next a material with a random distribution of uniaxial dipoles. From Eq. (30), the partition function is

$$Z_U = \frac{4\pi \, \mathfrak{D}\left(\omega\right)}{\omega} \exp\left(\omega^2\right), \tag{49}$$

where $\mathfrak{D}\left(\omega\right) = \exp\left(-\omega^2\right) \int_0^\omega \exp\left(t^2\right) \mathrm{d}t$ is the Dawson function or the Dawson integral. Therefore,

$$p_U = \frac{\omega}{4\pi \, \mathfrak{D}\left(\omega\right)} \exp\left(-\omega^2 \sin^2\left(\theta_i\right)\right). \tag{50}$$

Integration according to Eq. (45) yields

$$\mathbf{P}_U = \frac{n_0 \, \aleph}{2} \, \eta_U \, \omega \hat{\mathbf{E}}, \tag{51}$$

where $\eta_U = \frac{\omega - \mathfrak{D}(\omega)}{\omega^2 \mathfrak{D}(\omega)}$. In the limit of small electric fields $\eta_U = \frac{2}{3}$ and $\mathbf{P} \approx \frac{n_0 \aleph}{3} \, \omega \hat{\mathbf{E}}$. At the other limit, as $E \to \infty$ (or $\omega \to \infty$), $\eta_U \to 2$ and all the dipoles tend to align with the electric field. Consequently, $\mathbf{P}_U \to n_0 \, \frac{\aleph^2}{kT} \, \mathbf{E}$. We note that $\eta_U \left(\omega\right)$ is a smoothly varying bounded function between $\frac{2}{3}$ at $\omega = 0$ and 2 as $\omega \to \infty$.

Next we consider the case of a TI dipole Eq. (44). From Eq. (30), the partition function is

$$Z_{TI} = \frac{\left(2\,\pi\right)^{3/2}}{\omega} \exp\left(\frac{\omega^2}{2}\right) \mathrm{Erf}\left(\frac{\omega}{\sqrt{2}}\right), \tag{52}$$

where $\mathrm{Erf}\left(x\right)$ is the well-known error function, and the corresponding PDF is

$$p_{TI} = \frac{\omega}{\left(2\,\pi\right)^{3/2} \, \mathrm{Erf}\left(\frac{\omega}{\sqrt{2}}\right)} \exp\left(-\frac{\omega^2}{2} \cos^2\left(\theta_i\right)\right). \tag{53}$$

By means of Eq. (45) the resulting polarization is

$$\mathbf{P}_{TI} = \frac{n_0 \, \aleph}{2} \, \eta_{TI} \, \omega \hat{\mathbf{E}}, \tag{54}$$

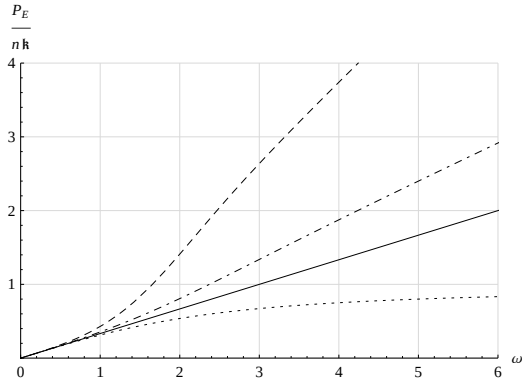


FIGURE 1. The normalized polarization versus ω. The continuous, dotted, dashed and dot-dashed curves correspond to the polarization according to the linear, the spontaneous, the uniaxial and the TI dipole models, respectively.

where $\eta_{TI} = 1 - \frac{1}{\omega^2} + \sqrt{\frac{2}{\pi}} \frac{\exp\left(-\frac{\omega^2}{2}\right)}{\omega \operatorname{Erf}\left(\frac{\omega}{\sqrt{2}}\right)}$. Again we note that at small electric fields $\eta_{TI} = \frac{2}{3}$ and $\mathbf{P}_{TI} = \frac{n_0 \mathfrak{K}}{3} \omega \hat{\mathbf{E}}$, and as $E \to \infty$ (or $\omega \to \infty$), $\eta_{TI} \to 1$ and $\mathbf{P}_{TI} \to \frac{1}{2} n_0 \frac{\mathfrak{K}^2}{kT} \mathbf{E}$. The function $\eta_{TI}(\omega)$ is a smoothly varying bounded function between $\omega = 0$ and $\omega \to \infty$.

The variations of the polarization with the electric field according to the three models together with a linear model with a constant susceptibility are compared in Fig. (1), where the polarization in the direction of the electric field normalized by $n_0 \mathfrak{K}$ is plotted versus the dimensionless quantity ω. The continuous curve corresponds to the commonly assumed linear model

$$P_E = \frac{n_0 \mathfrak{K}}{3} \omega. \tag{55}$$

This model does not take into account the evolution of the dipoles configuration in response to the external field. At small fields all three models agree with the linear one. The dotted curve represents the predictions according to the spontaneous model and at large electric fields, as the dipoles orient along the field, the overall polarization saturates. The dotted and the dot-dashed curves depict the predicted polarizations according to the uniaxial and the TI dipole models, respectively. We note that these curves admit a form of bilinear curves with distinct initial and final slopes. Due to the choice of the model constants, as $\omega \to \infty$ the ratio between the two predictions approaches 2 (in accordance with the limiting values of η_U and η_{TI}).

We conclude this section noting that by taking a linear combination of the three models described in section (4.1), dipoles of various orientations and intensities with respect to the electric field and the direction of the molecule $\hat{\boldsymbol{\xi}}$ can be considered.

4.3. **The electro-mechanical response of polymer networks.** Consider a polymer with N_0 chains per unit referential volume where each chain is composed of n dipolar monomers of length l. At the reference configuration the vector that connects the two ends of the k-th chain is aligned with the direction $\hat{\mathbf{r}}_0^{(k)}$ and has a length $\sqrt{n}\,l$ (Treloar, 1975). At the reference configuration the chains are randomly oriented and uniformly distributed such that

$$\langle \hat{\mathbf{r}}_0 \rangle = \mathbf{0}, \tag{56}$$

and

$$\langle \hat{\mathbf{r}}_0 \otimes \hat{\mathbf{r}}_0 \rangle = \frac{1}{3}\mathbf{I}, \tag{57}$$

where

$$\langle \bullet \rangle \equiv \frac{1}{N_0\,\mathrm{d}V_0}\int \bullet\, p\,\mathrm{d}\Gamma = \frac{\sum_k \bullet^{(k)}}{N_0\,\mathrm{d}V_0}, \tag{58}$$

denotes the average of a chain related quantity $\bullet$. Throughout this work, the averages are determined by application of the numerical micro-sphere technique that was employed, for example, by Miehe et al. (2004), Thylander et al. (2012), and Cohen et al. (2015). Relying on the experience gained in those works, we consider 42 integration points.

In accord with the works of Treloar (1975) and Flory (1953), we assume that when subjected to an electric field $\mathbf{E}$ and a deformation gradient $\mathbf{F}$ the chains undergo affine deformations, i.e. for the k-th chain

$$\mathbf{r}^{(k)} = \sqrt{n}\,l\,\mathbf{F}\hat{\mathbf{r}}_0^{(k)}. \tag{59}$$

We note that, while from this relation it follows that the electric field does not affect directly the distribution of the chains (i.e., $\mathbf{r}^{(k)} \neq \mathbf{r}^{(k)}(\mathbf{E})$), at the monomer level the electric field can lead to rearrangement and redirection of the dipolar monomers.

Next, we define the dipole of the k-th chain

$$\mathbf{m}_C^{(k)} = \sum_{i=1}^{n}\mathbf{m}^{(i)} = n\int \mathbf{m}\,p\,\mathrm{d}\Gamma, \tag{60}$$

where the summation is carried over all the dipoles composing the chain and, assuming a large n, we execute the summation in terms of an appropriate integral. According to Eq. (39) the polarization is

$$\mathbf{P} = \frac{N_0}{J}\,\langle \mathbf{m}_C \rangle\,. \tag{61}$$

Since $h \neq h(\mathbf{F})$, the mechanical stress Eq. (38) reduces to

$$\boldsymbol{\sigma}^m = \frac{N_0\, k\, T\, \sqrt{n}}{J} \left\langle \boldsymbol{\tau} \otimes \hat{\mathbf{r}}_0 \right\rangle \mathbf{F}^T. \tag{62}$$

Utilizing Eq. (61), we first determine the polarization of a polymer whose chains are made of spontaneous dipoles Eq. (42), and find that

$$\mathbf{P} = \frac{N_0\, n\, \aleph}{J} \left\langle \int \hat{\boldsymbol{\xi}}\, p\, \mathrm{d}\Gamma \right\rangle = \frac{N_0\, \sqrt{n}\, \aleph}{J} \mathbf{F} \left\langle \hat{\mathbf{r}}_0 \right\rangle = \mathbf{0}, \tag{63}$$

where Eqs. (60), (32), (59) and (56) are used. This result can be explained as follows: since the magnitude of the spontaneous dipoles is fixed, the electric field can only influence their local orientations. Due to the mechanical constraint Eq. (20), the directions of the end-to-end vector and the dipole of any polymer chain coincide. Upon integration from the chain to the macroscopic level, we follow the affine deformations assumption and find that the sum of the dipoles of any pair of chains lying along the same vector but pointing in opposite directions vanish.

The mechanical component of the stress can be derived from Eq. (13). We note that while the individual dipolar monomers would energetically favor orienting themselves along the electric field, they are constrained from doing so by the fact that the end-to-end vector is constrained by $\mathbf{F}$. While this constraint does not allow a net dipole moment to develop, it also leads to a mechanical stress that physically reflects the inability of the monomers to be oriented favorably. The emergence of mechanical stress in response to the affine deformation constraint will be discussed further in the following subsection.

We are interested in the electro-strictive properties of polymer networks, and therefore in the following we consider chains made out of dipolar monomers whose magnitudes do depend on the electric field. Particularly, we examine networks with uniaxial Eq. (43) and TI Eq. (44) dipoles. Accordingly, consider a polymer composed of long chains of uniaxial dipoles. The PDF Eq. (31) of the distribution of the dipolar monomers in a chain is

$$p\left(\hat{\boldsymbol{\xi}}, h\right) = \frac{1}{Z} \exp\left(\boldsymbol{\tau} \cdot \hat{\boldsymbol{\xi}} + \omega^2 \left(\hat{\boldsymbol{\xi}} \cdot \hat{\mathbf{E}}\right)^2\right). \tag{64}$$

Due to the assumed large number of dipolar monomers in a chain there is a finite range of deformations for which

$$\sqrt{\frac{\mathbf{r}}{n\,l} \cdot \frac{\mathbf{r}}{n\,l}} = \frac{1}{\sqrt{n}} \sqrt{\hat{\mathbf{r}}_0 \cdot \mathbf{C}\hat{\mathbf{r}}_0} \ll 1, \tag{65}$$

where Eq. (59) is used and $\mathbf{C} = \mathbf{F}^T\mathbf{F}$ is the right Cauchy-Green deformation tensor. Consequently, by approximating the PDF in Eq. (64) with its second order Taylor expansion and employing Eq. (32) we derive the approximation

$$\boldsymbol{\tau}_U = \frac{4}{2-\eta_U}\left(\mathbf{I} - a_U\,\hat{\mathbf{E}}\otimes\hat{\mathbf{E}}\right)\frac{1}{\sqrt{n}}\,\mathbf{F}\hat{\mathbf{r}}_0, \tag{66}$$

where $a_U = \frac{3\eta_U - 2}{2\,\eta_U}$. A closed-form estimate for the chain's dipole can be obtained from Eq. (60)

$$\mathbf{m}_C^{(k)} = \frac{n\,\Re\,\omega\,\eta_U}{2}\left(\mathbf{I} + \frac{1}{2\,\omega^2}\left(\frac{1}{2}\left(\left(a_U - b_U\right)\,\boldsymbol{\tau}_U\cdot\boldsymbol{\tau}_U + \left(3\,b_U - 5\,a_U\right)\left(\boldsymbol{\tau}_U\cdot\hat{\mathbf{E}}\right)^2\right)\mathbf{I} + a_U\,\boldsymbol{\tau}_U\otimes\boldsymbol{\tau}_U\right)\right)\hat{\mathbf{E}}, \tag{67}$$

where $b_U = \omega^2\left(1 - \frac{\eta_U}{2}\right)$. To calculate the polarization we make use of Eqs. (66), (56), (57) and (59) and arrive at the expressions

$$\left\langle\boldsymbol{\tau}_U\cdot\boldsymbol{\tau}_U\right\rangle = \frac{1}{3n}\left(\frac{4}{2-\eta_U}\right)^2\left(\mathrm{tr}\,(\mathbf{b}) + \left(a_U^2 - 2\,a_U\right)\hat{\mathbf{E}}\cdot\mathbf{b}\hat{\mathbf{E}}\right), \tag{68}$$

$$\left\langle\left(\boldsymbol{\tau}_U\cdot\hat{\mathbf{E}}\right)^2\right\rangle = \frac{1}{3n}\left(\frac{4}{2-\eta_U}\right)^2\left(1-a_U\right)^2\hat{\mathbf{E}}\cdot\mathbf{b}\hat{\mathbf{E}}, \tag{69}$$

and

$$\left\langle\boldsymbol{\tau}_U\otimes\boldsymbol{\tau}_U\right\rangle = \frac{1}{3n}\left(\frac{4}{2-\eta_U}\right)^2\left(\mathbf{b} - a_U\left(\mathbf{E}\otimes\mathbf{b}\mathbf{E} + \mathbf{b}\mathbf{E}\otimes\mathbf{E}\right) + a_U^2\,\hat{\mathbf{E}}\cdot\mathbf{b}\hat{\mathbf{E}}\,\hat{\mathbf{E}}\otimes\hat{\mathbf{E}}\right), \tag{70}$$

where $\mathbf{b} = \mathbf{F}\,\mathbf{F}^T$. Subsequently, Eq. (61) becomes

$$\mathbf{P}_U = \frac{N_0}{J}\frac{n\,\Re\,\omega\,\eta_U}{2}\left(\mathbf{I} + \frac{1}{6\,\omega^2\,n}\left(\frac{4}{2-\eta_U}\right)^2\left(\frac{1}{2}\left(\left(a_U - b_U\right)\,\mathrm{tr}\,(\mathbf{b}) + C_U^{(1)}\,\hat{\mathbf{E}}\cdot\mathbf{b}\hat{\mathbf{E}}\right)\mathbf{I} + a_U\,\mathbf{b} - \boldsymbol{C}_U^{(2)}\right)\right)\hat{\mathbf{E}}, \tag{71}$$

where

$$C_U^{(1)} = \left(a_U - b_U\right)\cdot\left(a_U^2 - 2\,a_U\right) + \left(3\,b_U - 5\,a_U\right)\cdot\left(1-a_U\right)^2, \tag{72}$$

and

$$\boldsymbol{C}_U^{(2)} = a_U^2\left(\hat{\mathbf{E}}\otimes\mathbf{b}\hat{\mathbf{E}} + \mathbf{b}\hat{\mathbf{E}}\otimes\hat{\mathbf{E}}\right) + a_U^3\,\left(\hat{\mathbf{E}}\cdot\mathbf{b}\hat{\mathbf{E}}\right)\hat{\mathbf{E}}\otimes\hat{\mathbf{E}}. \tag{73}$$

We point out that a Taylor series expansion around $\omega \to 0$ for the two functions reveals that $C_U^{(1)} \sim \omega^4 + O\left(\omega^6\right)$ and $\boldsymbol{C}_U^{(2)} \sim \omega^4 + O\left(\omega^6\right)$, whereas the coefficients of $\mathrm{tr}\,(\mathbf{b})$ and $\mathbf{b}$ are proportional to $\sim \omega^2 + O\left(\omega^4\right)$. Therefore, for $\omega < 0.3$ the polarization may be approximated via

$$\mathbf{P}_U \approx \frac{N_0}{J}\frac{\Re\,n}{3}\left(\mathbf{I} - \frac{1}{5\,n}\left(\mathrm{tr}\,(\mathbf{b})\,\mathbf{I} - 3\,\mathbf{b}\right)\right)\omega\hat{\mathbf{E}}. \tag{74}$$

The zero order term in Eq. (71) is isotropic and the associated contribution to the polarization field is aligned with the external electric field. This term corresponds to the initial macroscopic susceptibility of the polymer and is identical to the result obtained in Eq. (48) for amorphous dielectrics with $n_0 = N_0 n$. The first order term, which is proportional to $\frac{1}{n}$, stems from the finite length of the chain and has an influence on the polarization as the polymer deforms. We compare this result to the one obtained in the work of Cohen and deBotton (2015), where a deterministic analysis in which the entropy was not accounted for was introduced. While the zero order term from both analyses is identical, the first order term in the earlier work is different from the one obtained herein and proportional to $\frac{1}{\sqrt{n}}$. This discrepancy may be explained as follows: even though the analysis in Cohen and deBotton (2015) is based on valid chain configurations, these are not the most probable ones. We argue that the current analysis is more physically sound since the response of polymers is entropy-driven and the present work considers the configurations that maximize the entropy.

The stress is computed via Eq. (13), where the mechanical stress Eq. (62) is calculated with Eq. (66),

$$\boldsymbol{\sigma}_U = \frac{N_0\, k\, T}{3\, J}\left(\frac{4}{2-\eta_U}\left(\mathbf{I} - a_U\, \hat{\mathbf{E}}\otimes\hat{\mathbf{E}}\right)\right)\mathbf{b} + \mathbf{E}\otimes\mathbf{P}_U + \boldsymbol{\sigma}^v, \tag{75}$$

where Eqs. (57) and (66) are employed. By setting $\mathbf{E}\to\mathbf{0}$ (or $\omega\to 0$), the above expression reduces to the standard neo-Hookean stress, where

$$\mu = N_0\, k\, T, \tag{76}$$

is the shear modulus (Treloar, 1975).

By following similar steps for a polymer with chains that are composed of TI dipoles Eq. (44), we approximate $\boldsymbol{\tau}$ for long chains as

$$\boldsymbol{\tau}_{TI} = \frac{2}{\eta_{TI}}\left(\mathbf{I} + \frac{2-3\eta_{TI}}{2\,(\eta_{TI}-1)}\hat{\mathbf{E}}\otimes\hat{\mathbf{E}}\right)\frac{1}{\sqrt{n}}\mathbf{F}\hat{\mathbf{r}}_0. \tag{77}$$

The expression for the chain dipole in this case is similar to the one in Eq. (67), where a_U and b_U are replaced with $a_{TI} = \frac{2}{\eta_{TI}} - 3$ and $b_{TI} = \omega^2\,(\eta_{TI}-1)$, respectively. The resulting expression for the polarization is

$$\mathbf{P}_{TI} = \frac{N_0}{J}\frac{n\,\Re\,\omega\,\eta_{TI}}{2}\left(\mathbf{I} + \frac{1}{6\,\omega^2\,n}\left(\frac{2}{\eta_{TI}}\right)^2\left(\frac{1}{2}\left((a_{TI}-b_{TI})\ \mathrm{tr}\,(\mathbf{b}) + C^{(1)}_{TI}\,\hat{\mathbf{E}}\cdot\mathbf{b}\hat{\mathbf{E}}\right)\mathbf{I} + a_{TI}\,\mathbf{b} - \boldsymbol{C}^{(2)}_{TI}\right)\right)\hat{\mathbf{E}}. \tag{78}$$

Here the expressions for $C_{TI}^{(1)}$ and $\boldsymbol{C}_{TI}^{(2)}$ are given in Eqs. (72) and (73), respectively, and where here too a_U and b_U are replaced with a_{TI} and b_{TI}, respectively. Following arguments similar to the ones led to Eq. (74), we argue that for $\omega < 0.3$ the polarization may be approximated via the Taylor expansion series for small ω

$$\mathbf{P}_{TI} \approx \frac{N_0}{J}\frac{\Re\, n}{3}\left(\mathbf{I} + \frac{1}{10\, n}\left(\mathrm{tr}\,(\mathbf{b})\,\mathbf{I} - 3\,\mathbf{b}\right)\right)\omega\hat{\mathbf{E}}. \tag{79}$$

The total stress is

$$\boldsymbol{\sigma}_{TI} = \frac{N_0\, k\, T}{3J}\left(\frac{2}{\eta_{TI}}\left(\mathbf{I} - a_{TI}\,\hat{\mathbf{E}}\otimes\hat{\mathbf{E}}\right)\right)\mathbf{b} + \mathbf{E}\otimes\mathbf{P}_{TI} + \boldsymbol{\sigma}^{v}, \tag{80}$$

where $\mathbf{P}_{TI}$ is given in Eq. (78).

5. Applications to polymer films

The polarization and the stress in Eqs. (61) and (13) depend on three key microscopic factors: the type of the dipolar monomers composing the chains (i.e., uniaxial or TI dipoles), the local dipole constant ($\Re_u$ or $\Re_{TI}$), and n the number of dipolar monomers in a chain. These microscopic factors will dictate the macroscopic response and are therefore prominent for the electromechanical coupling at the macroscopic level. We investigate the impact of these three microscopic factors on the macroscopic behavior. To this end, we examine thin layers of polymers with different dipole types, dipole constants and chain lengths that are subjected to the equi-biaxial isochoric deformation

$$\mathbf{F} = \lambda\left(\mathbf{I} - \hat{\mathbf{E}}\otimes\hat{\mathbf{E}}\right) + \frac{1}{\lambda^2}\,\hat{\mathbf{E}}\otimes\hat{\mathbf{E}}. \tag{81}$$

This type of loading is common in experimental settings where the faces of the film are covered with flexible electrodes of negligible stiffness that are charged with opposite charges such that the electric potential difference (ΔV) induces an electric field $\mathbf{E} = E\,\hat{\mathbf{E}}$ across the film (see Fig. (2)). Throughout, we assume that the shear modulus of the polymer in its initial unloaded configuration is $\mu = 10^5$ Pa, and deduce N_0, the density of the chains, from Eq. (76).

5.1. **The role of the local dipole constant.** In order to examine the effect of the constant $\Re$ we compare the behaviors of two polymers with initial susceptibilities $\chi_0^{(1)} = 3.7$ and $\chi_0^{(2)} = 37$. The chains composing these polymers contain $n = 100$ uniaxial monomers. We choose the value of $\chi_0^{(1)}$ to be equal to the electric susceptibility of the commercially available VHB 4910, which is commonly used in electro-mechanical actuation experiments (Kofod et al. 2003; McKay et

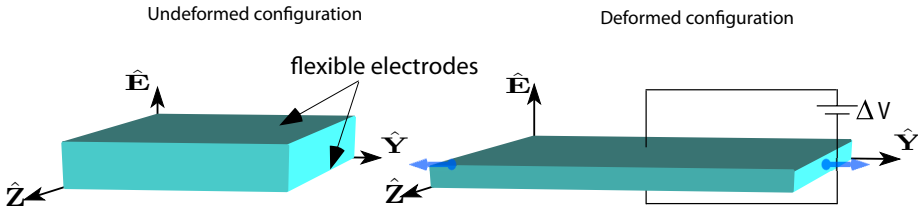


FIGURE 2. A sketch of a polymer film subjected to an electric field and a mechanical deformation.

al. 2009; Di Lillo et al. 2012; Qiang et al. 2012). As before, the dipole constants are $\mathfrak{K}_U^{(1)} = \frac{\mathfrak{K}_1^2}{kT}$ and $\mathfrak{K}_U^{(2)} = \frac{\mathfrak{K}_2^2}{kT}$, where $\mathfrak{K}_1$ and $\mathfrak{K}_2$ are determined from Eq. (48) with $n_0 = N_0\, n$.

Fig. (3) shows the distributions of the dipolar monomers belonging to a single chain whose end-to-end vector lies on the plane spanned by $\hat{\mathbf{E}}$ and $\hat{\mathbf{Y}}$. In these figures the length of the radius vector to a point on the curve is proportional to the number of dipolar monomers aligned with this vector. We note that an isotropic distribution of monomers in a chain whose end-to-end vector vanishes is represented by a circle with a radius $\frac{n}{4\pi}$. For convenience, in the polar distribution plots we normalize $n^{(i)}$ by this isotropic distribution such that if the directional distribution of the monomers in a chain is isotropic, the radius of the corresponding circle will be unity. To gain some quantitative information from these plots we also draw light circles with normalized radii 1/2, 1, 3/2 and so forth. Specifically, the number of monomers aligned with a ray from the origin to an intersection of these circles with the curves for the directional distribution is equal the normalized radius of the circle multiplied by the factor $\frac{n}{4\pi}$. Moreover, the amount by which the directional distribution is deviating from the unit circle provides an idea regarding its anisotropy.

Figures (3a) and (3b) correspond, respectively, to the two polymers with low and high dipole constants, where both polymers are subjected to a transverse stretch ratio $\lambda = 5$. In both figures the chain's end-to-end vector is aligned with the direction of the electric field, and the continuous, dashed and dot-dashed curves correspond to different intensities of the applied field. In the absence of an electric field and under the imposed stretch, the affine deformation assumption results in a significant shortening of the end-to-end vector of these chains and thus the distribution of the monomers is nearly uniform. When an electric field is imposed, since the response of a uniaxial dipole is quadratic in $\hat{\boldsymbol{\xi}}$, it causes the monomers to rotate toward either $\hat{\mathbf{E}}$ or $-\hat{\mathbf{E}}$. Indeed, in Fig. (3) we note the tendency of the monomers to align with the electric field, and the higher the electric field is the stronger this tendency becomes. Moreover, we

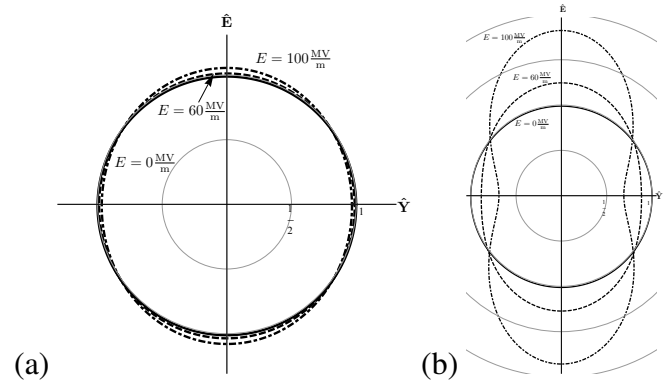


FIGURE 3. The distribution of the uniaxial dipolar monomers in chains aligned with the electric field belonging to polymers with (a) $\chi_0 = 3.7$ and (b) $\chi_0 = 37$ subjected to a biaxial stretch with $\lambda = 5$.

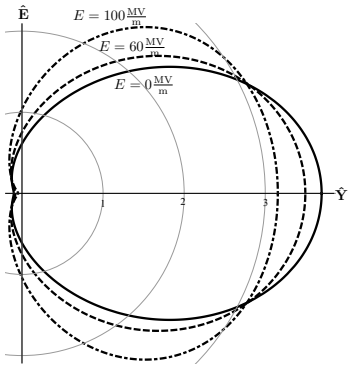


FIGURE 4. The distribution of the uniaxial dipolar monomers in chains whose end-to-end vectors are perpendicular to the electric field belonging to polymers with $\chi_0 = 37$ subjected to a biaxial stretch with $\lambda = 5$.

also note that the rate at which the monomers align with the field strongly depends on the local dipole constant, implying that at the chain level as well as at the macroscopic level the overall polarization is not linear with $\mathfrak{K}$.

Fig. (4) is similar to Fig. (3) but depicts the polar distribution of the dipolar monomers belonging to a chain whose end-to-end vector lies along the $\hat{\mathbf{Y}}$-direction. Since the variations in the distributions of the monomers in the polymer with $\chi_0 = 3.7$ are small, here and subsequently we show the polar distributions of the monomers polymers with $\chi_0 = 37$ only. Due to the imposed deformation, this chain is stretched and the monomers are inclined with the principle stretch direction. The electric field tends to reorient the monomers perpendicularly to increase their average projection in the field direction. Once again, the larger the field is, the stronger the monomers tendency to reorient is.

Regardless of the chain's end-to-end direction, we note in Figs. (3) and (4) the tendency of the monomers to align with the electric field. This, as demonstrated in Fig. (5a), results in an increase of the macroscopic polarization with the electric field. In Fig. (5a) the normalized component of the polarization vector $\tilde{P} = \frac{\mathbf{P}\cdot\hat{\mathbf{E}}}{\mathbf{P}_0\cdot\hat{\mathbf{E}}}$, with $\mathbf{P}_0 = \chi_0\varepsilon_0\mathbf{E}$, is plotted against E for polymers with the two susceptibilities. Accordingly, at $E = 0$ the limit $\tilde{P} = \lim_{E\to 0}\frac{\mathbf{P}\cdot\hat{\mathbf{E}}}{\mathbf{P}_0\cdot\hat{\mathbf{E}}}$ is taken. Note that due to the dependence of the coupled properties on the deformation, even in the absence of an electric field $\mathbf{P} \neq \mathbf{P}_0$. Fig. (5a) illustrates that the macroscopic susceptibility depends on the electric field and the intensity of this dependence is amplified in polymers with higher microscopic dipole constants. This can be explained with the aid of the PDF for the distribution of the monomers as follows: the dipole constant has a strong influence on the rearrangement of the dipolar monomers in response to the electric field. Thus, on top of the increase in the overall polarization due to the local behavior of the monomers, the freedom the monomers have to rotate further enhances this tendency. In accordance with this observation we note that even though the ratio between the initial susceptibilities of the two polymers shown in Fig. (5a) is 10, at high electric fields the ratio between the polarizations of the two polymers is much larger. For example, at $E = 100\,\frac{\mathrm{MV}}{\mathrm{m}}$ we find that $\frac{\tilde{P}(\chi_0=37)}{\tilde{P}(\chi_0=3.7)} \approx 1.2$. The foregoing analysis further contradicts the common assumption that the susceptibility of a polymer is constant (Dorfmann and Ogden, 2005; Shmuel and deBotton, 2013). In passing, we note that the second term in Eq. (75), namely the polarization stress $\mathbf{E}\otimes\mathbf{P}$, exhibits the same dependence on the electric field as the one discussed in connection with Fig. (5a).

We recall that the mechanical stress $\boldsymbol{\sigma}^m$ Eq. (62) is one of the three components of the stress in Eq. (13). Fig. (5b) depicts the normalized stress $\tilde{\sigma}^m_N = \frac{(\boldsymbol{\sigma}^m\hat{\mathbf{N}})\cdot\hat{\mathbf{N}}}{(\boldsymbol{\sigma}^m_0\hat{\mathbf{N}})\cdot\hat{\mathbf{N}}}$ as a function of E, where $\hat{\mathbf{N}}$ is a unit vector and $\boldsymbol{\sigma}^m_0 = \boldsymbol{\sigma}^m(\lambda, E = 0)$ is the purely mechanical stress (Kuhn and Grün, 1942; Treloar, 1975). Following the curves for this stress component in Fig. (5b) we observe that in polymers composed of uniaxial dipoles σ^m_E decreases with the electric field while σ^m_Y increases. To explain the observed variations of this stress component we recall that, as discussed in connection with Figs. (3) and (4), the dipolar monomers tend to reorient themselves along the electric field. From a mechanical-geometrical viewpoint this rotation will result in lengthening the projections of the monomers along the electric field and shortening their projections in the transverse direction. This local response prompts similar tendencies of the corresponding projections of the chains end-to-end vectors. However, since according to the affine deformation assumption the deformations of the end-to-end vectors are constraint,

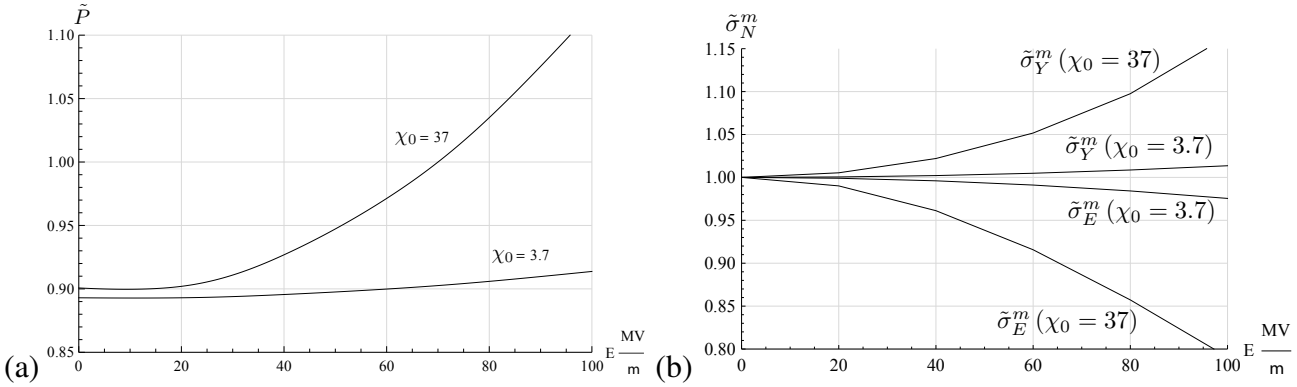


FIGURE 5. (a) $\tilde{P}$ and (b) $\tilde{\sigma}^m_E$ and $\tilde{\sigma}^m_Y$ versus E for polymers with uniaxial dipolar monomers and two dipole constants subjected to a stretch $\lambda = 5$.

the inability of the monomers to freely reorient manifest in terms of a compressive stress variation in the direction of the electric field and a tensile stress variation in the transverse direction. We note that while the applied electric field triggers these variations in the stress, this stress component stems from a mechanical constraint and not directly from the electric forces applied on the dipolar monomers. We also note that for the uniaxial dipolar monomers the variation of this stress component with the electric field opposes the corresponding variation of the polarization stress. A comparison between the two pairs of curves for the polymers with different dielectric constants demonstrates that the dependence of these stress variations on the local dipole constant is non-linear, and it is more pronounced in the polymer with the larger microscopic dipole constant.

We examine next the effect of the mechanical loading on the evolution of the micro-structure in chains with 100 uniaxial dipolar monomers. We consider a polymer with an electric susceptibility $\chi_0 = 37$ subjected to an equi-biaxial deformation. Figs. (6a) and (6b) illustrate the distribution of the dipolar monomers in a chain whose end-to-end vector lies along the $\hat{\mathbf{E}}$-direction for $\lambda = 1$ and $\lambda = 5$, respectively. The dotted and the continuous curves represent the polar distributions of the monomers in the absence of an electric field and when $E = 50\,\frac{\text{MV}}{\text{m}}$, respectively. Since the initial length of the end-to-end vector is fairly large in comparison with the chain contour length $r = 0.1\,n\,l$, the referential distribution of the monomers is asymmetric with respect to the plane transverse to the end-to-end vector. Application of electric field causes rotation of the monomers toward $\hat{\mathbf{E}}$ (or $-\hat{\mathbf{E}}$) but, since the length of the end-to-end vector is fixed, the distribution is still uneven with respect to the transverse plane. As the polymer deforms, the affine deformation assumption imposes a shortening of the end-to-end vector and hence a

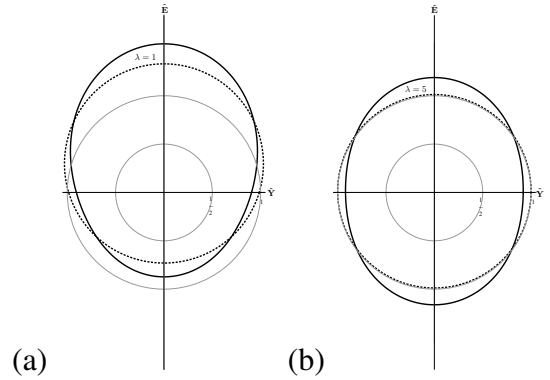


FIGURE 6. The distribution of the uniaxial dipolar monomers for chains aligned with the electric field belonging to polymers with $\chi_0 = 37$ subjected to a biaxial stretch (a) $\lambda = 1$ and (b) $\lambda = 5$. The dotted and the continuous curves correspond to $E = 0\,\frac{\text{MV}}{\text{m}}$ and $E = 50\,\frac{\text{MV}}{\text{m}}$, respectively.

reduction in the ratio $\frac{r}{nl}$. As a result a more symmetric distribution of the dipolar monomers is exhibited in Fig. (6b). We point out that the decrease in the ratio $\frac{r}{nl}$ increases the freedom of the monomers to reorient, and thus enhances the influence of the electric field on the distribution.

Fig. (7) depicts the variations in the distribution of monomers of a chain whose end-to-end vector lies along the $\hat{\mathbf{Y}}$-direction. In this case, at the referential state the distribution is symmetric about the $\hat{\mathbf{Y}}$-axis. Due to the quadratic dependence of the uniaxial dipoles on $\hat{\boldsymbol{\xi}}$ and the symmetric distribution with respect to the $\hat{\mathbf{Y}}$-axis, the rotation of the monomers toward $\hat{\mathbf{E}}$ and $-\hat{\mathbf{E}}$ is symmetric and hence the distribution remains symmetric when the chain is subjected to electric field. Figs. (7a) and (7b) show the distributions of the uniaxial dipolar monomers belonging to a polymer subjected to $E = 50\,\frac{\text{MV}}{\text{m}}$ and biaxial stretches with $\lambda = 1$ and $\lambda = 5$, respectively. We inspect the ratio between the maximum radii with (continuous curve) and without (dotted curve) an applied electric field, and note that this ratio decreases as the polymer is stretched. We therefore conclude that the influence of the electric field on the rearrangement of the dipolar monomers in a chain diminishes with the stretch. We stress that in general, under a volume preserving deformation, there are chains whose monomers gain degrees of freedom and become more sensitive to the application of E and chains in which the mechanical constraints become stricter, limiting the rotation of the monomers, and thus diminishing the effect of the electric field.

Next, we examine the effects of the deformation on the macroscopic response of polymers with different electric moduli. Fig. (8a) depicts the dependence of $\tilde{P}$ on the planar stretch λ^2 of two polymers with different susceptibilities. As the polymer deforms, the mechanical constraints

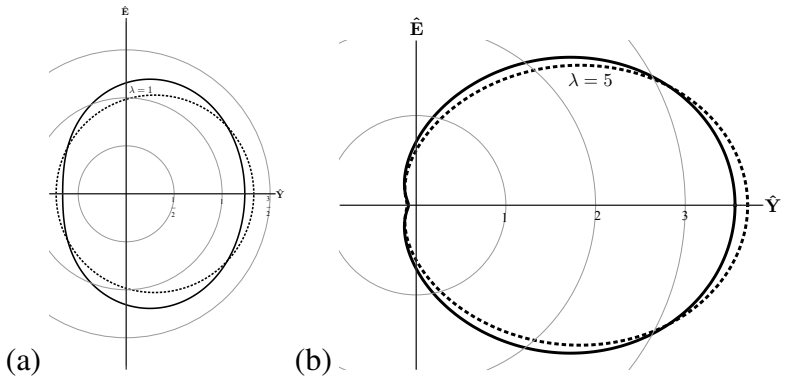


FIGURE 7. The distribution of the uniaxial dipolar monomers in chains whose end-to-end vectors are perpendicular to the electric field belonging to polymers with $\chi_0 = 37$ subjected to a biaxial stretch (a) $\lambda = 1$ and (b) $\lambda = 5$. The dotted and the continuous curves correspond to $E = 0 \frac{\text{MV}}{\text{m}}$ and $E = 50 \frac{\text{MV}}{\text{m}}$, respectively.

on chains with end-to-end vectors on the $\hat{\mathbf{Y}} - \hat{\mathbf{Z}}$ plane lead to a rotation of the uniaxial dipolar monomers away from $\hat{\mathbf{E}}$ and, as a result, the overall polarization decreases. We note that the curves describing the predicted polarization of the two polymers are roughly parallel. This is anticipated since the reorientation is due to a mechanical deformation at a fixed electric field and hence the influence of the susceptibility is fairly small.

Fig. (8b) shows the variation of the mechanically-dominated normalized stress components $\tilde{\sigma}^m$ along the $\hat{\mathbf{E}}$ and $\hat{\mathbf{Y}}$ directions versus λ^2 for the same two polymers. Before we proceed, we stress that $\boldsymbol{\sigma}^m$ strongly depends on the deformation and, as expected, admits the lock-up effect due to the limiting chain extensibility of the polymers. However, since in this work we explore the *coupled* behavior of the polymer, we examine the difference in the dependence of the stress on the deformation with and without the application of an electric field. For this reason we show the variations of the normalized quantity $\tilde{\sigma}^m$. Note that for the two polymers the two components of the normalized stress $\tilde{\sigma}^m$ are roughly constant. This implies that under a prescribed electric field, the trend of the mechanically-dominated stress is almost identical to the one obtained in the absence of the electric field. Nonetheless, due to the effect of the electric field at $\lambda^2 = 1$, $\tilde{\sigma}^m \neq 1$.

Next, we examine two polymers with transversely isotropic monomers. Their initial susceptibilities are 3.7 and 37 as before, and the chains are made up of 100 dipolar monomers. To highlight the response of these monomers to the electric field we examine first two specific chains of the polymer with $\chi_0 = 37$. In a manner similar to Figs. (3) and (4), Figs. (9a) and (9b) present polar plots of the distributions on the plane spanned by $\hat{\mathbf{E}}$ and $\hat{\mathbf{Y}}$ of the dipolar monomers

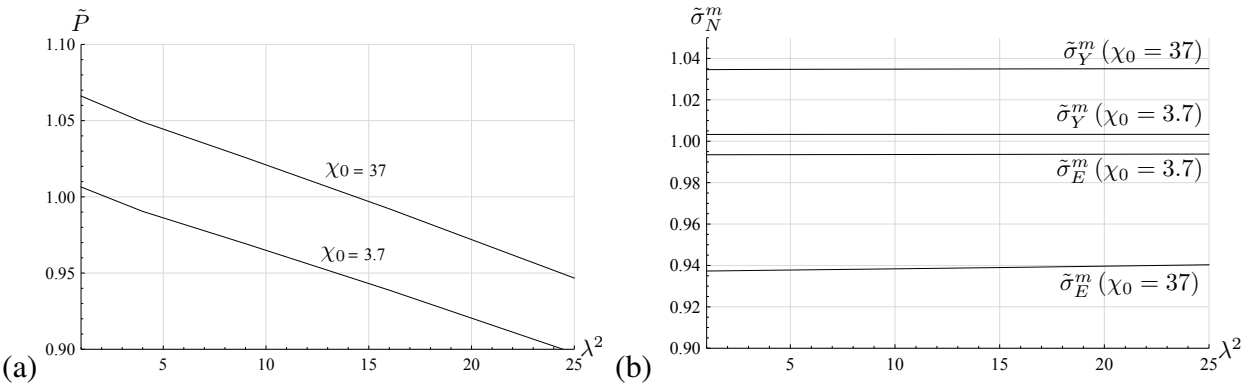


FIGURE 8. (a) $\tilde{P}$ and (b) $\tilde{\sigma}^m_E$ and $\tilde{\sigma}^m_Y$ versus the planar stretch λ^2 for chains composed of uniaxial dipolar monomers with two dipole constants subjected to an electric field $E = 50\ \frac{\text{MV}}{\text{m}}$.

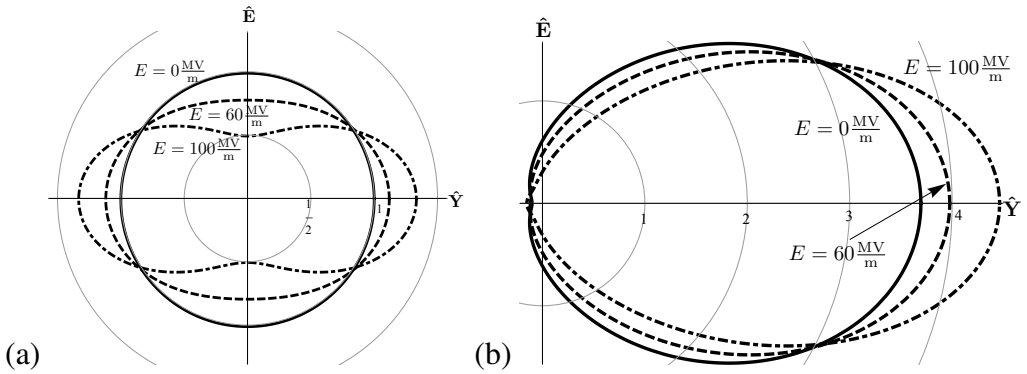


FIGURE 9. The distribution of the TI dipolar monomers in chains whose end-to-end vectors are along (a) the $\hat{\mathbf{E}}$ and (b) the $\hat{\mathbf{Y}}$ directions belonging to a polymer with $\chi_0 = 37$ under a stretch with $\lambda = 5$.

in chains whose end-to-end vectors are along the $\hat{\mathbf{E}}$ and the $\hat{\mathbf{Y}}$ directions, respectively. These plots show that the electric field causes the monomers in both chains to rotate away from the direction of the electric field. This is a consequence of the local behavior of the TI dipole. Thus, since the dipoles are perpendicular to $\hat{\boldsymbol{\xi}}$, the tendency of the electric field to reorient them in order to increase the projection of their electric dipoles in the direction of $\hat{\mathbf{E}}$ results in the observed behavior.

Fig. (10a) depicts the normalized polarization $\tilde{P}$ as a function of E. The legend of this figure is identical to the one used in Fig. (5a). The polarization increases non-linearly with the electric field. In contrast with polymers with uniaxial dipoles, the pre-stretch results in redistribution of the monomers such that their dipoles rotate toward the electric field, resulting in an initial enhancement of the polarization. Fig. (10b) shows the mechanical stress $\tilde{\sigma}^m_N$ as a function of

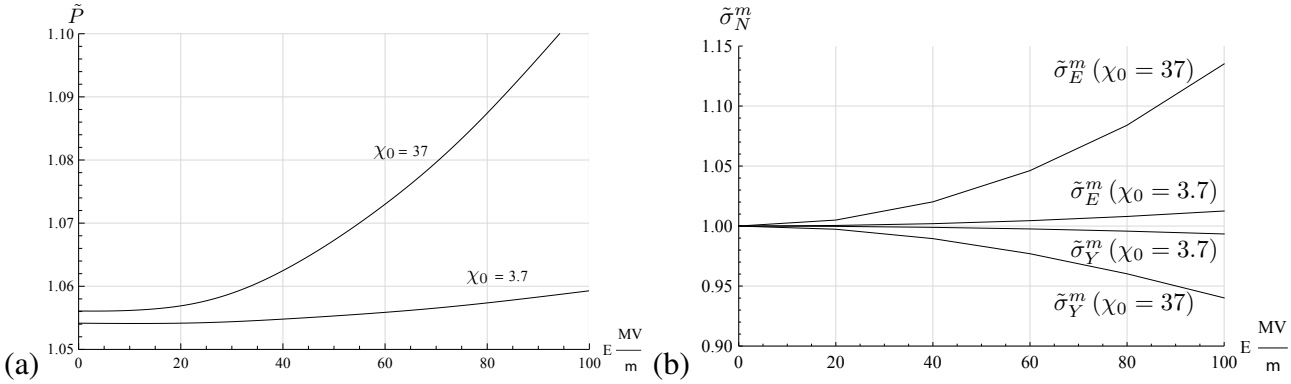


FIGURE 10. (a) $\tilde{P}$ and (b) $\tilde{\sigma}^m_E$ and $\tilde{\sigma}^m_Y$ versus E for polymers with TI dipolar monomers and two dipole constants subjected to a stretch $\lambda = 5$.

E, where we heed that the trends of the variations in σ^m_E and σ^m_Y are opposite to the ones revealed for polymers with uniaxial monomers. Thus, due to the shortening of the monomer projection in the $\hat{\mathbf{E}}$-direction, the variation in the mechanical stress along the direction of the electric field becomes more tensile, while in the perpendicular direction the stress becomes more compressive. We note that the dependence of the mechanical stress variations on $\mathbf{E}$ in polymers with TI monomers result in enhancement of the polarization stress in the direction of the electric field. This implies that polymers with TI dipoles may be preferable in applications for EAP actuators.

Figs. (11a) and (11b) depict the polar distributions of the 100 TI dipolar monomers composing a chain whose end-to-end vector is along the $\hat{\mathbf{E}}$-direction on the plane spanned by $\hat{\mathbf{E}}$ and $\hat{\mathbf{Y}}$ for various stretch values. Analogous plots for a chain whose end-to-end vector is along the $\hat{\mathbf{Y}}$-direction is shown in Figs. (12a) and (12b). When excited by an electric field (continuous curves) the TI dipolar monomers of both chains rotate away from the direction of the electric field in order to orient the dipoles along its direction. At high stretch ratios a chain with an end-to-end vector in the direction of the electric field shortens, resulting in a more symmetric distribution of the monomers orientations. This also provides the monomers more freedom to reoriet with the electric field. At the other hand, the end-to-end vectors that are perpendicular to the electric field elongate at $\lambda = 5$ and hence the monomers ability to reorient with the field diminishes. This can be seen from the proximity of the continuous and the dashed curves in Fig. (12b).

In Figs. (13a) and (13b) $\tilde{P}$ and the components of $\tilde{\boldsymbol{\sigma}}^m$ are plotted as functions of λ^2 for polymers composed of 100 TI dipolar monomers with two different susceptibilities, respectively. As discussed previously with relation to Figs. (12a) and (12b), as the planar deformation increases,

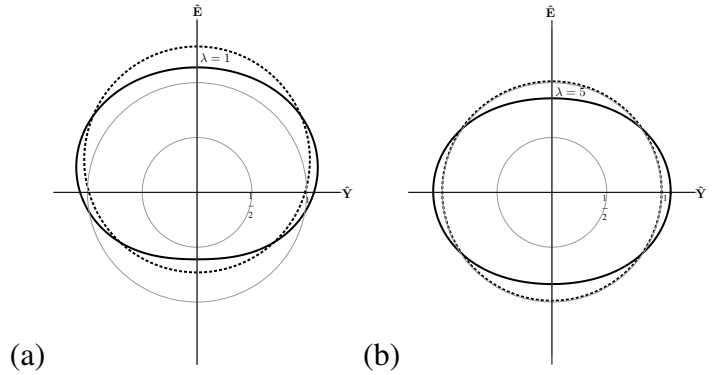


FIGURE 11. The distribution of the TI dipolar monomers in chains aligned with the electric field belonging to polymers with $\chi_0 = 37$ subjected to a biaxial pre-stretch (a) $\lambda = 1$ and (b) $\lambda = 5$. The dotted and the continuous curves correspond to $E = 0\ \frac{\text{MV}}{\text{m}}$ and $E = 50\ \frac{\text{MV}}{\text{m}}$, respectively.

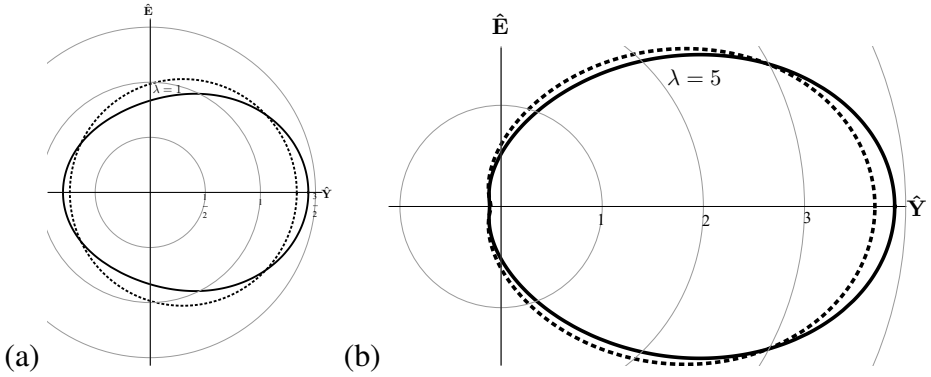


FIGURE 12. The distribution of the TI dipolar monomers in chains whose end-to-end vector is perpendicular to the electric field belonging to polymers with $\chi_0 = 37$ subjected to a biaxial pre-stretch (a) $\lambda = 1$ and (b) $\lambda = 5$. The dotted and the continuous curves correspond to $E = 0\ \frac{\text{MV}}{\text{m}}$ and $E = 50\ \frac{\text{MV}}{\text{m}}$, respectively.

the freedom of the monomers belonging to chains whose end-to-end vectors lie on the plane transverse to the electric field to rotate becomes limited. However, thanks to the local behavior of the TI dipoles, the planar deformation causes these dipoles to align with the electric field and, consequently, to increase the polarization. As expected, this effect is more pronounced in polymers with higher susceptibilities.

The trend of the mechanically-dominated stress components $\tilde{\sigma}^m_E$ and $\tilde{\sigma}^m_Y$ shown in Fig. (13b) is similar to the one predicted for polymers composed of uniaxial dipoles (Fig. (8b)). However, as mentioned in the context of Fig. (10b), the electric field increases the mechanically-dominated stress component in the direction of the electric field and decreases the component in the transverse direction.

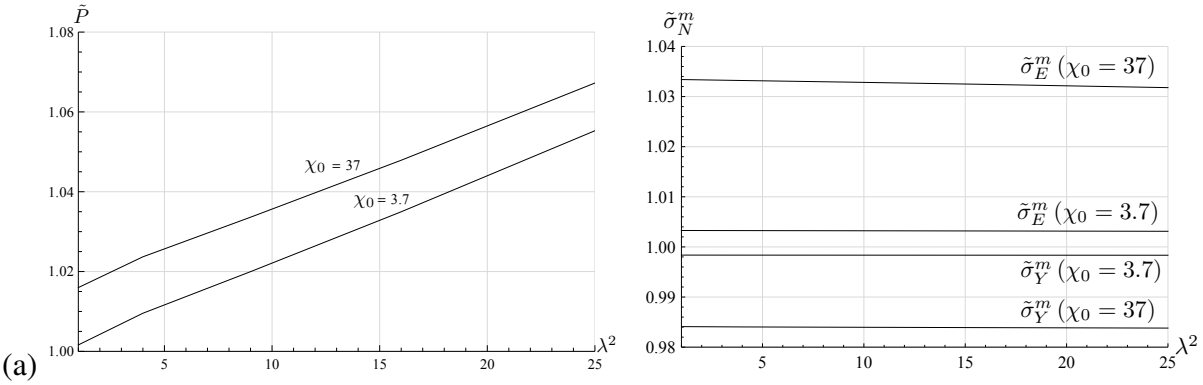


FIGURE 13. (a) $\tilde{P}$ and (b) $\tilde{\sigma}^m_E$ and $\tilde{\sigma}^m_Y$ versus λ^2 for polymers with TI dipolar monomers and two dipole constants subjected to an electric field $E = 50\,\frac{\text{MV}}{\text{m}}$.

5.2. **The role of the length of the chain.** The influence of the number of dipolar monomers per chain on the overall response is examined next. We consider four polymers with chains composed of 25, 100, 500 and 1000 uniaxial monomers and an initial susceptibility $\chi_0 = 3.7$. Figs. (14a) and (14b) depict $\tilde{P}$ as a function of the electric field in polymers subjected to biaxial pre-stretch with $\lambda = 3$ and $\lambda = 5$, respectively. The dashed and continuous curves correspond to the long-chain approximation (71) and the associated full model predictions, respectively. The polarization of polymers with $n = 500$ and $n = 1000$ is almost constant with the electric field under the imposed stretches. For these polymers the long-chains approximation provides excellent predictions. For polymers with chains composed of 100 monomers at $\lambda = 3$ this approximation still holds. If the polymer is further stretched up to $\lambda = 5$ the long-chain approximation slightly overestimates the polarization.

In general, Figs. (14a) and (14b) demonstrate that the polarization increases with the electric field. This effect is more pronounced in short-chain polymers as evident from the results for $n = 25$. This short-chain polymer locks-up at $\lambda = 5$, and hence up to $E = 100$ has a very low polarization ($\tilde{P}$ in the range between 0.4 and 0.44), which is not shown in Fig (14b).

Another important observation that can be drawn from these plots is that the polarization of polymers with uniaxial dipoles increases with the length of the chain. In order to explain this observation, consider two chains with 25 and 1000 monomers whose end-to-end vector lies on the plane perpendicular to $\hat{\mathbf{E}}$. In the limit $\lambda \to 5$ the short chain is fully stretched, and its uniaxial dipoles are oriented normal to the electric field. Consequently the dipole of this chain is practically zero. Conversely, at this stretch ratio the monomers of the long chain still possess freedom to reorient and some have projections along the electric field, rendering a non-zero

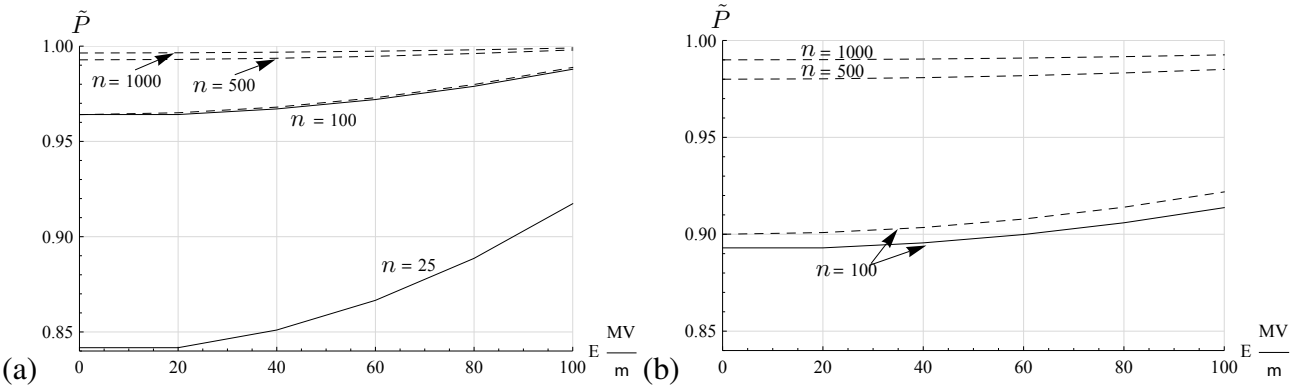


FIGURE 14. $\tilde{P}$ versus E according to the proposed model for polymers with $\chi_0 = 3.7$ and chains containing different numbers of uniaxial dipoles subjected to biaxial stretch loading with (a) $\lambda = 3$ and (b) $\lambda = 5$.

chain dipole. These two extreme examples demonstrate the higher sensitivity of polymers with shorter chains to the applied stretch.

It was shown in connection with Fig. (14) that the macroscopic behavior of polymers strongly depends on n when the deformation is held fixed and the electric field is varied. Next, we carry the opposite analysis and fix the electric field while varying the deformation. Figs. (15a) and (15b) depict $\tilde{P}$ as a function of the planar stretch with $E = 1\,\frac{\text{MV}}{\text{m}}$ and $E = 50\,\frac{\text{MV}}{\text{m}}$ for four different values of n, respectively. The polymers are made out of uniaxial dipolar monomers and their initial susceptibility is $\chi_0 = 3.7$. We once again employ the long-chains approximation Eq. (74) for the cases $n = 1000$ and $n = 500$. Due to the normalization of $\mathbf{P} \cdot \hat{\mathbf{E}}$, the curves obtained for $E = 1\,\frac{\text{MV}}{\text{m}}$ and $E = 50\,\frac{\text{MV}}{\text{m}}$ for the polymers with the long-chain approximation are practically identical. The long-chains approximation holds nicely even for polymers with 100 monomer chains. Furthermore, it is again demonstrated that the variation of the polarization is proportional to the chain length.

Figs. (16a) and (16b) show $\tilde{P}$ as a function of E for four polymers with chains of different lengths composed of TI dipolar monomers subjected to biaxial stretch with $\lambda = 3$ and $\lambda = 5$, respectively. Here, the stretch results in aligning of the dipoles of the chains whose end-to-end vectors are perpendicular to $\hat{\mathbf{E}}$ and consequently two main effects are observed. The first is an increase in the polarization with the stretch and the second is that short-chain polymers exhibit higher growth rate of the polarization with the stretch.

Lastly, we examine the dependence of the responses of polymers with different chain-lengths composed of TI dipolar monomers to the applied deformation. The predicted normalized

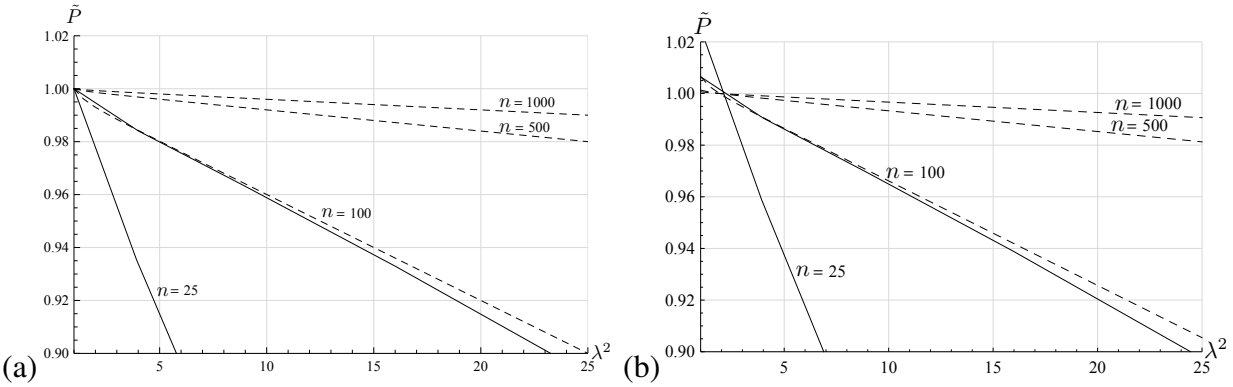


FIGURE 15. $\tilde{P}$ versus λ^2 for polymers with $\chi_0 = 3.7$ and chains composed of uniaxial dipoles with different chain lengths subjected to (a) $E = 1\,\frac{\text{MV}}{\text{m}}$ and (b) $E = 50\,\frac{\text{MV}}{\text{m}}$.

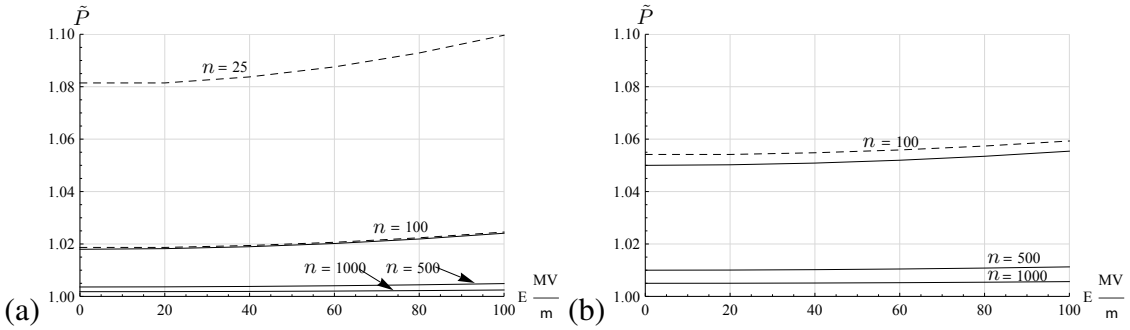


FIGURE 16. $\tilde{P}$ versus E according to the proposed model for polymers with $\chi_0 = 3.7$ and chains containing different numbers of TI dipoles subjected to biaxial stretch loading with (a) $\lambda = 3$ and (b) $\lambda = 5$.

polarization $\tilde{P}$ as a function of the planar stretch for applied electric fields $E = 1\,\frac{\text{MV}}{\text{m}}$ and $E = 50\,\frac{\text{MV}}{\text{m}}$ are shown in Figs. (17a) and (17b), respectively. The predicted polarization increases with the stretch, as explained in connection with Fig. (13a). In this case too the long-chains approximation holds for chains with 100 TI dipolar monomers.

6. Conclusions

This work introduces an entropy-based multiscale analysis of the electromechanical coupling in dielectric elastomers. Initially, the variational principles for the electrical enthalpy-density and the entropy-density are written in accordance with the first and the second laws of thermodynamics. Next, the conformations that a polymer chain can occupy are considered. Following common practice, we assume that the configuration of the chain that maximizes the entropy is

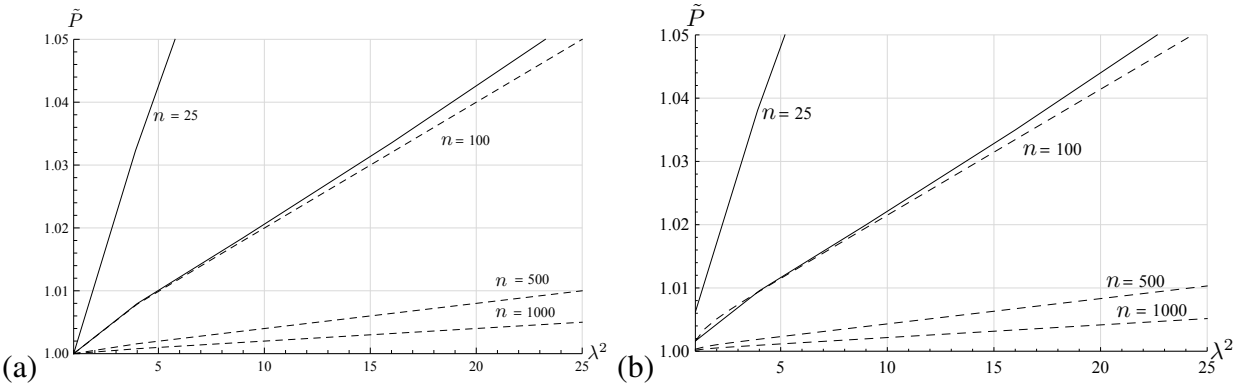


FIGURE 17. $\tilde{P}$ versus λ^2 for polymers with $\chi_0 = 3.7$ and chains that are composed of TI dipoles with different chain lengths subjected to (a) $E = 1\,\frac{\text{MV}}{\text{m}}$ and (b) $E = 50\,\frac{\text{MV}}{\text{m}}$.

the one corresponding to the most probable distribution of the dipolar monomers. Next, the general expressions for the polarization and the stress that develop in the dielectric are derived.

To determined the macroscopic coupled response of specific polymer networks three models for the local behaviors at the monomer level are considered: a spontaneous dipole (Blythe and Bloor, 2008), a uniaxial dipole and a TI dipole (Stockmayer, 1967; Cohen and deBotton, 2015). We first consider the purely electrical response of amorphous dielectrics. The predicted polarization of the dielectric in response to an electric field according to the three models is determined and compared with a macroscopic approach that assumes a constant permittivity. We find that none of these models agrees with the assumed linear behavior, and while the spontaneous dipole model leads to saturation of the polarization, the other two models admit a bi-linear response at the macroscopic level.

Next, a long-chain approximation for the polarization and the stress in polymers with chains composed of a large number of dipolar monomers is determined. We reveal that the macroscopic coupled response of the polymers crucially depends on three key parameters – the type of the dipolar monomers composing the chain, the magnitude of the microscopic dipoles and the number of dipolar monomers in a chain. Accordingly, a thorough investigation of the influence of these three parameters is carried out by tracking the variations of the directional distributions of the monomers along the chains. In passing, by comparing with the full model, we also demonstrate that the closed form long-chains approximation is valid for a wide range of polymeric chains and stretch ratios as large as 3. A particularly interesting result concerns the dependence of the mechanical stress on the electric field. We find that this dependence, which is

commonly neglected in phenomenological models, can have a large impact on the macroscopic response. Moreover, these electric field induced variations in the mechanical stress may enhance or oppose the polarization stress stemming from the interaction of the dipolar monomers with the field.

The findings of this work shed light on the relations between the molecular structure of polymers and the origin of their coupled electromechanical behavior. In turn, the analysis presented herein can pave the path to the enhancement of the poor electromechanical coupling in dielectric elastomers that hinders their widespread applications. Finally, while beyond the scope of this paper, one can also derive an electroelastic energy density starting either from the partition function or through transformation of the macroscopic thermodynamic quantities H and S. Such an energy density would provide microscopically-motivated constitutive input to calculations such as ones carried out by Xie et al. (2008); Rudykh et al. (2013); Tian et al. (2012); Galipeau and Ponte Castaneda (2012); Gei et al. (2013); Spinelli et al. (2015), among others.

Acknowledgement. The work of Noy Cohen and Gal deBotton was supported by the Israel Science Foundation founded by the Israel Academy of Sciences and Humanities (grant 1246/11). Kaushik Dayal thanks NSF Mechanics of Materials (CAREER 1150002), AFOSR Computational Mathematics (YI FA9550-12-1-0350), ARO Numerical Analysis (YI W911NF-12-1-0156), ONR Applied and Computational Analysis (N00014-14-1-0715), and Carnegie Mellon University College of Engineering for an Early Career Fellowship.

References

Arruda, E. M. and Boyce, M. C. (1993). A three-dimensional constitutive model for the large stretch behavior of rubber elastic materials, *J. Mech. Phys. Solids* **41**: 389–412.

Ask, A., Menzel, A. and Ristinmaa, M. (2012a). Electrostriction in electro-viscoelastic polymers, *Mechanics of Materials* **50**: 9–21.

Ask, A., Menzel, A. and Ristinmaa, M. (2012b). Phenomenological modeling of viscous electrostrictive polymers, *Int. J. Nonlinear Mech.* **47**: 156—165.

Bar-Cohen, Y. (2001). EAP history, current status, and infrastructure, *in* Y. Bar-Cohen (ed.), *Electroactive Polymer (EAP) Actuators as Artificial Muscles*, SPIE press, Bellingham, WA, chapter 1, pp. 3–44.

Blythe, T. and Bloor, D. (2008). *Electrical Properties of Polymers*, 2 edn, Cambridge University Press, Cambridge, UK.

Bustamante, R. (2009). Transversely isotropic non-linear electro-active elastomers, *Acta. Mech.* **206**: 237–259.

Carpi, F., Bauer, S. and De Rossi, D. (2010). Stretching dielectric elastomer performance, *Science* **330**(6012): 1759–1761.

Cohen, N. and deBotton, G. (2014). Multiscale analysis of the electromechanical response of dielectric elastomers, *Eur. J. Mech. A-Solids* **48**: 48–59.

Cohen, N. and deBotton, G. (2015). The electromechanical response of polymer networks with long-chain molecules, *Math. Mech. Solids* **20**: 721–728.

Cohen, N., Menzel, A. and deBotton, G. (2015). Application of the microsphere framework to model the electromechanical response of EAPs, *Submitted for publication*.

Coleman, B. D. and Noll, W. (1963). The thermodynamics of elastic material with heat conduction and viscosity, *Arch. Rational. Mech. Anal.* **13**: 167–178.

Davidson, N. (1962). *Statistical mechanics*, McGraw Hill series in advanced chemistry, McGraw-Hill, New York.

deBotton, G., Tevet-Deree, L. and Socolsky, E. A. (2007). Electroactive heterogeneous polymers: analysis and applications to laminated composites, *Mechanics of Advanced Materials and Structures* **14**: 13–22.

Debye, P. J. W. (1929). *Polar molecules*, The Chemical Catalog Company, Inc., New York.

Deng, Q., Liu, L. and Sharma, P. (2014). Electrets in soft materials: Nonlinearity, size effects, and giant electromechanical coupling, *Phys. Rev. E* **90**: 012603.

Di Lillo, L., Schmidt, A., Carnelli, D. A., Ermanni, P., Kovacs, G., Mazza, E. and Bergamini, A. (2012). Measurement of insulating and dielectric properties of acrylic elastomer membranes at high electric fields, *J. Appl. Phys.* **111**(2): 024904.

Dorfmann, A. and Ogden, R. W. (2005). Nonlinear electroelasticity, *Acta. Mech.* **174**: 167–183.

Dorfmann, A. and Ogden, R. W. (2014). *Nonlinear Theory of Electroelastic and Magnetoelastic Interactions*, Springer, New York.

Flory, P. J. (1953). *Principles of polymer chemistry*, Cornell Univ Press, Ithaca, NY.

Flory, P. J. and Rehner, J. (1943). Statistical mechanics of cross-linked polymer networks I. rubberlike elasticity, *The Journal of Chemical Physics* **11**(11): 512–520.

Fröhlich, H. (1949). *Theory of dielectrics; dielectric constant and dielectric loss*, first edn, Clarendon Press, Oxford, UK.

Galipeau, E. and Ponte Castaneda, P. (2012). The effect of particle shape and distribution on the macroscopic behavior of magnetoelastic composites, *International Journal of Solids and Structures* **49**: 1–17.

Gei, M., Colonnelli, S. and Springhetti, R. (2013). The role of electrostriction on the stability of dielectric elastomer actuators, *Int. J. Solids Struct.* **51**: 848—860.

Huang, C., Zhang, Q. M., deBotton, G. and Bhattacharya, K. (2004). All-organic dielectric-percolative three-component composite materials with high electromechanical response, *Applied Physics Letters* **84**: 4391–4393.

Hutter, K., van de Ven, A. A. F. and Ursescu, A. (2006). *Electromagnetic Field Matter Interactions in Thermoelasic Solids and Viscous Fluids*, number 710 in *Lecture Notes in Physics*, 2nd edn, Springer, Berlin Heidelberg.

James, R. and Müller, S. (1994). Internal variables and fine-scale oscillations in micromagnetics, *Continuum Mechanics and Thermodynamics* **6**: 291–336.

Jiménez, S. M. A. and McMeeking, R. M. (2013). Deformation dependent dielectric permittivity and its effect on actuator performance and stability, *Int. J. Nonlinear Mech.* **57**: 183–191.

Kofod, G., Sommer-Larsen, P., Kornbluh, R. and Pelrine, R. (2003). Actuation response of polyacrylate dielectric elastomers, *Journal of Intelligent Material Systems and Structures* **14**: 787–793.

Kuhn, W. and Grün, F. (1942). Beziehungen zwischen elastischen konstanten und dehnungsdoppelbrechung hochelastischer stoffe, *Colloid & Polymer Science* **101**: 248–271.

Lopez-Pamies, O. (2014). Elastic dielectric composites: Theory and application to particle-filled ideal dielectrics, *J. Mech. Phys. Solids* **64**: 61–82.

Marshall, J. and Dayal, K. (2014). Atomistic-to-continuum multiscale modeling with long-range electrostatic interactions in ionic solids, *J. Mech. Phys. Solids* **62**: 137–162.

McKay, T. G., Calius, E. P. and Anderson, I. A. (2009). The dielectric constant of 3m vhb: a parameter in dispute, *in* Y. Bar Cohen and T. Wallmersperger (eds), *Electroactive Polymer Actuators and Devices (EAPAD)*, Vol. 7287, Bellingham, WA.

McKay, T., O'Brien, B., Calius, E. and Anderson, I. (2010). An integrated, self-priming dielectric elastomer generator, *Applied Physics Letters* **97**: 062911.

McMeeking, R. M., Landis, C. M. and Jimenez, S. M. A. (2007). A principle of virtual work for combined electrostatic and mechanical loading of materials, *Int. J. Nonlinear Mech.* **42**(6): 831–838.

Miehe, C., Göktepe, S. and Lulei, F. (2004). A micro-macro approach to rubber-like materials–part i: the non-affine micro-sphere model of rubber elasticity, *J. Mech. Phys. Solids* **52**: 2617–2660.

Ogden, R. W. (1997). *Non-Linear Elastic Deformations*, Dover Publications, New York.

Pelrine, R., Kornbluh, R., Joseph, J., Heydt, R., Pei, Q. and A., C. (2000a). High-field deformation of elastomeric dielectrics for actuators, *Materials science and engineering* **11**: 89–100.

Pelrine, R., Kornbluh, R., Pei, Q.-B. and Joseph, J. (2000b). High-speed electrically actuated elastomers with strain greater than 100%, *Science* **287**: 836–839.

Qiang, J., Chen, H. and Li, B. (2012). Experimental study on the dielectric properties of polyacrylate dielectric elastomer, *Smart Mater. Struct.* **21**: 025006.

Rudykh, S., Bhattacharya, K. and deBotton, G. (2012). Snap-through actuation of thick-wall electroactive balloons, *Int. J. Nonlinear Mech.* **47**: 206–209.

Rudykh, S., Lewinstein, A., Uner, G. and deBotton, G. (2013). Analysis of microstructural induced enhancement of electromechanical coupling in soft dielectrics, *Appl. Phys. Lett.* **102**: 151905.

Shmuel, G. and deBotton, G. (2013). Axisymmetric wave propagation in finitely deformed dielectric elastomer tubes, *Proc. R. Soc. Lond. A* **469**: 20130071.

Shmuel, G., Gei, M. and deBotton, G. (2012). The Rayleigh-Lamb wave propagation in dielectric elastomer layers subjected to large deformations, *Int. J. Nonlinear Mech.* **47**: 307–316.

Spinelli, S. A., Lefèvre, V. and Lopez-Pamies, O. (2015). Dielectric elastomer composites: A general closed-form solution in the small-deformation limit, *Journal of the Mechanics and Physics of Solids* **83**: 263–284.

Stockmayer, W. H. (1967). Dielectric dispersion in solutions of flexible polymers, *Pure Appl. Chem.* **15**: 539–554.

Stoyanov, H., Kollosche, M., McCarthy, D. N. and Kofod, G. (2010). Molecular composites with enhanced energy density for electroactive polymers, *J. Mater. Chem.* **20**: 7558–7564.

Su, T. and Purohit, P. K. (2012). Semiflexible filament networks viewed as fluctuating beam-frames, *Soft Matter* **8**: 4664–4674.

Thylander, S., Menzel, A. and Ristinmaa, M. (2012). An electromechanically coupled micro-sphere framework: Application to the finite element analysis of electrostrictive polymers, *Smart Materials and Structures* **21**: 094008.

Tian, L., Tevet-Deree, L., deBotton, G. and Bhattacharya, K. (2012). Dielectric elastomer composites, *J. Mech. Phys. Solids* **60**: 181–198.

Tiersten, H. F. (1990). *A Development of the Equations of Electromagnetism in Material Continua*, Vol. 36 of *Springer Tracts in Natural Philosophy*, Springer-Verlag, New York.

Toupin, R. A. (1956). The elastic dielectric, *Indiana Univ. Math. J.* **5**: 849–915.

Treloar, L. R. G. (1946). The elasticity of a network of long-chain molecules. III, *Trans. Faraday Soc.* **42**: 83–94.

Treloar, L. R. G. (1975). *The Physics of Rubber Elasticity*, Clarendon Press, Oxford.

Wang, M. C. and Guth, E. (1952). Statistical theory of networks of non-gaussian flexible chains, *J. Chem. Phys.* **20**: 1144–1157.

Warner, M. and Terentjev, E. M. (2003). *Liquid Crystal Elastomers*, Oxford University Press, Oxford, UK.

Wissler, M. and Mazza, E. (2007). Electromechanical coupling in dielectric elastomer actuators, *Sensors and Actuators A: Physical* **138**: 384–393.

Xie, S. H., Liu, Y. Y. and Li, J. Y. (2008). Comparison of the effective conductivity between composites reinforced by graphene nanosheets and carbon nanotubes, *Applied Physics Letters* **92**: 243121.

Zhao, X. and Suo, Z. (2008). Electrostriction in elastic dielectrics undergoing large deformation, *J. Appl. Phys.* **104**: 123530.

Disclinations without Gradients: A Nonlocal Model for Topological Defects in Liquid Crystals

Robert Buarque de Macedo*, Hossein Pourmatin†, Kaushik Dayal‡

*Department of Physics, Carnegie Mellon University

†‡Department of Civil and Environmental Engineering, Carnegie Mellon University

October 11, 2015

Abstract

Nematic liquid crystals composed of rod-like molecules have an orientational elasticity that accounts for the energetics of the molecular orientation. This elasticity can be described by a unit vector field; the unit vector constraint interacts with even fairly simple boundary conditions to cause disclination defects. Disclinations are entirely a topological consequence of the kinematic constraint, and occur irrespective of the particular energetic model. Because disclinations are topological defects, they cannot be regularized by adding higher gradients, as in phase-field models of interface defects. On the contrary, the higher gradient terms would cause even greater singularities in the energy. In this paper, we formulate an integral-based nonlocal regularized energy for nematic liquid crystals. Our model penalizes disclination cores and thereby enforces a finite width, while the integral regularization ensures that the defect core energy is bounded and finite. The regularization at the same time tends to the standard gradient-based energies away from the disclination, as well as building in the head-tail symmetry. We characterize the formulation in its ability to describe disclinations of various strengths, and then apply it to examine: (1) the stability and decomposition of various disclinations, and the competition between bend and splay energies in determining the relative stability of integer and half-integer disclinations (2) the coalescence of a $+\frac{1}{2}$ and $-\frac{1}{2}$ disclination pair; we find the disclinations do *not* move at the same velocities towards each other, suggesting that the asymmetry of the director field plays a dominant role despite the equal-and-opposite topological strengths of the disclinations.

1 Introduction

Nematic liquid crystals are composed of rod-like molecules that have no positional ordering but tend to align along the same direction. There is therefore an energetic penalty – an orientational elasticity – for spatial variations in the direction. In a continuum mesoscale description, the kinematics of the

*Email: rabm1993@gmail.com

†Email: mpourmat@andrew.cmu.edu

‡Email: kaushik@cmu.edu

orientational ordering can be described by a unit vector field $\boldsymbol{n}$– the *director field* – that tracks the average ordering of the molecules. The orientational elasticity is then described by an energy that depends on $\nabla \boldsymbol{n}$ in a very nonlinear way [Ste04, KL07, CL00]. There are two key challenges associated with using $\nabla \boldsymbol{n}$. First, the director is constrained to be a unit vector field because it represents directions, i.e. $|\boldsymbol{n}| = 1$. Second, the head-tail symmetry of nonpolar liquid crystal molecules imposes the constraint that the energy is invariant under the transformation $\boldsymbol{n} \leftrightarrow -\boldsymbol{n}$.

These constraints make the model severely nonlinear. In addition, the constraints – in combination with boundary conditions – can lead to the formation of topological defects. Fig. 1 shows classical examples. The $+1$ disclination forms when the boundary conditions set the director on the boundaries. At some point in the interior, the director field must be discontinuous if it satisfies the unit constraint; in this ideal case, the disclination is at the center by symmetry. There is no way to set up the director field to be continuous everywhere with the given boundary conditions. The $+\frac{1}{2}$ disclination forms when the boundary conditions are as shown in the figure. In addition to the discontinuity at the center, the head-tail symmetry also leads to a discontinuous line (in 2D) if it is represented by a director vector field $\boldsymbol{n}$. If we assume that the vectors on the right edge all point upwards and follow the vectors anti-clockwise in the upper half and clockwise in the lower half, we find that the vectors point in opposite directions on either side of the line $(x_1 < 0, x_2 = 0)$.

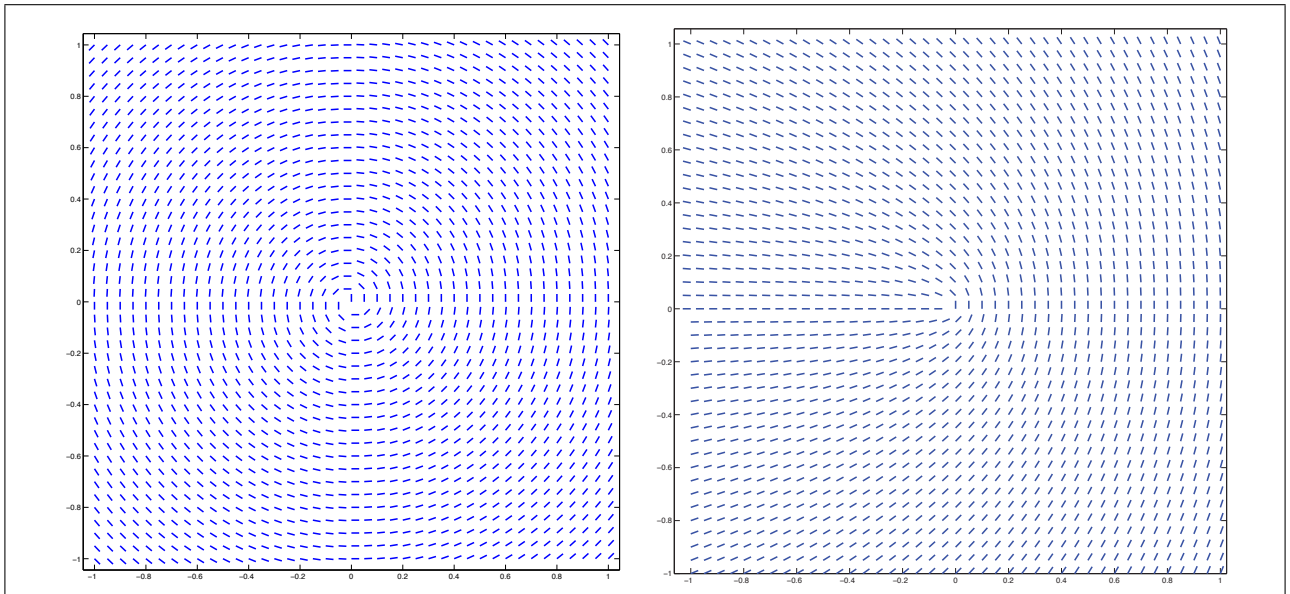


Figure 1: Left: A $+1$ disclination with a discontinuous director field at the center. Right: A $+\frac{1}{2}$ disclination with a discontinuous director field at the center, and a change in sense along any line running out from the disclination.

The topological nature of disclinations and their connection to boundary conditions is in contrast to interfaces, cracks, and other defects that are not topological. In the latter, boundary conditions certainly play an important role, but through the energy rather than geometry; i.e., whether a defect forms or not depends on the energetics of the particular model. An important consequence of this distinction is that phase-field models are readily constructed for the latter class of defects, because adding gradient contributions to the energy (accounting for surface energies) smooths out the discontinuities. In contrast, there is no such simple approach for disclinations which are driven by the boundary. Adding gradient contri-

butions to the energy cannot smooth out the defect; on the contrary, the presence of higher derivatives makes the energy more singular at a disclination.

A proposed approach for disclinations is by Ericksen [Eri91], in which he introduces a new scalar order parameter in addition to the director field. The scalar order parameter is used to track the disclination cores and evolves using a separate equation. Another approach in this spirit of introducing another field to track defects is [AD14, PAD15], where a tensor order parameter is introduced, and a geometrically-motivated evolution equation is posed. In contrast to these, we regularize the energy, but do not introduce a new field variable nor an associated evolution equation.

The most widely-applied regularized model that is used to model disclinations is the Q-tensor model [MN14]. Briefly, the order parameter is a tensor $\boldsymbol{Q}$ that is related to the tensor dyad $\boldsymbol{n} \otimes \boldsymbol{n}$[1] away from a defect, and at a defect the material is no longer uniaxial and cannot be described by a single director. At the defect core, the eigenvectors of $\boldsymbol{Q}$ aim to capture some key information about the orientational distribution function [MN14]. Core effects are introduced by energetic contributions in terms of the gradients of $\boldsymbol{Q}$. Q-tensor models, however, also make certain predictions that are significantly at odds with the director-based models. In the static setting, consider 2 infinite parallel plates with tangential anchoring and normal anchoring on the top and bottom respectively. As observed by [PMGK94], there are regimes in which the Q-tensor model predicts a loss of uniaxiality throughout the domain, i.e., the entire domain is defect-like. In contrast, the simple 1-constant director-based model has a solution with a linear variation of the angle from top to bottom. Similarly contrasting predictions are observed with the Q-tensor model in various geometries and boundary conditions, e.g. [BGJRV03, CLB$^+$09, BVD04]. In the dynamic setting, Ericksen and Leslie provided a clear physical model based on angular momentum balance for the evolution of the director [Ste04], whereas there is no similar clear principle for the evolution of $\boldsymbol{Q}$ in the Q-tensor model. Ideas from kinetic theory are sometimes used, e.g. [KLGCC08, YFMW09], but the issue of the closure law for the moments of the orientation distribution function is not clear.

The issues above motivate the current work. We propose a nonlocal (integral) regularization of the energy that accounts for core effects in a natural way, yet retains the many attractive features of a director field based model. First, the regularization introduces a length scale that enables us to describe disclinations with a finite width; second, using integrals rather than derivatives enables us to have disclinations of finite energy even when the director field is topologically constrained to be singular; third, we do not need to relax the unit vector constraint as some other models require; and finally, retaining the director field description enables the use of angular momentum principles to prescribe the evolution.

We note that it is particularly important not to relax the unit vector constraint; it is based on the direction corresponding to the orientation of the molecules, and hence relaxing the constraint to allow for non-unit vectors is not physically meaningful. Therefore, a regularization based on relaxing the unit-vector constraint is not particularly physical, even if it is computationally convenient.

We emphasize 3 important features of the proposed integral regularization of the energy:

- For homogeneous – i.e. linearly varying – director fields, we should recover the classical energy;
- Only a constant director field must have zero energy; any other spatial variation of the director field must cost energy;
- It should not require continuity of the field

[1] This ensures the head-tail symmetry is captured.

The first requirement ensures that we recover the standard Ericksen-Leslie model when we are far from disclinations or in disclination-free configurations. The second requirement ensures that our solutions are not "polluted" by unphysical zero-energy soft modes; except for rigid motions, the energy must increase when deformed. The third requirement ensures that disclinations can be modeled.

Our integral model is motivated largely by the peridynamic model of fracture, in which integral operators are used to approximate standard elasticity operators, thereby allowing fields to be discontinuous as is essential for fracture [Sil00, SL10].

We have ignored the coupling to fluid flow in this work. It is conceptually straightforward to replace the classical energy by our regularized energy to construct a model with director evolution coupled to flow.

1.1 Organization

The paper is organized as follows.

- In Section 2, we briefly outline the key features of the energetics of the classical model of liquid crystals. This is primarily to show the analogies and contrasts with our proposed model.
- In Section 3, we describe the proposed nonlocal regularized energy without gradients. Specifically, we (1) motivate the connection between integral operators and gradient operators, (2) formulate the nonlocal analog of the classical energy, (3) discuss the evolution equation and boundary conditions, and (4) extend the energy to account for head-to-tail symmetry.
- In Section 4, we incorporate the effects of different moduli for bend and splay.
- In Section 5, we examine the structure of disclinations, and the role of bend and splay in the stability of integer vs. half-integer disclinations.
- In Section 6, we examine the coalescence of a $+\frac{1}{2}$ disclination and $-\frac{1}{2}$ disclination coming together.

1.2 Notation, Definitions and Values of Model Parameters

Boldface denotes vectors and tensors. We have used Einstein convention, i.e. repeated indices imply summation over those indices, except when noted.

Hats appended to functions refer to their value at $\hat{\boldsymbol{x}}, \hat{\hat{\boldsymbol{x}}}, \ldots$, i.e. for a field $f(\boldsymbol{x})$, we write $\hat{f} \equiv f(\hat{\boldsymbol{x}}), \hat{\hat{f}} \equiv f(\hat{\hat{\boldsymbol{x}}}), \ldots$.

$\gamma_1 \equiv \alpha_3 - \alpha_2 \geq 0$ is the rotational or twist viscosity of the director. It sets the relaxation time of the director field. We set $\gamma_1 = 1$ in our model system. α_3 and α_2 are the Leslie viscosities [Ste04].

δ is a characteristic defect lengthscale, that we set to 5. Numerical calculations use a grid spacing of at least 1.

$C_\delta(|\boldsymbol{x} - \hat{\boldsymbol{x}}|)$ is the nonlocal weight function; we assume the form

$$C_\delta(|\boldsymbol{x} - \hat{\boldsymbol{x}}|) = \begin{cases} \frac{1}{\delta^2} & \text{if } |\boldsymbol{x} - \hat{\boldsymbol{x}}| < \delta \\ 0 & \text{if } |\boldsymbol{x} - \hat{\boldsymbol{x}}| \geq \delta \end{cases} \tag{1.1}$$

The normalization is appropriate for 2D.

2 Classical Model of Nematic Liquid Crystals

We briefly summarize the key features of classical nematic director dynamics to enable us to point out the key differences and similarities with our proposed nonlocal model. The classical model of nematic liquid crystals was formulated by Frank, and Ericksen and Leslie, and is very well described in [Ste04]. For simplicity, we neglect in this paper the effect of flow, i.e., we assume that the only dynamics is due to director reorientation. In addition, we use the standard assumption that the inertia associated with director reorientation is negligible.

The Frank free energy density w is in general a function of the local values of $\boldsymbol{n}$ and $\nabla\boldsymbol{n}$. The energy of the body Ω is $E[\boldsymbol{n}] = \int_\Omega w(\boldsymbol{n}, \nabla\boldsymbol{n})\, d\Omega$. We fix $\boldsymbol{n}$ or set $\epsilon_{ikl} n_{i,j} n_l \hat{\nu}_j = 0$ on the boundary $\partial\Omega$, and $|\boldsymbol{n}| = 1$.

In the simplified 1-constant approximation, $w = \frac{K}{2}|\nabla\boldsymbol{n}|^2$.

The classical approach relies on angular momentum balance [Ste04] to derive the evolution equation for $\boldsymbol{n}$. Equivalently, we can derive this using a gradient descent approach. We prefer the latter method here because it is easier to adapt to the nonlocal energy because we do not have to first identify a nonlocal torque, but can instead do so from the final form of the equation.

The gradient dynamics has the form $\gamma_1\langle\dot{\boldsymbol{n}}, \delta\boldsymbol{n}\rangle = -\frac{d}{d\varepsilon}E[\boldsymbol{n} + \varepsilon\delta\boldsymbol{n}]\big|_{\varepsilon=0}$. To preserve $|\boldsymbol{n}| = 1$, the variations in $\boldsymbol{n}$ must have the form $\delta n_i = \epsilon_{ijk} n_j p_k$, where p_k is arbitrary. The dynamical equation is then:

$$\gamma_1\dot{\boldsymbol{n}} \times \boldsymbol{n} = -\left(\frac{\partial w}{\partial \boldsymbol{n}} - \operatorname{div}\frac{\partial w}{\partial \nabla\boldsymbol{n}}\right) \times \boldsymbol{n} \Rightarrow \gamma_1\dot{\boldsymbol{n}} = -\left(\frac{\partial w}{\partial \boldsymbol{n}} - \operatorname{div}\frac{\partial w}{\partial \nabla\boldsymbol{n}}\right) + \lambda\boldsymbol{n} \tag{2.1}$$

where λ is the Lagrange multiplier conjugate to the constraint $|\boldsymbol{n}| = 1$. Enforcing $\boldsymbol{n}\cdot\boldsymbol{n} = 1 \Rightarrow \dot{\boldsymbol{n}}\cdot\boldsymbol{n} = 0$ to eliminate λ gives the dynamical equation:

$$\gamma_1\dot{\boldsymbol{n}} = -\left(\frac{\partial w}{\partial \boldsymbol{n}} - \operatorname{div}\frac{\partial w}{\partial \nabla\boldsymbol{n}}\right) + \left(\boldsymbol{n}\cdot\frac{\partial w}{\partial \boldsymbol{n}} - \boldsymbol{n}\cdot\operatorname{div}\frac{\partial w}{\partial \nabla\boldsymbol{n}}\right)\boldsymbol{n} \tag{2.2}$$

The dissipation associated with this dynamics is:

$$\begin{aligned} -\frac{dE}{dt} &= -\int_{\boldsymbol{x}\in\Omega}\left(\frac{\partial w}{\partial \boldsymbol{n}} - \operatorname{div}\frac{\partial w}{\partial \nabla\boldsymbol{n}}\right)\cdot\dot{\boldsymbol{n}}\, d\Omega \\ &= \frac{1}{\gamma_1}\int_{\boldsymbol{x}\in\Omega}\left|\left(\frac{\partial w}{\partial \boldsymbol{n}} - \operatorname{div}\frac{\partial w}{\partial \nabla\boldsymbol{n}}\right)\right|^2 - \left(\boldsymbol{n}\cdot\frac{\partial w}{\partial \boldsymbol{n}} - \boldsymbol{n}\cdot\operatorname{div}\frac{\partial w}{\partial \nabla\boldsymbol{n}}\right)^2 d\Omega \geq 0 \end{aligned} \tag{2.3}$$

The dissipation is strictly non-negative[2].

Equilibrium configurations are obtained by setting $\dot{\boldsymbol{n}} = 0$. In the 1-constant energy, this gives $\epsilon_{ikl} n_{i,jj} n_l = 0$.

[2] Gradient dynamics with a unit vector constraint is not necessarily dissipative. The Landau-Lifshitz-Gilbert (LLG) dynamics in micromagnetism (e.g., [AKST14]) is given by $\langle\dot{\boldsymbol{n}}, \boldsymbol{p}\rangle = -\frac{d}{d\varepsilon}E[\boldsymbol{n} + \varepsilon\delta\boldsymbol{n}]\big|_{\varepsilon=0}$ with $\delta n_i = \epsilon_{ijk} n_j p_k$, where p_k is arbitrary, in the undamped case. The inner product above is not the same as the Ericksen-Leslie dynamics, and it can be shown that the energy in the undamped LLG dynamics is conserved.

Alternatively, we can parametrize $\boldsymbol{n} = (\sin\theta(\boldsymbol{x}), \cos\theta(\boldsymbol{x}))$ which automatically satisfies the unit vector constraint[3]. Then, $n_{1,i} = \cos(\theta)\theta_{,i}$ and $n_{2,i} = -\sin(\theta)\theta_{,i}$, giving for 1-constant energy:

$$E[\theta] = \frac{K}{2}\int_\Omega \theta_{,i}\theta_{,i}\, d\Omega \tag{2.4}$$

The equilibrium configuration is described by $\theta_{,ii} = 0$ in Ω, with boundary conditions $\theta = \theta_0$ or $\theta_{,i}\nu_i = 0$ at each point on the boundary $\partial\Omega$. The description in terms of θ has the advantage that the unit vector constraint is exactly satisfied at all times for numerical solutions that discretize in time and use finite time steps. The description in terms of $\boldsymbol{n}$ will require a careful projection scheme at each time step to bring the director back to the unit sphere. Our approach for the nonlocal energy will be to formulate in terms of a unit vector field $\boldsymbol{n}$, but use θ for the numerical solution.

The head-tail symmetry is important to describe half-integer disclinations: even away from the core, there is a line (in 2D) across which the sense changes by π. Using either θ or a vector field for $\boldsymbol{n}$ does not allow us to do this easily with the classical energy, but will be possible with the proposed nonlocal regularization.

3 Nonlocal Regularized Free Energy Without Gradients

Our nonlocal regularized energy is motivated by the peridynamic model for fracture [Sil00, SL10] with some key differences. Peridynamics has provided an important model for fracture calculations because of the key feature that spatial derivatives are not required in the theory, hence allowing for discontinuous displacement fields.

3.1 A Motivating One-Dimensional Example

Consider the operator $\tilde{D}$ that acts on a function f as defined:

$$\tilde{D}f(x) = \frac{3}{2\delta^3}\int_{x-\delta}^{x+\delta} \left(f(x) - f(\hat{x})\right)(x-\hat{x})\; d\hat{x} \tag{3.1}$$

When $f(x) = Ax + B$, we evaluate $\tilde{D}f(x) = A$. For linear functions, $\tilde{D}f$ matches the derivative. Consider the Taylor expansion $f(x) - f(\hat{x}) = (x-\hat{x})f'(x) + \frac{1}{2}(x-\hat{x})^2 f''(x) + \ldots$. Then, $\tilde{D}f(x) = f'(x) + C_3\delta^2 f'''(x) + \ldots$, where the even derivatives vanish by symmetry. Therefore, the operator $\tilde{D}$ provides an approximation to the derivative when δ and the higher derivatives are sufficiently small. However, when f is not smooth such as at a discontinuity or other singularity where the derivatives are not well-defined, the original integral expression continues to be well-defined.

Physically, the operator can be understood as averaging the slope of f over a neighborhood of x of size δ, i.e., averaging $\frac{f(x)-f(\hat{x})}{x-\hat{x}}$. However, to avoid singularities from the denominator, we use the weight $(x-\hat{x})^2$ in the process of averaging. When the slope is constant, i.e. a linear function, we recover exactly the derivative; when the function is slowly varying, we get higher-order regularizing terms; and when the function does not have well-defined derivatives, we obtain a finite value that is physically related to the average slope in the neighborhood.

[3]This is in 2D, but the extension to 3D is straightforward.

While $\tilde{D}f$ provides an attractive alternative to the derivative df/dx, there is one key drawback. The derivative $df/dx = 0$ only when $f = \text{const.}$ and not otherwise. However, while $\tilde{D}f = 0$ when $f = \text{const.}$, it can also be 0 for other functions; in fact, any non-constant function that is antisymmetric about x will have the slopes exactly cancel out to give an average value of 0. Therefore, one can have spurious soft modes with zero energy that have no physical basis.

To get around this, we first observe that the free energy density consists of terms that are all components of the gradient raised to the second power [Ste04]. In the specific case of the 1-constant energy, the energy density is simply the gradient squared. In one dimension, this would require us to approximate $\left(\frac{df}{dx}\right)^2$. Motivated by the discussion immediately above, the operator

$$\tilde{D}_2 f(x) = \int_{x-\delta}^{x+\delta} \left(\frac{f(x) - f(\hat{x})}{x - \hat{x}} \right)^2 \, d\hat{x} \tag{3.2}$$

would provide a nonlocal regularized approximation up to normalization. The integrand is always non-negative, thereby not allowing any cancellations. For $\tilde{D}_2 f(x)$ to evaluate to 0, the integrand must be 0 everywhere, ensuring that $f = \text{const.}$ is the only possibility.

3.2 Nonlocal Regularization in Three Dimensions

Following ideas from peridynamics [Sil00], we write the nonlocal analog to the Frank energy as:

$$E[\boldsymbol{n}] = \frac{K}{2} \int_{\boldsymbol{x} \in \Omega} \int_{\hat{\boldsymbol{x}} \in \Omega} \frac{1}{2} C_\delta(\boldsymbol{x}, \hat{\boldsymbol{x}}) \, (\hat{n}_i - n_i) \, \frac{\hat{x}_j - x_j}{|\hat{\boldsymbol{x}} - \boldsymbol{x}|} \, (\hat{n}_i - n_i) \, \frac{\hat{x}_j - x_j}{|\hat{\boldsymbol{x}} - \boldsymbol{x}|} \, dV_{\hat{\boldsymbol{x}}} \, dV_{\boldsymbol{x}} \tag{3.3}$$

where C_δ is a function that is symmetric in the arguments.

What motivates this expression? The classical gradient is the vector pointing in the direction in which the increase of η is maximum. Our expression examines the change in $\boldsymbol{n}$ between $\boldsymbol{x}$ and every point $\hat{\boldsymbol{x}}$ in Ω, and weights the direction $\hat{\boldsymbol{x}} - \boldsymbol{x}$ by the change in that direction; the larger the increase, the greater the weight for that direction. So the direction of largest increase features most prominently in the average.

It is natural for points $\hat{\boldsymbol{x}}$ that are closer to $\boldsymbol{x}$ to play a larger role in the averaging, and this weighting is introduced by the function $C_\delta(\boldsymbol{x}, \hat{\boldsymbol{x}})$. This introduces a lengthscale, denoted δ, into our model that is not present in the classical Frank free energy. In this paper, we will restrict ourselves to isotropic and spatially homogeneous systems, and hence we will write $C_\delta(|\boldsymbol{x} - \hat{\boldsymbol{x}}|)$. Further, we use C_δ to introduce a cut-off distance, i.e. $C_\delta(|\boldsymbol{x} - \hat{\boldsymbol{x}}|) = 0$ when $|\boldsymbol{x} - \hat{\boldsymbol{x}}| > \delta$. Finally, for conciseness, we absorb $\frac{\hat{x}_j - x_j}{|\hat{\boldsymbol{x}} - \boldsymbol{x}|} \cdot \frac{\hat{x}_j - x_j}{|\hat{\boldsymbol{x}} - \boldsymbol{x}|}$ in (3.3) within C_δ by redefining it appropriately, but retaining the same symbol for convenience. Putting this together, we can write:

$$E[\boldsymbol{n}] = \frac{K}{2} \int_{\boldsymbol{x} \in \Omega} \int_{\hat{\boldsymbol{x}} \in \Omega} \frac{1}{2} C_\delta(|\boldsymbol{x} - \hat{\boldsymbol{x}}|) \cdot (\hat{\boldsymbol{n}} - \boldsymbol{n})^2 \, dV_{\hat{\boldsymbol{x}}} \, dV_{\boldsymbol{x}} \tag{3.4}$$

We now consider a physical interpretation of (3.4). From a physical perspective, the classical Frank model states that there is an energetic cost to molecules not being aligned with each other. Loosely, it penalizes changes in the molecular orientations at "adjacent" material points, and in the limit this becomes the gradient. Our model compares the molecular orientation at a point $\boldsymbol{x}$ with the molecular orientation at every point $\hat{\boldsymbol{x}}$ contained in Ω. To leading order, the energy contained in the interaction

between molecules at these points is $\frac{1}{2}C_\delta(|\boldsymbol{x}-\hat{\boldsymbol{x}}|)\left(\boldsymbol{n}(\boldsymbol{x})-\boldsymbol{n}(\hat{\boldsymbol{x}})\right)^2$, where $C_\delta(\boldsymbol{x},\hat{\boldsymbol{x}})$ is analogous to a spring constant and depends on the distance between the points. The total free energy simply sums over all pairs of molecules in Ω, with an additional factor of $\frac{1}{2}$ to correct for double-counting of bonds. While molecular interactions are typically very local, in homogeneous non-defect regions we can think of the molecular interactions as being renormalized.

3.3 Accounting for Head-Tail Symmetry

Typical nematic liquid crystal molecules are non-polar and have head-tail symmetry. That is, changing $\boldsymbol{n} \leftrightarrow -\boldsymbol{n}$ should not change any physical quantities. This is particularly important in half-integer disclinations, e.g. Fig. 1, where there is a plane – or line in 2D – across which the sense of the director changes. If represented by a unit vector field, the vector flips head-to-tail; if represented by θ in 2D, there is discontinuity of π. These discontinuities should not contribute to the energy or equilibrium equation. However, the energy in (3.4) is sensitive to such a transformation. We now discuss how to modify the energy to reflect the physics.

Consider two directors that are within δ. The minimum energy configuration is $\boldsymbol{n}_1 \cdot \boldsymbol{n}_2 = 1$ (they are parallel). The highest energy configuration is $\boldsymbol{n}_1 \cdot \boldsymbol{n}_2 = 0$ (they are normal). We further want that the configuration $\boldsymbol{n}_1 \cdot \boldsymbol{n}_2 = -1$ (they are anti-parallel) is a minimum energy state, with the same energy as the parallel state. Some choices of energy that satisfies this are $-|\boldsymbol{n}_1 \cdot \boldsymbol{n}_2| \equiv -|\cos(\theta_1-\theta_2)|$, $-(\boldsymbol{n}_1 \cdot \boldsymbol{n}_2)^2 \equiv -\cos^2(\theta_1-\theta_2)$, etc.

Consider now the integrand from (3.4). We can write $(\boldsymbol{n}-\hat{\boldsymbol{n}})^2 = 2-2\boldsymbol{n}\cdot\hat{\boldsymbol{n}} = 2-2\cos(\theta-\hat{\theta})$. Since it is an energy, we can ignore constants and write the energy as $-2\boldsymbol{n}\cdot\hat{\boldsymbol{n}} = -2\cos(\theta-\hat{\theta})$. From the discussion in the previous paragraph, it is clear that this does not behave well when $\boldsymbol{n}$ and $\hat{\boldsymbol{n}}$ are anti-parallel, and shows the problem with (3.4).

Based on these physical considerations, we replace the integrand in nonlocal energy density by $-\left|2-(\boldsymbol{n}-\hat{\boldsymbol{n}})^2\right| = -2\left|\boldsymbol{n}\cdot\hat{\boldsymbol{n}}\right|$. That is, we propose the following nonlocal regularized free energy:

$$E[\boldsymbol{n}] = \frac{K}{2}\int_{\boldsymbol{x}\in\Omega} \underbrace{\int_{\hat{\boldsymbol{x}}\in\Omega} \frac{1}{2}C_\delta(|\boldsymbol{x}-\hat{\boldsymbol{x}}|)\cdot -\left|2-(\boldsymbol{n}-\hat{\boldsymbol{n}})^2\right| \, dV_{\hat{\boldsymbol{x}}}}_{\text{free energy density at } \boldsymbol{x}} \, dV_{\boldsymbol{x}} \tag{3.5}$$

This recovers the classical model when the anti-parallel nature is not an issue because it is quadratic in $\boldsymbol{n}-\hat{\boldsymbol{n}}$. It is obvious that our proposed expression does not impose any continuity requirements on $\boldsymbol{n}$. The energy density – and therefore the total energy – is bounded and well-defined even if $\boldsymbol{n}$ has all kinds of discontinuities, as long as $\boldsymbol{n}$ itself remains bounded; this is automatic due to the unit vector constraint. It is also obvious that the energy density is non-zero except for constant fields if we restrict $C_\delta(|\boldsymbol{x}-\hat{\boldsymbol{x}}|) \geq 0$ because the integrand is non-negative.

We could, in principle, use many other expressions that resolve the head-tail issue, e.g. $-2(\boldsymbol{n}\cdot\hat{\boldsymbol{n}})^2$ for the free energy density. But these would not recover the classical model in the limit.

3.4 Equilibrium and Evolution Equations

The equilibrium equation is obtained from setting the functional derivative of the energy from (3.5) to 0. That is, $\frac{d}{d\varepsilon}E\left[\boldsymbol{n}+\varepsilon\delta\boldsymbol{n}\right]\big|_{\varepsilon=0} = 0$. To satisfy the unit vector constraint on $\boldsymbol{n}$, we use the variation

$\delta n_i = \epsilon_{ijk} n_j p_k$ where $\boldsymbol{p}$ is an arbitrary vector field. This gives:

$$\begin{aligned} 0 &= \frac{K}{2}\int_{\boldsymbol{x}\in\Omega}\int_{\hat{\boldsymbol{x}}\in\Omega} C_\delta(|\boldsymbol{x}-\hat{\boldsymbol{x}}|)\cdot \operatorname{sign}(2-(\boldsymbol{n}-\hat{\boldsymbol{n}})^2)\cdot \epsilon_{ijk}\left(n_i-\hat{n}_i\right)\left(n_j p_k-\hat{n}_j\hat{p}_k\right)\, dV_{\hat{\boldsymbol{x}}}\, dV_{\boldsymbol{x}} \\ &= \frac{K}{2}\int_{\boldsymbol{x}\in\Omega}\int_{\hat{\boldsymbol{x}}\in\Omega} C_\delta(|\boldsymbol{x}-\hat{\boldsymbol{x}}|)\cdot \operatorname{sign}(2-(\boldsymbol{n}-\hat{\boldsymbol{n}})^2)\cdot \epsilon_{ijk}\left(n_i-\hat{n}_i\right) n_j p_k\, dV_{\hat{\boldsymbol{x}}}\, dV_{\boldsymbol{x}} \\ &\quad - \frac{K}{2}\int_{\boldsymbol{x}\in\Omega}\int_{\hat{\boldsymbol{x}}\in\Omega} C_\delta(|\boldsymbol{x}-\hat{\boldsymbol{x}}|)\cdot \operatorname{sign}(2-(\boldsymbol{n}-\hat{\boldsymbol{n}})^2)\cdot \epsilon_{ijk}\left(n_i-\hat{n}_i\right)\hat{n}_j\hat{p}_k\, dV_{\hat{\boldsymbol{x}}}\, dV_{\boldsymbol{x}} \\ &= K\int_{\boldsymbol{x}\in\Omega} p_k \int_{\hat{\boldsymbol{x}}\in\Omega} C_\delta(|\boldsymbol{x}-\hat{\boldsymbol{x}}|)\cdot \operatorname{sign}(2-(\boldsymbol{n}-\hat{\boldsymbol{n}})^2)\cdot \epsilon_{ijk}\left(n_i-\hat{n}_i\right) n_j\, dV_{\hat{\boldsymbol{x}}}\, dV_{\boldsymbol{x}} \end{aligned} \tag{3.6}$$

where we have relabeled $\boldsymbol{x} \leftrightarrow \hat{\boldsymbol{x}}$ to combine integrals in the second line.

Using that p_k is an arbitrary field, we eliminate the integration over $\boldsymbol{x}$:

$$\epsilon_{ijk} n_j \int_{\hat{\boldsymbol{x}}\in\Omega} C_\delta(|\boldsymbol{x}-\hat{\boldsymbol{x}}|)\cdot \operatorname{sign}(2-(\boldsymbol{n}-\hat{\boldsymbol{n}})^2)\cdot (n_k-\hat{n}_k)\, dV_{\hat{\boldsymbol{x}}} = 0 \tag{3.7}$$

We compare this with the statement of equilibrium in the classical 1-constant model: $\epsilon_{ijk} n_j n_{k,ll} = 0$.

In 2D, an orientational description $\boldsymbol{n} = (\sin\theta(\boldsymbol{x}), \cos\theta(\boldsymbol{x}))$ gives:

$$E[\theta] = \frac{K}{2}\int_{\boldsymbol{x}\in\Omega}\int_{\hat{\boldsymbol{x}}\in\Omega} \frac{1}{2} C_\delta(|\boldsymbol{x}-\hat{\boldsymbol{x}}|)\left(1-|\cos(\hat{\theta}-\theta)|\right)\, dV_{\hat{\boldsymbol{x}}}\, dV_{\boldsymbol{x}} \tag{3.8}$$

for the energy, and equilibrium configurations are described by:

$$K\int_{\hat{\boldsymbol{x}}\in\Omega} C_\delta(|\boldsymbol{x}-\hat{\boldsymbol{x}}|)\operatorname{sign}\left[\cos(\theta-\hat{\theta})\right]\, \sin(\hat{\theta}-\theta)\, dV_{\hat{\boldsymbol{x}}} = 0 \tag{3.9}$$

As in the classical case, we deduce the evolution equation using $\gamma_1\langle\dot{\boldsymbol{n}}, \delta\boldsymbol{n}\rangle = -\frac{d}{d\varepsilon} E\left[\boldsymbol{n}+\varepsilon\delta\boldsymbol{n}\right]\big|_{\varepsilon=0}$ using the variation $\delta n_i = \epsilon_{ijk} n_j p_k$, where $\boldsymbol{p}$ is arbitrary. This gives us:

$$\begin{aligned} \gamma_1\dot{\boldsymbol{n}}\times\boldsymbol{n} &= \left(K\int_{\hat{\boldsymbol{x}}\in\Omega} C_\delta(|\boldsymbol{x}-\hat{\boldsymbol{x}}|)\cdot \operatorname{sign}(2-(\boldsymbol{n}-\hat{\boldsymbol{n}})^2)\cdot(\boldsymbol{n}-\hat{\boldsymbol{n}})\, dV_{\hat{\boldsymbol{x}}}\, dV_{\boldsymbol{x}}\right)\times\boldsymbol{n} \\ \Rightarrow \gamma_1\dot{\boldsymbol{n}} &= K\int_{\hat{\boldsymbol{x}}\in\Omega} C_\delta(|\boldsymbol{x}-\hat{\boldsymbol{x}}|)\cdot \operatorname{sign}(2-(\boldsymbol{n}-\hat{\boldsymbol{n}})^2)\cdot(\boldsymbol{n}-\hat{\boldsymbol{n}})\, dV_{\hat{\boldsymbol{x}}}\, dV_{\boldsymbol{x}} + \lambda\boldsymbol{n} \end{aligned} \tag{3.10}$$

Enforcing $\boldsymbol{n}\cdot\boldsymbol{n} = 1 \Rightarrow \dot{\boldsymbol{n}}\cdot\boldsymbol{n} = 0$ to eliminate λ gives:

$$\gamma_1\dot{\boldsymbol{n}} = (\boldsymbol{I}-\boldsymbol{n}\otimes\boldsymbol{n})\cdot K\int_{\hat{\boldsymbol{x}}\in\Omega} C_\delta(|\boldsymbol{x}-\hat{\boldsymbol{x}}|)\cdot \operatorname{sign}(2-(\boldsymbol{n}-\hat{\boldsymbol{n}})^2)\cdot(\boldsymbol{n}-\hat{\boldsymbol{n}})\, dV_{\hat{\boldsymbol{x}}}\, dV_{\boldsymbol{x}} \tag{3.11}$$

The corresponding 2D orientational description is:

$$-K\int_{\hat{\boldsymbol{x}}\in\Omega} C_\delta(|\boldsymbol{x}-\hat{\boldsymbol{x}}|)\operatorname{sign}\left[\cos(\theta-\hat{\theta})\right]\, \sin(\hat{\theta}-\theta)\, dV_{\hat{\boldsymbol{x}}} = \dot{\theta} \tag{3.12}$$

The dissipation associated with the nonlocal model can be computed:

$$\begin{aligned} -\frac{dE}{dt} &= \frac{K}{2}\int_{\boldsymbol{x}\in\Omega}\int_{\hat{\boldsymbol{x}}\in\Omega} C_\delta(|\boldsymbol{x}-\hat{\boldsymbol{x}}|)\cdot \operatorname{sign}\left(2-(\boldsymbol{n}-\hat{\boldsymbol{n}})^2\right)\cdot(\boldsymbol{n}-\hat{\boldsymbol{n}})\cdot\left(\dot{\boldsymbol{n}}-\dot{\hat{\boldsymbol{n}}}\right)\, dV_{\hat{\boldsymbol{x}}}\, dV_{\boldsymbol{x}} \\ &= K\int_{\boldsymbol{x}\in\Omega}\dot{\boldsymbol{n}}\cdot\int_{\hat{\boldsymbol{x}}\in\Omega} C_\delta(|\boldsymbol{x}-\hat{\boldsymbol{x}}|)\cdot \operatorname{sign}\left(2-(\boldsymbol{n}-\hat{\boldsymbol{n}})^2\right)\cdot(\boldsymbol{n}-\hat{\boldsymbol{n}})\, dV_{\hat{\boldsymbol{x}}}\, dV_{\boldsymbol{x}} \\ &= \frac{1}{\gamma_1}\int_{\boldsymbol{x}\in\Omega}\boldsymbol{A}\cdot(\boldsymbol{I}-\boldsymbol{n}\otimes\boldsymbol{n})\cdot\boldsymbol{A}\, dV_{\boldsymbol{x}} \end{aligned} \tag{3.13}$$

where $\boldsymbol{A} := K \int_{\hat{\boldsymbol{x}} \in \Omega} C_\delta(|\boldsymbol{x} - \hat{\boldsymbol{x}}|) \cdot \operatorname{sign}\left(2 - (\boldsymbol{n} - \hat{\boldsymbol{n}})^2\right) \cdot (\boldsymbol{n} - \hat{\boldsymbol{n}}) \; dV_{\hat{\boldsymbol{x}}}$. Since $\boldsymbol{I} - \boldsymbol{n} \otimes \boldsymbol{n}$ is positive semi-definite, it follows that the dissipation is always non-negative.

3.5 Boundary Conditions

As in the peridynamic model of elasticity, boundary conditions cannot be applied in the classical sense. Roughly, imposing conditions on the boundary – a set of measure 0 in the integral – provides an infinitesimal contribution to the integral. However, a physically-natural solution to this issue is to instead impose conditions over a layer of finite thickness – with thickness of order δ – on the boundary. Given that in our model molecules interact over a finite range, it is natural to provide boundary conditions with more structure than holding them fixed on a low-dimensional set (the boundary). For instance, to impose that the nematic molecules have a specific orientation on the boundary, we hold the orientation fixed for all molecules within the boundary layer region. That is, $\theta(\boldsymbol{x}) = \theta_0 \; \forall \boldsymbol{x} \in \Omega_{bl}$ where Ω_{bl} is a portion of the Ω with finite volume. In this paper, this is the only type of boundary condition that we use, but other boundary conditions can be similarly smeared-out following the techniques used in peridynamics [Sil00, SL10, DB06].

4 Bend and Splay: Extension Beyond the 1-Constant Energy

In the classical 1-constant model, a single modulus K defines the energy in the bend, splay, and twist modes. The more general Frank free energy has different moduli for each of these modes. We examine the same issue in the nonlocal regularized energy. We restrict ourselves to 2D and therefore only distinguish between bend and splay, but an extension to 3D that also incorporates twist is conceptually analogous.

The physical basis for 3 different moduli is seen from Fig. 2. We can differentiate between these modes as follows. Splay can be differentiated from both bend and twist by noticing that the quantity $(\boldsymbol{n}-\hat{\boldsymbol{n}})\cdot(\boldsymbol{x}-\hat{\boldsymbol{x}})$ is 0 for both bend and twist, but is nonzero – and can be normalized to 1 – for splay. Similarly, bend can be differentiated from both splay and twist by using the quantity $\boldsymbol{n} \cdot (\boldsymbol{x} - \hat{\boldsymbol{x}})$, which is 0 for both splay and twist but is nonzero and normalizable to 1 for bend.

Since we are currently only working in 2D and considering only bend and splay modes, we need only differentiate these 2 modes here. We write for the modulus $K = K_s \left(1 - \left|\boldsymbol{n} \cdot \hat{\delta\boldsymbol{x}}\right|\right) + K_b \left|\boldsymbol{n} \cdot \hat{\delta\boldsymbol{x}}\right|$, where $\hat{\delta\boldsymbol{x}} \equiv \frac{\hat{\boldsymbol{x}}-\boldsymbol{x}}{|\hat{\boldsymbol{x}}-\boldsymbol{x}|}$. Then, K_s is the coefficient for splay and K_b is the coefficient for bending. When $\boldsymbol{n} \cdot \hat{\delta\boldsymbol{x}} = 0$, then we have splay, and when $\boldsymbol{n} \cdot \hat{\delta\boldsymbol{x}} = 1$ we have bending.

Using the orientational description for compactness, the energy can now be written:

$$E[\theta] = \int_{\boldsymbol{x} \in \Omega} \int_{\hat{\boldsymbol{x}} \in \Omega} \frac{K(\theta, \boldsymbol{x}, \hat{\boldsymbol{x}})}{2} \cdot \frac{1}{2} C_\delta(|\boldsymbol{x} - \hat{\boldsymbol{x}}|) \left(1 - |\cos(\hat{\theta} - \theta)|\right) \; dV_{\hat{\boldsymbol{x}}} \; dV_{\boldsymbol{x}} \tag{4.1}$$

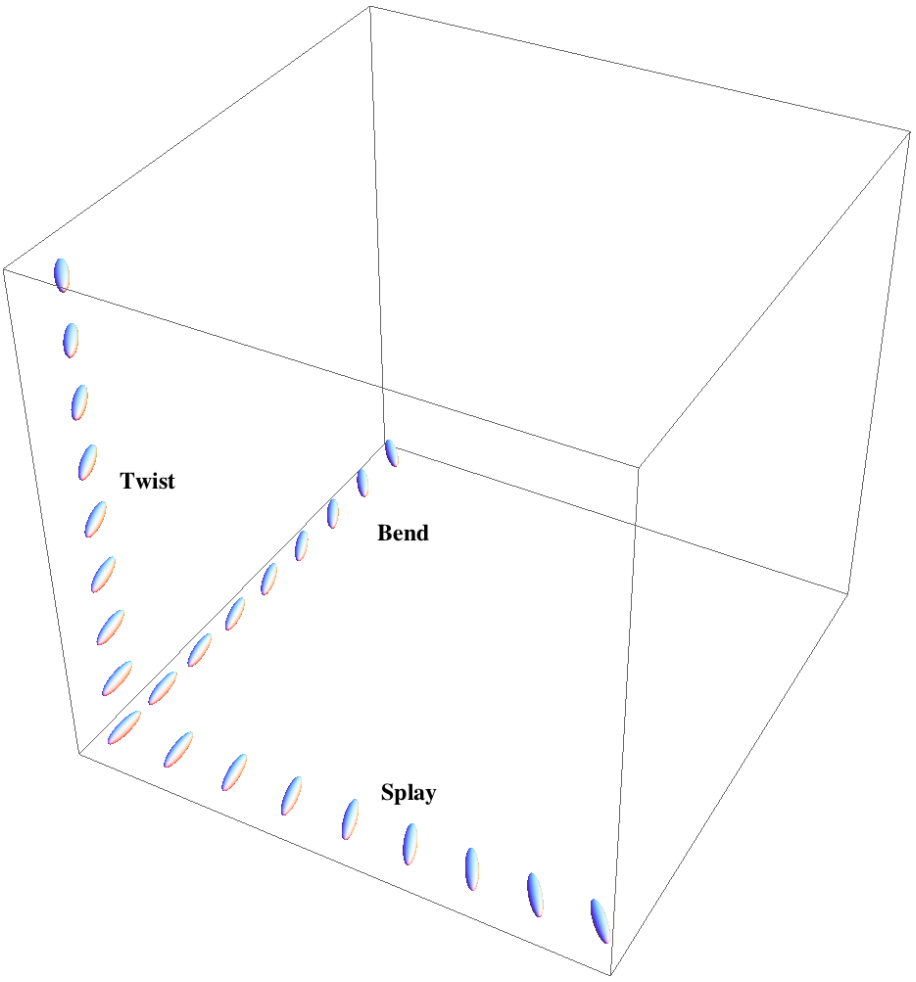


Figure 2: Bend, Splay and Twist modes. These modes can be differentiated in our nonlocal model by using the quantities $(\boldsymbol{n}-\hat{\boldsymbol{n}})\cdot(\boldsymbol{x}-\hat{\boldsymbol{x}})$ and $\boldsymbol{n}\cdot(\boldsymbol{x}-\hat{\boldsymbol{x}})$. When normalized, these quantities are both 0 for twist, 0 and 1 respectively for bend, and 1 and 0 respectively for splay.

We can also identify the bending and splay contributions individually:

$$\begin{aligned} E[\theta] = &\underbrace{\frac{1}{2}K_b\int_{\boldsymbol{x}\in\Omega}\int_{\hat{\boldsymbol{x}}\in\Omega}\frac{1}{2}C_\delta(|\boldsymbol{x}-\hat{\boldsymbol{x}}|)\left|\boldsymbol{n}\cdot\hat{\delta\boldsymbol{x}}\right|\Big(1-|\cos(\hat{\theta}-\theta)|\Big)\,dV_{\hat{\boldsymbol{x}}}\,dV_{\boldsymbol{x}}}_{\text{bend}} \\ &+\underbrace{\frac{1}{2}K_s\int_{\boldsymbol{x}\in\Omega}\int_{\hat{\boldsymbol{x}}\in\Omega}\frac{1}{2}C_\delta(|\boldsymbol{x}-\hat{\boldsymbol{x}}|)\Big(1-\left|\boldsymbol{n}\cdot\hat{\delta\boldsymbol{x}}\right|\Big)\Big(1-|\cos(\hat{\theta}-\theta)|\Big)\,dV_{\hat{\boldsymbol{x}}}\,dV_{\boldsymbol{x}}}_{\text{splay}} \end{aligned} \tag{4.2}$$

The evolution equation is obtained from a gradient descent based on θ without any constraints:

$$-\int_{\hat{\boldsymbol{x}}\in\Omega}C_\delta(|\boldsymbol{x}-\hat{\boldsymbol{x}}|)\left(\frac{dK}{d\theta}\cdot\Big(1-|\cos(\hat{\theta}-\theta)|\Big)+K(\theta)\cdot\operatorname{sign}\Big[\cos(\theta-\hat{\theta})\Big]\,\sin(\hat{\theta}-\theta)\right)dV_{\hat{\boldsymbol{x}}}=\dot{\theta} \tag{4.3}$$

The equilibrium equation is obtained by setting the right side above to 0.

5 Structure and Stability of Individual Disclinations

We use the model to examine the stability and structure of various half-integer and integer disclinations. We examine these using the 1-constant nonlocal energy as well as the energy that differentiates between bend and splay.

5.1 The 1-Constant Nonlocal Energy

In the 1-constant nonlocal energy, we find that only $\pm\frac{1}{2}$ disclinations are stable; disclinations of higher strength always split into the appropriate number of $\pm\frac{1}{2}$ disclinations. We show some examples of this below.

In all of these calculations, we use a discretization mesh size of 1 with $\delta = 5$, except where stated otherwise. We use a square domain with size 200×200. For the starting configuration, we use the classical formula for a disclination $\boldsymbol{n}(\boldsymbol{x}) = (\sin(k\theta_0(\boldsymbol{x}) + \alpha), \cos(k\theta_0(\boldsymbol{x}) + \alpha)$, where $\tan\theta_0 = x_2/x_1$, and then evolve using the equations presented above. The initial and final configurations are shown in Fig. 3.

This finding agrees qualitatively with calculations in [MHML05, BKŽ98] which use the Q-tensor and molecular dynamics methods respectively, in that only $\pm\frac{1}{2}$ defects are stable in the 1-constant energy. It is consistent also with the heuristic that the energy of a disclination scales with the square of the charge that it carries [dP95], as well as rigorous work [BPP12].

While the final states are largely in agreement with other aproaches, the dynamics is qualitatively different in our model compared to the Q-tensor calculations from [MHML05]. They find that a $+2$ defect first splits into two $+1$ defects, and then splits a second time into four $+\frac{1}{2}$ defects. In our calculations, all of the defects split almost instantly into $\pm\frac{1}{2}$ disclinations that are then repelled from each other and move apart. While their geometry is circular and hence different from our square domain, in both their work and ours the domain is large enough that it is unlikely that this is the reason for the difference. It is likely a consequence of the differences between the evolution equations in the Ericksen-Leslie model with our energy vs. the Q-tensor model.

We also notice that the energy (3.4) has stable ± 1 disclinations and does not form $\pm\frac{1}{2}$ disclinations. However, this occurs due to the unphysical feature that the lack of head-tail symmetry associates a very high energy to the line (in 2D) across which the director changes sense that accompanies $\pm\frac{1}{2}$ disclinations.

We then examine the detailed structure of the core for $\pm\frac{1}{2}$ defects. For these calculations, we use a much finer discretization of 0.1 with the same value of δ. In an initial set of calculations, we began with the classical solution as above, and evolved to find the relaxed configuration. The solutions in our model are extremely close to the starting classical solution, and the changes are dominated by numerical discretization errors. So we instead use as initial the classical solution everywhere outside a core region of radius 2; within this region, we set all directors to point vertically. The director field relaxes to a solution that is again very similar to the classical solution, but the disclination translates during the relaxation due to the severe perturbation that we have induced in the initial conditions. We therefore perform a best fit of the relaxed configuration against the formula for a translated disclination, treating the disclination center as the parameters to optimize over. Fig. 4 shows the change in the director angle. The difference between our solution and the classical disclination solution is confined to the core region, and even there is small.

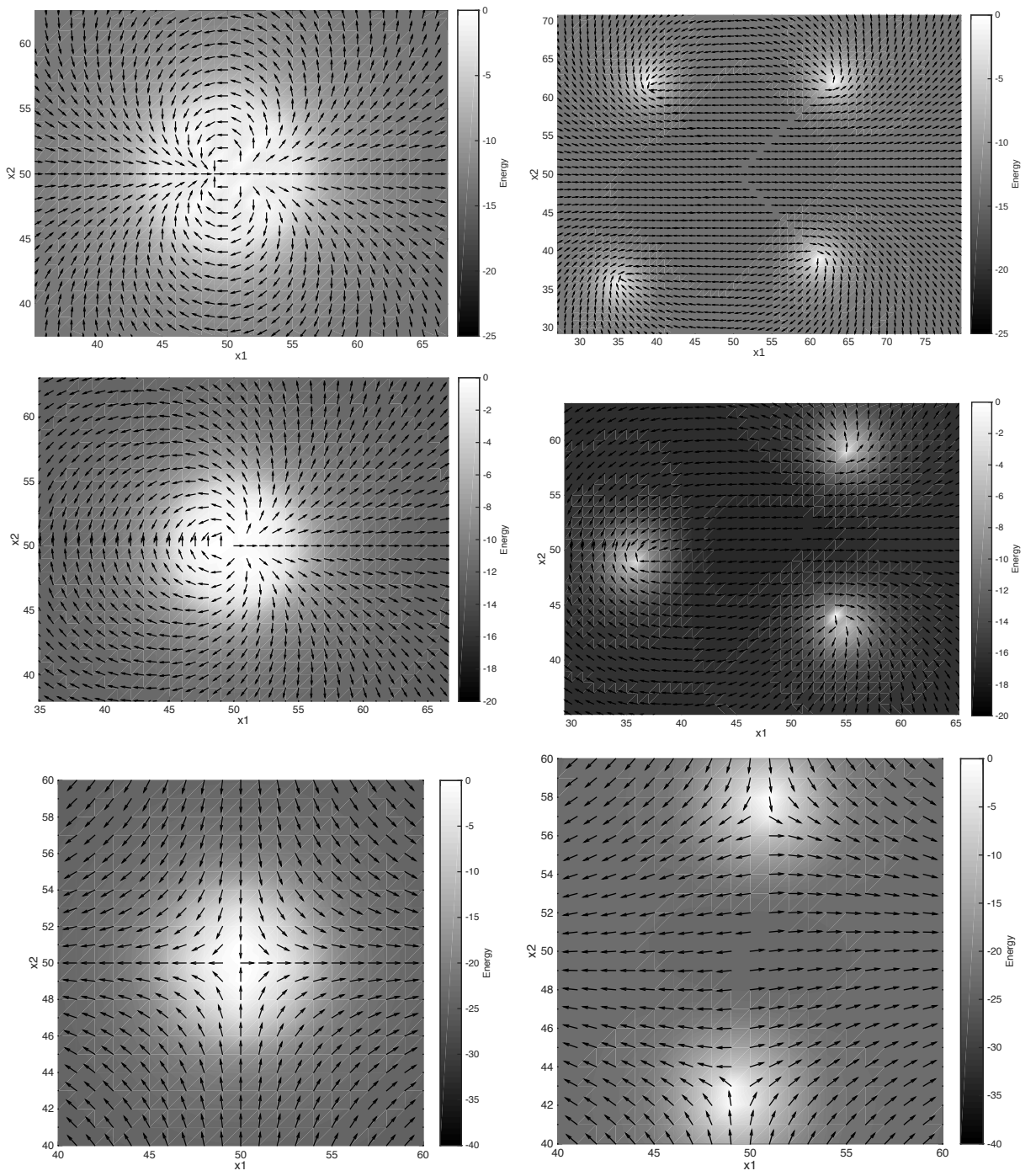


Figure 3: Top: A $+2$ disclination constructed using the classical solution (right), and the final configuration of four well-separated $+\frac{1}{2}$ disclinations (right). Middle: The similar process for a $+3/2$ disclination decomposing into three $+\frac{1}{2}$ disclinations. Bottom: A -1 disclination decomposing into two $-\frac{1}{2}$ disclinations. The vector field is overlaid on the energy density. We observe similar decompositions in $+1, -3/2$, and other disclinations stronger than $\pm\frac{1}{2}$.

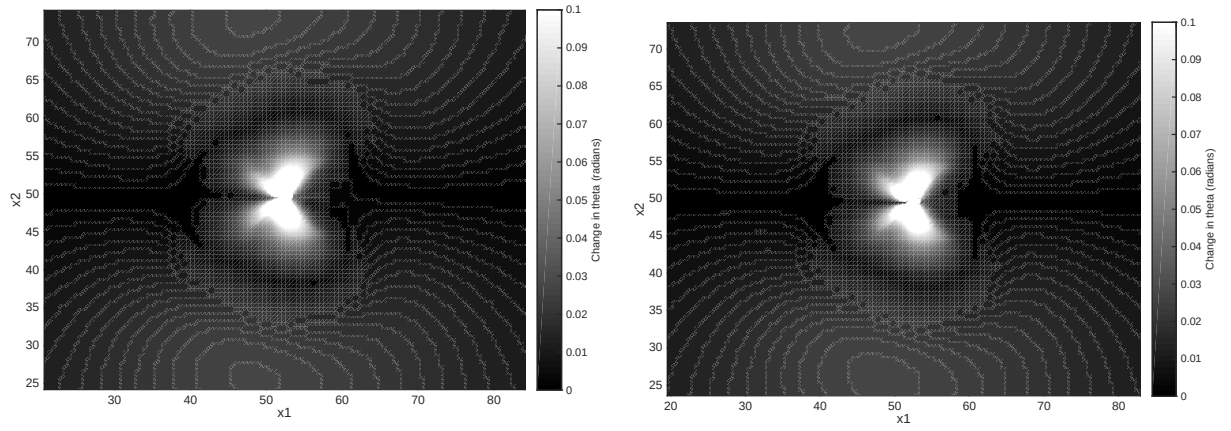


Figure 4: Angular difference between a classical disclination solution and our relaxed disclination configuration for $+\frac{1}{2}$ (left) and $-\frac{1}{2}$ (right).

5.2 Disclinations in the Bend-Splay Energy

In the previous subsection, we see that the nonlocal 1-constant energy has only $\pm\frac{1}{2}$ disclinations. In experiments, however, it has been noticed that ± 1 defects dissociate into two closely-spaced $\pm\frac{1}{2}$ cores [MPR14]. As described in [YR02], the dissociation of ± 1 disclinations is controlled by the ratio of bend to splay energies. Looking at Fig. 1, we see that the $+1$ disclination is dominated by bend, whereas the $+\frac{1}{2}$ disclination has a significant amount of both splay and bend. We notice that in our approach to differentiating between bend and splay based on $\boldsymbol{n} \cdot (\boldsymbol{x} - \hat{\boldsymbol{x}})$, there will be some level of splay character in the classical $+1$ defect because of contributions from points that are at around $\pm\pi/4$ to the director orientation. We examine the behavior of a $+1$ disclination in our model at two limits, one with $K_s = 10K_b$ and the other with $K_s = 0.1K_b$.

We first plot the partitioning of energy between bend and splay in the classical solution with $K_b = K_s$ in Fig. 5. As we expect, the bending energy is generally dominant, though the splay energy is not vanishing as explained above.

We then evolve the director field from this initial configuration. In the case when the bending modulus is large compared to the splay modulus ($K_b \gg K_s$), bending is expensive energetically and hence the system dissociated into two $+\frac{1}{2}$ disclinations in which some of the distortion can be accommodated as splay (Fig. 6, top). In the case when the bending modulus is small compared to the splay modulus ($K_b \ll K_s$), bending is not expensive and hence the system retains roughly the original disclination configuration thereby reducing the amount of splay (Fig. 6, bottom). Intermediate configurations between these two limits lead to partially dissociated disclinations that are qualitatively comparable to the observations in [MPR14] and the theoretical model in [YR02].

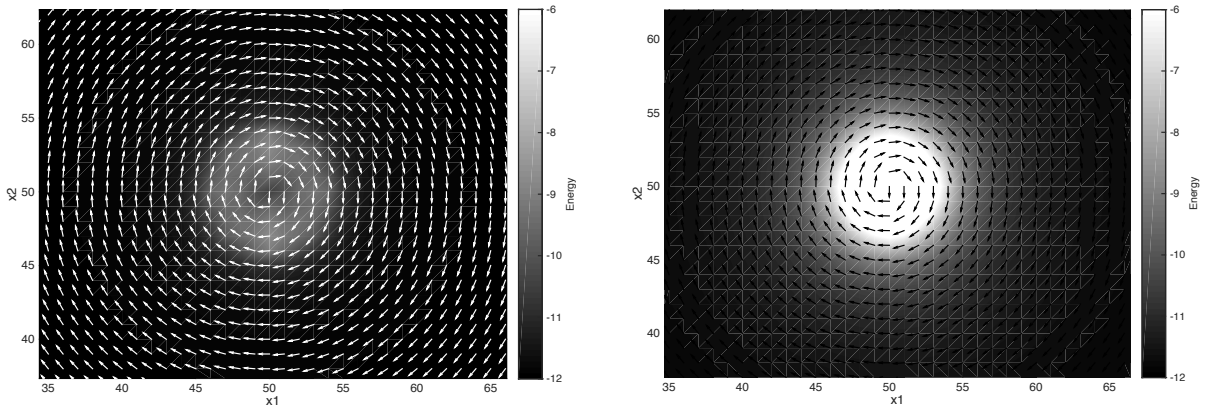


Figure 5: Partitioning of the energy into splay (left) and bend (right) energies with $K_b = K_s$. The bending distortion has significantly higher energy. Both are localized around the disclination core.

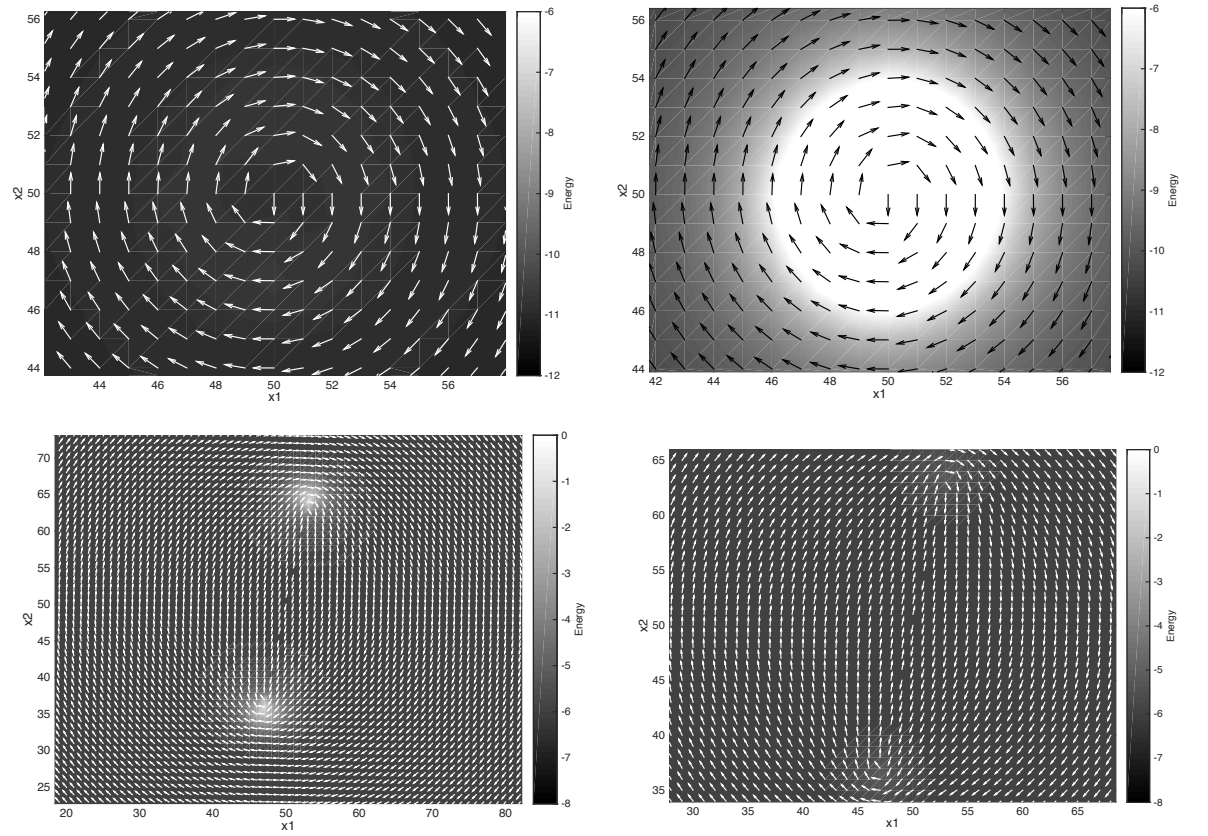


Figure 6: Top row: Energy partitioning into splay (left) and bend (right) in the final configuration for $K_s = 10K_b$, i.e., splay is much more expensive than bending. The defect retains a $+1$ character to minimize splay distortion. Bottom row: Energy partitioning into splay (left) and bend (right) in the final configuration for $K_s = 10K_b$, i.e, bending is much more expensive than splay. The defect dissociates to reduce the bending distortion and compensates with a higher splay distortion.

6 Coalescence of $+\frac{1}{2}$ and $-\frac{1}{2}$ Disclinations

We next use our model to examine the evolution of 2 disclinations of equal-and-opposite $\pm\frac{1}{2}$ topological charge. Two such disclinations will attract each other, causing them to move towards each other and eventually coalesce to form a disclination-free material. Whether these defects move at the same velocity towards each other, and hence coalesce at the midpoint between the initial defect positions, has been an important question. This has been the focus of both experimental and theoretical investigation. A key experiment observing coalescence of *point* defects in nematics shows that there is asymmetry in their motion [CB03]. Closely related situations have been studied numerically [SŽ03, TDY02, SŽ02] and theoretically [GSV02]; while some of these systems are significantly different from the nematics studied here, a key broad finding is the significant influence from hydrodynamic effects.

A priori, there is no reason for equal-and-opposite topological disclinations to move at the same velocity. Disclinations are *not* analogous to electrical point charges which have no internal structure and are therefore perfectly anti-symmetric. Rather, the topological charge is simply one average measure – admittedly an extremely important measure – of the defect structure. The detailed structure of the disclination plays an important role in the dynamics, and even if different disclinations of the same strength have the same force acting on them, the detailed structure is essential in setting the dynamics in response to the force. Returning to the electrical analogy, a complex charge distribution can be characterized by the net charge, but the dynamics of the charge distribution in response to another charge distribution cannot be characterized solely in terms of the net charges of both distributions.

We examine this situation using our simple 1-constant regularized model using $\pm\frac{1}{2}$ disclinations. Fig. 7 shows the initial configuration with two $\pm\frac{1}{2}$ disclinations and the final defect-free configuration. The force between disclinations falls off very rapidly with distance, and hence there is initially little movement. However, as the disclinations begin to come closer, the force increases, thereby further increasing the velocity, and so on. Eventually, the disclinations coalesce and leave behind a disclination-free material. A movie of the coalescence process is part of the supplementary material, and we quantify the approach in Fig. 8. While small, there is an unmistakable difference in the velocities of the positive and negative defects. Given that our 1-constant regularized model contains no complexities such as flow, or even different moduli for bend and splay, it suggests that this asymmetry in disclination velocity has its origin in the asymmetry of the director field; flow further enhances this effect when present [TDY02, SŽ02].

7 Conclusions

We present a nonlocal regularized model that exploits integral operators to achieve a generalization of the classical Ericksen-Leslie model for nematics. Near disclinations, the model regularizes defect cores, and as the distortion becomes uniform, it recovers the Ericksen-Leslie model. The use of integral operators – as opposed to differential operators in the classical approach – enables us to model situations in which the disclination field is not continuous. As we describe, the integral operators tend to the differential operators in a physically meaningful way.

Our approach uses in an essential way the important ideas behind peridynamics [Sil00, SL10]. However, the head-tail asymmetry that is essential in describing liquid crystals does not have an analog in peridynamics which is tailored to deformation fields. For this reason, it is not possible to directly use

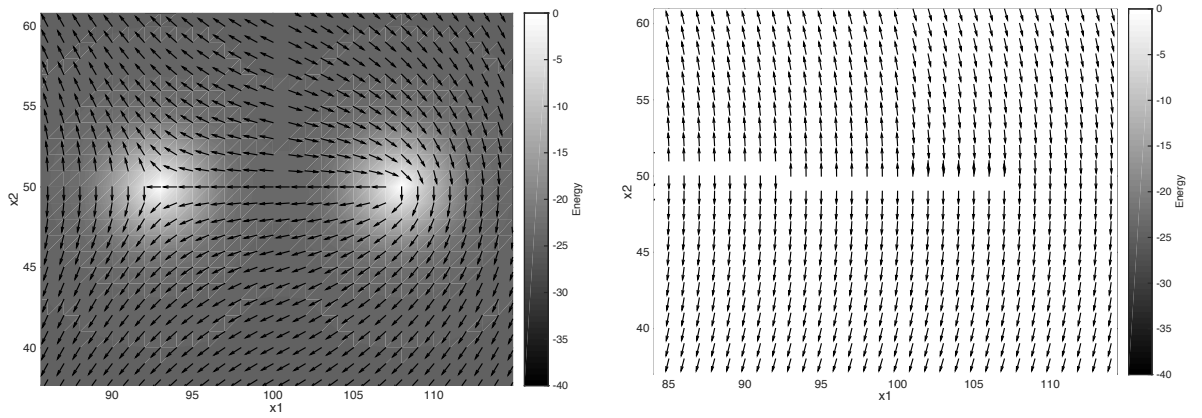


Figure 7: Initial configuration (left) with two $\pm\frac{1}{2}$ defects, and the final defect-free configuration (right).

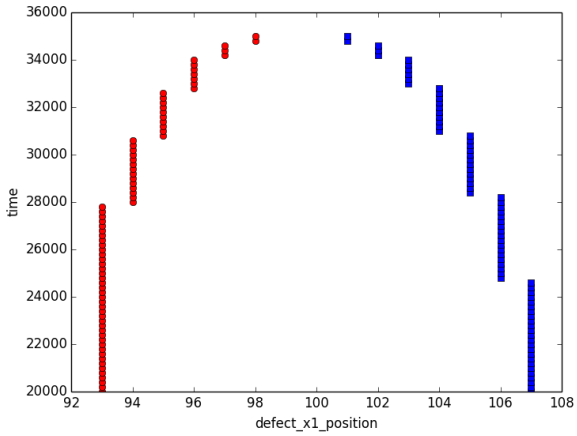


Figure 8: Disclination core positions as a function of time. Red circles are $-\frac{1}{2}$ and blue squares are $+\frac{1}{2}$. The disclination cores are located by finding the mesh point with the highest energy density. The motion appears discontinuous because we only sample over a discrete mesh. The higher velocity of the $+\frac{1}{2}$ disclination is clear from the plot. The velocity increases as the disclinations approach, as is expected.

generalizations of peridynamics to construct energies in liquid crystals. In particular, the 3-constant Frank free energy that we construct appears quite different from, and does not seem to have analogies to, strategies used in peridynamics to model complex materials.

This is a preliminary step towards the formulation of this class of models. While we have demonstrated it in the context of nematics, it is readily generalizable to other liquid crystalline material such as smectics. The key issues that we have dealt with here – namely unit vector fields that have discontinuities – are the central challenges in this class of materials. In addition, we have not fit the many material parameters here to specific materials. For instance, the regularization scale δ, the precise form of the kernel C_δ, and the precise angular dependence of K, can all be tailored to capture specific types of physics; for instance, if detailed dynamic behavior is to be predicted. We have also restricted ourselves to 2D for simplicity, but an extension to 3D is conceptually simple. Such an extension would enable the interrogation of more realistic geometries, as well as enable us to examine twist distortions.

Our numerical approximations have used finite differences for simplicity. However, powerful numerical techniques such as discontinuous Galerkin finite elements (DGFEM) can enable the efficiency of adaptive meshing and finite elements to attack much bigger problems and complex geometries with our model. While defect tracking can be enormously expensive, results from [DGLZ12, CG11] suggest that DGFEM offers an efficient approach: it is a conforming approximation for peridynamics, and the results appear not very sensitive to the errors in tracking the defect.

Acknowledgments

We thank Noel Walkington and Chuck Gartland for useful discussions and pointers to the literature, and Nigel Mottram for pointing us to [PMGK94, BGJRV03]. For financial support, we all thank NSF (CAREER 1150002); Hossein Pourmatin also thanks AFOSR (YI FA9550-12-1-0350); and Kaushik Dayal also thanks ARO (YI W911NF-12-1-0156) and Carnegie Mellon University College of Engineering for the Early Career Fellowship. This research was also supported in part by the National Science Foundation through TeraGrid resources provided by Pittsburgh Supercomputing Center.

References

[AD14] Amit Acharya and Kaushik Dayal, *Continuum mechanics of line defects in liquid crystals and liquid crystal elastomers*, Quarterly of Applied Mathematics **72** (2014), no. 1, 33–64.

[AKST14] François Alouges, Evaggelos Kritsikis, Jutta Steiner, and Jean-Christophe Toussaint, *A convergent and precise finite element scheme for landau–lifschitz–gilbert equation*, Numerische Mathematik **128** (2014), no. 3, 407–430.

[BGJRV03] Fulvio Bisi, Eugene C Gartland Jr, Riccardo Rosso, and Epifanio G Virga, *Order reconstruction in frustrated nematic twist cells*, Physical Review E **68** (2003), no. 2, 021707.

[BKŽ98] Zlatko Bradač, Samo Kralj, and Slobodan Žumer, *Molecular dynamics study of nematic structures confined to a cylindrical cavity*, Physical Review E **58** (1998), no. 6, 7447.

[BPP12] Patricia Bauman, Jinhae Park, and Daniel Phillips, *Analysis of nematic liquid crystals with disclination lines*, Arch. Ration. Mech. Anal. **205** (2012), no. 3, 795–826. MR 2960033

[BVD04] Fulvio Bisi, Epifanio G Virga, and Georges E Durand, *Nanomechanics of order reconstruction in nematic liquid crystals*, Physical Review E **70** (2004), no. 4, 042701.

[CB03] PE Cladis and Helmut R Brand, *Hedgehog–antihedgehog pair annihilation to a static soliton*, Physica A: Statistical Mechanics and its Applications **326** (2003), no. 3, 322–332.

[CG11] Xi Chen and Max Gunzburger, *Continuous and discontinuous finite element methods for a peridynamics model of mechanics*, Computer Methods in Applied Mechanics and Engineering **200** (2011), no. 9, 1237–1250.

[CL00] Paul M Chaikin and Tom C Lubensky, *Principles of condensed matter physics*, vol. 1, Cambridge Univ Press, 2000.

[CLB+09] Giovanni Carbone, Giuseppe Lombardo, Riccardo Barberi, Igor Muševič, and Uroš Tkalec, *Mechanically induced biaxial transition in a nanoconfined nematic liquid crystal with a topological defect*, Physical review letters **103** (2009), no. 16, 167801.

[DB06] Kaushik Dayal and Kaushik Bhattacharya, *Kinetics of phase transformations in the peridynamic formulation of continuum mechanics*, Journal of the Mechanics and Physics of Solids **54** (2006), no. 9, 1811–1842.

[DGLZ12] Qiang Du, Max Gunzburger, Richard B Lehoucq, and Kun Zhou, *Analysis and approximation of nonlocal diffusion problems with volume constraints*, SIAM review **54** (2012), no. 4, 667–696.

[dP95] P deGennes and J Prost, *The physics of liquid crystals*, no. 83, Oxford university press, 1995.

[Eri91] Jerald L Ericksen, *Liquid crystals with variable degree of orientation*, Archive for Rational Mechanics and Analysis **113** (1991), no. 2, 97–120.

[GSV02] Eugene C Gartland, Jr, André M Sonnet, and Epifanio G Virga, *Elastic forces on nematic point defects*, Continuum Mechanics and Thermodynamics **14** (2002), no. 3, 307–319.

[KL07] Maurice Kléman and Oleg D Lavrentovich, *Soft matter physics: an introduction*, Springer Science & Business Media, 2007.

[KLGCC08] D Harley Klein, L Gary Leal, Carlos J García-Cervera, and Hector D Ceniceros, *Three-dimensional shear-driven dynamics of polydomain textures and disclination loops in liquid crystalline polymers*, Journal of Rheology (1978-present) **52** (2008), no. 3, 837–863.

[MHML05] Dmitri Miroshnychenko, NA Hill, NJ Mottram, and JE Lydon, *Evolution from a+ 2 defect to+ 1/2 defects in a cylindrical geometry*, Molecular Crystals and Liquid Crystals **437** (2005), no. 1, 251–1495.

[MN14] Nigel J Mottram and Christopher JP Newton, *Introduction to q-tensor theory*, arXiv preprint arXiv:1409.3542 (2014).

[MPR14] Bryce S Murray, Robert A Pelcovits, and Charles Rosenblatt, *Creating arbitrary arrays of two-dimensional topological defects*, Physical Review E **90** (2014), no. 5, 052501.

[PAD15] Hossein Pourmatin, Amit Acharya, and Kaushik Dayal, *A fundamental improvement to ericksen-leslie kinematics.*, Quarterly of Applied Mathematics **73** (2015), no. 3, 435–466.

[PMGK94] P Palffy-Muhoray, EC Gartland, and JR Kelly, *A new configurational transition in inhomogeneous nematics*, Liquid Crystals **16** (1994), no. 4, 713–718.

[Sil00] Stewart A Silling, *Reformulation of elasticity theory for discontinuities and long-range forces*, Journal of the Mechanics and Physics of Solids **48** (2000), no. 1, 175–209.

[SL10] SA Silling and RB Lehoucq, *Peridynamic theory of solid mechanics*, Advances in Applied Mechanics **44** (2010), no. 1, 73–166.

[Ste04] Iain W Stewart, *The static and dynamic continuum theory of liquid crystals: a mathematical introduction*, Crc Press, 2004.

[SŽ02] Daniel Svenšek and Slobodan Žumer, *Hydrodynamics of pair-annihilating disclination lines in nematic liquid crystals*, Physical Review E **66** (2002), no. 2, 021712.

[SŽ03] D Svenšek and S Žumer, *Hydrodynamics of pair-annihilating disclinations in s m c films*, Physical review letters **90** (2003), no. 15, 155501.

[TDY02] Géza Tóth, Colin Denniston, and Julia M Yeomans, *Hydrodynamics of topological defects in nematic liquid crystals*, Physical review letters **88** (2002), no. 10, 105504.

[YFMW09] Xiaofeng Yang, M Gregory Forest, William Mullins, and Qi Wang, *Dynamic defect morphology and hydrodynamics of sheared nematic polymers in two space dimensions*, Journal of Rheology (1978-present) **53** (2009), no. 3, 589–615.

[YR02] Jun Yan and AD Rey, *Theory and simulation of texture formation in mesophase carbon fibers*, Carbon **40** (2002), no. 14, 2647–2660.